UNIVERSITY OF STRATHCLYDE

Faculty of Engineering

Department of Biomedical Engineering

DOCTORATE DISSERTATION

PhD Biomedical Engineering

A NOVEL METHOD FOR KNEE LIGAMENT TENSION DETERMINATION USING DYNAMIC CT IMAGING AND FINITE ELEMENT ANALYSIS

By

Yunlong Gu

Supervised by Dr Philip Riches

A dissertation submitted in fulfilment of the requirements of the award of a

Doctor of Philosophy of the University of Strathclyde

May 2025

DECLARATION

This thesis is the result of the author's original research. It has been composed by the author and has not been previously submitted for examination which has led to the award of a degree.

Signature of Student   Yunlong Gu

Date

ACKNOWLEDGEMENTS

The completion of this thesis marks the culmination of a challenging yet rewarding journey, made possible through the unwavering support, guidance, and encouragement of many individuals to whom I owe immense gratitude.

First and foremost, I extend my deepest appreciation to my doctoral advisor, Dr. Philip Riches. His profound knowledge and extensive experience in the field have been a beacon of guidance throughout my doctoral studies. Dr. Philip Riches invested countless hours, demonstrating remarkable patience and dedication, to ensure that my research was rigorous and meaningful. His insightful feedback and encouragement not only shaped this thesis but also fostered my growth as a scholar. I am truly honoured to have worked under his mentorship.

I am also deeply indebted to Dr. Andre Attard, whose foundational contributions were pivotal in shaping the early stages of my research. His expertise and willingness to share his insights provided a solid framework upon which this work was built.

Finally, I owe an immeasurable debt of gratitude to my parents and family, whose unconditional love and steadfast support have boned my anchor. Their encouragement sustained me through the highs and lows of this academic journey, offering strength in moments of doubt and celebration in times of success. Their belief in my aspirations, coupled with their care in both my academic and personal life, has been a constant source of inspiration.

To all who have contributed to this milestone, whether through intellectual guidance, emotional support, or quiet encouragement, I offer my heartfelt thanks. This thesis stands as a testament to your collective impact on my journey.

Abstract

Background: The knee joint is a critical component of the human skeletal system, essential for facilitating movement and supporting load-bearing activities. Each ligament contributes uniquely to restricting the joint's range of motion across multiple degrees of freedom, ensuring biomechanical stability. However, ligament tensions in vivo are not well known. By estimating ligament tensions during knee flexion, we will not only understand the biomechanics of the native knee better but will inform the soft tissue balancing during knee arthroplasty. This study therefore proposes a novel methodology to quantify ligament tensions in the knee using FEA, informed by four-dimensional computed tomography (4dCT). **Methods:** High-resolution 4dCT scans from a healthy participant captured the dynamics of the knee joint across a full range of motion. An FEA model of the knee was constructed, and a novel iterative scheme was used to estimate the tension in the patella tendon and four main ligaments of the knee. Point clouds were used to track the knee during movement, self-validating the model, and providing insight into the accuracy of the model in replicating the knee's kinematic behaviour. **Results:** Integration of 4dCT imaging with iterative finite element analysis (FEA) generated a robust model of knee biomechanics, accurately estimating ligament tensions during flexion. Cloud Compare analysis of patellar point clouds showed 75–86% of nodes within ±2.8–4 mm for early flexion (F02–F06), improving to 93–98% within ±1–3.6 mm in later frames, indicating enhanced alignment accuracy. For the tibia, spatial errors were more variable. During the initial flexion phase, 85–88.3% of nodes were within ±5 mm of the reference. Accuracy decreased in the mid-range of motion, with only 63.9–74.8% of nodes within this threshold, before recovering in the final phase of flexion to 91–92.1% within ±5 mm. Combining FEA with 4dCT imaging refined in vivo ligament tension estimates, correlating with observed kinematic motion across flexion angles, validating the model's efficacy in capturing knee biomechanics. **Conclusions:** This study successfully developed and validated an innovative methodology for assessing ligament tension and knee kinematics, combining 4dCT imaging with iterative FEA. The approach provided a more accurate

quantification of native ligament tensions compared to traditional methods, addressing a critical gap in soft tissue balancing for TKR. The high accuracy of the FEA model, as evidenced by its alignment with 4dCT data, underscores its potential as a reliable tool for biomechanical analysis and clinical applications.

Table of Contents

1 Introduction 25

1.1 Clinical Need and Research Direction...27

1.2 Structure of the Thesis 28

2 Literature Review 29

2.1 Bony morphology..29

2.1.1 Femur 31

2.1.2 Tibia... 33

2.1.3 Patella 34

2.2 Soft-Tissues of the Knee Joint...35

2.2.1 Ligaments.. 36

2.2.2 Muscles and Tendons.. 41

2.2.2.1 Muscles... 41

2.2.2.2 Tendons 43

2.2.3 Meniscus and cartilage... 46

2.2.3.1 Articular Surface 46

2.2.3.2 Meniscus... 48

2.2.4 Lubrication system 50

2.3 Soft Tissue Biomechanics..52

2.3.1 Ligaments and Tendon 52

2.3.2 Insertion of Ligaments and Patellar Tendon 54

2.3.3 Ligament stress and strain 56

2.3.4 Joint Stability and Soft Tissue Balancing... 60

2.3.5 In vivo tension 62

2.3.6 Measurement of ligament tension, strain, and stress 64
2.3.6.1 In Vitro Techniques 64
2.3.6.2 In Vivo Techniques 69
2.3.6.3 In Silico Modelling Techniques 70
2.4 4D Computed Tomography (4dCT) 79
2.5 Computational Simulation 82
2.5.1 Finite Element Modelling / Analysis (FEM/A) 83
2.5.2 FEA combined with 4dCT 85
2.5.3 Boundary conditions 88
2.5.3.1 Geometric boundary conditions 90
2.5.3.2 Load Boundary Conditions 90
2.5.4 Initial conditions 90
2.5.5 Knee ligaments as springs 91
2.5.6 Indeterminacy 92
2.5.7 Necessity of Integrating 4dCT with Finite Element Analysis for Knee Biomechanics 95
2.6 Thesis Aims 97
2.6.1 To develop a novel methodology to determine ligament tensions in the knee through inverse FE analyses. 98
2.6.2 To self-validate the novel FE model of the knee by predicting knee kinematics throughout the range of motion 99
3 Materials and Methods 101
3.1 4dCT Data Collection 103
3.1.1 DICOM Image Resolution 105

3.2 3D-Geometry Model Generation 105

3.2.1 Image Process flow 107

3.2.1.1 Segmentation... 108

3.2.2 Modelling Cartilage.. 115

3.2.3 Surface and Volume Remeshing 118

3.3 Finite Element Analysis 121

3.3.1 Material Properties 122

3.3.2 Ligament and patella tendon insertion 124

3.3.3 Ligament and tendon mechanical properties 128

3.3.3.1 Spring Material Properties 129

3.3.3.2 Ligament Pre-strain Modelling and Iterative Solution Consistency......... 130

3.3.4 Contact specification 133

3.3.5 Boundary and loading conditions 136

3.4 Primary research aim: to estimate knee ligament tensions throughout knee flexion/extension 140

3.4.1.1 Ligament and patella tendon under static equilibrium conditions 142

3.5 Secondary research aim: Tibia movement tracking and location verification 145

3.5.1 How can the position of the femur and patella be aligned between two frames of the model?... 145

3.5.2 Tibia position analysis using direct node analysis... 151

3.5.3 Bony position analysis using CloudCompare™ 151

3.5.4 Bony position workflow using Cloud-Compare™ 153

4 Results 155

4.1 Finite Element Model Accurately Segmented and Generated from 4D CT Data **155**

4.2 Estimation and Balancing of Ligament Tension **157**

4.3 Secondary aim: comparison **177**

4.3.1 Patella and femur tracking results 177

4.3.1.1 Repeat analysis 180

4.3.1.2 Patella matching error verification 181

4.3.2 Tibia tracking results 192

4.3.2.1 Tibia position analysis using direct node analysis 192

4.4 Cloud-to-Mesh Signed Distance Analysis of Patellofemoral Tracking **210**

4.5 Patellar matching analysis results based on cloud comparison **215**

4.6 Tibia matching analysis results based on cloud comparison **232**

5 Discussion and Conclusion ***235***

5.1 Implications for Knee Biomechanics and Orthopaedic Applications . **242**

5.2 Limitations **245**

5.3 Future Research Directions **247**

5.4 Conclusion **248**

Reference ***250***

Appendix A ***284***

Appendix B ***288***

Appendix C ***296***

List of Figures

Figure 1. The human knee joint. This figure shows the femur (thigh bone) with its lateral and medial condyles, the patella (kneecap), the tibia (shin bone), and the fibula, illustrating their positions and structural connections (redrawn from Regenerative Spine and Joint, 2023). [1] 30

Figure 2. Medial view of the knee showing key anatomical structures. MPFL, medial patellofemoral ligament; AMR, anteromedial retinaculum; sMCL, superficial medial collateral ligament (proximal and distal portions, cut and retracted); POL, posterior oblique ligament; dMCL, deep medial collateral ligament; SM, semimembranosus muscle (retracted); G, gracilis tendon insertion; SA, sartorius tendon insertion; ST, semitendinosus tendon insertion. (Reprinted from Wierer et al., 2024). [42] 37

Figure 3. Anatomy of the human knee ligaments. (redrawn from Cleveland Clinic, "Knee Ligaments", 2024) [45] 38

Figure 4. Anterior and posterior views of the major muscles, tendons, and ligaments of the human lower limb. (redrawn from Musculoskeletal Key "Basic Sciences", 2016) [61]...42

Figure 5. The knee joint illustrating key ligamentous and tendinous structures. (redrawn based on "Muscles and Tendons" from The Knee Doc website) [70] 44

Figure 6. Superior view of the knee joint highlighting intra-articular meniscus structures. (Source: Thrive Now Physio, 2023) [80] 48

Figure 7. Insertion of the posteromedial angle of the femur and the superficial and deep medial collateral ligaments of the tibia. AT, adductor tubercle; AMT, anterior medial epicondyle tubercle; GT, gastrocnemius tubercle; MGT, medial gastrocnemius tubercle; MPFL, medial patellofemoral ligament; POL, posterior oblique ligament; ME, medial epicondyle; sMCL, superficial medial collateral ligament (femoral, proximal tibial, and distal tibial attachments). The

meniscofemoral and monoconidial ligaments connecting the medial meniscus to the femur and tibia are also indicated (Reprinted from LaPrade et al., 2007). [125]......54

Figure 8. Cadaveric testing for the measurement of ligament strain (Reprinted from Hinterwimmer et al., 2002). [162] 66

Figure 9. FE model of the knee joint with mesh elements. (Reprinted from Khot et al., 2021) [174]......71

Figure 10. FEA processing flow 102

Figure 11. 4dCT scanning and RAW data collection. 103

Figure 12. Convert and segment the DICOM into 9 frames in MIMICS and 3-Matic 110

Figure 13. LCL insertion modelling optimization method 112

Figure 14. 3D image of the knee model in MIMICS 113

Figure 15. Visual comparison of the model interior with and without filling (polyline growth)......114

Figure 16. The soft tissue (articular cartilage) was created in ‘3-Matic’. 115

Figure 17. The knee joint assembly models underwent surface and volume remeshing operations for meshing purposes. 118

Figure 18. The parameters and details of surface and volume mesh operation in’3-Matic’. 119

Figure 19. FE model of Knee Joint Range of Motion 65-Degree Flexion Sequence. 122

Figure 20. The chosen 'Anchor Region' refers to the specific area on the bone where the ligaments are attached. 128

Figure 21. The distal femoral cartilage contacts the lateral meniscus in Ansys$^{TM.}$ 135

Figure 22. The distal femoral cartilage contacts the patella cartilage in Ansys^{TM}. 136

Figure 23. Fixed support conditions applied on the Knee Joint. 137

Figure 24. Center of mass on the tibia..138

Figure 25. 'Remote Force' location 139

Figure 26. Relative distance analysis of cloud compares................................151

Figure 27. The nearest neighbour distance Vs. true distance between compared cloud and reference cloud. 152

Figure 28. Enhancing Distance Accuracy in Cloud-Compare: From Nearest Points to Mathematical Surface Modelling. 153

Figure 29. Frame of simulation model from 02-18, a) Frame 02, b) Frame 06, c) Frame 10, d) frame 14, e) Frame 18 156

Figure 30. The Frame 02–18 models were used to iteratively calculate the tension curves. Specifically, the models from a) Frame 02, b) Frame 06, c) Frame 10, d) Frame 14, and e) Frame 18 iteratively calculated the tension curves of all ligaments (ACL, PCL, LCL, and MCL) and the patellar tendon (PT) under an initial preload of 100 N. 159

Figure 31. The Frame 02–18 models were used to iteratively calculate the tension curves. Specifically, the models from a) Frame 02, b) Frame 06, c) Frame 10, d) Frame 14, and e) Frame 18 iteratively calculated the tension curves of all ligaments (ACL, PCL, LCL, and MCL) and the patellar tendon (PT) under an initial preload of 200 N. 162

Figure 32. Comparative analysis of the iterative test results for the knee joint model is presented in panels (a) to (e). Panel (a) shows the tension profiles of the patellar tendon (PT; a1), lateral collateral ligament (LCL; a2), medial collateral ligament (MCL; a3), posterior cruciate ligament (PCL; a4), and anterior cruciate ligament (ACL; a5) under two initial pre-tension conditions

(100 N, black line; and 200 N, red line) for Frame 02. Panels (b–e) present the corresponding iterative results for Frames 06 (b1–b3), 10 (c1–c3), 14 (d1–d3), and 18 (e1–e3), respectively, focusing on the PT, MCL, and ACL under the same pre-tension conditions (100N and 200N). It is noteworthy that both LCL and PCL exhibit zero tension during the iterative tests for Frames 06–18; therefore, their results are not displayed in panels (b–e). 171

Figure 33. Ligament tension along the flexion curve has been systematically estimated under initial pre-tension (0N, 100N and 200N). 175

Figure 34. Definition of the femoral and patellar tracking node sets used to drive inter-frame alignment of the knee joint model in ANSYS (F1–P1 to F4–P4). Pink-highlighted regions indicate the selected mesh nodes and are presented in magnified views to clearly show the node locations. 178

Figure 35. Example from Frame 06: anatomical locations of the tracked equivalent landmarks on the patella and tibia. Red-highlighted regions indicate the selected mesh nodes and are shown in magnified views to provide a clearer illustration of the node locations. 182

Figure 36. Patella 3D motion trajectories across all frames (F02–F18). Three-dimensional trajectories of the tracked patellar landmarks Patella-LAT (green), Patella-MED (blue), and Patella-SUP (red) are plotted in the global coordinate system (X: mediolateral, ML; Y: anteroposterior, AP; Z: superoinferior, SI;). Solid lines connect the same landmark between consecutive frames to visualise frame-to-frame displacement throughout the extension sequence (≈65° flexion at F02 to 0° at F18). Dashed lines link the three landmarks within each frame, illustrating the instantaneous triangular configuration of the patella and its evolution across the motion cycle. The annotated inter-frame tracking intervals (e.g., F02′/06) denote the displacement-driving step that maps the patellar configuration from F02 to F06; similarly, F06′/10, F10′/14, and F14′/18 represent the corresponding driving displacements from F06 to F10, F10 to F14, and F14 to F18. These interval-specific displacements were

used as inputs for subsequent model alignment and FE-driven analyses. (Units: mm) 184

Figure 37. Two-dimensional sagittal- and coronal-plane projections of patellar landmark trajectories. This figure shows the patellar landmark motion obtained from 3D tracking, projected onto the 2D sagittal and 2D coronal planes to visualise the dominant in-plane displacement patterns during knee extension. (A) 2D sagittal-plane (Y–Z) projection: AP (mm) versus SI (mm) trajectories for Patella-SUP (blue), Patella-MED (orange), and Patella-LAT (green). (B) 2D coronal-plane (X–Z) projection: ML (mm) versus SI (mm) trajectories for the same three patellar landmarks (units: mm). 185

Figure 38. Euclidean distance trends for the tracked patellar landmarks across the flexion–extension sequence (F02–F18). Curves show the Euclidean discrepancy between finite element model–predicted landmark positions and the corresponding locations from the 4dCT-derived reference geometry, reported for the anatomically defined landmarks Patella-SUP, Patella-MED, and Patella-LAT (maintained as equivalent anatomical locations across frames). Panel (a) shows the F02–F06 transition, (b) F06–F10, (c) F10–F14, and (d) F14–F18. (Units: mm) 190

Figure 39. Average Euclidean distance trends for grouped tibial nodes across flexion Frames 02–14. The figure shows mean displacement errors for each predefined node group, providing a summary measure of tibial tracking performance and highlighting differences in positional accuracy among anatomical regions. (Units: mm). 191

Figure 40. Tibia 3D motion trajectories across all frames (F02–F18). Three-dimensional trajectories of the tracked tibial landmarks Tibia-LAT (blue), Tibia-MED (green), and Tibia-ANT (red) are plotted in the global coordinate system (X: mediolateral, ML; Y: anteroposterior, AP; Z: superoinferior, SI; mm). Solid lines connect the same landmark between consecutive frames to visualise

frame-to-frame displacement throughout the extension sequence ($\approx 65^\circ$ flexion at F02 to 0° at F18). Dashed lines link the three landmarks within each frame, illustrating the instantaneous triangular configuration and its evolution across the motion cycle. The annotated inter-frame tracking intervals (e.g., F02′/06) denote the displacement-driving step that maps the tibial configuration from frame F02 to frame F06; similarly, F06′/10, F10′/14, and F14′/18 represent the corresponding driving displacements from F06 to F10, F10 to F14, and F14 to F18, respectively. These interval-specific displacements were used as inputs for subsequent model alignment and FE-driven analyses. 194

Figure 41. Two-dimensional sagittal- and coronal-plane projections of tibial landmark trajectories. This figure presents the tibial landmark motion obtained from 3D tracking, projected onto the 2D sagittal and coronal planes to visualise the dominant in-plane displacement patterns during knee extension. (A) 2D sagittal-plane (Y–Z) projection: AP (mm) versus SI (mm) trajectories for Tibia-ANT (blue), Tibia-LAT (orange), and Tibia-MED (green). (B) 2D coronal-plane (X–Z) projection: ML (mm) versus SI (mm) trajectories for the same three tibial landmarks (units: mm). 195

Figure 42. Frame 02–06 comparison showing the translational errors of equivalent tibial nodes. Errors are reported for Tibia-ANT (orange), Tibia-LAT (green), and Tibia-MED (purple), with a mean line indicating the average translational error across the three nodes included in each test (units: mm)................. 201

Figure 43. Frame 06–10 comparison showing the translational errors of equivalent tibial nodes. Errors are reported for Tibia-ANT (orange), Tibia-LAT (green), and Tibia-MED (purple), with a mean line indicating the average translational error across the three nodes included in each test (units: mm)................. 204

Figure 44. Frame 10–14 comparison showing the translational errors of equivalent tibial nodes. Errors are reported for Tibia-ANT (orange), Tibia-LAT (green), and Tibia-MED (purple), with a mean line indicating the average translational

error across the three nodes included in each test (units: mm)................207

Figure 45. Frame 14–18 comparison showing the translational errors of equivalent tibial nodes. Errors are reported for Tibia-ANT (orange), Tibia-LAT (green), and Tibia-MED (purple), with a mean line indicating the average translational error across the three nodes included in each test (units: mm)................209

Figure 46. Cloud-to-Mesh Signed Distance Analysis of Patellofemoral Tracking (Frames 02–06, Flexion 65°–48°). Top: Patella view showing anterior errors (red positive deviations); Bottom: Tibia view with peripheral plateau discrepancies (blue negative deviations). (CloudCompare C2M signed distances; units in metres; 0.001 m = 1 mm)..211

Figure 47. Cloud-to-Mesh Signed Distance Analysis of Patellofemoral Tracking (Frames 06–10, Flexion 48°–32°). Top: Patella with superior deviations; Bottom: Tibia showing anterior-inferior errors. (CloudCompare C2M signed distances; units in metres; 0.001 m = 1 mm)..212

Figure 48. Cloud-to-Mesh Signed Distance Analysis of Patellofemoral Tracking (Frames 10–14, Flexion 32°–16°). Top: Uniform patella alignment; Bottom: Tibia with distal/posterior discrepancies. (CloudCompare C2M signed distances; units in metres; 0.001 m = 1 mm)..213

Figure 49. Cloud-to-Mesh Signed Distance Analysis of Patellofemoral Tracking (Frames 14–18, Flexion 16°–0°). Top: Consistent patella matching; Bottom: Tibia with distal errors. (CloudCompare C2M signed distances; units in metres; 0.001 m = 1 mm) 214

Figure 50. Patella displacement between frames 02 to 06 (CloudCompare; C2M signed distances; node set P1). Frame 02 is the driven frame and frame 06 is the target frame; the green→yellow→orange ramp indicates increasing magnitude (Units in metres (m); 0.001 m = 1 mm). 216

Figure 51. Patella displacement between frames 02 to 06 (CloudCompare; C2M signed distances; node set P2). Frame 02 is the driven frame and frame 06

is the target frame; the green→yellow→orange ramp indicates increasing magnitude (Units in metres (m); 0.001 m = 1 mm). 217

Figure 52. Patella displacement between frames 02 to 06 (CloudCompare; C2M signed distances; node set P3). Frame 02 is the driven frame and frame 06 is the target frame; the green→yellow→orange ramp indicates increasing magnitude (Units in metres (m); 0.001 m = 1 mm). 218

Figure 53. Patella displacement between frames 02 to 06 (CloudCompare; C2M signed distances; node set P4). Frame 02 is the driven frame and frame 06 is the target frame; the green→yellow→orange ramp indicates increasing magnitude (Units in metres (m); 0.001 m = 1 mm). 219

Figure 54. Patella displacement between frames 06 to 10 (CloudCompare; C2M signed distances; node set P1). Frame 06 is the driven frame and frame 10 is the target frame; the green→yellow→orange ramp indicates increasing magnitude (Units in metres (m); 0.001 m = 1 mm). 220

Figure 55. Patella displacement between frames 06 to 10 (CloudCompare; C2M signed distances; node set P2). Frame 06 is the driven frame and frame 10 is the target frame; the green→yellow→orange ramp indicates increasing magnitude (Units in metres (m); 0.001 m = 1 mm). 221

Figure 56. Patella displacement between frames 06 to 10 (CloudCompare; C2M signed distances; node set P3). Frame 06 is the driven frame and frame 10 is the target frame; the green→yellow→orange ramp indicates increasing magnitude (Units in metres (m); 0.001 m = 1 mm). 222

Figure 57. Patella displacement between frames 06 to 10 (CloudCompare; C2M signed distances; node set P4). Frame 06 is the driven frame and frame 10 is the target frame; the green→yellow→orange ramp indicates increasing magnitude (Units in metres (m); 0.001 m = 1 mm). 223

Figure 58. Patella displacement between frames 10 to 14 (CloudCompare; C2M signed distances; node set P1). Frame 10 is the driven frame and frame 14

is the target frame; the green→yellow→orange ramp indicates increasing magnitude (Units in metres (m); 0.001 m = 1 mm). 224

Figure 59. Patella displacement between frames 10 to 14 (CloudCompare; C2M signed distances; node set P2). Frame 10 is the driven frame and frame 14 is the target frame; the green→yellow→orange ramp indicates increasing magnitude (Units in metres (m); 0.001 m = 1 mm). 225

Figure 60. Patella displacement between frames 10 to 14 (CloudCompare; C2M signed distances; node set P3). Frame 10 is the driven frame and frame 14 is the target frame; the green→yellow→orange ramp indicates increasing magnitude (Units in metres (m); 0.001 m = 1 mm). 226

Figure 61. Patella displacement between frames 10 to 14 (CloudCompare; C2M signed distances; node set P4). Frame 10 is the driven frame and frame 14 is the target frame; the green→yellow→orange ramp indicates increasing magnitude (Units in metres (m); 0.001 m = 1 mm). 227

Figure 62. Patella displacement between frames 14 to 18 (CloudCompare; C2M signed distances; node set P1). Frame 14 is the driven frame and frame 18 is the target frame; the green→yellow→orange ramp indicates increasing magnitude (Units in metres (m); 0.001 m = 1 mm). 228

Figure 63. Patella displacement between frames 14 to 18 (CloudCompare; C2M signed distances; node set P2). Frame 14 is the driven frame and frame 18 is the target frame; the green→yellow→orange ramp indicates increasing magnitude (Units in metres (m); 0.001 m = 1 mm). 229

Figure 64. Patella displacement between frames 14 to 18 (CloudCompare; C2M signed distances; node set P3). Frame 14 is the driven frame and frame 18 is the target frame; the green→yellow→orange ramp indicates increasing magnitude (Units in metres (m); 0.001 m = 1 mm). 230

Figure 65. Patella displacement between frames 14 to 18 (CloudCompare; C2M signed distances; node set P4). Frame 14 is the driven frame and frame 18

is the target frame; the green→yellow→orange ramp indicates increasing magnitude (Units in metres (m); 0.001 m = 1 mm). 231

Figure 66. Comparison of previous research results with the results of this study. 239

List of Tables

Table 1. Biomechanical properties of major knee ligaments and the patellar tendon. Summary of tensile strength, stiffness, and key viscoelastic characteristics of primary knee stabilizing structures, with values compiled from relevant literature. 52

Table 2. Details of articular cartilage thickness 117

Table 3. Material properties of the model components a.) Bone b.) Cartilage .. 124

Table 4. Specifications of Stiffness Parameters for Ligaments and Patellar Tendon (PT) Implemented in ANSYS (Units: mm). 130

Table 5. The frame 06 spring force loaded after multi-iteration test. 133

Table 6. Single frame model tested based on the combinations of different random set nodes. Units in metres (m); 0.001 m = 1 mm 150

Table 7. a) The model can always achieve convergence through the iterative calculation process, with Pre-load at 0N; b) The model can always achieve convergence through the iterative calculation process, with Pre-load at 100N; c) The model can always achieve convergence through the iterative calculation process, with Pre-load at 200N. Ligament and patellar-tendon tensions are reported in Newtons (N), and knee angle is reported in degrees (°). 172

Table 8. Segment-wise mean inter-frame coordinate differences for the tracked patellar landmarks. For each tracking segment (F02–06, F06–10, F10–14, and F14–18), the mean translational differences and corresponding standard deviations are reported along the medial–lateral (ML–X), anterior–posterior (AP–Y), and superior–inferior (SI–Z) directions for Patella-SUP, Patella-MED, and Patella-LAT. All values are in millimetres (mm). 187

Table 9. Set of nodes Euclidean displacement error, average and standard deviation results. (Units: mm) 188

Table 10. Segment-wise mean inter-frame coordinate differences for the tracked

tibial landmarks. For each tracking segment (F02–06, F06–10, F10–14, and F14–18), the mean translational differences and corresponding standard deviations are reported along the medial–lateral (ML–X), anterior–posterior (AP–Y), and superior–inferior (SI–Z) directions for Tibia-ANT, Tibia-LAT, and Tibia-MED. All values are in millimetres (mm). 197

Table 11. Mean difference (Units: mm) between equivalent nodes of 16 different sets of nodes for a given tracking frame segment. 199

Table 12. The table shows the distance error (Units: mm) of the equivalent nodes on Frame 02-06, as well as the average and standard deviation of the equivalent node combination and each equivalent node across all tests. Summary: P4-F1 best (2.21mm average), P3-F1 worst (6.16mm), with anterior node most variable. (P1–P4 and F1–F4 are the patellar and femoral driving node sets defined in Figure 34.) 201

Table 13. The table shows the distance error **(Units: mm)** of the equivalent nodes on Frame 06-10, as well as the average and standard deviation of the equivalent node combination and each equivalent node across all tests. Summary: P4-F1 best (5.65mm), P1-F3 worst (13.44mm), with medial node most variable. (P1–P4 and F1–F4 are the patellar and femoral driving node sets defined in Figure 34.) 203

Table 14. The table shows the distance error (Units: mm) of the equivalent nodes on Frame 10-14, as well as the average and standard deviation of the equivalent node combination and each equivalent node across all tests. Summary: P2-F3 best (6.82mm), P3-F4 worst (10.68mm), with anterior node most variable. (P1–P4 and F1–F4 are the patellar and femoral driving node sets defined in Figure 34.) 206

Table 15. The table shows the distance error (Units: mm) of the equivalent nodes on Frame 14-18, as well as the average and standard deviation of the equivalent node combination and each equivalent node across all tests.

Summary: P2-F3 best (4.13mm), P4-F1 worst (6.36mm), with medial node most variable. (P1–P4 and F1–F4 are the patellar and femoral driving node sets defined in Figure 34.) 209

Table 16. Tibia node-based tracking error summary (Units: mm) 234

List of Abbreviations

Acronym	Definition
1D	One-dimensional
3D	Three-dimensional
4D	Four-dimensional
4dCT	Four-dimensional computed tomography
ACL	Anterior Cruciate Ligament
ACR	Axial Centre of Rotation
AHF	Anterior Horn Facet
ALL	Anterolateral Ligament
AM	Anteromedial
AMT	Adductor Magnus Tendon
AT	Adductor Tubercle
BOBQAT	Biomechanics Objective Basic Science Quality Assessment Tool
CMC	Cloud Model Computing
CNN	Convolutional Neural Networks
CoR	Centre of Rotation
CT	Computed Tomography
CT-RSA	Computed Tomography-Based Radio Stereometry Analysis
DIC	Digital Image Correlation
DICOM	Digital Imaging and Communication in Medicine
dMCL	Deep Medial Collateral Ligament
dMRI	Dynamic Magnetic Resonance Imaging
DOF	Degrees of Freedom
EF	Extension Facet
FEA	Finite Element Analysis
FEM	Finite Element Model
FF	Flexion Facet
fMRI	Functional Magnetic Resonance Imaging
GT	Gastrocnemius Tubercle
IGA	Isogeometric Analysis
LCL	Lateral Collateral Ligament
MCL	Medial Collateral Ligament
ME	Medial Epicondyle
MM	Musculoskeletal Modelling
MPFL	Medial Patello Femoral Ligament
MRI	Magnetic Resonance Imaging
NURBS	Non-uniform Rational B-splines
PCL	Posterior Cruciate Ligament
PET	Positron Emission Tomography

PHF	Posterior Horn Facet
PL	Posterolateral Bundle
PMHS	Postmortem Human Subjects
POL	Posterior Oblique Ligament
PT	Patellar Tendon
RG	Region Growing
ROI	Regions of Interest
ROM	Range of Motion
SG	Strain Gauges
sMCL	Superficial Medial Collateral Ligament
SPECT	Single-photon Emission Computed Tomography
SRG	Seeded Region Growing
TAF	Tibial Articular Facet
TKA	Total Knee Arthroplasty
TKR	Total Knee Replacement
US	Ultrasound

1 Introduction

The knee joint is an important part of the human skeletal structure. It plays a vital role in human movement and carrying loads. Ligaments provide important passive support and stability during the movement of the knee joint. The anterior cruciate ligament (ACL), posterior cruciate ligament (PCL), lateral collateral ligament (LCL), medial collateral ligament (MCL), and patellar tendon (PT) are the main elements responsible for maintaining stability of the knee joint [1]. Every ligament has a role to play in controlling the movement of the joint, in directions to maintain its stability effectively. These knee ligaments, while relatively independent, function complementarily, with their intricate biomechanical interactions critically enhancing joint stability. Therefore injuring one can have repercussions, on others well. This highlights the importance of having a grasp of knee ligament injuries and managing them with caution. Recent research has brought attention to the complexities of knee ligament injuries by pointing out the occurrence of ACL and MCL injuries even in cases that seem to involve only an ACL rupture at first glance [2]. These connections highlight the pathophysiological relationships, within the anatomical structures of the knee joint, within the knee joint [3].

Total knee replacement (TKR) surgery holds significant importance in the field of orthopaedic medicine, particularly for patients suffering from severe knee joint diseases such as osteoarthritis, rheumatoid arthritis, or post-traumatic arthritis. The surgery is crucial for reducing pain, restoring joint function and enhancing mobility. Severe knee joint conditions can lead to stiffness, deformity, and loss of movement. TKR surgery realigns and stabilizes the joint, enabling patients to regain a greater range of motion, perform daily activities with ease, and in many cases, return to an active lifestyle. Following TKR, soft tissue balancing of the knee is a critical process to improve the outcome of the surgery. Whilst gap balancing and/or force balancing can assist surgeons, a quantitative understanding of the native tension of each ligament would greatly assist this process. Due to the number of ligaments, a static or dynamic analysis of the forces in knee joint structures is indeterminant. Evaluating knee joint mechanics is a complex undertaking due to the complexity and diversity of the unique structures and functions that each ligament plays in movement and stability. Additional and in-depth research is needed to fully understand the function of each ligament, the impact of different loading on knee injuries, and the most effective treatments for common knee problems. Understanding these elements is essential to improve treatments and health of patients suffering from knee-related conditions.

Although the knee joint has been the focus of extensive research, a comprehensive dynamic model of the knee joint remains elusive. Specifically, no existing model fully incorporates the menisci, articular cartilage, and all major ligaments—including the patellar tendon (PT), anterior cruciate ligament (ACL), posterior cruciate ligament (PCL), medial collateral ligament (MCL), and lateral collateral ligament (LCL)—while also accounting for the initial stresses within these ligaments.

Computed tomography (CT) is widely used in the diagnosis of articular defects, fragmentation, and tibial plateau fracture depression. Traditionally, CT technologies were initially designed to deliver very precise three-dimensional scanning for non-moving targets. It has rarely previously, accurately, scanned a moving target, which has limited its use. For example, soft tissue can move the rib cage considerably during respiration rendering such image difficult to acquire. Four-Dimensional Computed Tomography (4dCT) is a technique in which CT images are acquired in quick succession building up a frame-by frame description of motion, comprehensive visualisations of moving anatomical components. Research in the field has been crucial in reducing the obstacles caused by motion-induced scanning errors. The use of 4dCT in medical imaging has greatly enhanced the ability to record the spatial and temporal movements of organs and the skeletal system in the human body. For example, 4dCT has been shown to successfully identify lack of ligament integrity in the ankles [265]. The effective use of 4dCT to observe complex joints in the human body in real-time highlights its significant impact on improving patient care in orthopaedics [221].

The understanding of knee joint ligament tension is crucial for advancing biomechanical research and improving clinical applications especially in orthopaedic surgery. This study develops a new method which combines finite element analysis (FEA) with four-dimensional computed tomography (4dCT) scanning technology to measure knee ligament stresses during flexion. The research method involves creating a three-dimensional knee joint model from 4dCT images which then undergoes FEA biomechanical testing. The primary objective of this study is to examine whether exact measurements of natural ligament tension enable better soft tissue balancing after knee arthroplasty to achieve optimal surgical results. The current research uses an iterative FEA approach with 4dCT images to calculate ligament prestresses during flexion which surpasses previous approximation methods.

1.1 Clinical Need and Research Direction

Accurately determining in-vivo ligament tensions has been a longstanding challenge. Conventional cadaveric testing offers controlled conditions but lacks physiological muscle tone and dynamic loading. Standard finite element analysis (FEA) models can simulate ligament mechanics but are limited by uncertainties in geometry, material properties, and boundary conditions. Consequently, no existing method reliably quantifies native ligament tension throughout the full range of knee motion in a living subject.

From a clinical perspective, this limitation directly affects TKR outcomes. Surgeons must make tensioning decisions without precise reference values, increasing the risk of instability, altered kinematics, or abnormal wear patterns in prosthetic components. Moreover, the inability to replicate native ligament forces can compromise proprioception and functional recovery. Addressing this knowledge gap is therefore essential to advancing patient-specific surgical strategies, not only in TKR but potentially across other orthopaedic interventions involving ligament balancing.

The research presented here responds to this need by integrating 4dCT imaging with an iterative FEA approach to estimate ligament prestress dynamically and non-invasively. By reconstructing subject-specific knee models from sequential 4dCT frames and iteratively fitting FEA-predicted motion to observed motion, the method aims to yield physiologically realistic ligament tension profiles across the flexion–extension range. This capability could provide surgeons with clinically actionable data to guide intra-operative decisions and postoperative rehabilitation planning.

1.2 Structure of the Thesis

Following this introduction, Chapter 2 presents a comprehensive literature review covering the anatomy and biomechanics of the knee joint, the mechanical behaviour of ligaments and other soft tissues, in-vivo and in-vitro methods of ligament tension measurement, and the state-of-the-art in dynamic imaging and FEA-based modelling. It also formally states the research aims, expanding upon the clinical need identified here, and defines the specific objectives guiding the methodology.

Chapter 3 details the materials and methods, including acquisition of 4dCT data, segmentation and reconstruction of three-dimensional knee models, specification of ligament insertion sites, and the iterative FEA protocol for tension estimation. It also introduces the use of CloudCompare, an open-source point-cloud analysis tool, to quantify spatial differences between observed and simulated bony positions as part of the model validation strategy.

Chapter 4 presents the results of the modelling and validation process, including ligament tension profiles and comparative kinematic analyses.

Chapter 5 discusses the implications of the findings for knee biomechanics and orthopaedic surgery, outlines methodological limitations, and suggests directions for future research.

2 Literature Review

The knee joint, anatomically termed the patella-tibiofemoral joint, is an important synovial joint and a crucial pivot of the human lower extremity. The unique structural arrangement enables support functions while allowing various complex movements including flexion and extension and restricted rotational and translational movements. The knee joint consists of three main anatomical components which include the distal femur, proximal tibia and patella. The fibula provides lateral stability but its function in the knee joint remains secondary thus it is not included in this study.

2.1 Bony morphology

The knee joint consists of multiple components which function as a strong system to provide stability and flexibility and weight distribution for the lower limb. The knee joint consists of four essential components: femur, tibia, fibula and patella which enable the connection between the thigh and calf regions for movement. The articular skeleton of the knee joint contains specific bones which both bear axial loads and enable extensive movement. The femur, the longest bone in the human body, articulates primarily with the tibia, while the fibula contributes to lateral stability. The knee joint is stabilized and supported by a complex network of ligaments, in conjunction with tendons and surrounding musculature. The joint receives support from ligaments together with tendons and muscles. The kneecap functions as a protective shield located in front of the knee to enhance movement during activities such as walking and jogging and bending the lower limbs.

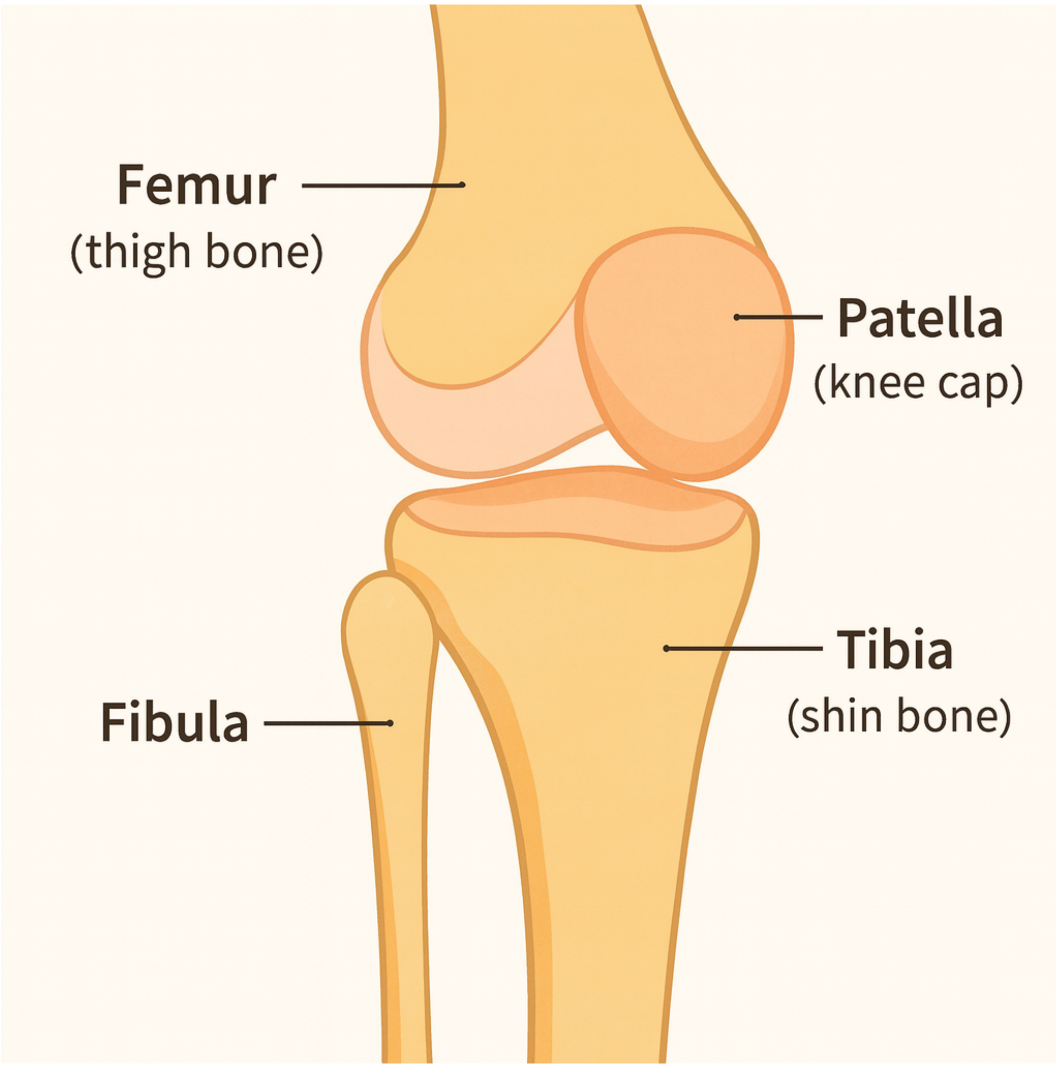

Figure 1. The human knee joint. This figure shows the femur (thigh bone) with its lateral and medial condyles, the patella (kneecap), the tibia (shin bone), and the fibula, illustrating their positions and structural connections (redrawn from Regenerative Spine and Joint, 2023). [1]

The different components, in the knee joint collaborate to create a flexible system that helps bear the body's weight and allows various movements to take place smoothly. Connective tissues like ligaments, tendons, muscles and cartilage play roles in ensuring stability, flexibility and absorbing shocks effectively. Bones are essential, for upholding the knees integrity during activities.

The complex kinematics of the knee joint have been the subject of ongoing research debate due to the asymmetrical shape of the knee bone [4]. The anatomical features of the distal femur, which serve as the basis for these movements, have a significant influence [5]. The different kinematic patterns of the femur are determined at the proximal end by the interaction between the femur and the pelvis and at the distal end by the relationship between the tibia and the femoral condyles [6]. In addition, the patella, a component of the tendon of the quadriceps femoris muscle, plays a crucial role in biomechanical processes, particularly in knee extension [7]. In addition, the patella fulfils a vital function by minimising frictional loads on the femoral condyle, which significantly influences the movement and function of the knee joint [7]. The tibiofemoral joint and the patellofemoral joint are the main joints that regulate the kinematic properties of the knee joint. This study focussed on the tibiofemoral joint, which is the joint connection between the femur and tibia. It plays a crucial role in the range of motion of the knee [6]. The patella and the trochlear groove on the front surface of the lower end of the thigh bone (femur) touch each other. This is known as the patellofemoral joint [8]. These complex connections and interactions play a crucial role in the development of prostheses that aim to restore the functionality of the natural knee [9-11]. However, the current design paradigm is not perfect, emphasising the significant need for research into knee kinematics and their impact on prosthesis design [9-11]. The morphology and kinematics of the knee joint provide essential information for the design and functionality of prostheses [9-11]. The complex interaction between the femur, tibia and patella further emphasises the need for individualised and patient-specific approaches in prosthesis design to ensure the reproduction and restoration of native functionality of the knee joint [6-7].

2.1.1 Femur

Morphological characteristics of the femur and its biomechanical importance. The biomechanics of the femur has been extensively studied using various methods, including finite element analysis and computed tomography. Research has focused on both proximal and distal regions, examining bone quality, morphometry, and stress distribution. Local bone mineral density and quality in the distal femur are highest in the posterior region, which is crucial for implant anchorage [12]. Finite element analysis has been widely used to understand force distribution, fracture patterns, and implant design [13]. Morphometric studies have revealed correlations between proximal and distal femur features, which are important for biomechanical function and implant design [14]. Advanced modelling techniques, incorporating isotropic and orthotropic trabecular structures, have been developed to create biomechanical finite element models that accurately represent bone physiology and structural behaviour, potentially improving prosthetic implant design [15].

The human femur exhibits several structural adaptations for bipedal locomotion. The anterior curvature of the diaphysis helps absorb shock and maintain balance during walking [16]. The obliquity of the femoral shaft, measured by the bicondylar angle, allows for an adducted knee position and develops during childhood in response to bipedal gait [17]. The linea aspera, a ridge on the posterior femur, emerges during puberty but its mechanical role is debated [18]. The femur's shape is optimized to resist forces from various directions and absorb energy during falls [19]. Cross-sectional geometry changes during childhood reflect developing locomotor abilities [20]. The curvature of the femur may help reduce bending strains during locomotion, as demonstrated in animal models [21]. These features collectively contribute to the femur's role in bipedal locomotion [22].

In addition, the femur has an adaptive feature in its composition that includes layers of cortical and cancellous bone that increase strength while minimising weight [23-24]. This feature improves functional efficiency and preserves the structural integrity of the femur. The distal femur exhibits asymmetric condyles, contributing to the knee's complex movements and kinematics [16-26]. This asymmetry results in tibial rotation during flexion [27]. The femur adapts to mechanical demands through various mechanisms, including trabecular eccentricity, which affects stress distribution in the femoral neck [28]. Multiple load cases, representing different daily activities, significantly influence bone adaptation and material property distribution [29]. Therefore, each part of the femur is specifically adapted to fulfil certain biomechanical requirements, illustrating the sophistication inherent in the evolutionary development of the skeletal system. Further research is needed to gain a complete understanding of the complex relationship between these structures in different movement patterns and potential therapeutic treatments.

2.1.2 Tibia

The tibia is a bone that plays a role, in bearing weight and is located in the leg region. Its structure is well suited for providing support and enabling a range of actions. The top portion of the tibia features two condyles known as the medial and lateral condyles. These tibial condyles interact with the femur to create the knee joint, a structure fundamental to maintaining support and balance during knee movements. The medial and lateral meniscuses are crescent shaped bits of cartilage that enhance the strength of the knee joint serving as buffers to absorb impact and distribute weight evenly for added stability thus being pivotal, in bending and extending the knee.

The tibial shaft is an essential part of the skeletal system and supports the body's weight when standing and walking on two legs. The article "Biomechanics of Skeletal Muscles" [30] provides a comprehensive analysis of the biomechanics associated with the tibial shaft and emphasises its importance in supporting weight and distributing the load during various physical activities.

Another notable feature of the tibia is the tibial crest, which serves as an attachment point for several muscles and patella tendon that help stabilise the knee joint. The book "Clinically Oriented Anatomy" discusses in detail the importance of the tibial crest for the attachment of muscles and its role in stabilising the knee joint and facilitating movement [31]. The distal end of the tibia articulates with the talus, which facilitates smooth movement of the ankle joint.

The tibia consists of a robust outer layer of cortical bone, which gives it strength and stability, and an inner layer of spongy bone, which reduces the weight of the bone and absorbs shock.

To truly comprehend how the knee joint works –, from its default position to how it bends and rotates – is key in grasping its purposefulness. The femur tilts inward compared to the tibia. The degree of tilt can fluctuate between 5 to 12 degrees to guarantee contact between the condyles and the tibia. This enables an array of movements for actions like walking and squatting as well, as the twisting needed for agile manoeuvres.

2.1.3 Patella

The kneecap is also referred to as a patella. Is a bone, with three sides that is found in front of your knee joint area. The connection between your thigh muscles called quadriceps and shinbone known as tibia is made possible by a tendon called the quadriceps tendon. The patella has roles in your knee joints functionality. It acts as a type of pulley that enhances how effective your quadriceps muscles are when extending your knee improving performance in activities, like jumping sprint and climbing mountains. The kneecap serves to shield parts of knee joints, like cartilage on femur and tibia from harm by lessening risks of injuries resulting from frontal impacts, on knees. It also enhances knee stability by directing tendon and ensuring precise positioning of the kneecap in the femur's trochlear groove during motion.

The significance of patella, in movement is well acknowledged in biomechanical research. Its pivotal role in knee mechanics is crucial for mobility during daily activities like walking and running. The kneecap functions as a pulley enhancing quadriceps muscle efficiency in extending knee movement. This process significantly influences mobility. Additionally the patella aids in improving limb movements by enabling effective force transfer from quadriceps to tibia. Even though it may be small, in size the patella plays a role in ensuring movement of our knee joint. It plays a part in helping our quadriceps muscle work efficiently to extend our leg distributing weight evenly and decreasing stress on our knee bones and cartilage. Academic studies are placing emphasis on how crucial it is for the patella to uphold stability within the knee joint effectively over time. Earlier research highlights how essential it is to have a kneecap and to closely monitor its positioning to ensure alignment while in motion. The patella plays a role, in safeguarding against conditions by ensuring proper knee joint mobility and evenly distributing weight thanks to its monitoring mechanism and distinct anatomical structure comprising ligaments and muscles that interact with the femurs anterior surface to support load distribution within the knee joint. The curved back surface functions, as a place where you can attach your tendon to help with extending your knee joint. The broad part of your kneecap joins up with your thigh bones end while its narrower tip connects to your shinbone. This shows how its shape lines up perfectly with what its meant to do. Furthermore, the kneecap consists of a layer made of cortical bone that provides durability and flexibility, with an inner layer of spongy bone that helps absorb impact and lessen weight. It is essential to comprehend how effective movement and muscle performance are affected by understanding how this unique structure interacts within knee complex. This knowledge is crucial, for improving both treatments and biomechanical studies [32].

2.2 Soft-Tissues of the Knee Joint

When looking at the structure of bones, in the body is one part of the picture; we also need to think about how various soft tissues work to support movement and overall function effectively in the knee joint system. Understanding how these different parts interact is key to making sure the knee can move smoothly and handle the stresses it faces in our bodies. Ligaments and tendons are especially vital, for maintaining the knees balance and keeping it working as it should. The ACL and PCL are essential for maintaining front-back stability, while the MCL and LCL help with side-to-side stability [33]. These ligaments help keep the joint intact during different movements. The significance of tendons such as quadriceps and patellar tendon, in transferring muscle forces for knee flexing and extending has also been emphasized [33]. Additionally, the menisci and articular cartilage are elements that contribute to creating a biomechanical environment within the knee joint. The menisci are crucial, in spreading weight and impacts while improving the alignment of joints [34]. The smooth motion, between bone surfaces is facilitated by cartilage to maintain function and overall joint health in the long term [35]. However, this intricate relationship between soft tissue and bony components can be disrupted by injury or degeneration, leading to significant consequences for knee stability, mobility, and functionality. For instance, researchers have shown that imbalances in quadriceps strength after ACL repair might change the way the knee joint moves, which may impact functional abilities [33]. Thus, it has been proposed that after reconstruction, rehabilitation should focus on optimising quadriceps strength in order to get more balanced knee biomechanics [33]. An in-depth analysis of the structure and mechanical characteristics of the knee, such as the anterolateral ligament (ALL), is crucial for understanding how the joint functions [36]. In a study conducted by Kumar V et al., the authors aimed to systematically review the anatomy, histology, radiology, and biomechanical characteristics of the ALL, contributing to the understanding of knee joint dynamics and stability [36]. The scientific integrity and interplay of the knee tissues, with its bony framework have been thoroughly explored in studies [37]. Studying these links, in depth could greatly help us understand how the knee joint works and adapts physiologically when its injured or deteriorating; this knowledge could enhance the development of rehab and prevention methods in the run.

2.2.1 Ligaments

The lateral collateral ligament (LCL) is cord-like, averaging 66 mm in length and 3.4 mm in width [38]. The significant contribution of the MCL is evident in its crucial role in ensuring the stability of the knee joint by meticulously limiting lateral and rotational movements. The medial collateral ligament (MCL) is fan-shaped, longer, wider, and thinner than the LCL [39], characterised by dimensions of approximately 10-15 cm in length and 6-8 mm in diameter. The origin of the MCL lies in a bulge on the inner side of the femur that extends to connect with the upper surface of the tibia along the medial aspect of the tibia. The fibrous components of the medial collateral ligament run obliquely through the femur to the tibia, forming a complex cruciate structure that effectively prevents lateral and rotational displacement of the tibia. The medial collateral ligament (MCL) complex is a primary stabilizer of the knee joint, preventing valgus motion and limiting external rotation [40-41].

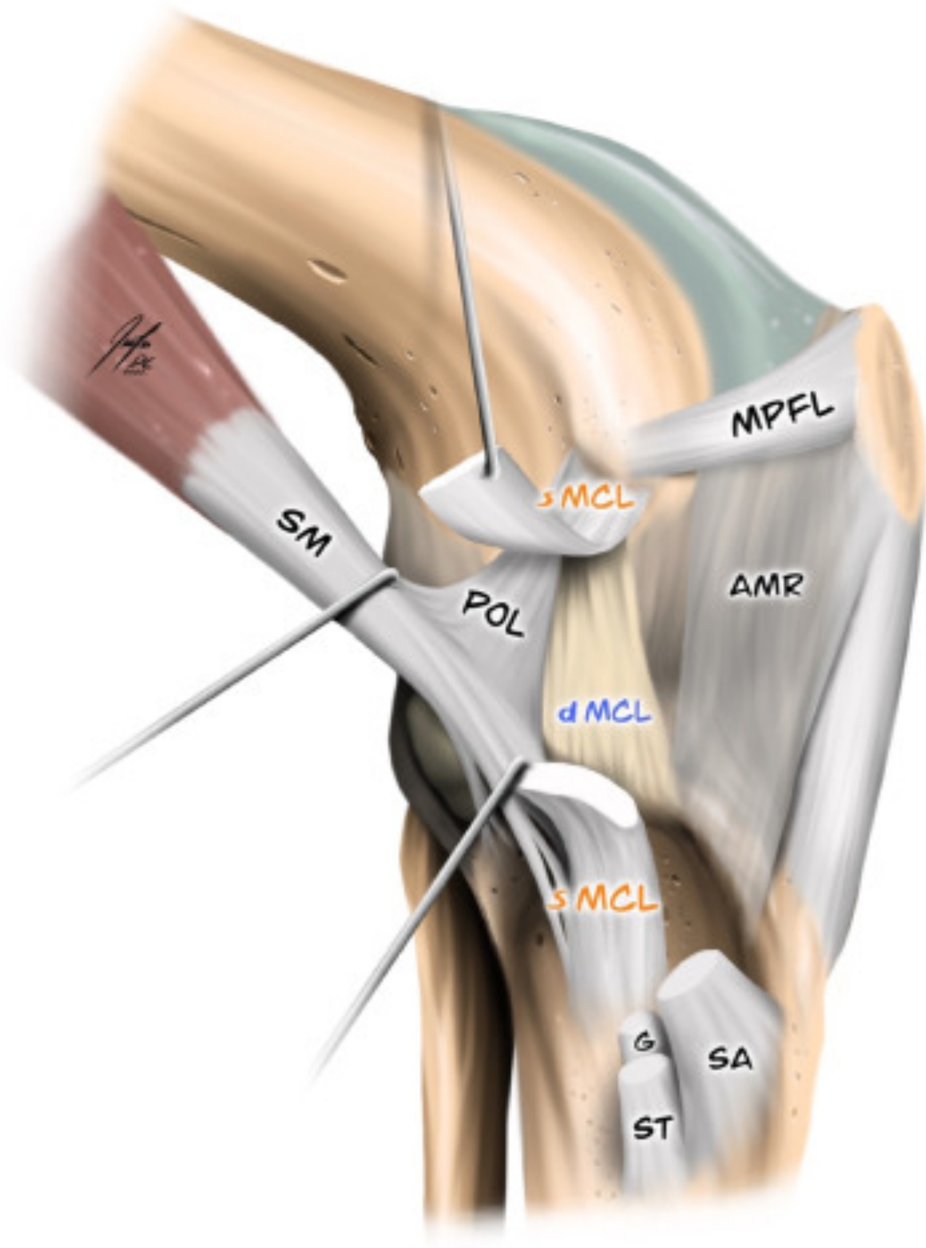

Figure 2. Medial view of the knee showing key anatomical structures. MPFL, medial patellofemoral ligament; AMR, anteromedial retinaculum; sMCL, superficial medial collateral ligament (proximal and distal portions, cut and retracted); POL, posterior oblique ligament; dMCL, deep medial collateral ligament; SM, semimembranosus muscle (retracted); G, gracilis tendon insertion; SA, sartorius tendon insertion; ST, semitendinosus tendon insertion. (Reprinted from Wierer et al., 2024). [42]

The superficial MCL (sMCL) is the main valgus stabilizer, with its proximal division being primary and its distal division limiting external rotation at 30 degrees knee flexion

[43]. The deep MCL and posterior oblique ligament (POL) contribute to internal rotation stability at various flexion angles [43]. The MCL's long fibers maintain tension from full extension to 90° flexion, crucial for knee stability [44].

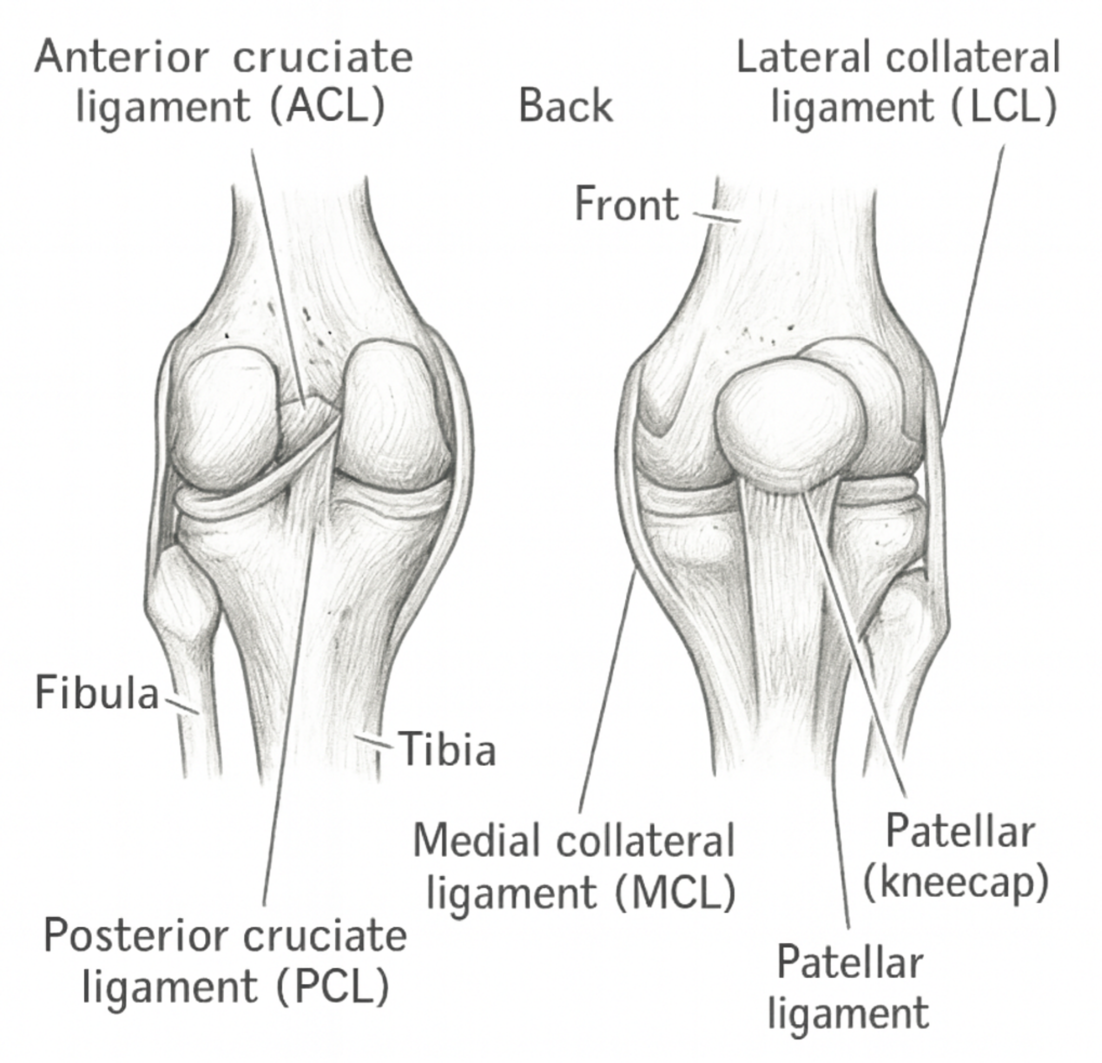

Figure 3. Anatomy of the human knee ligaments. (redrawn from Cleveland Clinic, “Knee Ligaments”, 2024) [45]

Figure 3 presents a detailed anatomical view of the human knee joint, presented from both posterior and anterior perspectives, depicting the femur, tibia, fibula, and patella (kneecap), along with key ligaments including the anterior cruciate ligament (ACL), posterior cruciate ligament (PCL), medial collateral ligament (MCL), lateral collateral ligament (LCL), and patellar ligament.

The MCL has a flexible shape that allows the knee joint to move through a wider range of motion. However, it is strong enough to withstand significant pressure, especially when there is a direct impact on the side of the knee. The literature also demonstrates that MCL injuries are common during various sporting activities, as are composite injuries to the anterior cruciate ligament (ACL) and medial ligament complex, emphasizing the need to understand the function and healing capabilities of MCL injuries. There is a study showing a high incidence of superficial and deep medial collateral ligament injuries in the setting of isolated ACL rupture, suggesting an interaction between these ligaments in maintaining knee stability [46].

The lateral collateral ligament (LCL) plays a role, in the knee joints structure and function as it is composed of woven fibrous tissue, with a distinct arrangement that enhances its strength and stability. Starting from the part of the femur (epicondyle) the LCL extends to connect with the head of the fibula bone in a diagonal pattern that forms a cross like structure to assist in avoiding displacement and inward rotation of the fibula bone. Due to its composition of fibrous connective tissue and its unique architecture, it has a high structural elasticity [47]. It plays an important role in maintaining the stability of the knee joint and is less elastic than the other ligaments of the knee joint [48]. Compared to the other ligaments of the knee joint, the structure of the LCL is elongated and less elastic, corresponding to its relative ability to withstand low pressure. Nevertheless, it is strong enough to ensure knee stability and effectively prevent serious knee injuries.

Its main function is to prevent inward movement of the joint and limit posterior and outward rotation [49-50]. The lateral collateral ligament (LCL) attaches anteriorly and laterally to the head of the fibula, starting from the lateral epicondyle of the femur. The primary function of the LCL is to restrain inward motion of the joint between 5 and 25 degrees of flexion, while its secondary function is to limit backward and outward rotation of the joint below 50 degrees of flexion [51].

The ACL is a part of the knee joint. It has been the focus of extensive research because of its vital role, in keeping the knee joint stable [52-53]. The optimal angle to evaluate

ACL stiffness is when the knee is moving normally and bent, at an angle of 20 to 30 degrees. A key characteristic of the ACL is its tissue that comprises two functional bundles known as the anteromedial bundle (AM) and the posterolateral bundle (PL). The anterior cruciate ligament, known as the ACL is a ligament located at the centre of the knee that links the thigh bone (femur) and shinbone (tibia). This ligament is vital, for maintaining stability in the knee joint. The iliotibial band runs from the femur to the tibia forming a resilient structure. Composed of connective tissue the ACL exhibits a well-defined structure that enhances its strength and functionality. The typical range, for the ACLs length falls between 10 and 12 centimetres with a width of 6 to 8 millimetres. The AM and PL bundles play roles in restricting the tibias movements both backward as well as inward and outward rotations. These functional roles were confirmed through a study that highlighted the significance of the AM bundle, in countering the tibias anterior drawer motion – a function of the ACL [54]. Researchers have delved into the effects of ACL injuries, in sports that involve shifts in direction and movements, like jumping and landing. They have pinpointed high knee abduction moments as factors linked to ACL injuries [54]. The structure of the ACL is primarily defined by the intertwining of its fibbers.

The posterior cruciate ligament (PCL) is a major ligament in the knee joint that provides stability to the knee by preventing the tibia (shin bone) from sliding backwards in relation to the femur (thigh bone). The posterior cruciate ligament (PCL) is located at the back of the knee joint and connects the femur (thigh bone) and the tibia (shin bone). Its main function is to regulate the posterior displacement of the tibia. The posterior cruciate ligament (PCL) is a broad, flat structure consisting of a thick, fibrous connective tissue, including anterior, central, posterior-longitudinal, and posterior-oblique bundles [55]. It measures approximately 32 mm in length and 7-12 mm in width [56]. The PCL primarily resists posterior tibial translation and acts as a secondary restraint against varus, valgus, and external rotation [57]. Its anterolateral bundle is significantly stronger than the posteromedial bundle, with an estimated strength of 4 kN in young adults [58]. It has a clearly defined arrangement that reinforces its durability and function. The posterior cruciate ligament (PCL) originates on the posterior and medial side of the femoral condyle and attaches to the posterior and lateral side of the tibial plateau. The PCL fibers travel diagonally from the femur to the tibia in a like pattern to prevent backward movement and rotation of the tibia effectively. The PCL is larger and stronger than the ACL, as it must withstand substantial load-bearing forces. It is also more flexible than the ACL, enabling a wider range of motion in the knee joint.

Research findings have revealed aspects and concerns related to the cruciate ligament (ACL) and posterior cruciate ligament (PCL) which play a crucial role in maintaining the knee joints stability. Studies indicate that individuals who undergo ACL reconstruction surgery typically experience decreased knee flexibility during walking potentially resulting in pressure, within the knee joint and a higher likelihood of developing knee osteoarthritis. These discoveries underscore the influence of ACL injuries, on knee functionality post reconstruction [59].

2.2.2 Muscles and Tendons

2.2.2.1 Muscles

Fifteen muscles surround the knee joint, eight of which originate near the hip, coordinating a sophisticated interplay of activation and co-activation to facilitate smooth and stable movement. These muscles—including the rectus femoris, gluteus maximus, sartorius, tensor fasciae latae, biceps femoris (long head), semitendinosus, and semimembranosus—attach via tendons to the fibula, proximal tibia, and iliotibial band, forming a dynamic support network. The muscles function collectively to actively flex and extend the knee, and but they also co-activate to stabilise the joint. The four quadriceps muscles (the rectus femoris, the vastus lateralis, the vastus intermedius and the vastus medialis) primarily act to extend the knee. Whilst during knee flexion, the biceps femoris—originating at the ischial tuberosity and inserting at the lateral tibial condyle and fibular head—activates in conjunction with the semitendinosus and semimembranosus. These hamstring muscles contract concentrically, shortening to generate posterior tibial displacement. The extent of their activation depends on task-specific demands, modulated by neural input and motor unit recruitment—ranging from low-level engagement during walking to maximal activation during sprinting [60].

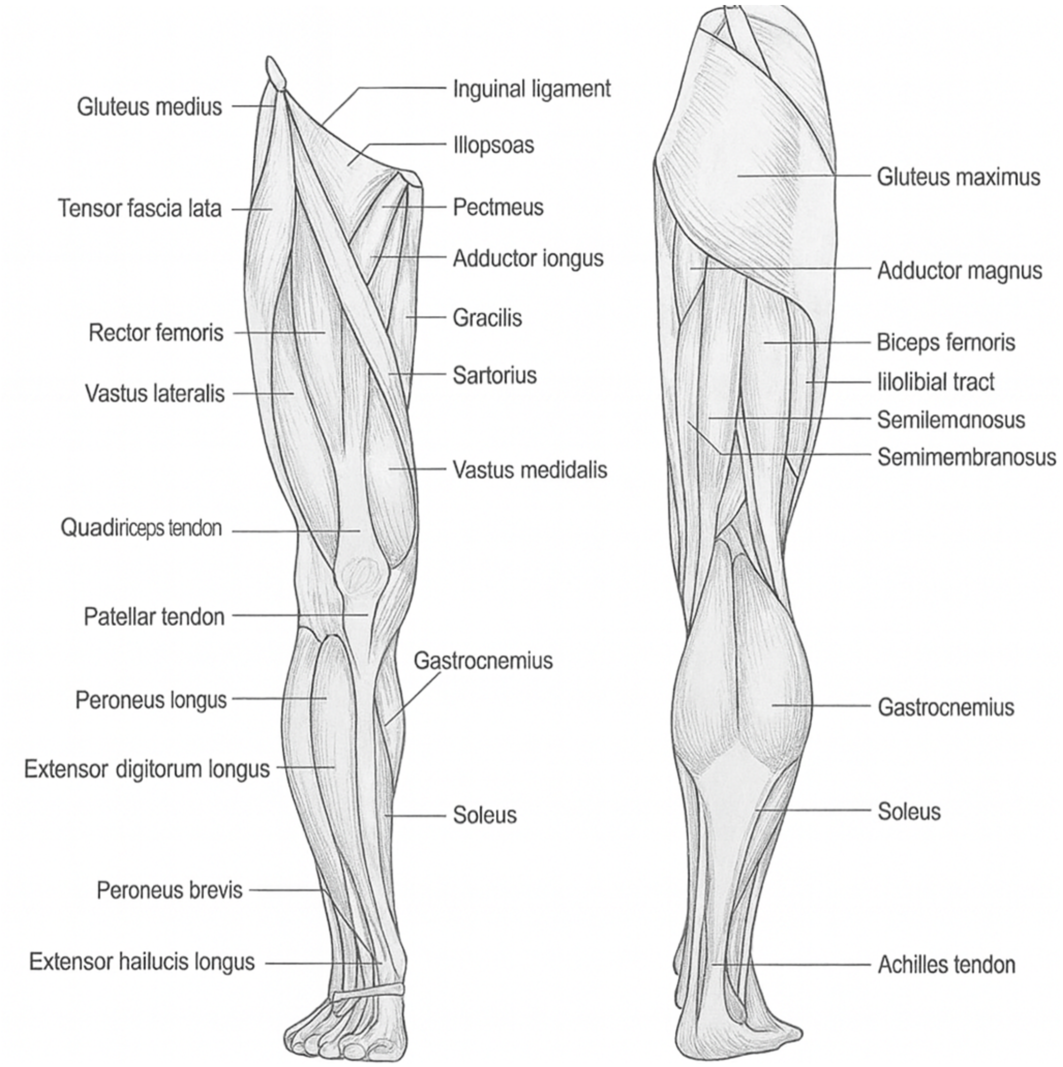

Figure 4. Anterior and posterior views of the major muscles, tendons, and ligaments of the human lower limb. (redrawn from Musculoskeletal Key “Basic Sciences”, 2016) [61]

Figure 4 shows anatomical illustration highlights key structures including the quadriceps femoris group, patellar tendon, gastrocnemius, hamstrings, and Achilles tendon.

Co-activation refines joint control by synchronizing the contraction of the agonist muscles (primary movers) with antagonists (opposing muscles) to enhance stability, regulate movement speed, and mitigate injury risk [62]. For instance, during knee flexion, the hamstrings co-activate with the gluteus maximus and tensor fasciae latae, which stabilize the hip and iliotibial band to ensure proper knee tracking [63]. Simultaneously, the rectus femoris may exhibit low-level antagonistic co-activation, preventing excessive hyperextension or uncontrolled motion [64-65]. This process is precisely regulated by the central nervous system, which adjusts muscle tension through proprioceptive feedback from muscle spindles and Golgi tendon organs, maintaining optimal biomechanical harmony.

The gastrocnemius and plantaris have their origin on the posterior aspect of the femoral condyles and insert, via the Achilles tendon, to the calcaneus. They contribute not only to plantar flexion but also to knee flexion. During a squat, it co-activates eccentrically with the hamstrings to control descent and concentrically to assist in ascent.

The balance between activation and co-activation is highly context dependent. In knee extension, the rectus femoris (as part of the quadriceps group) recruits additional motor units under increased resistance, such as during stair climbing [66]. Concurrently, the hamstrings may co-activate at low levels to prevent excessive anterior tibial displacement [67]. Conversely, during controlled flexion (e.g., a leg curl), the hamstrings act as primary agonists while the quadriceps co-activate minimally to smooth the motion and protect the joint capsule [68]. This equilibrium is especially crucial in weight-bearing activities, where the sartorius, tensor fasciae latae, and gluteus maximus reinforce lateral stability via the iliotibial band, counteracting shear forces on the knee [69].

2.2.2.2 Tendons

The operational functionality of the knee joint depends largely on the crucial tendon structures that facilitate the transmission of the forces generated by the muscles and thus enable movement. The robust patellar tendon serves as a fibrous band that connects the quadriceps muscle group to the kneecap and extends to the tibia. It plays a central role in the extension of the knee, which is essential for activities such as kicking and forward propulsion.

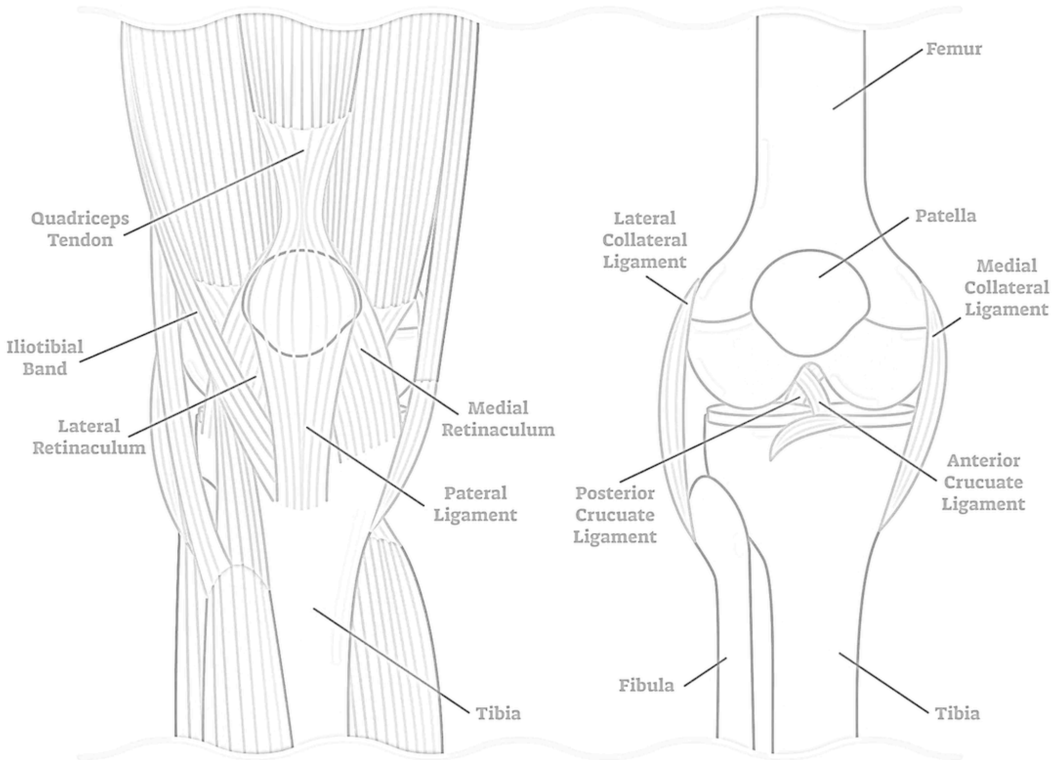

Figure 5. The knee joint illustrating key ligamentous and tendinous structures. (redrawn based on "Muscles and Tendons" from The Knee Doc website) [70]

Figure 5 shows the anatomical positioning of major stabilizing components, including the quadriceps tendon, patellar ligament, medial and lateral retinacula, iliotibial band, and collateral ligaments.

The quadriceps tendon is a robust, fibrous structure that serves as the primary stabilizer of the knee joint and a critical regulator of patellar tracking. This tendon originates from the confluence of the four quadriceps muscles (rectus femoris, vastus lateralis, vastus medialis, and vastus intermedius) and inserts onto the superior pole of the patella. Distally, the patellar tendon—a continuation of the quadriceps tendon—extends from the patella’s inferior pole to the tibial tuberosity. Together, these structures form the quadriceps mechanism, a unified system that ensures knee stability and coordinates precise patellar movement during extension.

The patellar tendon plays a role in extending the knee joint. It acts, as a sturdy connection between the quadriceps muscles and tibia to transmit force effectively during activities like running and jumping. It originates from the outer side of the kneecap. It starts at the upper and outer part of the kneecap and extends to the bony prominence on the front of the tibia.

The patellar tendon consists mainly of type I collagen fibres, which give it the tensile strength that is important for its function. This dense fibre structure is interspersed with fibroblasts, which contribute to the maintenance and repair of the tissue. A synovial sheath surrounds the tendon and reduces friction with the surrounding tissue when the knee moves. The patellar tendon plays a crucial role in the extension mechanism of the knee by acting as a lever arm for the quadriceps muscle group. The contraction of the quadriceps transmits force to the tibia via the quadriceps tendon, patella and patellar tendon, helping to extend the knee.

The correlation between the characteristics of the patellar tendon and the mechanical function of the quadriceps during knee extension is a topic that has been investigated in a number of renowned studies [71-73]. First, Seynnes et al. pointed out that changes in the mechanical and material properties of the patellar tendon are more closely linked to overall loading history, highlighting how the tendon's ability to respond to loading may affect the biomechanical behaviour of the knee joint [74]. This relationship between loading history and the tensile property of the patellar tendon plays a fundamental role in understanding knee joint stability and its ability to withstand high impact loads. When assessing the load-bearing capacity of the tendon, a key aspect to consider is its material tensile properties. Although these are lanyards and not the patellar tendon itself, the results of this study contribute to our understanding of tendon mechanics that can be extended to the patellar tendon. Another study drew attention to the complex relationship between the patellar tendon and its attachment to the knee joint and emphasised the importance of anatomically accurate fixation in the context of ligament reconstruction [75]. Specific fixation of the patellar tendon emphasises the critical role that the tendon plays in maintaining stability of the knee joint, which may be consistent with its properties influencing the mechanical advantage of the quadriceps. Furthermore, the potential variation in tensile strength as a function of loading angle emphasises the importance of the role of the patellar tendon in knee joint biomechanics [74]. This consideration may have implications for the interconnected mechanical role of the patellar tendon and quadriceps muscle group in knee extension. In summary, the existing literature highlights the critical role of patellar tendon properties in the mechanical behaviour of the knee joint, particularly in the context of high impact force loading. Factors such as loading history, tensile properties, fixation type and loading angle all contribute to the delicate balance of forces experienced during knee extension and are critical to understanding the mechanical advantage of the quadriceps [71-75]. The relationships between these factors suggest that more sophisticated studies are required in this area.

Posteriorly, the hamstring tendons—comprising the biceps femoris (long and short heads), semimembranosus, and semitendinosus—mediate knee flexion and dynamic stabilization. The biceps femoris connects to the head and outer tibial condyle whereas the semimembranosus links to the inner side of the tibia with different expansions including the oblique popliteal ligament. The semitendinosus attaches lower down at pes anserinus and merges with tendons, from gracilise and sartorius muscles. The tendons carry forces, from the muscles to the tibia and fibula to allow for bending movements while walking or running and engaging in activities that require bearing weight on the legs. This coordinated effort is crucial for keeping the muscles and bones strong and stable while evenly distributing force, around the knee joint.

2.2.3 Meniscus and cartilage

Within the complex biomechanical structure of the knee joint, the menisci and cartilage play a crucial role in load distribution, shock absorption, and joint stabilisation.

2.2.3.1 Articular Surface

The articulating surfaces of the knee joint are critical to its biomechanical stability and functional efficiency. The femur, tibia and patella are the three bony components of the knee joint that meet at these surfaces. The articular surfaces of each bone are covered by specially formulated hyaline articular cartilage. The smooth, lubricated, low-friction surface of the avascular cartilage layer is necessary to ensure a continuous joint connection. These properties are essential for athletic manoeuvres such as running, bending and walking.

Akbarshahi et al [76] provide specific insights into the biomechanics of the patellofemoral joint during functional activities. This study showed that increased loads placed on the lateral surface correlated with the clinical observation that the lateral surface of this joint was more prone to osteoarthritis. This complicates the understanding of joint wear and may lead to further research into joint pathology and rehabilitation procedures. A study by Lee et al [77] contributed to the discussion of factors affecting the biomechanics of the patellofemoral joint by examining what happens to the patellofemoral joint when the quadriceps, the muscles that help stabilise the knee, become weaker or stronger. Although they found no significant influence on joint kinematics and contact pressure under normal conditions, extreme conditions could have an effect on the joint's biomechanics. Their study adds another dimension to understanding how muscle weaknesses can potentially influence joint pathologies such as osteoarthritis. Brazaitis et al. [78] provides further insights into abnormal patellofemoral joint biomechanics in the context of anterior knee pain. They suggest that altered femur dynamics under a relatively stable patella as the primary cause of pain, which adds to the multifaceted understanding of joint pain relationship to biomechanics. The complexity of the joint biomechanics and their multifaceted role in joint pathologies such as osteoarthritis detailed in the papers reviewed here [79] aligns with the importance of these areas of research outlined in the researcher's description. Understanding the specifics of joint biomechanics requires a detailed exploration of the diverse factors at play, from muscle strength and joint loading to cell self-degradation processes. Further, these insights could potentially inform the development of targeted therapeutic interventions and rehabilitation protocols for joint pathologies. Thus, understanding the nuances of these joint’s biomechanics is not only critical for improving scholarly knowledge but also has significant implications for improving people's lives.

2.2.3.2 Meniscus

The knee joint has two semilunar fibrocartilaginous structures known as menisci, which is crucial for supporting important biomechanical functions and maintaining the stability and strength of the joint's structure. The lateral meniscus is positioned in the compartment while the medial meniscus is located in the compartment of each knee. These menisci perform roles that are essential, for the proper functioning of the knees biomechanics.

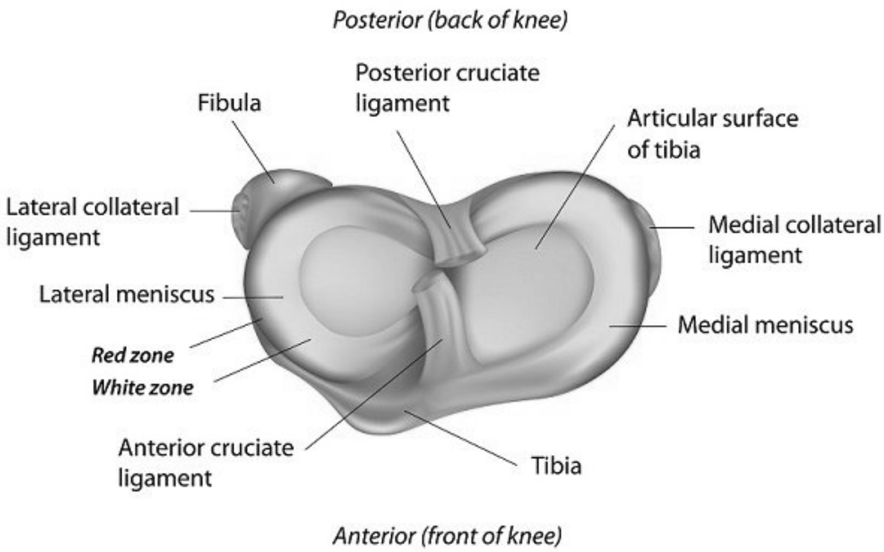

Figure 6. Superior view of the knee joint highlighting intra-articular meniscus structures. (Source: Thrive Now Physio, 2023) [80]

Menisci play a role, in reducing the impact of forces on the bone during activities involving movement such as walking or running by absorbing shocks and distributing axial loads evenly across the joint cartilage to prevent damage and disintegration of the joint structure itself [81][82]. Additionally, the menisci help stabilize the knee by enhancing the alignment and contact, between the plates and femoral condyles thereby improving stability [83]. Furthermore, they assist in distributing fluid within the knee joint to ensure lubrication and smooth movement during motion.

Numerous biomechanical research studies have focused on the knee meniscus [84-85]. Have shown its role, in maintaining joint stability and distributing weight effectively in the knee joint area. It has been validated through these studies that the meniscus is responsible for carrying a portion of the load. Around 50 to 70%. When the knee is flexed. Moreover, the meniscus acts as a shield, for the cartilage by transforming loads into circular loads and thus prevents overloading issues [84]. The researchers observed that investigations, into the effects of meniscectomy causing looseness and instability have indicated the significance of menisci in preserving stability—particularly the medial meniscus. Paletta et al. in an effort to showcase the relevance of the ligaments in surgical interventions, for meniscal extrusion treatment brought forth a biomechanical study highlighting these ligament roles [84]. Their study contributed to our understanding of the biomechanical factors involved in meniscal extrusion and their relationship to joint stability. Chung et al. investigated the relationship between the size of the medial femoral condyles and the occurrence of posterior root tears of the medial meniscus, leading to a better understanding of the biomechanical factors contributing to meniscal injuries [85]. In addition, Ghosh and Taylor's study on how chondroprotection’s can help protect articular cartilage after meniscectomy suggested a way to mitigate the biomechanical effects of meniscal injuries on the joint [86]. Studying these studies has provided us with insights, into how the meniscus contributes to keeping joints stable and distributing loads efficiently while reducing the strain, on the cartilage in our joints. Indicating that this area of research spans multiple disciplines.

The menisci are highly flexible, durable, and reliable, and are composed of collagen fibres, collagen, and proteoglycans. The menisci have a unique crescent-shaped shape with elongated edges, providing support to the lateral areas of the joint, which are subject to great mechanical strain during active movement. [87-88]

Two-thirds of the meniscus, known as the "white zone," has no blood flow. This lack of blood supply makes it more difficult for the tissue to heal after an injury, as the body's natural healing process is less effective in this area. [89]

The medial meniscus is not as mobile as the lateral meniscus due to its C-shaped structure and tight connection to the medial collateral ligament. [90-91] The rounded structure of the medial meniscus, however, makes it more flexible during movement.

These structural and functional differences play an important role in the development of meniscal injuries, and the extent and type of injury is largely determined by the mobility or restriction of each meniscus.

The lateral meniscus ensures joint alignment by protecting the articular cartilage from excessive biomechanical stress that could cause joint damage [92], while also providing proprioception to prevent potential damage from irregular movements [93].

In summary, the complex arrangement of the menisci and articular cartilage within the knee embodies an intricate relationship between biological structure and biomechanical function. Maintaining their integrity is essential to ensure long-term health and mobility of the knee. Given the role of the menisci in knee biomechanics and their susceptibility to injury, their anatomy has been extensively studied. Multiple studies consistently emphasize that maintaining the integrity of the menisci after surgery is essential to maintaining balance and joint function [94-95].

2.2.4 Lubrication system

In the knee joint, the synovial fluid plays a key role in ensuring its health. By acting as a biological lubricant, this viscous fluid that the synovial membrane secretes lessens wear and friction between the bones and the surrounding soft tissues [96]. In addition to its lubricating function, synovial fluid facilitates the supply of nutrients to joint tissues such as articular cartilage [97]. Furthermore, it helps to absorb and distribute mechanical stresses across the joint during weight-bearing exercises, lessening the pressure on the articular cartilage and subchondral bone [98]. Moreover, it aids in keeping the intra-articular environment healthy by removing metabolic waste from the joint region [98]. Changes in the content and amount of synovial fluid can lead to increased friction, cartilage wear, and joint degeneration, particularly in pathological conditions like osteoarthritis [99]. Kung et al. looked into the properties of synovial fluid after joint replacement surgery, showing how important implanted joint synovium is for good clinical performance [96]. Galandáková et al. studied the properties of synovial fluid that are needed to make the best lubrication fluid for bio tribological experiments.

They stressed how important it is to find a wear testing lubricant that is useful in real life [97]. Jansen et al. studied how joint repair looked on x-rays and how it related to changes in synovial fluid markers after knee joint distraction treatment. Their findings shed light on the link between joint repair, synovial fluid markers, and clinical outcomes [100]. Martin-Alarcon et al. explored the scale-dependent rheology of synovial fluid lubricating macromolecules, providing insights into the rheological characteristics of synovial fluid and its constituents [101].

The complex lubrication system of the knee joint is frequently not explicitly modelled in biomechanical simulations for a variety of reasons, including computational and modelling limitations and the biological lubrication processes of the joint's intrinsic complexity.

Biomechanical models use the principles of mechanics to forecast knee joint motion. In order to save computing burden, these simulations frequently use reduced joint models. The intricate details of joint lubrication, such molecular interactions in synovial fluid and fluid film dynamics, must be modelled using advanced fluid dynamics simulations, which would take a long time and increase computing complexity. The macroscopic or gross movement patterns of the knee joint, such as range of motion, reaction forces, and stresses on ligaments and tendons, are often the focus of bio kinematic simulations. Rather than the molecular or cellular biochemical processes, the main focus is on the structural and mechanical elements of joint mobility. Thus, although though the lubricating system is acknowledged to be vital, in many modelling situations it is regarded as a secondary element that does not materially influence the principal results of interest.

A common goal of biomechanical simulations is to deliver data that may be used immediately in clinical settings, including preoperative planning or rehabilitation techniques. Rather than extensive explanations of biological processes, clinicians need models that provide straightforward and useful information. Therefore, in order to make models that are more understandable and applicable to clinical settings, the lubricating system is often left out.

2.3 Soft Tissue Biomechanics

2.3.1 Ligaments and Tendon

Ligaments and tendons surrounding the patella are essential for knee stability, guiding joint motion, and resisting loads that could cause instability or injury. Composed mainly of collagen types I and III and elastin, they connect bones and contribute to the biomechanical integrity of the joint.

Structure	Tensile Strength	Stiffness	Other Biomechanical Properties
ACL	2160–3690 N	182–242 N/mm	Nonlinear stress–strain curve (toe, linear, failure regions); ~50% stress relaxation in 100 s (viscoelasticity); stiffness increases with higher strain rate
PCL	739–1627 N	150–250 N/mm	Viscoelastic; energy dissipation during rapid load/unload
MCL	700–800 N	20–120 N/mm	Creep and stress relaxation behavior; nonlinear viscoelastic response
LCL	N/A	N/A	Tension highest in extension; modulated by surrounding muscles; works with popliteus tendon, lateral capsule, and PFL
Patellar Tendon (PT)	50–100 MPa	1800–2200 N/mm	Viscoelastic (creep and stress relaxation); adapts to varying load rates

Table 1. Biomechanical properties of major knee ligaments and the patellar tendon. Summary of tensile strength, stiffness, and key viscoelastic characteristics of primary knee stabilizing structures, with values compiled from relevant literature.

Anterior Cruciate Ligament (ACL):

The ACL limits anterior tibial translation and excessive internal rotation, enhancing rotational stability. It comprises an anteromedial (AM) bundle, resisting anterior translation during flexion, and a posterolateral (PL) bundle, contributing to rotational stability during extension [102][104]. ACL loading increases during landing and cutting movements [103], with strain patterns influenced by flexion angle [105]. Its ultimate tensile strength is 2160–3690 N, linear stiffness 182–242 N/mm, and stress–strain response is nonlinear (toe, linear, failure regions) [106]. Viscoelasticity results in ~50% stress relaxation within 100 s under constant strain [107], while strain-rate sensitivity increases stiffness under rapid loading [108], both vital for injury prevention and reconstruction strategies.

Posterior Cruciate Ligament (PCL):

The PCL resists posterior tibial translation, especially in flexion, with the anterolateral (AL) bundle most active in flexion and the posteromedial (PM) bundle in extension [109-110]. It also assists in controlling femoral–tibial rotation. Tensile strength is 739–1627 N, stiffness 150–250 N/mm, and viscoelasticity allows energy dissipation during rapid load changes [110-111].

Medial Collateral Ligament (MCL):

The MCL resists valgus stress, being taught in extension and lax in flexion [112]. The superficial MCL (sMCL) prevents medial opening during flexion, while the deep MCL (dMCL) transmits load via its attachment to the medial meniscus. Tensile strength is 700–800 N, stiffness 20–120 N/mm [113], and viscoelastic behavior (creep, stress relaxation) enables adaptation to variable loading [114-115].

Lateral Collateral Ligament (LCL):

The LCL counteracts varus stress and external tibial rotation [116], functioning with the popliteus tendon, lateral capsule, and popliteofibular ligament (PFL) [117]. Tension is highest in extension, decreasing with flexion. Synergistic muscle action (e.g., biceps femoris) modulates LCL loading, and reconstruction often involves adjacent lateral structures [118].

Patellar Tendon (PT):

The patellar tendon, integral to the extensor mechanism, works with the quadriceps tendon to enable knee extension. Medial and lateral patellar retinacula maintain patellar alignment [119-120]. Tensile strength is 50–100 MPa [121-122], stiffness 1800–2200 N/mm [123-124], and viscoelasticity allows creep and stress relaxation, supporting load adaptation.

2.3.2 Insertion of Ligaments and Patellar Tendon

Ligaments are strong bands of connective tissue that link one bone to another. The anatomical placement and details of the ligaments that stabilize the knee joint are crucial elements in understanding their function and contribution to knee joint stability.

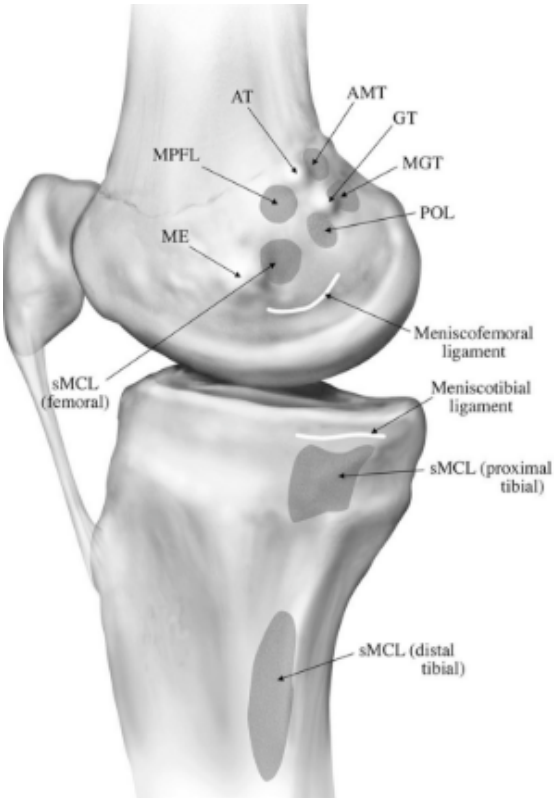

Figure 7. Insertion of the posteromedial angle of the femur and the superficial and deep medial collateral ligaments of the tibia. AT, adductor tubercle; AMT, anterior medial epicondyle tubercle; GT, gastrocnemius tubercle; MGT, medial gastrocnemius tubercle; MPFL, medial patellofemoral ligament; POL, posterior oblique ligament; ME, medial epicondyle; sMCL, superficial medial collateral ligament (femoral, proximal tibial, and distal tibial attachments). The meniscofemoral and monoconidial ligaments connecting the medial meniscus to the femur and tibia are also indicated (Reprinted from LaPrade et al., 2007). [125]

Figure 7 illustration by LaPrade et al. highlights key anatomic landmarks of the posteromedial corner insertions on the femur, as well as the superficial and deep medial collateral ligament insertions on the tibia. Notably, the femoral insertion of the superficial medial collateral ligament (sMCL) lies just posterior and proximal to the medial epicondyle (ME), with its two tibial insertions located 12.2 mm and 61.2 mm distal to the joint line. The deep medial collateral ligament’s meniscofemoral and meniscotibial ligament insertions are also depicted. The posterior oblique ligament (POL) is positioned, on average, 7.7 mm distal and 6.4 mm posterior to the adductor tubercle (AT) and 1.4 mm distal and 2.9 mm anterior to the gastrocnemius tubercle (GT). Additionally, the medial patellofemoral ligament (MPFL) and adductor magnus tendon (AMT) are included in the diagram. [125]

The anterior cruciate ligament (ACL), posterior cruciate ligament (PCL), medial collateral ligament (MCL), and lateral collateral ligament (LCL) have unique placements and functions relative to the femur and tibia [126-129].

The ACL attaches to the femur at the posterior aspect of the lateral femoral condyle, which is a bony prominence on the lateral (outer) side of the femur. Its other end inserts into the tibia on the anterior intercondylar area, which is a flat, bony surface located between the tibial plateaus [126][130-131]. The attachment of the ACL to the femur is at the back of the lateral femoral condyle. This limits the tibia's ability to move forward and has an effect on the knee's ability to rotate steadily [132].

The PCL, a major knee stabilizer, is noteworthy for its attachment sites on the femur and tibia. Its femoral attachment point is located on the medial side of the medial femoral condyle, near the posterior border of the knee [128]. Its other end inserts into the tibia in the posterior intercondylar region, also known as the "tibial groove". As highlighted by Greiner et al [128], CT protocols allow detailed localisation of the PCL attachment site.

The MCL resists valgus loading and controls tibial rotation by attaching to the medial epicondyle of the femur and inserting proximally into the medial tibia [133-134]. Studies of MCL femoral insertion injuries have provided valuable information to understand the mechanism of injury and treatment strategies for this ligament [134].

The LCL attaches to the lateral epicondyle of the femur and the fibular head and inserts into the lateral epicondyle of the femur, which is a bony prominence on the lateral surface of the femur. The other attachment point is the fibular head, which is the tibia on the lateral surface of the knee. plays a key role in knee joint stabilization [129][135]. Its full anatomical pathway and implications are captured in studies like Yan et al., providing a better understanding of the LCL and its surgical implications [129].

The patellar tendon, also known as the patellar ligament, is a strong and flexible fibrous anatomical tissue that connects the patella to the tibia. The patellar tendon connects to the patella, a tiny, flat, triangular bone at the front of the knee joint. Its specific location is at the lower end of the tendon connecting to the patella, that is, the downward part of the patella. There is a protrusion made of bone on the front side of the tibia, called the tibial tubercle, where it attaches as the lower end of the patellar tendon [136]. The tibial tubercle is located below the knee joint and serves as the attachment site for the patellar tendon.

2.3.3 Ligament stress and strain

The tension in knee ligaments varies throughout the range of motion (ROM) of the knee joint, with changes occurring as the joint moves through different phases. The motion of the knee is highly intricate, with immense dependence on the function and tension of the ligaments that surround it, particularly the anterior cruciate ligament (ACL) and the posterior cruciate ligament (PCL). Research in biomechanics has mapped out these kinematic dynamics across the range of motion (ROM) of the knee, shedding light on how the ACL and PCL, in addition to other ligaments, contribute to joint stability. During the extension phase as the knee gradually straightens from a bent position to full extension, the tension in the ACL increases as it works to resist hyperextension and anterior translation of the tibia [137]. In contrast, the PCL encounters a decrease in tension during this phase, as it plays a lesser role in limiting extension. On the other hand, the ACL is under the most stress during the transition phase, especially during the last 30 degrees of knee extension (also called terminal extension). The ACL's strain is said to increase by about 6% for every 30 degrees of knee flexion [138]. Progressing to higher degrees of flexion, the tension in the PCL begins to increase as the ACL eases because of its lesser involvement in controlling flexion. It is stated that the PCL reaches its peak tension around 90 degrees of flexion and can bear a load of up to 250% more when the knee is flexed at this angle compared to full extension [139]. This makes the PCL more involved in controlling posterior tibial translation and hyperflexion. The ACL and PCL are not the only ligaments contributing to the stability of the knee.

Others, like the medial collateral ligament (MCL) and lateral collateral ligament (LCL), also exhibit changes in tension throughout the knee's ROM. The MCL, in particular, reveals variable tension throughout the knee's ROM with its posterior fibers undergoing maximal loading at full extension and a subsequent reduction in strain with progressing flexion [140]. The LCL experiences its maximum tension during varus loading when the knee is flexed at around 30 degrees. The knowledge of ligament tension changes plays a crucial role in maintaining knee joint stability and enabling controlled movement across the entire ROM from extension to hyperflexion. Research in this field will continue to guide surgical decisions about implant design and placement and may lead to better results in total knee arthroplasty procedures [141].

The patellar tendon functions as a biomechanical efficiency component which matches the knee ligaments in maintaining joint stability and function during knee flexion. The patellar tendon tension changes dynamically with knee joint ROM because of the shifting geometric positions between the quadriceps tendon and patella and patellar tendon during knee flexion and extension. The changing tension in the patellar tendon produces significant biomechanical effects that affect force transmission and joint stability and overall knee movement efficiency. The following discussion elaborates on these dynamics, drawing on relevant literature to provide a comprehensive analysis of patellar tendon behaviour during knee flexion, with a particular focus on the tension changes described in the researcher’s inquiry.

The patellar tendon’s tension is intricately linked to the knee’s ROM, exhibiting distinct patterns as the joint moves from full extension to varying degrees of flexion. When the knee is fully extended (0 degrees), the tension in the patellar tendon is at its lowest, primarily due to the near-parallel alignment of the quadriceps force vector with the patellar tendon. This alignment minimizes the moment arm and resultant tensile forces acting on the tendon. However, as the knee flexes, the angle between the quadriceps tendon, patella, and patellar tendon increases, altering the mechanical advantage and elevating tendon tension. Research indicates that this tension rises significantly—by up to 30%—during the transition from full extension to 90 degrees of knee flexion [142], with peak tension typically occurring at approximately 60 degrees of flexion [143]. This peak is attributed to the optimal combination of increased moment arm and quadriceps force vector angulation at this angle, which maximises the tensile load on the patellar tendon [144].

Considerable research has been devoted to elucidating the biomechanics of the knee joint, particularly the behaviour of the patellar tendon under varying conditions. Among the relevant studies, the paper titled "Nonuniform Deformation of the Patellar Tendon During Passive Knee Flexion" [145] provides valuable insights that align closely with the researcher's focus. The authors of this study demonstrate that the patellar tendon undergoes complex, nonuniform deformation during passive knee flexion, a phenomenon likely attributable to the differential attachments of the tendon. Specifically, the deep portion of the patellar tendon anchors directly to the patella, while the superficial portion connects to the quadriceps tendon, resulting in heterogeneous strain patterns as the knee flexes. These findings corroborate the assertion that patellar tendon tension is not constant but varies dynamically with knee ROM, reflecting the intricate interplay of anatomical structures and biomechanical forces.

Despite the contributions of this study, a gap remains in the literature concerning the specific tension profiles described by the researcher—namely, the 30% increase in tension from full extension to 90 degrees of flexion and the peak tension at approximately 60 degrees. While the aforementioned paper provides evidence of nonuniform tendon deformation, it does not explicitly quantify the magnitude of tension changes or pinpoint the precise angle of peak tension. Other studies in the field, while valuable for understanding knee joint mechanics, similarly fall short of addressing these specific aspects. For instance, research on patellar tendon strain often focuses on active muscle contraction or pathological conditions, such as tendinopathy, rather than passive flexion dynamics. This highlights the need for further investigation to validate and expand upon the described tension profiles, potentially through advanced imaging techniques or computational modelling to capture real-time tendon behaviour across the full ROM.

The patellar tendon functions as more than a simple force transmission system in its biomechanical role. The tendon's adaptive tension response to joint angle changes enables the knee to effectively absorb and distribute loads during activities such as walking, running and jumping. The tension increase during flexion helps stabilize the joint by resisting rotational forces and the peak at 60 degrees might represent an evolutionary adaptation for optimal force generation at typical functional movement angles. The tendon faces increased risk of overuse injuries when tension becomes excessive or persists at higher flexion angles which demonstrates the clinical importance of studying these biomechanical dynamics.

A comprehensive and systematic understanding of the biomechanical properties of knee ligaments—such as tension, strain, and stress—is crucial for advancing various aspects of knee care, including diagnosis, treatment, surgical interventions, and the design of biomechanically compatible prostheses. While the existing literature has extensively examined knee ligament biomechanics, covering areas such as diagnostic methods, treatment strategies, biomechanical testing, computational modelling, and in vivo experiments, certain limitations persist. Many studies tend to focus on isolated aspects, failing to fully capture the complexity of ligament behaviour under dynamic, real-world conditions. For instance, computational models often simplify the interactions between ligaments and surrounding tissues, while in vivo testing may struggle to accurately measure ligament forces during movement.

Acknowledging these gaps is essential, as they directly affect clinical outcomes. A more nuanced understanding would not only enhance diagnostic accuracy and improve treatment results but also enable more precise surgical procedures and the development of prostheses that more effectively replicate the natural biomechanics of the knee. In the following sections, I will delve deeper into the characteristics and limitations of these existing techniques and propose potential solutions to address these challenges.

2.3.4 Joint Stability and Soft Tissue Balancing

In total knee arthroplasty, restoration of physiological knee kinematics requires preservation of ligament integrity and attainment of appropriate soft-tissue balance [146-147]. In conventional approaches, ligament balancing is performed intraoperatively through an assessment of joint laxity and force distribution, with feedback derived from tactile resistance and visual appraisal of gap symmetry. When imbalance is identified, controlled and incremental soft-tissue releases—targeted surgical relaxations of contracted ligaments or capsular structures—are undertaken to achieve coronal alignment and stability [147] The assessment of ligament balancing is predominantly concerned with assessing the size of the flexion gap which occurs during implantation of a posterior cruciate ligament-retaining total knee replacement. A quantifiable relationship was mapped between the gap size and anterior tibial translation in flexion [146]. However, recent developments in the field offer the potential for even more precise techniques towards maintaining appropriately mimicked tension and kinematic behaviour to that of a natural joint.

Joint stability is integral to the biomechanical integrity of the knee, with static and dynamic factors collaboratively ensuring its functional competence. When the body is at rest, non-contractile parts keep the joints in place. Static stability comes from these parts, while dynamic stability comes from neuromuscular control and active musculotendinous contributions.

Passive elements like the joint capsule, ligaments, menisci, and the geometry of the articular surfaces are primarily responsible for the knee joint's static stability. The knee ligaments, including the ACL, PCL, MCL, and LCL, are pre-tensioned to provide inherent stability. These ligaments act as mechanical restraints that limit excessive motion and guide the joint through a normal range of motion (ROM). For instance, the

ACL maintains a degree of tension throughout the ROM to check anterior tibial translation.

In the realm of static stability, the role of ligaments is well documented. The lateral collateral ligament, deep ligament complex, and the posterior cruciate ligament function together in preventing varus rotation, external rotation, and posterior translation of the tibia [148]. Consistent with the researcher's assertion, these ligaments not only limit excessive motion but guide the joint through a normal range of motion. The lateral collateral ligament and posterolateral capsular structures work with the popliteus muscle, tendon, and ligament complex to keep the knee stable [149]. This supports the idea that these structures work together. Highlighting the importance of the meniscus in maintaining stability, it contributes to more aligned joints between the tibia and femur, helping absorb shock while distributing synovial fluid, thereby providing a counterbalance to transverse forces on the knee [148-149]. The semilunar cartilages provide a crucial counterbalance to the transverse forces experienced by the knee.

Dynamic stability includes the active control systems of the joint, mainly the muscles and the tendons that connect to them, as well as the neuromuscular control systems that decide when to use them. The quadriceps and hamstring muscles, functioning through neuromuscular processes, provide great responses in strength and balance in anterior cruciate ligament reconstruction patients [150]. Dynamic stability, in this case, entails improvements in both static and dynamic posture stability. Lastly, considerations in the quadriceps muscle group represent an area of growing interest. The patellar tendon functions as part of this group to maintain knee stability throughout movement and when the knee is stationary. The patellar tendon tension varies with knee flexion and functions as a primary stabilizing factor for the knee joint. The ligament functions to absorb shock during walking while enabling proper knee extension [151].

The literature demonstrates how different elements create both static and dynamic knee stability through complex interactions. These contributions underline the importance of an interlinked system of ligamentous structures, tendons, and muscle groups, corroborating the researcher's emphasis on mechanical constraints, muscle strengths, and the adaptability of these structures.

2.3.5 In vivo tension

The intricate kinematics of the knee joint, encompassing a wide range of movements from flexion and extension to slight rotational and translational motions, are significantly influenced by the baseline tension within its constituent ligamentous tissues and the patellar tendon. This baseline tension, also referred to as the pre-strain or pre-stress in biomechanical terms, plays a critical role in maintaining joint stability, ensuring efficient load transmission, and facilitating smooth joint articulation. This in-depth study looks at the biomechanical reasons behind baseline tension in the knee ligament tissue and the patellar tendon. It looks at how it affects the kinematics of the knee joint and uses relevant literature to show how important it is.

Knee ligaments, including the Anterior Cruciate Ligament (ACL), Posterior Cruciate Ligament (PCL), Medial Collateral Ligament (MCL), and Lateral Collateral Ligament (LCL), are endowed with a baseline tension that is pivotal for joint stability. This inherent tension ensures that ligaments are taut, yet not overstretched, under physiological loads, thereby preventing excessive joint movements that could lead to instability or injury.

The research by Yasuda et al. shows that a relatively high initial tension after ACL reconstruction lowers the anterior laxity of the knee joint after surgery [152]. Brady et al. also say that different initial graft tension protocols can change the joint positions and compressive forces between the tibia and femur, especially when a patellar tendon graft is used [153]. In the case of ACL reconstruction, Cuomo et al. show that which grafts are tensioned first affects knee laxity. This supports the idea that the tension sequence in ACL reconstruction is very important for restoring knee joint stability [154]. However, it's also crucial to understand that abnormal changes in the baseline tension of these ligaments due to injury or malpractice during surgery can significantly disturb normal knee joint kinetics. Similar considerations apply to the Medial Collateral Ligament (MCL) and Lateral Collateral Ligament (LCL) that maintain the medial and lateral stability of the knee [155].

The role of the patellar tendon goes beyond just providing stability. The baseline tension in the patellar tendon is instrumental in facilitating efficient knee extension, as it transmits forces from the quadriceps muscle to the tibia. However, altered tension in the patellar tendon, whether due to tendinopathy or surgical intervention, can impair normal knee function by disrupting weight distribution. Stephen et al. further elaborates on this by highlighting how incorrect femoral tunnel location and graft tension can negatively affect patellar contact mechanics and kinematics post-Medial Patellofemoral Ligament Reconstruction [156]. In conclusion, it's evident from the state-of-art research that baseline tension within knee ligaments is vital for maintaining joint stability, efficient force transmission, and smooth joint articulation.

The complexity of the biomechanical context of knee ligaments, and principally of the Anterior Cruciate Ligament (ACL), raises the need for efficient and reliable measurement and simulation methods. Investigating the baseline tension, i.e., pre-strain, values within ACL can contribute significantly to physiological modelling and testing of knee joint behaviour. Harris et al. [157] demonstrated how customized constraint models offer significant insights into the complexity of knee joint laxity, suggesting the need for such tools to be adaptable to different individuals. Their research highlights the need for accurate verification to ensure that ligament engagement agrees with current research literature, underlining the dynamic nature of this area of study. Navacchia et al. [158] offer another viewpoint on these biomechanical complexities. They stressed how important it is to pick out key parameters when making subject-specific models so that the inherent uncertainty of in vivo conditions can be captured well. By employing a global probabilistic analysis, the study underscored the potential for more realistic estimates of muscle and joint loads in the knee.

However, it is hard to say exactly what the range of baseline tension (pre-strain) is in the knee ligaments and the patellar tendon because measurement methods vary, people are different (for example, in age, activity level, and health), and the knee joint itself is biomechanically complex. However, some studies have attempted to provide estimates or describe methods to measure these values in a biomechanical context. [157-158]

For knee ligaments such as the ACL, reported baseline tensions can vary significantly. Some experimental setups have applied pre-strains ranging from 1% to 3% to simulate physiological conditions for biomechanical testing. However, these values are primarily derived from in vitro studies or computational models and may not directly translate to in vivo conditions due to the dynamic nature of the knee joint's biomechanics.

Direct measurement of baseline tension in vivo is challenging because it requires isolating the ligament or tendon from the influences of surrounding muscle forces and joint positions. Non-invasive imaging techniques and computational modelling provide insights but often offer indirect estimations. Consequently, most of the available data on baseline tension are derived from biomechanical studies using cadaveric specimens or mathematical models, which attempt to replicate physiological loading conditions. Further research employing advanced imaging and biomechanical modelling techniques may provide more accurate insights into these values, enhancing our understanding of knee joint function and informing surgical practices.

2.3.6 Measurement of ligament tension, strain, and stress

2.3.6.1 In Vitro Techniques

In vitro research involves cadaveric studies or the use of synthetic knee models. Ligament tension is often measured by applying controlled forces to the knee joint and recording the resultant strain on the ligaments. These studies allow for a controlled environment where variables can be systematically manipulated to understand ligament behaviour under different conditions.

The cadaveric testing allows for the direct measurement of ligament forces, strains (shown in Figure 8. Cadaveric testing for the measurement of ligament strain), and responses to various loading conditions without the variability introduced by living tissues. Based on this, mechanical testing of isolated ligaments was also derived. This method involves isolating individual ligaments from the knee joint and subjecting them to uniaxial or biaxial tensile tests. The isolated ligament is typically clamped at both ends and stretched while measuring the force and displacement to generate stress-strain. This approach minimises variability associated with living tissues, as cadaver specimens can be precisely mounted in mechanical testing systems. High-precision devices, such as robotic manipulators and universal testing machines, facilitate the replication of physiological knee motions while accurately recording ligament responses [159]. The research by Wascher et al. [160] stands as a pioneering effort in this domain, employing specially designed load-transducers to measure the forces exerted by the posterior and anterior cruciate ligaments in response to multiplane loading on cadaveric knees. This investigation provided a foundational understanding of ligamentous force distribution, which is crucial for the development of sensor-equipped implants intended for in vivo applications. The ethical considerations surrounding the use of Postmortem Human Subjects (PMHS) are crucial, emphasising the need for adherence to established guidelines to ensure the integrity of research outcomes [161]. Furthermore, the development of quality assessment tools like the Biomechanics Objective Basic Science Quality Assessment Tool (BOBQAT) enhances the methodological rigor of cadaveric biomechanics studies, ensuring that essential elements such as loading conditions are thoroughly considered [159].

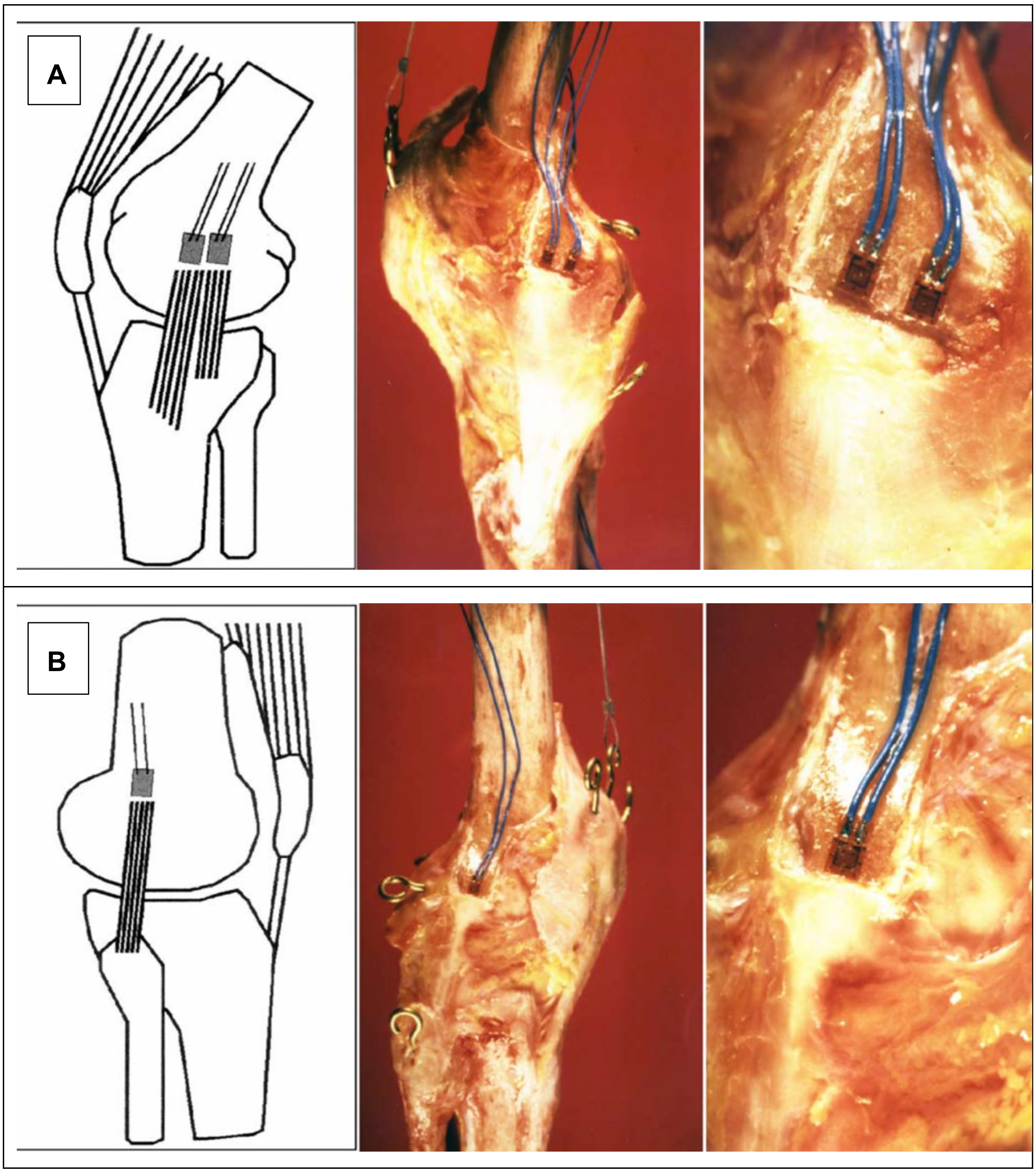

Figure 8. Cadaveric testing for the measurement of ligament strain (Reprinted from Hinterwimmer et al., 2002). [162]

Figure 8 shows both strain gauges were placed at the femoral ligament insertion where the segmentation into two portions is most obvious (see Figure 8. A); The lateral collateral ligament is a very homogeneous cord-like structure without division into different bundles. It was measured with only one gauge at its femoral insertion (see Figure 8. B). [162]

Through an extensive review of the literature, it has been observed that the current research landscape prominently features techniques that facilitate the direct measurement of ligament forces, strains, and responses under various loading conditions while also minimising the variability typically associated with living tissues. Maletsky et al. [163] provide a seminal contribution in this area, offering a thorough review of the different rigs, machines, and experimental methodologies used to study the kinetics and kinematics of the knee joint. Their work underscores the importance of high-precision instruments, such as robotic manipulators and universal testing machines, in replicating physiological knee movements and capturing ligament responses with great accuracy. This contribution is foundational in advancing our understanding of cadaveric knee testing.

Moreover, Prusa et al. [164] delve into the technological advancements in measurement tools essential for these studies, particularly focusing on a comparative analysis between directly attached foil-type strain gauges (SG) and 3D digital image correlation (DIC) methodologies. Their research highlights the superiority of optical systems based on DIC for measuring superficial strains in human ligaments. This advancement not only enhances the accuracy of cadaveric testing but also enriches the methodological toolbox by promoting non-invasive, high-precision strain measurement techniques.

There is a study by Ross J. Fox et al. [165] that examines the in-situ forces within the posterior cruciate ligament (PCL) and its two bundles—the anterolateral and posteromedial bundles—using robotic technology on cadaveric knee models. The research involved applying varying posterior tibial loads (22 to 110 N) at different knee flexion angles (0° to 90°), allowing for precise measurement of the forces on the PCL. The study found that these forces varied significantly depending on the knee flexion angle and load magnitude. The anterolateral bundle's maximum force occurred at 60° of flexion, while the posteromedial bundle peaked at 90°, with no significant differences between the bundles across flexion angles. The findings are crucial for improving PCL reconstruction techniques, particularly in graft placement and tensioning, and highlight the need for further research to optimize postoperative rehabilitation. While the use of elderly cadaveric specimens may affect absolute force values, the trends observed are considered generally applicable, offering valuable insights for future clinical applications.

The anterior cruciate ligament (ACL) is vital for knee stability, particularly in resisting anterior tibial translation. Cadaveric studies provide insights into its in situ forces across flexion angles, informing ACL reconstruction. Sakane et al. (1997) investigated in situ forces in the ACL and its anteromedial (AM) and posterolateral (PL) bundles using nine cadaveric knees (mean age: 71 years). A robotic manipulator and universal force-moment sensor measured forces under anterior tibial loads (22–110 N) at 0°, 15°, 30°, 60°, and 90° flexion, allowing unconstrained knee motion. [166]

In vitro research, involving cadaveric studies or synthetic knee models, plays a critical role in advancing our understanding of knee ligament biomechanics. By applying controlled forces to the knee joint and recording the resultant ligament strain, these studies provide a controlled environment that allows for systematic manipulation of variables to observe ligament behaviour under specific conditions. This approach has the advantage of eliminating the variability inherent in living tissues, thereby enabling a more precise examination of ligament forces, strains, and biomechanical responses.

The advancement of knee ligament biomechanics through in vitro research methodologies including cadaveric testing and isolated ligament mechanical testing comes with certain limitations. The controlled testing environments of these studies provide valuable information about specific variables, but they fail to duplicate the complete dynamic and multifactorial characteristics of living knee joints. The use of cadaveric specimens from elderly donors restricts the applicability of research findings to younger or more diverse population groups. The advancement of strain measurement tools has not yet solved the problem of fully understanding ligament behaviour complexity. The current research shows the necessity to improve in vitro techniques while using in vivo studies and computational modelling to achieve complete understanding of knee ligament biomechanics.

2.3.6.2 In Vivo Techniques

Researchers conduct in vivo research by directly measuring ligament tension inside living subjects through implanted strain gauges or non-invasive MRI imaging with motion capture data. The research methods focus on observing ligament function in its natural state to study the intricate knee joint interactions. The method provides essential knowledge about knee ligament behaviour during sports activities and daily movements under physiological conditions.

The non-invasive tool ultrasound strain elastography enables reliable knee collateral ligament stiffness measurement which helps clinicians better understand knee collateral ligament biomechanics in clinical practice [167]. Magnetic Resonance Imaging (MRI) serves as the primary diagnostic tool for knee ligament evaluation because it delivers essential information about tissue health and damage severity [168].

Innovative techniques for measuring ligament strain non-invasively using MRI have been explored. The study by Phatak et al. [169] proved deformable image registration techniques suitable for non-invasive human medial collateral ligament strain assessment. The new approach enables researchers to study ligament behaviour under different physiological conditions through non-invasive methods which replace traditional surgical interventions. The creation of MRI-based methods for ligament elongation measurement represents a significant advancement in ligament analysis. Csapo et al. [170] showed MRI can measure ACL elongation which could serve as a diagnostic tool to assess ligament load-bearing potential. The assessment of ligament health and post-injury or surgical rehabilitation planning could experience a revolution through this new technique.

Moatshe et al. (2017) emphasized the significance of stress radiographs for diagnosing ligamentous injuries and evaluating postoperative stability [171]. This method underscores the significance of imaging methods in complete knee ligamentous structure evaluation and establishes guidelines for diagnosing multiple knee ligament injuries.

Bae and Cho (2020) performed a simulation study to externally examine the biomechanics effects of tunnel position and pre-tension on the stress and strain of implanted grafts during ACL reconstruction surgery [172]. from a biomechanics perspective. The study revealed that the stress on implanted grafts was mainly affected by tunnel placement rather than pre-tension force which demonstrates the importance of surgical technique for achieving optimal postoperative results.

The use of in vivo techniques enables researchers to study knee ligament behaviour in real time within living organisms. The combination of implanted strain gauges with non-invasive MRI imaging and motion capture technology enables researchers to study ligament function in its natural state. The method delivers precise observations of ligament behaviour during sports activities and daily movements which are essential for knee biomechanics understanding. The methods deliver important information, but researchers need to resolve their built-in constraints to enhance both their effectiveness and clinical utility.

The valuable insights from in vivo methods regarding ligament biomechanics and function come with specific limitations. The knee joint's complex dynamic interactions remain partially invisible to non-invasive imaging tools including ultrasound elastography and MRI. Simulation studies and stress radiographs help explain ligament function and postoperative stability, yet they fail to duplicate the complete complexity of in vivo conditions. Research and clinical applications of ligament biomechanics require an integrated method which combines advanced imaging techniques with computational modelling and clinical assessments to overcome current limitations and achieve better accuracy and reliability.

2.3.6.3 In Silico Modelling Techniques

The development of ligament mechanics research has been significantly enhanced through Finite Element Analysis (FEA). Accurate biomechanics modelling of knee ligaments under various conditions has become possible through advanced finite element analysis techniques which enable precise determination of stress and strain states. Khmyzov et al. (2022) created a finite element model of the lower limb to investigate knee joint stress-strain behaviour with and without cruciate ligaments for pre- and post-surgical knee joint structural evaluation [173]. The computational modelling system delivers essential data about knee ligament biomechanics under various conditions to develop optimal treatment approaches. The models' accuracy depends heavily on the exactness of their input parameters which include material properties and boundary conditions and knee joint geometric representations. The reliability of these models depends heavily on both correct geometrical reconstruction and precise mathematical descriptions of biological tissue behaviour and their environmental interactions. We need to enhance our understanding of constitutive behaviour for common biological tissues including ligaments, tendons and menisci.

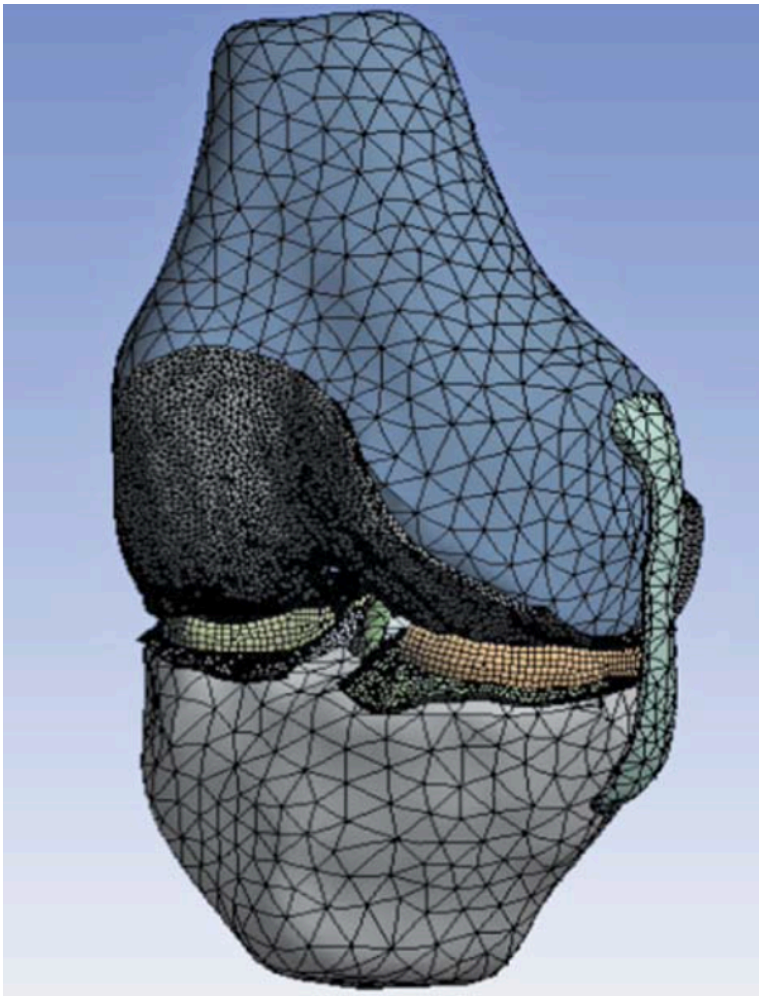

Figure 9. FE model of the knee joint with mesh elements. (Reprinted from Khot et al., 2021) [174]

In exploring the intricate biomechanics of the human knee joint, a range of computational models have been developed to analyse its behaviour under various conditions. A notable gap in current research is the comprehensive inclusion of menisci, articular cartilages, and all main ligaments with initial stresses in computational analyses.

The development of knee ligament modelling has progressed from basic one-dimensional (1D) models to advanced three-dimensional (3D) models which provide more precise representations. The advancement represents a fundamental step forward in understanding knee anatomy and biomechanics and pathophysiology of injuries and disorders. Three-dimensional modelling has become a vital research focus because it helps improve diagnostic precision and surgical planning while enabling individualized therapeutic approaches. A groundbreaking study Beidokhti et al. [175]addresses the limitations inherent in 1D ligament models by developing and comparing two distinct finite element knee models based on 3D ligament modelling approaches. This work underscores the importance of leveraging 3D models for a more nuanced and precise representation of knee ligaments, which are critical for accurately simulating knee mechanics and understanding ligament behaviour under various physiological loads.

Heegaard et al. [176] made a significant contribution to the field with their development of a three-dimensional model for analysing human patella biomechanics during passive knee flexion. Their comprehensive computer model based on the finite element method calculates the joint's kinematics, tendinous and ligamentous forces, articular contact pressures, and stresses. This work set a precedent for the complexity required in modelling the knee to understand its dynamics thoroughly.

Building on the need to understand the control mechanisms of knee joint kinematics, Beynnon et al. [177] presented a sagittal plane model of the knee and cruciate ligaments. Their study focused on sensitivity analysis to better comprehend how cruciate ligament bundles influence joint behaviour. Although offering significant insights, this model, like Heegaard et al.'s, did not incorporate a fully three-dimensional representation of all main ligaments with initial stresses.

The quest to represent ligaments more accurately in computational models is evident in the work of Wan et al. [178] They advanced the field by analysing the effect of ACL constitutive model variations on joint kinematics and biomechanics under different loads, employing a three-dimensional finite element model. Their findings underscored the importance of representing the ACL realistically, guiding future model development towards incorporating comprehensive ligament behaviours.

Open Knee [179] by Erdemir on the other hand, represents a significant leap towards open-source modelling in knee biomechanics. This project provides a detailed finite element representation of the tibiofemoral joint, including major tissue structures and their mechanical interactions, aligning with the necessity for comprehensive, accessible models in advancing the understanding of knee biomechanics.

These studies collectively underscore the ongoing challenge in biomechanics modelling to replicate the knee's complex behaviour accurately. While advancements have been made in three-dimensional modelling and understanding individual components of knee mechanics, such as patella tracking [176], cruciate ligament behaviours [177-178], and opening avenues for open-source modelling [179], a cohesive model that includes menisci, articular cartilages, and all main ligaments with initial stresses as specified remains unmapped.

The research by Song et al. [180] demonstrates how three-dimensional finite element modelling (FEM) of the human anterior cruciate ligament (ACL) has improved our knowledge of ACL biomechanics under different loading scenarios. The research focused on evaluating force and stress patterns in the anteromedial (AM) and posterolateral (PL) bundles of the ACL through a validated three-dimensional FEM model that utilized experimental data.

The FEM used MRI-derived anatomical details together with experimental kinematic data obtained from a cadaveric knee through robotic/universal force-moment sensor testing. The model validation was possible through experimental measurement comparison which enabled further stress distribution analysis of the ACL bundles. The PL bundle carries substantially more load than the AM bundle when the knee extends fully under anterior tibial loading conditions. The stress distribution across both bundles showed non-uniform patterns with maximum stress concentrations occurring near the femoral insertion site which matches clinical observations of typical ACL injury locations.

Despite its contributions, the study's methodology is not without limitations. The most significant limitation is the boundary conditions for the FEM were derived from kinematic data at full knee extension with an anterior tibial load. While this condition is relevant for understanding certain injury mechanisms, it does not encompass the full range of motion and loading scenarios encountered by the ACL in vivo. The exclusion of compressive and bending loads, as well as the omission of higher flexion angles and rotational loads, limits the model's ability to simulate more complex and realistic joint movements, such as those experienced during pivoting or cutting motions in sports. This limitation reduces the model's utility in predicting ACL injuries that occur in more dynamic and multi-planar contexts.

An exploration of the biomechanical behaviour of the human knee joint using finite element (FE) modelling was done by Pena et al [181]. The study integrates key structures such as bones, ligaments, patellar tendon, meniscus, articular cartilage and includes initial strains in the ligaments and the patellar tendon, aiming to replicate realistic knee joint conditions into a comprehensive 3D model to simulate and analyse the behaviour of the joint under various loading conditions. However, the model examines static conditions only which does not capture the complete movement dynamics of knee activities during walking and running. The model's ability to predict dynamic situations remains restricted because of this limitation. The model depends on data from previous studies, but this data may not match the exact characteristics of the modelled subject. The results become less accurate because of this potential variability. The model fails to consider the viscoelastic characteristics of ligaments and menisci which would impact the accuracy of stress-strain predictions especially when loading persists for extended periods.

Traditional methodologies depend on static conditions together with single-plane models which fail to properly represent the dynamic multi-planar knee joint motion. The approaches examine particular motion ranges and loading conditions but fail to account for the complete range of physiological knee movements. These studies encounter boundary condition problems and initial assumption sensitivity which leads to unreliable or incomplete results.

Finite Element Analysis (FEA) has emerged as a powerful tool that addresses these limitations. The combination of detailed anatomical data with material properties and complex boundary conditions in FEA enables a detailed simulation of knee biomechanics. FEA surpasses traditional methods because it enables stress and strain and ligament force analysis across various motion planes under different loading conditions to study ligament behaviour which static or isolated tests cannot measure. FEA models can accurately model realistic knee joint interactions through simulations of dynamic loads and rotational forces and multi-planar movements which leads to better understanding of ligament responses during real-world conditions.

The accuracy of FEA models for knee ligament research depends on the quality of the input data although the method provides significant improvements to ligament research. The precision and reliability of FEA models can be improved by integrating them with dynamic imaging techniques which include real-time medical image techniques. The combination of real-time motion-capturing imaging technologies with FEA computational power enables the development of dynamic in vivo models which simulate ligament behaviour during continuous motion.

The integration enables real-time data collection of ligament deformation and strain which can directly enhance FEA models by reducing initial assumptions and improving boundary condition accuracy. The combination of dynamic imaging with FEA allows researchers to model intricate interactions between knee ligaments and cartilage and other soft tissues which better represents the actual biomechanical environment. The improved reliability of ligament tension estimates through this method enhances both injury mechanism prediction and treatment strategy development for ACL reconstruction and rehabilitation planning.

The combination of dynamic imaging methods with finite element analysis provides a solution to overcome the current challenges in knee biomechanics research. The combined method produces a more precise model of knee movement and better predicts how ligaments behave in actual knee conditions. The advancement will deliver enhanced knowledge about knee joint mechanics which will lead to better clinical applications and improved patient results.

The knee joint functions through its complex structure which enables ligaments to work with muscles and joint geometry to achieve its purpose. The knee achieves its wide range of motion and multiple loading capabilities across different planes through its complex interconnection of structures which enables efficient movement and activity. The knee joint performs its movements of flexion and extension along with internal and external rotation and abduction and adduction through the combined action of the medial and lateral collateral ligaments (MCL and LCL) and the anterior and posterior cruciate ligaments (ACL and PCL). The hip and tibia and patella musculature together with their joint geometry play a major role in controlling knee function. The musculoskeletal model of Frigo and Donno [182] illustrates this interaction. The model includes the femur, tibia, and patella along with crucial ligamentous and muscular elements which consist of the quadriceps, hamstrings, gastrocnemius, cruciate ligaments and collateral ligaments. The model delivers exclusive data about the equilibrium between different muscles and ligaments.

The knee joint behaviour can be completely understood through the combination of kinematic analysis and complex 3D modelling. These methods enable researchers to study how the soft tissue and skeletal structures of the knee joint work together when the joint moves. Researchers can use 3D modelling to simulate and analyse and predict how the knee joint will respond to various loads and movements which enables them to understand the joint's anatomy in detail. Through motion capture and dynamic MRI kinematic analyses researchers can obtain information about the knee joint's motion timing and coordination as well as its range of motion. The knee joint's ability to move in multiple directions demonstrates its intricate biomechanical structure. Advanced 3D modelling together with kinematic analysis serve as essential tools for studying the dynamic behaviour of the knee joint. The combination of these tools enables better understanding of knee function which leads to improved patient outcomes in orthopaedic practice through clinical decision making.

The existing research documents multiple approaches to study the dynamic knee behaviour through various methods. Advanced 3D modelling and kinematic analysis represents a limited aspect of the intricate biomechanical operations of the knee joint. The main function of kinematic analysis is to deliver essential data regarding knee motion timing and coordination and movement extent. Harris et al [157] demonstrated in their research that stress models serve as essential tools for knee joint loosening analysis. The research demonstrated that model modifications enabled accurate predictions of knee responses to various activities and stressors which matched the findings from existing studies. Navacchia et al [158] reinforced the necessity of creating individualized models to forecast knee stress during in vivo conditions. The research applied global probability analysis to demonstrate how general scaling models' inherent uncertainty affects the calculations of muscle and joint loading. The method enables better predictions of knee reactions to different physical activities during loading.

Three-dimensional modelling aids in the visualization and measurement of the knee's motion patterns. The work by Zeng et al. [183] advances the discussion, underscoring the utility of 3D continuum approach in capturing the intricate interactions of active skeletal muscles. The described modelling framework was found to be reliable and anatomically accurate, further cementing the value of 3D modelling in biomechanical knee studies.

The cutting-edge technology of four-dimensional computed tomography (4dCT) and musculoskeletal simulations, especially Finite Element Analysis (FEA) and Musculoskeletal Modelling (MM), have brought a new era in the field of biomechanical research, particularly focusing on the knee joint [184-186]. 4dCT has been recognized as an advent technology in capturing high-resolution images of the knee in various positions throughout its range of motion [187]. It highlights joint motion over time, hence providing a dynamic assessment and supplementing traditional static imaging methods. The examination on its accuracy in analysing knee joint movements was conducted by Adachi et al., demonstrating that the position-posture of knee joint movements could be recorded with a minor error when compared with a highly accurate motion-capture system [187]. The conjunction of 4dCT with computational modelling and musculoskeletal simulations has been pivotal in evaluating joint mechanics and, more importantly, assessing the relationship between bony structures during a motion [185-186]. The FEA scan adds to the 4dCT scan by looking at the stress on the knee joint after a partial meniscectomy for meniscus horizontal cleavage tears. It shows a lot more about the pressure and shear force in the knee joint [184]. On the other hand, MM has shown promising outcomes in reducing knee contact force when inspired by musculoskeletal simulations, reflecting its potential use for optimizing coordination for a variety of rehabilitation applications [185]. Studies have also unveiled the pivotal role of MM in investigating the effects of external loads and muscle forces on knee joint ligaments during movements like walking [186]. The advancements in 4dCT imaging and computational modelling facilitate a more comprehensive understanding of knee joint mechanics. Its discrepant usage in biomechanical research presents a bright perspective on the potential of these technologies in expediting efficient and accurate studies of intricate knee joint interactions. Collectively, these studies significantly contribute to the state of the art of three-dimensional modelling and kinematic analysis of the knee joint.

2.4 4D Computed Tomography (4dCT)

Computed Tomography (CT) operates as an essential diagnostic tool and research facilitator through its sophisticated radiological imaging technique to deliver precise anatomical details [200]. The imaging technique produces cross-sectional images through computational algorithms that process X-ray measurements obtained from different body angles. The X-ray beam technology in CT imaging produces body cross-sections which deliver precise detailed anatomical information. Medical professionals use CT imaging for diagnostic procedures and treatment planning and therapeutic interventions because of its diagnostic effectiveness and versatility. The fast image acquisition capabilities of CT make it essential for emergency medical situations because it provides quick accurate diagnoses. A medical study demonstrates how CT helps identify hollow visceral lesions during blunt trauma diagnosis [201]. CT serves as an essential tool for trauma patient evaluation because it detects fractures while assessing internal injuries and provides precise guidance for surgical procedures. CT imaging functions as a research instrument to develop medical understanding and therapeutic breakthroughs in addition to its diagnostic applications. CT imaging serves as a vital diagnostic and therapeutic tool in contemporary medical practice across multiple medical specialties. The assessment of trauma patients requires strict decision rules according to [202] even though CT imaging remains an essential tool.

While conventional CT imaging is undoubtedly important, 4dCT promises to improve conventional 3D CT scans by adding time-dependent dynamic assessments [203]. 4dCT extends the capabilities of conventional CT by incorporating time as a fourth dimension, allowing the capture of dynamic processes and movements in the body.

CT and 4dCT work together to enhance combined multidimensional motion analysis through their beneficial relationship. The anatomical details from CT enable doctors to detect structural issues while preparing for medical procedures. 4dCT extends the current foundation by incorporating motion data to create a comprehensive view of joint functionality and biomechanics. The combined analysis improves therapeutic choices by enabling precise treatments and customized rehabilitation plans which result in better patient results.

4dCT presents an innovative method to study multidimensional joint movements by enabling the visualization and quantification of joint structure interactions during movement. The technology enables better understanding of joint biomechanics and prosthetic implant functionality and rehabilitation therapy planning through joint motion assessment and stability evaluation and load distribution analysis.

The imaging technique serves as an essential tool for studying complex organic systems including the knee joint in orthopaedics. The knee joint benefits significantly from 4dCT technology because of its complex biomechanical characteristics [203]. The main use of knee joint studies involves using 4dCT to display joint mechanics while the joint moves. These movements remain poorly represented by traditional imaging methods. 4dCT proves essential for real-time observation of tibiofemoral and patellofemoral knee joint kinematics under natural loading conditions.

The 4dCT imaging technique enables researchers to study joint functionality through motion integration which helps evaluate joint biomechanics during movement [204-205]. 4dCT has proven useful for researchers who study the complex movements of joints including the knee and wrist [204-207]. The assessment of surgical intervention success through 4dCT involves analysing motion patterns before and after surgery [207]. The accuracy level of 4dCT has been confirmed through positive verification. The accuracy of 4dCT knee joint motion imaging was validated through a study which reported errors below 3mm and 2 degrees [208]. The reliability of 4dCT is demonstrated through these findings which also establish its importance for joint motion analysis.

4dCT stands as an essential tool in orthopaedic surgery for TKA and ligament reconstruction procedures [203]. Surgeons can use the dynamic knee joint views from 4dCT scans to enhance their predictions of surgical outcomes and create patient-specific surgical procedures. The success of surgeries in restoring normal joint functions can be assessed through postoperative 4dCT scans. Postoperative 4dCT scans help reveal knee joint compensation patterns which surgeons can use to develop better rehabilitation strategies. The clinical applications of 4dCT expand past treatment planning into the field of knee prostheses design and assessment [203]. 4dCT serves to evaluate how knee prostheses function when implanted and moving in dynamic situations. The use of 4dCT applications will improve our knowledge of prosthetic design matching natural knee kinematics which can enhance implant placement strategies and explain prosthetic failure reasons. The integration of 4dCT data with computational biomechanical models represents an advanced application of this technology which has the potential to become the most impactful [203].

Modern medical imaging depends on CT and 4dCT as fundamental elements for diagnosis. The static images obtained from CT serve as crucial elements for injury evaluation. Through its functionality 4dCT enhances the comprehension of joint movements while assisting surgeons in planning their interventions. The connection between CT and 4dCT allows healthcare professionals to achieve better diagnostic and therapeutic planning capabilities across various medical fields. The detailed dynamic measurements provided by 4dCT enable the development of reliable models which predict knee mechanical behaviour across different conditions. The models enable doctors to predict how knee function will change due to anatomical modifications from injuries or surgeries thus allowing personalized treatment planning. The advantages of 4dCT remain limited by complex software requirements for dynamic movement interpretation and data acquisition and processing complexity as well as higher radiation levels than standard CT scans. Research teams together with medical staff must assess the benefits of 4dCT particularly focusing on radiation exposure and technical needs for conducting 4dCT studies.

2.5 Computational Simulation

Medical simulation research of knee kinematics shows promise to advance our understanding of essential topics particularly for surgical planning and procedure prediction. Computer simulation provides surgeons with multiple benefits for knee surgery planning because it enables them to see the effects of procedures such as ligament reconstruction or arthroplasty before actual surgery takes place. The acquired information helps surgeons develop better surgical plans which leads to improved patient results. Through computer modelling researchers can analyse the knee joint forces that occur during different activities. The analysis of implant wear risks during total knee arthroplasty becomes possible through this understanding [209]. Medical simulations help identify mechanical causes of common knee injuries such as ACL tears while analysing surgical intervention long-term effects. The simulations enable researchers to study various loading conditions which helps them identify the mechanical failures that lead to these injuries [210]. In turn, innovative ways to prevent such injuries can be explored and potentially implemented. This utility was demonstrated in a study that harnessed a computer model to mimic the removal of the meniscus; the objective of this experiment was to discern how a partial meniscectomy influences the stability of the knee joint and the allocation of stress on the cartilage. This study accentuated the pivotal role of the meniscus in load-bearing and joint stability and suggested the preservation of the meniscus should be prioritised during surgical intervention [210]. Rehabilitation exercises can not only be designed, but optimized using simulations, which allow for a detailed examination of the stresses imposed on healing tissues during movement [211]. This was aptly demonstrated in a study involving a three-dimensional model of the knee, which was employed in a study investigating the mechanics of isolated knee flexion. This research revealed the complexity of the balance of forces required for smooth motion and underscored the importance of muscle coordination for maintaining joint stability [211].

Particularly evident in studies on knee joint kinematics, such approaches offer valuable insights into the interaction between forces, motion, and structural integrity of the knee joint across its full range of movement, with implications for surgical interventions, injury aetiology, and rehabilitation protocols [212]. One method is to make anatomical and functional models of the knee that include the different ligaments, cartilage, and muscle supports so that motion and load distribution can be simulated [213]. For instance, Kang et al. have undertaken pioneering work in this field, using computational methodologies to evaluate the biomechanical influence of posterior condylar offset and tibial slope in total knee arthroplasty. This article is about how changes in the posterior condylar offset affect the contact stress in the patellar button and the forces acting on the posterior cruciate ligament, the patellar tendon, and the quadriceps muscles when the knee bends deeply [212]. Meanwhile, Beynnon et al. developed a sagittal plane model of the knee and cruciate ligaments. This model enables closer examination of tibiofemoral compressive loading and the force/strain values of cruciate ligament elements. The findings, however, pointed to rigidity between the articular surfaces, indicating the potential need for more realistic assumptions in the modelling process [213]. Despite the potential of these modelling techniques for understanding knee kinematics, challenges persist in ensuring the exactness and predictive power of the models. The model calibration phase remains a crucial step in ensuring the precision of the models, which necessitates further research [214].

The future of knee kinematics study will depend on better computational methods and more detailed biomechanical data to achieve personalized medicine in orthopaedics. Medical simulation analysis, which includes computational models, anatomical data, and advanced simulation software, provides an essential framework for studying knee kinematics. This approach, as shown in the examined research, enables the understanding of complex biomechanical behaviour and the development of efficient clinical solutions.

2.5.1 Finite Element Modelling / Analysis (FEM/A)

The advanced computational tools FEM and FEA are widely used in biomechanics to study complex systems including the knee joint as explained in Section 2.3.6.3. These methods serve as essential tools for studying biological tissue mechanics while revealing the complex dynamics of musculoskeletal systems. The simulation tool FEA generates detailed models that duplicate knee joint forces and motions and interactions which enables powerful knee mechanics and ligament behaviour and tissue response analysis under different loading scenarios.

The simulation of complex biological tissues like ligaments through FEA provides the best possible method to model their non-linear anisotropic and viscoelastic properties. The mechanical properties of knee stabilizing ligaments change according to loading direction and speed. Through FEA researchers can model precise ligament material characteristics to simulate their behaviour during physiological conditions. The work of Burgio et al. [215] stands as an important reference point in this context. The researchers conducted a comprehensive review and comparison of animal ligament mechanical properties to identify suitable human ligament surrogates. This research fills an important need by connecting theoretical models to practical surrogates that scientists can use for more precise simulations. The recognition of similar mechanical properties between ligaments from different species strengthens both animal model validity in biomedical research and FEA model accuracy for human ligament prediction across different conditions. Through FEA modelling of ligaments researchers gain essential knowledge about stress distribution and strain localization and tissue deformation which helps explain injuries and develop better treatment approaches.

The accuracy of simulations depends heavily on proper boundary condition and loading scenario definitions which are fundamental elements of FEA [216-217]. The definition of boundary conditions for knee joint simulations requires precise representation of physiological conditions which includes ligament attachment points and joint constraints and soft tissue interactions. The simulation of joint motion becomes more realistic when these conditions are properly defined especially when dealing with complex multi-planar forces that occur during daily activities. The Open Knee(s) project led by Chokhandre et al. has advanced the field through their development of open-source sample-specific knee models which accurately simulate knee behaviour under different physiological conditions [218]. The simulation of dynamic loading scenarios which track time-dependent forces across multiple planes allows researchers to predict ligament responses in real-world conditions thus delivering essential information for clinical practice and research purposes.

FEA demonstrates exceptional capability in studying the effects that different loading conditions have on knee biomechanics. Researchers can study how different loads affect ligament tension and joint stability and tissue stress through controlled force applications in the simulation. The ability to simulate various loading conditions from low-impact daily activities to high-stress athletic movements enables FEA to develop more effective rehabilitation protocols and surgical interventions and orthopaedic devices including prosthetics and orthotics. The precise control of loading applications helps researchers understand the role of particular forces in ligament strain thus making FEA essential for injury prevention and treatment planning.

The combination of dynamic medical imaging technologies with FEA through real-time MRI or ultrasound elastography has improved the field by enabling the development of personalized models. The incorporation of real-time tissue deformation and motion data from dynamic imaging into FEA models enables researchers to create simulations that accurately represent the actual physiological knee joint conditions of individual patients. The use of real-time data in FEA leads to more accurate boundary conditions and material properties which produces more precise simulations of ligament behaviour and joint mechanics.

Research teams can create highly individualized models through the combination of detailed geometric and material data from dynamic imaging with FEA computational power which takes into account each patient's unique anatomical and biomechanical characteristics. The personalized approach enhances FEA predictive power which makes it a better clinical decision-making and treatment planning tool.

2.5.2 FEA combined with 4dCT

The combination of finite element analysis (FEA) with 4dCT technology produces highly precise knee models that use patient-specific data to simulate motion and track tissue mechanical behaviour throughout time. Researchers use time-point knee motion data to build finite element models which enable them to study how different loading conditions and kinematic behaviours, and surgical interventions affect knee joint mechanics.

The combined application of four-dimensional computed tomography (4dCT) and finite element (FE) analysis has been reported in the literature, but remains relatively uncommon, with the majority of work concentrated in thoraco-abdominal organ motion modelling. One of the earliest examples can be traced back to Brock et al. (2002) [219], who employed paired liver CT scans and FE analysis to construct a four-dimensional model of hepatic deformation during respiration. Subsequently, Werner et al. (2009) [220] developed patient-specific respiratory motion models for lung tumours based on 4D-CT datasets, using FE methods to simulate the displacement of pulmonary landmarks. In contrast, within the musculoskeletal field—particularly in relation to joints—4dCT is primarily used to capture dynamic kinematics, whilst FE analysis is typically based on static CT or MRI geometries for the evaluation of stress and strain (Wong, 2022) [221]. To date, studies that directly utilise complete 4dCT time series as input for FE simulations in musculoskeletal biomechanics are exceedingly rare, underscoring the novelty and potential impact of approaches that explicitly couple dynamic imaging with computational modelling in this context.

The rapid development of 4dCT technology has greatly improved our understanding and ability to analyse the dynamics of the knee joint. This advancement allows time-resolved imaging, providing a revolutionary view of knee joint motion and facilitating the construction of highly accurate finite element analysis (FEA) models. A critical review of the literature shows a growing interest in the use of these technologies to elucidate knee joint mechanics, especially in the context of surgical interventions and biomechanical assessments. A related study by Adachi et al [222-223]. highlights the accuracy of 4dCT in analysing knee joint motion, using a knee joint model and motion capture system to validate the accuracy of 4dCT. The results showed an error of less than 3 mm and less than 2 degrees when compared to a high precision optical motion capture system, highlighting the potential of 4dCT in capturing the complex dynamics of knee motion [222-223]. This seminal work lays the foundation for the use of dynamic imaging in the assessment of postoperative knee kinematics. An integral part of integrating 4dCT data with finite element analysis is the assignment of accurate material properties to the different tissues of the knee model. Kang et al. developed a computational model focused on probabilistic estimation of material properties of articular surfaces in vivo. Their approach, based on in vivo measurements, paves the way for future specialised studies, especially for scaffold, allograft and biologics-based treatments in the tibiofemoral (TF) joint [224]. This study demonstrates the care taken to ensure that tissue behaviour modelled using FEA models accurately reflects physiological responses, which is a key factor in the prediction accuracy of these models. The study by Watanabe et al, which extends the application of FEA models derived from 4dCT data, focuses on the development of a CT-FEM model of the knee joint suitable for analysing the load response during the stance walking phase. Studying knee mechanics in the context of dynamic activities such as walking not only allows for a better understanding of knee mechanics but also identifies potential mechanisms of injury and prevention strategies [225]. This information is invaluable for optimising surgical techniques to take into account the biomechanics of each patient, thus increasing the effectiveness of reconstructive surgery. The discussion on the biomechanical consequences of surgical interventions has been broadened by the study by Indelli et al, which critically examines kinematic recovery after sensory total cruciate knee arthroplasty. Their results indicate a significant deviation from native knee kinematics, prompting further investigation into the effects of surgical modifications on knee kinematics, which has a direct impact on preoperative planning and prediction of postoperative outcomes [226]. It is evident from the reviewed literature that the interplay between advanced 4dCT imaging technologies and FEA models holds a promising frontier in the biomechanical examination and surgical intervention planning of knee joints. These studies collectively underscore the paramount importance of accurate imaging, material property assessment, and dynamic simulation in not only understanding but also enhancing knee joint treatments and outcomes.

This study used the 4dCT scanning technique to study the kinematic knee joint to assess the efficacy of such an approach for the diagnosing and monitoring of knee pathologies and treatments. 4dCT may help the relevant medical staff to accurately assess the patient's kinematic and kinetic of the knee joint and based on above analysis results develop a targeted treatment plan. Further, by comparison of analysis results of kinematic and kinetics in healthy volunteers, before and after arthroplasty, and across different implant designs, it may be able to quantitatively and functionally compare between different makes and designs of knee implants to determine which, if any, achieves native knee biomechanics.

Finite element analysis has emerged as a powerful tool in the study of knee kinematics and the multidimensional motion of the knee joint. By providing a detailed understanding of the biomechanical behaviour of the knee, FEA facilitates the optimization of surgical techniques, the design of orthopaedic implants, and the development of targeted rehabilitation protocols. As computational resources and modelling techniques continue to evolve, the application of FEA in knee biomechanics is expected to yield even more profound insights into the functioning of this complex joint.

It is important to note that the reliability of these models strongly depends on an appropriate geometrical reconstruction and on accurate mathematical descriptions of the behaviour of the biological tissues involved and their interactions with the surrounding environment. In this sense, we still need to improve our information about the constitutive behaviour of some of the most common biological tissues, such as ligaments, tendons, and menisci.

2.5.3 Boundary conditions

In advancing the finite element (FE) analysis of knee joint kinematics, the understanding and application of boundary conditions have become quintessential for the accurate simulation of joint behaviour. The bone, cartilage and soft tissues operate under multiple loading conditions in complex ways which makes identifying boundary conditions challenging yet essential for determination. Research on the topic continues to grow with a particular focus on boundary conditions and loading conditions effects on modelling results that enhances knee joint mechanics understanding. The various surgical approaches for treating posterior root tears of the lateral meniscus demonstrate why accurate surgical modelling stands essential for knee joint functionality restoration. Wang et al [227] show through finite element analysis that different surgical repair approaches including double and single suture methods result in substantial modifications to knee joint contact mechanics and kinematics. This research demonstrates how surgical procedures affect knee joint modelling because boundary conditions remain essential for finite element analysis of knee kinematics. The study by Hu et al [228], demonstrates how difficult it is to accurately simulate knee joint movement during gait cycles when natural knee joint architecture is incorporated into musculoskeletal models. The study demonstrates how force-dependent kinematics works to explain natural knee movements and shows that boundary conditions must be carefully defined to replicate natural kinematic responses. The computational model presented by Dussan-Delvasto et al [229], extends finite element analysis applications in knee biomechanics for preoperative planning particularly for ACL reconstruction. The research offers a valuable method to analyse biomechanical modifications before surgical procedures through accurate boundary condition modelling for predicting ACL stresses. The groundbreaking method developed by Muller et al [230], uses combined rigid body dynamics modelling with nonlinear finite element analysis to advance knee joint prediction capabilities. This research breaks down the knee modelling processes to demonstrate why proper boundary condition understanding and application remains vital for achieving both reproducibility and meaningful knee mechanics interpretation. The cumulative story of finite element analysis in knee biomechanics receives support from these studies which demonstrate the necessity of precise boundary condition definition and implementation. External boundary conditions serve as the fundamental basis for understanding the intricate mechanics of the knee joint when performing surgical interventions or analysing natural joint movement or pre-surgical planning or innovative modelling approaches.

For FE modelling the kinematics of the knee joint, external boundary conditions are generally divided into two main categories: geometric boundary conditions and load boundary conditions.

2.5.3.1 Geometric boundary conditions

The geometric boundary conditions require the physical constraints and geometry that establish the structure of the joint. The contact surfaces of the femur, tibia and patella must be accurately defined. The model requires precise definitions of joint geometry together with contact zones and articular cartilage biomechanical properties. The geometric boundaries can be described through displacement, velocity and acceleration but zero displacement in 3 dimensions is commonly used to constrain model movement.

2.5.3.2 Load Boundary Conditions

The knee joint model requires load boundary conditions to simulate external forces and motions that affect its behaviour. The knee joint model receives external forces and moments or displacements that simulate physiological movements during loading scenarios. The accuracy of finite element models for knee kinematics depends heavily on proper boundary condition representation. Researchers can achieve better understanding of knee mechanics and clinical decision making through experimental data integration with biomechanical knowledge to strike a balance between physiological realism and computational efficiency.

2.5.4 Initial conditions

The model requires initial conditions to be specified for particular parts which serve as starting values for the upcoming analysis. The tension of knee ligaments and tendons needs to be proscribed because they do not start at zero tension.

2.5.5 Knee ligaments as springs

The accuracy of finite element analysis (FEA) of knee joint kinematics depends heavily on boundary conditions because they establish how bones and cartilage and soft tissues interact when subjected to different loading scenarios. The difficulty of defining these conditions especially when modelling ligament and tendon behaviour makes it necessary to evaluate the possibility of simplification or optimization without compromising biomechanical integrity. The manual creation of elastic materials to replace ligaments and the patellar tendon represents a promising method to simplify boundary conditions within specific FEA models of the knee joint.

The modelling of ligaments and patellar tendon becomes challenging because these structures exhibit non-linear tensile behaviour while maintaining essential knee joint stability under dynamic loading conditions. The manual creation of these structures through simplified elastic materials serves as a practical solution for particular modelling applications. The representation of ligaments and the patellar tendon as elastic materials with specific biomechanical properties such as stiffness and tensile limits helps decrease the computational requirements.

The literature supports this approach because researchers have proven that spring elements work effectively to model ligaments and tendons. The study by Kiapour et al. [231], used uniaxial nonlinear elastic truss (spring) elements to model ACL, PCL, MCL and LCL ligaments because it reduced computational complexity while maintaining essential ligament biomechanical properties. The elastic element modelling technique produced accurate knee movement predictions and ligament force measurements which showed that elastic simplification maintains both biomechanical accuracy and computational speed.

The study by Dastgerdi et al. [232] demonstrates how spring elements can effectively model key ligaments such as ACL, PCL, MCL and LCL in paediatric knee modelling. Their subject-specific finite element models used bundles of nonlinear springs to capture the mechanical behaviour of these ligaments while facilitating model convergence. This method of simplification underscores the practicality of using elastic elements to model complex soft tissue behaviours in knee FEA models.

Similarly, Abidin et al. (2019) [233] used spring elements in their FEA model to simulate ligamentous structures in the knee joint. The model achieved biomechanically relevant results by assigning linear stiffness properties to these springs while simplifying the representation of ligaments. The elastic spring elements in knee joint modelling were validated through experimental data comparison which supported their feasibility.

The process of building elastic materials to replace ligaments and tendons requires these materials to demonstrate equivalent behaviour to their biological counterparts. The materials need to replicate both their load-carrying properties and their non-linear elastic behaviour. Elastic materials can be designed to show different stiffness levels based on strain magnitude which matches the tension responses of ligaments and tendons. The simplified approach helps researchers avoid complex soft tissue modelling so they can concentrate on essential joint forces and movements.

The construction of elastic materials to replace ligaments and the patellar tendon serves as a viable simplification method for finite element analysis of knee joint kinematics. The method provides the most benefit when modelling joint behaviour and load distribution and preoperative planning instead of detailed ligament mechanics. Spring elements provide a strong method to simplify soft tissue modelling according to Kiapour et al. (2014), Dastgerdi et al. (2023), and Abidin et al. (2019) [231-233] while preserving biomechanical accuracy.

2.5.6 Indeterminacy

The biomechanical analysis of knee systems becomes complex when unknown forces exceed the number of governing equations which defines an indeterminate system. The force calculations of soft tissues including ligaments and tendons become unfeasible because of their complex interactions which create an unresolvable computational problem. The knee joint model shows stability through multiple structural contributors according to Silva & Ambrósio (2002) [234] because the number of unknowns exceeds the available equations which defines an indeterminate system. According to Challis (1991) the determination of forces in such systems becomes difficult because joints contain numerous muscles that exceed the available degrees of freedom for movement [235]. The joint stability depends heavily on the ACL and PCL along with the MCL and LCL and the patellar tendon, but these structures create major difficulties when determining the system's force distribution (Hefzy & Grood, 1982) [236].

The biomechanical properties of soft tissues introduce nonlinearity which makes the modelling process more complex. The force-deformation response of ligaments and tendons shows non-linear material behaviour when subjected to loading forces because their stiffness does not grow linearly with increased loads. The nonlinearity in knee biomechanics poses additional difficulties because linear models fail to represent the changing joint stiffness that occurs with different flexion angles (Grood & Hefzy, 1982) [236]. The non-linear properties of the knee joint along with its hyperstatic nature require the use of finite element analysis (FEA) and iterative solution methodologies for analysis. The methods use iterative force estimation to reach dynamic equilibrium while handling the joint's interconnected structure (Madeti et al., 2015) [237].

The resolution of indeterminate systems often depends on optimization techniques as a primary methodological approach. The addition of objective functions through optimization techniques produces supplementary equations which enables models to determine force distribution with higher accuracy. Optimization-based models according to Komistek et al. (2005) provide excellent benefits for ligament tension estimation through pattern-based force distribution adjustments yet anatomical differences create obstacles for model standardization [238]. Optimization methods today need to handle anatomical structure and tissue composition variations because these factors affect the generalizability and robustness of knee joint models (Küpper et al., 2006) [239].

The intrinsic indeterminacy of knee biomechanics continues to be a difficult problem despite the progress made with FEA and optimization. The standardization of knee joint models becomes difficult because of individual variations in ligament stiffness and tendon elasticity and joint geometry which require adaptive methods to accurately model knee joint dynamics. The indeterminate nature of knee models requires a refined iterative approach according to Hefzy and Grood (1988) which continuously adapts to soft tissue biomechanical properties to enhance predictive reliability [240]. The current models successfully simulate complex knee mechanics yet additional advancements in data resolution and computational methods are needed to overcome indeterminate system limitations and achieve accurate knee joint biomechanics representations. The study proposes iterative solution methodologies to handle these complexities. The method begins with initial ligament tension assumptions which are repeatedly adjusted until equilibrium is reached. The calculation of forces and moments occurs during each iteration until the successive iterations match a predetermined tolerance. The model runs its iterative process until it reaches a solution which fulfils both equilibrium requirements and knee joint mechanical limitations. This iterative approach can be mathematically represented as follows:

$$T_n + 1 = T_n + \alpha(F_{external} - F_{internal})$$

Where T_n represents the ligament tensions at the n-th iteration, α is a relaxation parameter, and $F_{external}$ and $F_{internal}$ represent the external and internal forces, respectively.

The equilibrium solution requires testing for robustness by changing initial conditions (e.g., initial ligament tension values) to verify consistency. The model stability is confirmed when the converged solution shows stability under different initial assumptions. The system's uncertainty leads to multiple solutions even when the model reaches a set of forces. The iterative approach delivers a practical solution which produces dependable equilibrium solutions for the knee model despite its complex nature.

2.5.7 Necessity of Integrating 4dCT with Finite Element Analysis for Knee Biomechanics

While three-dimensional (3D) imaging and finite element analysis (FEA) have been widely employed in orthopedic biomechanics, both approaches have intrinsic limitations when applied independently to the study of knee ligament mechanics. Conventional static imaging modalities, such as MRI or standard CT, provide high-resolution anatomical information but capture only a single joint configuration, thus neglecting the dynamic changes in geometry, contact conditions, and ligament strain throughout the range of motion. Similarly, many existing knee FEA models are constructed from static geometries or cadaveric specimens, which do not reflect in vivo ligament pre-strain, muscle activation, or the influence of dynamic loading conditions. As a result, such models often require assumed or literature-based inputs for ligament tensions, contact parameters, and boundary constraints, potentially limiting their clinical relevance.

Other limitations in previous FE knee models include the use of generic or simplified ligament geometries with idealized attachment sites, the omission or oversimplification of physiological pre-strain, and the adoption of static boundary conditions that cannot replicate the coupled rotations and translations of the tibiofemoral and patellofemoral joints during motion. Contact interactions are sometimes modelled with unrealistically high friction coefficients, which can inadvertently stabilize the joint and mask the mechanical role of ligaments. These simplifications, while computationally convenient, reduce the capacity of such models to capture subject-specific joint mechanics and to predict clinically relevant outcomes under dynamic conditions.

Four-dimensional computed tomography (4dCT) addresses several of these constraints by capturing sequential volumetric images over time, enabling the reconstruction of joint kinematics with high temporal and spatial resolution. This technique provides in vivo motion data without the invasive procedures associated with direct ligament force measurement, offering precise, frame-by-frame bony kinematics.

However, 4dCT alone cannot provide stress, strain, or contact pressure distributions, nor can it directly quantify ligament forces.

Integrating 4dCT data with an iterative FEA framework overcomes these limitations by combining the high-fidelity, subject-specific kinematic inputs from imaging with the predictive capabilities of mechanical simulation. The 4dCT-derived geometries ensure anatomical accuracy, while sequential positional data inform displacement-driven boundary conditions in the FEA model. This enables iterative adjustment of ligament forces until the simulated motion reproduces the observed in vivo kinematics. The FEA environment can then be used to derive contact pressures, ligament force–flexion profiles, and stress distributions—metrics unattainable from imaging data alone.

By capturing both kinematics and kinetics in a physiologically relevant, dynamic context, this 4dCT–FEA approach bridges the gap between purely imaging-based motion analysis and purely simulation-based biomechanics. It provides a platform for evaluating surgical interventions, such as total knee arthroplasty, under patient-specific conditions, and for estimating native ligament tensions in vivo. This capability offers significant potential for improving preoperative planning, achieving more accurate soft tissue balancing, and ultimately enhancing postoperative functional outcomes. The novelty and necessity of the present method therefore lie in its ability to unite the complementary strengths of 4dCT and FEA, producing a robust and clinically meaningful representation of knee joint mechanics.

2.6 Thesis Aims

From the above review of the literature, it is understood that the knee joint is a biomechanically complex synovial structure, integrating stability, mobility, and load bearing through the synergistic interplay of ligaments—the anterior cruciate ligament (ACL), posterior cruciate ligament (PCL), medial collateral ligament (MCL), lateral collateral ligament (LCL), and the patellar tendon. These ligaments collectively restrict excessive motion whilst enabling dynamic function, though their interdependence often complicates injury diagnosis.

Modelling of the native knee holds potential for understanding its biomechanical function in healthy and pathological states (and following replacement) and in particular the role and importance of knee ligament tension in the balance of the knee. The need of quality imaging is paramount for such models and four-dimensional computed tomography (4dCT) has significant potential for furthering our understanding. By capturing dynamic, high-resolution spatial and temporal kinematics, 4dCT enables the construction of anatomically accurate three-dimensional (3D) models, revolutionising preoperative planning. Integrating 4dCT with finite element analysis (FEA) may offer a transformative approach to quantify native ligament tensions during flexion.

By integrating established literature, it is proposed that a multidisciplinary framework that combines dynamic imaging and computational modelling (FEA) is developed to overcome the limitations of static or cadaveric analyses. However, the indeterminate nature of ligamentous forces demands a novel approach to their determination and the validation of the models from which they are derived. This is the topic of this thesis.

This review highlights gaps in prior finite element models and the critical need for 4dCT integration to advance ligament tension and contact pressure analyses.

2.6.1 To develop a novel methodology to determine ligament tensions in the knee through inverse FE analyses.

The literature review has highlighted that the prior methodologies of determining ligament tension can be put into essentially two categories: cadaveric experimental modelling or FEA. Cadaver tests do not have any muscle activation and also involve intrusion into the joint capsule. FEA analyses have been limited to single frames of joint position, often focusing on single ligaments. There is a desire to develop a methodology to determine tension of multiple ligaments and tendons in the knee, throughout the range of motion, based on image data from live humans. It is postulated that this may be achieved through the inverse fitting of an FE model. This approach aims to more accurately simulate the behaviour of the ligaments during knee flexion and may have potential to be applied to a variety of loading scenarios.

It has been shown that multiple images of the knee joint, throughout the range of motion, can be collected using 4dCT at 3Hz [241]. Can this data set be used to construct FEA models of the knee joint in order to determine ligament tensions? The workflow would need to include segmentation and meshing of bony elements, the creation of soft tissue structures and the subsequent creation of an FE model with appropriate boundary conditions.

Ligament and patella tensions will be unknown variables in any such model. It is proposed that by initially estimating these tensions, and through iterative calculations and matching resulting positions to the experimental images, it is possible to converge to single ligament tensions that describe the knee environment. Starting this process from different initial estimates of tension may address the concern of indeterminacy in the system of forces. It is suggested that if the forces converge on the same tensions, irrespective of starting estimate, then this would give confidence to the resulting tensions in representing the unknown true values.

In essence, the study aims to establish a proof-of-concept methodology for iteratively assessing ligament stresses during knee flexion, with the potential to be applied to many situations, including post-TKA function. The use of 4dCT imaging and iterative finite element analysis represents an innovative approach to quantitatively understand ligament behaviour, potentially aiding in the development and improvement of soft tissue balancing procedures in knee surgery. This new methodology has the potential to impact the field of orthopaedic surgery, allowing surgeons to make more informed decisions and ultimately improve patient outcomes. By providing a quantitative basis for understanding the complex biomechanical interactions in the knee joint, this study lays the foundation for developing more targeted and personalised surgical interventions.

Furthermore, the knowledge gained from this study may have far-reaching implications beyond knee arthroplasty. The process of iterative finite element analysis combined with the use of 4dCT imaging can be adapted to study other joint systems and soft tissue structures, leading to advances in the treatment of a wide range of musculoskeletal conditions. The integration of these advanced technologies and computational methods represents a significant advancement in the field of biomechanics, paving the way for a new era of precision medicine in orthopaedics.

Thesis aims connect to these insights, using 4dCT/finite element to derive contact pressures and inform TKR soft tissue balancing. [242]

2.6.2 To self-validate the novel FE model of the knee by predicting knee kinematics throughout the range of motion

It is well-established that experimental validation of FE analysis is important in order to give confidence to the computational accuracy. Furthermore, often the validation experiments focus on one experimentally measurable variable of interest. In taking legacy images, from live patients, it is not possible to experimentally validate the FE model developed above through conventional means. Given there are sequential images of the same knee at different flexion angles, this may give a unique opportunity to develop a novel method of validation of the model. The second research question is therefore can we accurately predict the kinematic motion of the knee from one frame to another? If this is accurately achieved, given the estimated tensions, then this approach may go some way to self-validate the model itself.

The basic knee joint complex consists of three bones (femur, tibia and patella), connected by ligaments and tendons. By applying the known movements of the femur and patella from one frame to the next, it is possible to compare the estimated (FE model) position of the tibia to the known (image). If the two tibiae match well, we may conclude that the interconnecting structures, i.e. the ligaments, are well described in the model.

Quantification of Euclidean displacement variables can reveal subtle changes in joint mechanics occurring during flexion-extension, such as the motion of kinematic variables between two frames of the model. This is done by calculating the straight-line distance and direction between two points in 3D space, as well as the translational motion (linear motion along the x, y, and z axes) and rotational motion (rotation about these axes) of the knee assembly. Furthermore, we use Cloud-Compare's advanced functions, such as point cloud registration and distance calculation, to further verify the calculation results.

In summary, the objectives of the second aim of this work is to analyse the knee joint displacements during dynamic flexion-extension using a comparative approach based on grid node coordinates and the Cloud-Compare software tool. By quantifying Euclidean variable displacements between a frame of image data and that predicted by FE analysis, including the formerly determined ligament tensions, then this will go some way to self-validating the model with regards to these tensions.

3 Materials and Methods

The creation of a three-dimensional (3D) musculoskeletal-ligament model and subsequent analysis of the comparative kinematics and kinetics of the loaded knee joint (KJ) during flexion-extension movements are necessary to achieve the project aims and objectives. This analysis necessitated the use of finite element analysis (FEA) combined with bespoke, comparative modelling techniques. This chapter describes the development of these two techniques.

Following data acquisition (section 3.1), the first computational step in the process was the creation of 3D solid models based on DICOM data from 4d computed tomography (CT) scans of each patient (section 3.2). Briefly, this translation was facilitated through the use of Mimics software (Materialise NV, Belgium), which decomposes the original DICOM data into nine images. These images provided a solid basis for the subsequent modelling procedures as they captured the full range of motion of the knee up to approximately 65 degrees.

In the next step, the meniscus and cartilage were created using the "Base Creation" and "Boolean Subtraction" procedures. The shapes of the meniscus and cartilage were defined using the "Create Base" function, and any overlap between the contact surfaces was removed using the "Boolean Subtraction" function to ensure structural congruence.

Drawing from known research, the material characteristics of menisci, articular cartilage, and bones were modelled as being elastic, linear, and isotropic. The patellar tendon (PT), lateral collateral ligament (LCL), medial collateral ligament (MCL), posterior cruciate ligament (PCL), and anterior cruciate ligament (ACL) were modelled using spring components. These components were dispersed across a predetermined, representative region and fastened at projected bone insertion sites. The tibia was subjected to a vertical force of 40N, acting 20 cm from the knee joint centre, without kinematic restrictions, whereas the femur and patella were fully limited by the application of constraints. All ligaments and PTs were initially tensioned to 100 N, followed by iterative adjustments and modifications. The procedure was repeated with an initial preload of 200 N to achieve convergence, which is characterised by a tension difference of less than 1% across all ligaments and PTs.

This analytical approach allowed for a thorough investigation of the comparative kinetics of the knee joint during flexion-extension motions. Based on the accurate translation of patient-specific DICOM information into intricate 3D solid models, it made use of the sophisticated capabilities of simulation modelling and finite element analysis.

Figure 10 below illustrates the overall FEA processing flow, which is key to understanding the iterative methodology for determining ligament tensions.

FEA Processing Flow

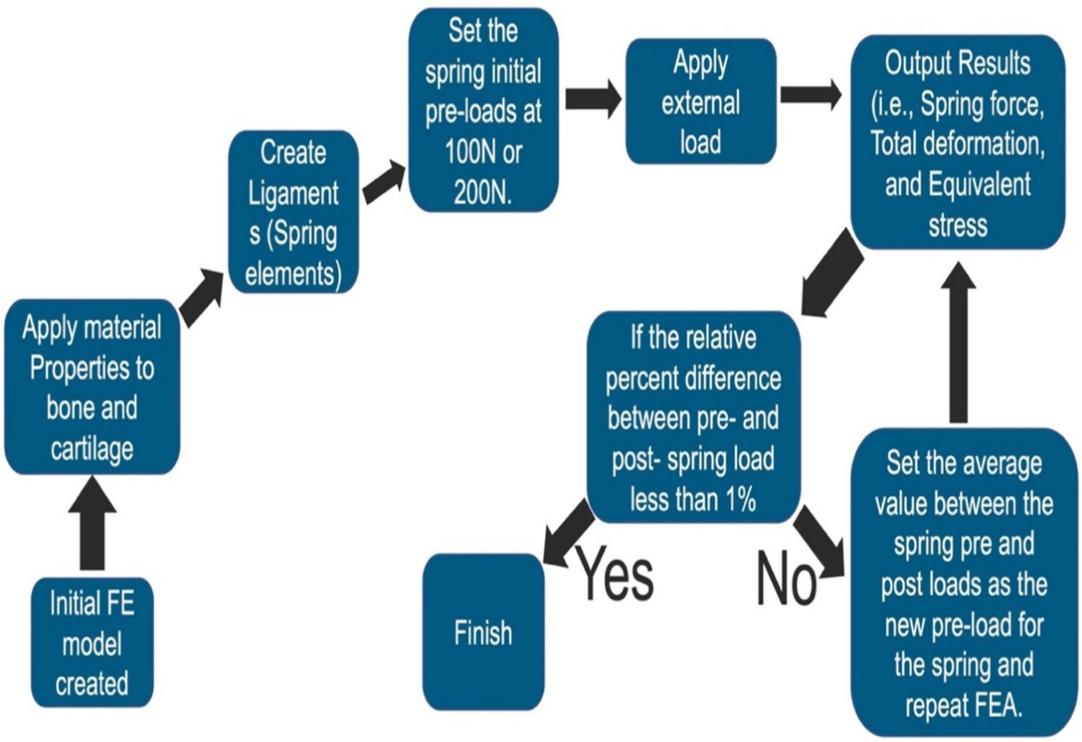

Figure 10. FEA processing flow

3.1 4dCT Data Collection

The collection of the 4dCT data used in this study is detailed elsewhere [241]. Briefly, the 320-multidetector CT (320-MDCT) scanner, namely the Toshiba Aquilion ONE™ 4d, was employed to capture the dynamic movements of the knee joint (Queen Elizabeth University Hospital (QEUH), Glasgow). The scanner is equipped with SEMAR (Single Energy Metal Artefact Reduction) technology, which uses an iterative reconstruction method to reduce the appearance of metal streak artefacts. This technology improves implant detectability while preserving bone and soft tissue integrity. This can enable scans of metallic knee implants to be taken [241], although such data was not part of the current study. The scanner is capable of generating real-time 4d images across a significant 16-cm range without the need for table movement (as shown in Figure 11. 4dCT scanning and RAW data collection.). This capability facilitates non-invasive dynamic kinematic assessments of tissue movement and enabling comparative functional study.

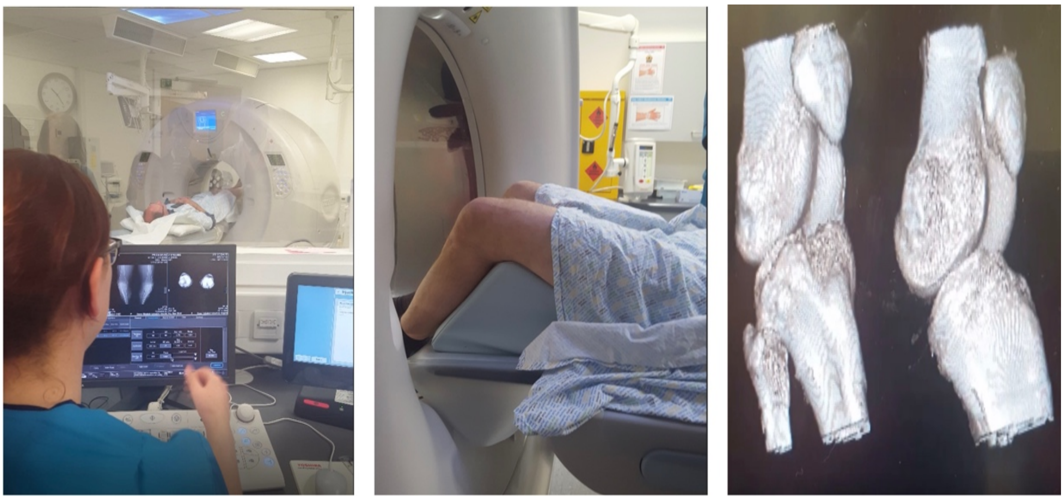

Figure 11. 4dCT scanning and RAW data collection.

To gather the dynamic knee joint data, a new scanning methodology was developed by the QEUH radiologists. The experimental and scanning settings were developed iteratively to maximise participant comfort, enhance kinematic accuracy, and to improve radiological precision. The level of radiation to which patients are exposed is one concern associated with CT scans and since dynamic CT involves multiple sequential images to be captured, the risk is potentially greater for this collection modality. The Aquilion ONE™ 4dCT uses the Adaptive Integrated dosage Reduction (AIDR 3D) control system, an innovative algorithm that adjusts tube current in real time to optimise radiation dose based on the area of interest and patient anatomy. The calculated cumulative effective dose for knee CT was 0.8 mSv, which is comparable to background radiation levels in the UK over a nine-week period. This dose is associated with a very low lifetime risk of fatal cancer and therefore the risk was deemed negligible by the Head of Health Physics in the Radiology Department at QEUH. This information ensured ethical approval for this study [241]. This thesis utilises anonymised patient data and therefore has no ethical considerations.

Nine volunteers were recruited: three healthy controls and six total knee arthroplasty (TKA) recipients, comprising three with ultra-congruent fixed-bearing (UC-FB) implants and three with ultra-congruent mobile-bearing (UC-MB) implants. Upon entering the scanning room, participants positioned themselves in a supine posture on the CT plinth, with a cushion put under their knees creating a 90° knee flexion angle. Full active extension of the knee followed by knee flexion back to 90° was requested. A metronome was used to help provide timing of the action over four beats. A total of nine frames of image data per participant were acquired over a period of 4.55 seconds, each acquired at a constant interval of 0.35 seconds (approximately 3Hz). Bilateral knee data were collected from a 16cm region containing the distal femur and proximal tibia. These images potentially allow for the development of approximately 162 individualised three-dimensional finite element (FE) models of the patients' knees. This number results from scanning the knee joints of nine participants, with each participant contributing data for two knees. Each knee was further subdivided into nine distinct knee joint models, enabling subject-specific analyses at the compartmental level and ensuring anatomical and biomechanical individuality across all models: $9 \times 2 \times 9 = 162$. In doing so these models will be able to enable comparative functional analyses and expanded our understanding of knee dynamics. However, to do so, a methodology needs to be developed to convert these images into validated FE models, including soft tissue structures which are not easily extracted from CT images. As described in Section 2.7, this is the focus of this dissertation.

Although multiple volunteers were recruited [241], only one time sequence of frames was used in this thesis to develop and show the potential of the analysis technique.

3.1.1 DICOM Image Resolution

The dynamic CT datasets were acquired with an in-plane pixel size of 0.625 mm × 0.625 mm and a slice thickness of 0.625 mm, using a 512 × 512 acquisition matrix and a field of view (FOV) of 320 mm × 320 mm. The interslice spacing was equal to the slice thickness. These acquisition parameters define the spatial resolution of the volumetric data, influencing the geometric fidelity of segmented anatomical structures and the subsequent finite element mesh quality. High in-plane resolution and small slice thickness reduce partial volume effects, which is critical for accurately capturing thin cartilage layers and small ligament attachment areas.

3.2 3D-Geometry Model Generation

This study utilises a systematic approach to develop anatomically accurate models of the knee joint for finite element analysis (FEA). At the time of development, the Department of Biomedical Engineering had licenses for Materialise Mimics™ and 3-Matic™. These two software tools were adopted in the model development process, although there is other software, freely available, which may be able to conduct the same analysis.

This procedure is based on the need to create accurate and complex anatomical models that accurately represent the complex shapes seen in human anatomy, especially in the knee joint. The knee joint consists of a complex topology of bones, ligaments and cartilage. Mimics™ software facilitates the initial conversion of medical imaging data, such as computed tomography (CT) or magnetic resonance imaging (MRI), into accurate 3D models offering a wide range of capabilities for processing, analysing and interpreting medical imaging data. Mimics was used in this study to segment the image data into specific bony, anatomical regions using a combination of automated algorithms and manual refinement tools. After the segmentation process, Mimics was used to recreate 3D models allowing anatomical features to be visualised and studied in a 3D environment. These models can be modified, examined for structural features or used as the basis for computer simulations such as Finite Element Analysis (FEA) to predict biomechanical behaviour in different environments.

Once the anatomical structures are segmented, the 3D models are further processed using 3-Matic. 3-Matic plays an essential role in the refinement and enhancement of these models, particularly in preparation for FEA. The software is employed to create detailed meshes and to develop soft tissue structures, such as cartilage and the meniscus, which are vital for accurately simulating the biomechanical behaviour of the knee joint. The quality of the mesh is paramount, as it directly influences the accuracy and stability of the simulations. 3-Matic offers advanced meshing tools that ensure the generation of high-quality, optimised meshes that maintain the structural integrity of the original anatomical features. 3-Matic also facilitates the creation of soft cartilage and meniscus structures. These elements are essential for capturing the complex interactions within the knee joint, including load distribution and joint articulation. The software allows for the integration of material properties and geometries that closely replicate the physiological conditions of these tissues, enhancing the realism and predictive capability of the FEA.

The integration of Mimics and 3-Matic in this methodology ensures a seamless transition from raw medical imaging data to fully developed models ready for FEA. The combination of precise anatomical segmentation with advanced model refinement techniques results in 3d geometric representations of the knee joint. Their accuracy is unknown, but it has been shown (Asadirad, 2024) [243] that segmentation is a reproducible activity which gives confidence to the process. The models created are not only suitable for FEA but also hold potential for other applications, such as pre-surgical planning and the design of patient-specific medical devices.

The specific details of the workflow involved in using Mimics™ and 3-Matics™ is given in the following subsections.

3.2.1 Image Process flow

An overview of the workflow is given here, with additional detail in the following subsections.

1. Importing DICOM Files

DICOM files were outputted by the CT scanner and each DICOM file contained multiple images per time frame (providing a 3d representation), as well as multiple time frames, providing the 4^{th} dimension (i.e. 4dCT). The first step is to import a single DICOM file (one **healthy** volunteer knee joint scan data) into Mimics.

2. Segmentation of Images (see 3.2.1.1)

After importing the DICOM data, each time frame of the image is segmented. This important step involves several techniques. Firstly, thresholding techniques are used in Mimics to differentiate between different areas, such as bone and soft tissue, by analysing the intensity level of pixels. This allows specific areas of interest to be identified. This was achieved by region growing, or by manual techniques. Region growing is a pixel-level method that grows a region by combining neighbouring similar pixels to create coherent segmented regions. Region growing was applied for the primary extraction of long, continuous, high-contrast bone regions—particularly in frames with thick cortices and clean boundaries (minimal motion or beam-hardening)—allowing rapid filling of intrabone spaces from thresholder masks without spill over. Manual segmentation is used in situations where automatic methods may not work, either because of the complexity of the images or because the structures being analysed require subtle differences. Manual segmentation was reserved for thin cortices, narrow joint spaces, and bony contact zones where partial-volume effects promote leakage; for frames affected by motion, metal, or beam-hardening artefacts that disrupt intensity continuity; for cartilage and other soft tissues whose Hounsfield unit (HU) distributions overlap adjacent structures; and to enforce temporal consistency when masks were propagated between time frames.

Relying on a single method was suboptimal, region growing is vulnerable to overruns through partial-volume bridges and to missed regions across subtle discontinuities, whereas purely manual delineation is accurate but impractically time-consuming and less reproducible across the full 4d dataset. Accordingly, we combined both—using region growing for fast, reproducible bulk segmentation and manual refinement to preserve anatomical fidelity in challenging areas—yielding consistent, high-quality segmentations throughout the sequence.

3. Three-dimensional Reconstruction and FE Modelling

Following, the segmentation step, the method proceeds to 3D reconstruction and modelling. Using surface reconstruction techniques such as the marching cubes algorithm, the segmented data was converted into a 3D surface model that accurately represents the anatomical structure in virtual form. Additionally, the articular cartilage was created in 3-matic using CAD modelling techniques. The meniscus was not modelled as its shape is very difficult to create, and the resulting mechanics would involve highly complex and multiple contact regions reducing the ability of the model to solve. It is acknowledged that any contact stresses are more likely to be a maximum estimate than would be expected if the meniscus was created. Ligaments were created in the FEA software. Once all solid structures were created, 3-Matic facilitated the creation of a mesh representing the 3D structure. This mesh is required for finite element analysis (FEA).

The resulting mesh was exported as a .cdb file to be imported into the FEA software (Ansys™).

3.2.1.1 Segmentation

Segmentation of DICOM 4dCT raw data is an important process that involves identifying and highlighting specific structures or areas of interest in the image data. Depending on the properties of the dataset and the structures under investigation, different segmentation approaches may be used.

Manual, semi-automatic, and automatic segmentation:

i. Manual segmentation involves, on a pixel-by-pixel basis, identifying and delineating structures of interest in each image of the dataset. Although labour intensive, manual segmentation is often considered the most accurate method.

ii. Automatic segmentation involves the use of algorithms to autonomously recognise and highlight specific structures of interest. Common methods include threshold selection, region growing, and active contours. Automated segmentation methods are faster than manual methods but sacrifice accuracy to some extent.

iii. Semi-automatic methods, as the name suggests, involves both automatic and manual methods. Initially an automatic algorithm is used, the outcome of which is then fine-tuned, manually. Semi-automatic methods find a balance between accuracy and efficiency, integrating automatic segmentation with human modifications.

MIMICS™ is one software which uses segmentation algorithms to create 3D models from DICOM files, and it allows for both manual and semi-automatic segmentation techniques. The process involves importing the 4dCT DICOM files into MIMICS, which automatically converts them into separate images for each frame of movement. Each image may be used to develop a different 3D model, allowing complete analysis of the segmented structures over the time history of the movement. Separate segmentations were carried out for each frame, rather than having a reference segmentation with the mesh for each bone transformed based on anatomical landmarks for each frame.

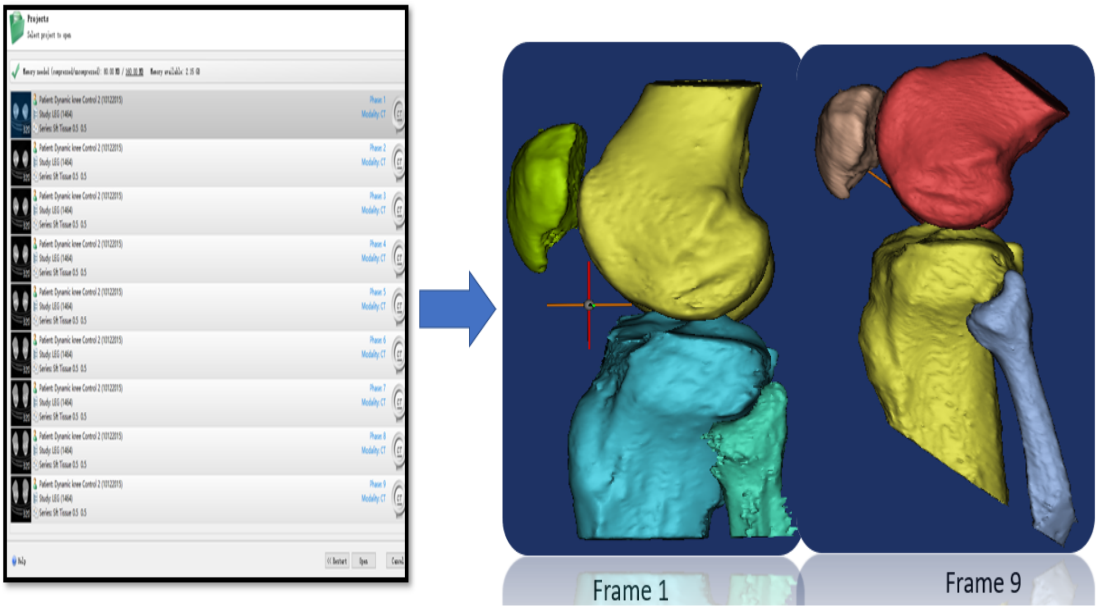

Figure 12. Convert and segment the DICOM into 9 frames in MIMICS and 3-Matic

Ideally, each model would require the inclusion of several key anatomical structures, such as the tibia, femur, patella, ligaments, cartilage, and meniscus. However, due to the similarity in the Hounsfield Unit (HU) values of various soft tissues, these structures were challenging to segment either automatically or manually. Since multiple models were to be created, a streamlined and efficient workflow was required and the decision was made not to segment non-bony anatomy. The 4dCT dataset was therefore used to identify the geometry and pose of the femur, tibia, fibula and patella only.

The process of segmenting the bony anatomy began by defining bone boundaries using "threshold extraction", a method in which pixels indicating the presence of bone in a particular slice were extracted based on HU intensity values. To facilitate segmentation, threshold values were strategically set between 226 and 2513. In the segmentation of DICOM 4dCT images, the selection of the correct threshold values between 226 and 2513 is based on systematic trial and error to make the process of highlighting certain structures or regions of interest as efficient as possible. The following explanations address several critical factors that influence this choice.

The threshold range is carefully selected according to the radioactivity characteristics of the target anatomical structures, measured in Hounsfield units (HU). This ensures that these structures are selectively enhanced with respect to the surrounding tissue matrix, which facilitates their accurate segmentation. For example, a lower threshold of 226 HU is designed to exclude irrelevant soft tissue or fluid densities, while an upper limit of 2513 HU effectively covers the range of high densities characteristic of bone or calcified tissue, without including artefacts or noise that may be present at higher densities.

Using upper and lower threshold values contributes to computational efficiency by limiting the amount of data fed to segmentation algorithms. This concentration on meaningful data points not only speeds up processing time, but also reduces computational load, allowing more efficient use of resources and facilitating the processing of large data sets inherent in 4dCT images.

Following threshold extraction, the next objective was to create accurate masks for the three bones of interest: femur, tibia, and patella. To achieve this goal, a "regional growth" technique combined with "Boolean operations" to refine the segmentation, was used.

To simplify the model as much as possible, it was decided that, as the fibula did not contact with the femur or patella, it may be removed from the model. Obviously, the lateral collateral ligament (LCL) inserts onto lateral femoral epicondyle (Figure 13, point A) and the fibular head (Figure 13, point B), but it was assumed the line of action of this ligament passed so close to the lateral aspect of the tibia (Figure 13, point C), insertion of the LCL to this anatomical location was a reasonable and justifiable simplification.

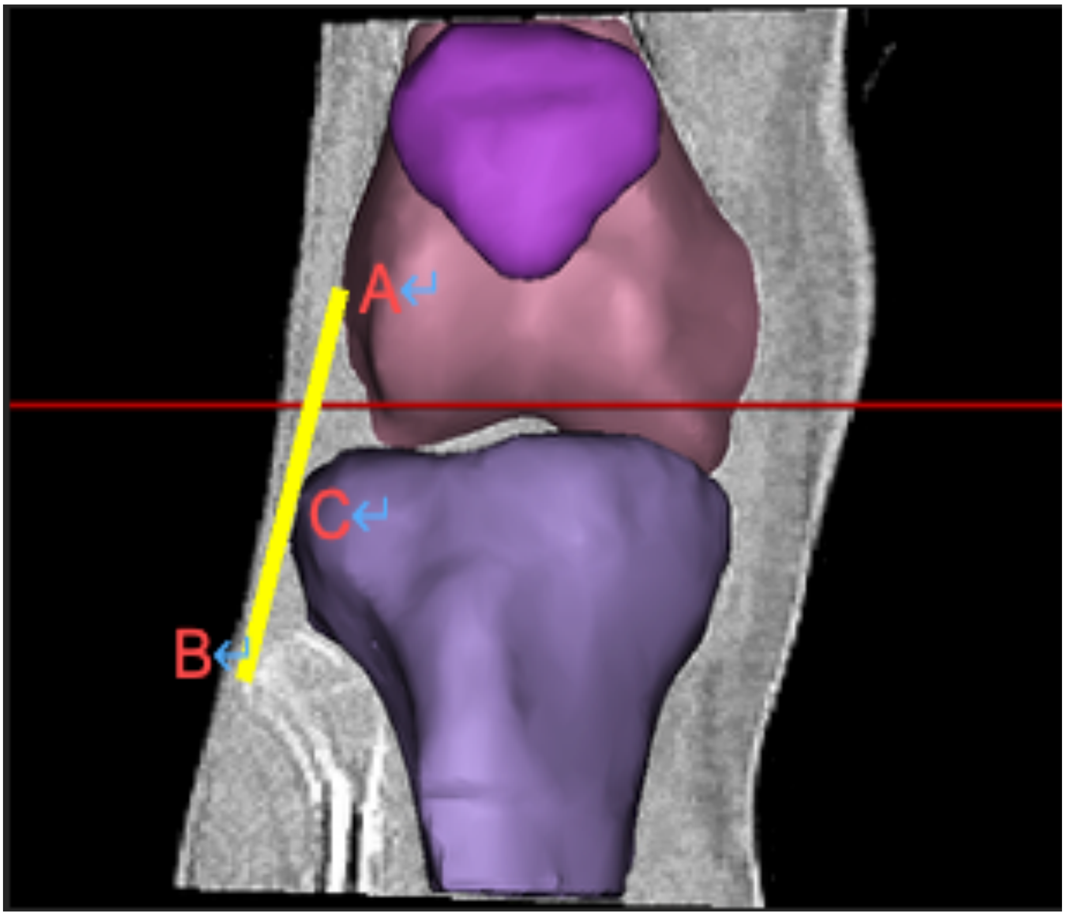

Figure 13. LCL insertion modelling optimization method

Therefore, the fibula mask was carefully separated from the combined tibial and fibula mask using the "Minus" operation from the "Boolean operations" set. The result is a separate mask that accurately represents the tibia, femur and patella, laying a solid foundation for the subsequent modelling steps.

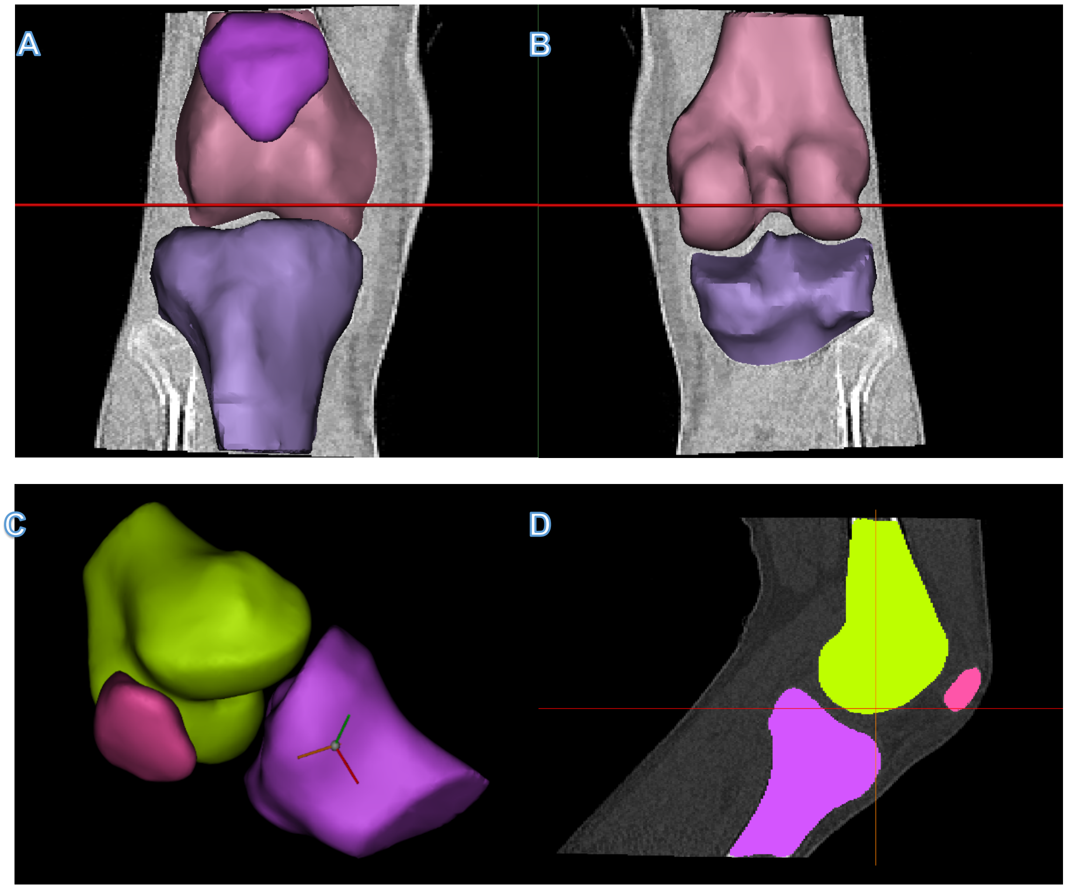

Figure 14. 3D image of the knee model in MIMICS

Figure 14 shows a set of 3D images of a knee joint reconstructed from medical imaging data. A: This is a coronal view of the knee, showing the femur, tibia, and patella; B: This is a front view of the knee joint; C: 3D representation of the kneecap structure, highlighting specific areas of interest; D: Sagittal view, 3D volume rendering superimposed on 2D image slices.

The process then progressed to the meticulous definition of contours and areas for the femur, tibia, and patella across each axial slice and from three different anatomical planes. This was achieved through the application of "Edit Mask" functions to manually delineate target areas and "Polyline Growing" methods to generate comprehensive contours that encapsulated the entire area defined by the polylines. The ambition of this phase was to establish well-delineated contours and areas for each bone across every slice and from all perspectives. As ultimately, the bony structures were to be assumed rigid, identification of cancellous bone was not important and so the bone structure was defined as a solid structure. Appropriate filling was applied inside the bony surfaces (Figure 15. Visual comparison of the model interior with and without filling (polyline growth).). The approach we took accurately and repeatably restored the bony surface topology for the contacting surfaces, essential for the subsequent analysis phase.

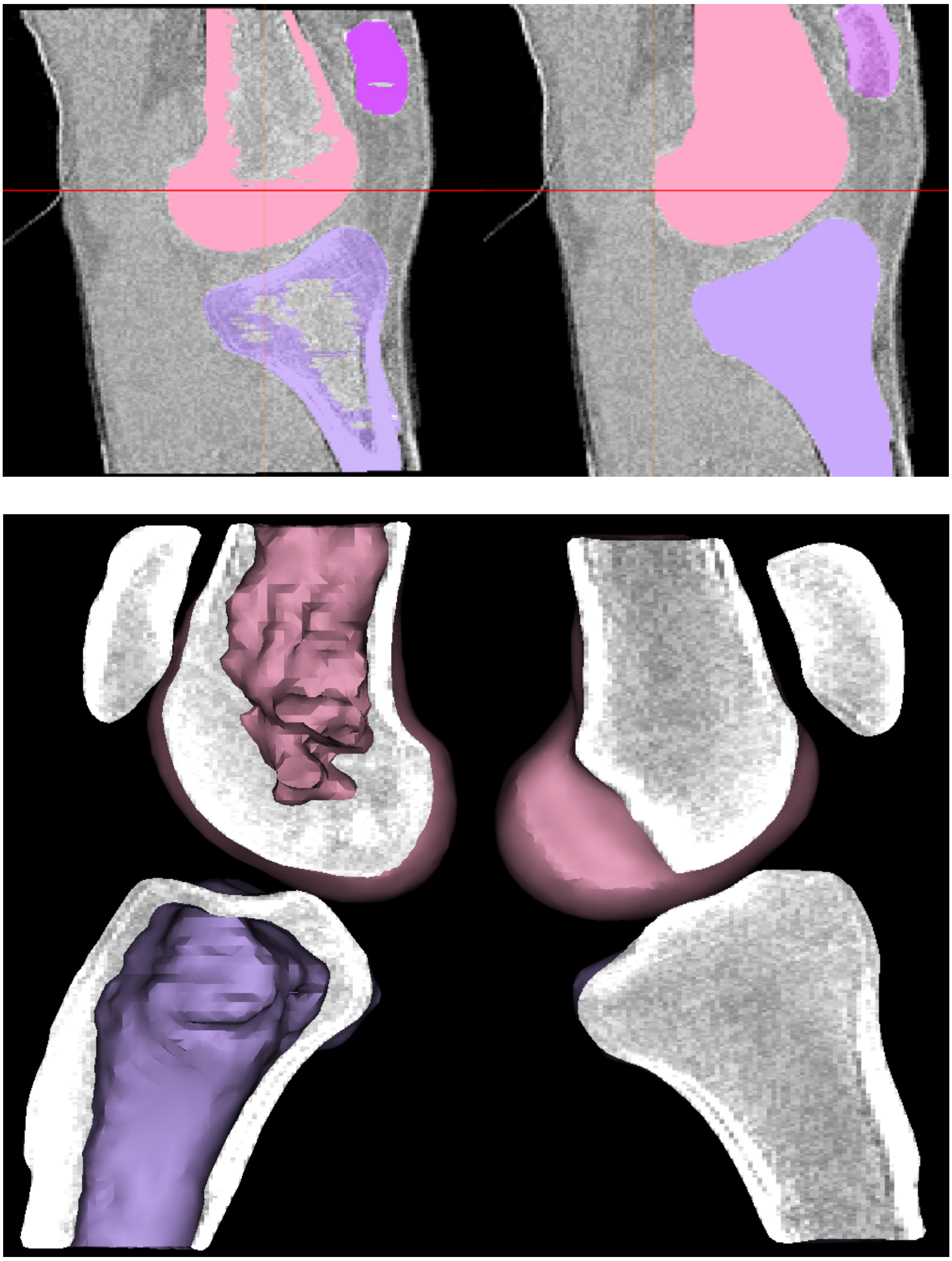

Figure 15. Visual comparison of the model interior with and without filling (polyline growth).

3.2.2 Modelling Cartilage

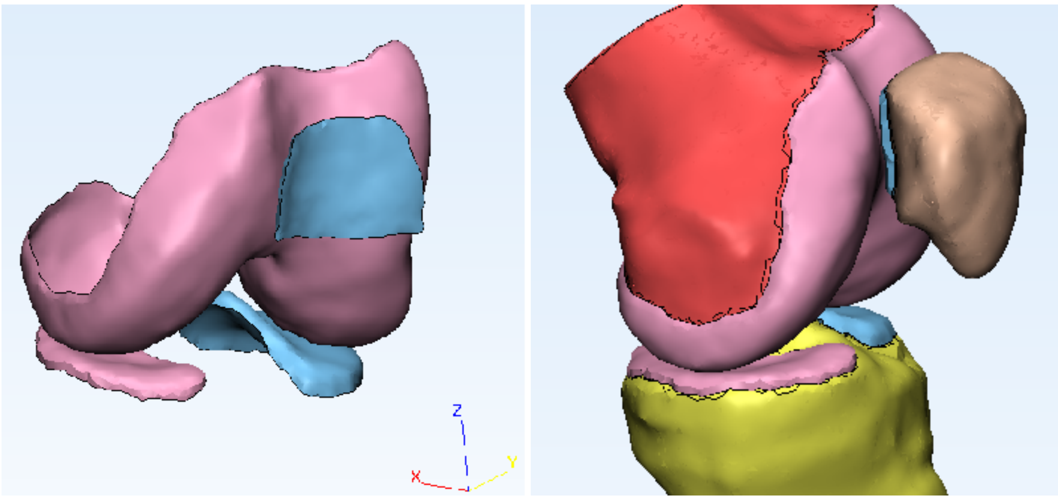

Figure 16. The soft tissue (articular cartilage) was created in '3-Matic'.

This section describes the methodology used to synthesise the soft tissue structures of the knee joint, particularly the articular cartilage. Due to the multiple contact zones introduced by the meniscus, which often cause convergence issues in finite element analysis (FEA), it was decided not to include the meniscus in the model. The mobility of the meniscus in vivo is such that its omission was assumed not to significantly affect the predicted ligament and tendon stresses, which are the primary focus of this study. However, as the meniscus plays a key role in distributing knee joint contact forces over a wider area, its exclusion inevitably reduces the effective contact surface, leading to an overestimation of contact stresses. Consequently, any reported contact stress values should be interpreted as upper-bound estimates and considered with caution.

Before generating cartilage tissue, the first thing that should be determined is how they will contact each other. The concept of tissue contact mode in articular cartilage of the knee is important for understanding the dynamics of the interaction between cartilage surfaces in the knee joint. There are two main types of contact: point contact and surface contact.

i. Point contact is characterised by a node on one surface interacting with the face of an element on the other surface. The contact ensures the node does not penetrate the opposing face.

ii. Surface contact describes the contact between two element faces ensuring one face does not penetrate the other.

The current model adopted the point contact modelling strategy primarily due to its computational efficiency. Again, as ligament tension was the focus of the study, the simpler point contact definition was a sensible simplification over the more computationally demanding surface contact definition.

The construction of the articular cartilage geometries was accomplished using the 3-MaticTM software suite, which provides the flexibility to create and manipulate the desired structures. Soft tissue geometries were manually created for each framework, and thickness was customised to ensure point contact throughout the joint movement. This was achieved utilising the “Create Base” function in 3-MaticTM. This function takes a selected surface and “Region Growing” the surfaces in a certain direction, so that the two surfaces are perfectly parallel. The gap is then filled to become a solid representing the cartilage. Due to it is impossible to accurately estimate the specific contact position of the cartilage tissue of the knee model in each frame, this poses a challenge to the selection of articular cartilage thickness. To address this, it is crucial to ensure that the femoral cartilage consistently maintains contact with both the patellar and tibial cartilage, while simultaneously striving to keep the contact area as uniform as possible across all frames. The most effective solution to this challenge is to manually adjust the thickness of the articular cartilage, either increasing or decreasing it as needed. For instance, the thickness of the femoral cartilage varies across frames, ranging from 0.5 mm to 2 mm, while the lateral tibial cartilage thickness ranges from 2.65 mm to 4 mm. These variations are essential to maintaining stable contact points between the cartilage surfaces throughout the full range of joint motion, ensuring that the model accurately reflects the biomechanical behaviour of the joint.

The femoral cartilage was created first, followed by the lateral and medial tibial plateau cartilage. One thing to note and observe during this soft tissue creation process is that the surface of the cartilage on the tibial plateau was constructed to slightly penetrate (less than 0.1mm) the femoral articular cartilage. Similarly, the cartilage on the underside of the patella was extruded from the bony surface giving a slight penetration into the femoral cartilage. After these articulating surfaces were created, the "Boolean Subtraction" function was then applied to remove the penetrated areas between the lateral and medial tibial plateaus and the patella. This step was critical to perfecting the point contact model, eliminating excess material, and achieving high congruency in the contact zones.

Due to the anatomy varying in location between frames, the process in creating articular cartilage resulted in different cartilage thicknesses being created in each frame (Table 2). This is not ideal, but again, as this thesis focusses on ligament tension, it is thought that these differences do not manifest themselves in any ligament tension calculations. One argument for the variation in thickness between frames could be that there are different levels of cartilage compression between frames, and that a constantly applied thickness across all the frames is not possible or should be expected.

Unit/mm	Frame 18	Frame 16	Frame 14	Frame 12	Frame 10	Frame 08	Frame 06	Frame 04	Frame 02
Femur Cartilage	1.5	0.5	1.5	2	2	2	2	2	2
Tibia Lateral Cartilage	2.8	4	2.7	2.9	3.5	3.6	3.2	2.85	2.65
Tibia Medial Cartilage	2.3	3.6	2.8	2.5	2.78	2.4	1.8	1.8	1.65
Patella Cartilage	0.6	0.5	1.2	1.1	2	2.3	1.9	1	1.65

Table 2. Details of articular cartilage thickness

The specific goals of the simulation study and the available computational resources influence the choice of the appropriate contact mode in knee joint simulation models. Typically, the following contact modes are included in these models:

i. Frictional contact: this mode models the complex interaction between bone and cartilage, considering the frictional forces between the joint parts.

ii. Rigid contact: this mode considers the joint components as non-deformable, which simplifies the modelling process but may not accurately reflect the natural behaviour of the joint.

iii. Elastic contact: this mode considers the elastic deformation of the joint components, which provides a better approximation to the physical behaviour of the joint.

The choice of a specific contact mode depends on the balance between modelling accuracy, computational efficiency and research objectives. Careful evaluation of these elements is necessary to obtain an accurate and computationally efficient representation of knee joint dynamics. In this study of multidimensional knee kinematics, different contact modes were used to simulate different tissue interactions. For example, a combination of frictional and elastic contact is applied to cartilage-cartilage surfaces, while a "rigid contact" mode is applied to cartilage-bone interactions. The complexity of the friction types and associated coefficients is fully described in the Finite Element Analysis (FEA) section.

The specific contact mode settings and parameters are presented in the following Ansys^{TM} workbench section.

3.2.3 Surface and Volume Remeshing

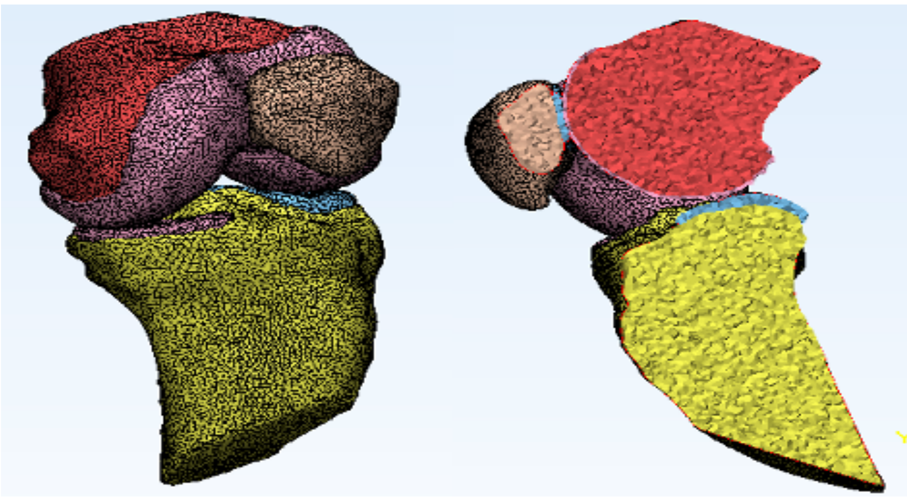

Figure 17. The knee joint assembly models underwent surface and volume remeshing operations for meshing purposes.

The knee joint geometries were meshed using a semi-automatic process within the 3-Matic software following their creation. Initially, triangular surface (shell) elements were generated on the model to facilitate surface meshing. To enhance the geometric quality of the components, smoothing operations were applied using the Laplacian first-order method, with a smoothing factor of 0.7 and three iterations. These steps were aimed at improving the structural quality of the three key components. Additional refinement was achieved through re-meshing procedures.

The "Reduce" and "Inspection Scene" tools were employed to optimize the triangle count and improve the form of the mesh elements. The goal of these operations was to reduce the number of triangles while maintaining or improving their geometric shape. Once a surface mesh of sufficient quality for Finite Element Analysis (FEA) was obtained, the next step involved generating a volume mesh for the model. Systematic mesh refinement was not conducted due to computational constraints, as doubling the element count (e.g., from 50,000 to 100,000) would increase simulation times beyond feasible limits on available hardware. Mesh refinement was not prioritized, as the study's focus was on validating the iterative scheme for ligament tension prediction rather than resolving localized stress concentrations. Future studies targeting cartilage contact mechanics may require finer meshes to resolve high-gradient regions. The specifications for both surface and volume meshing are outlined below.

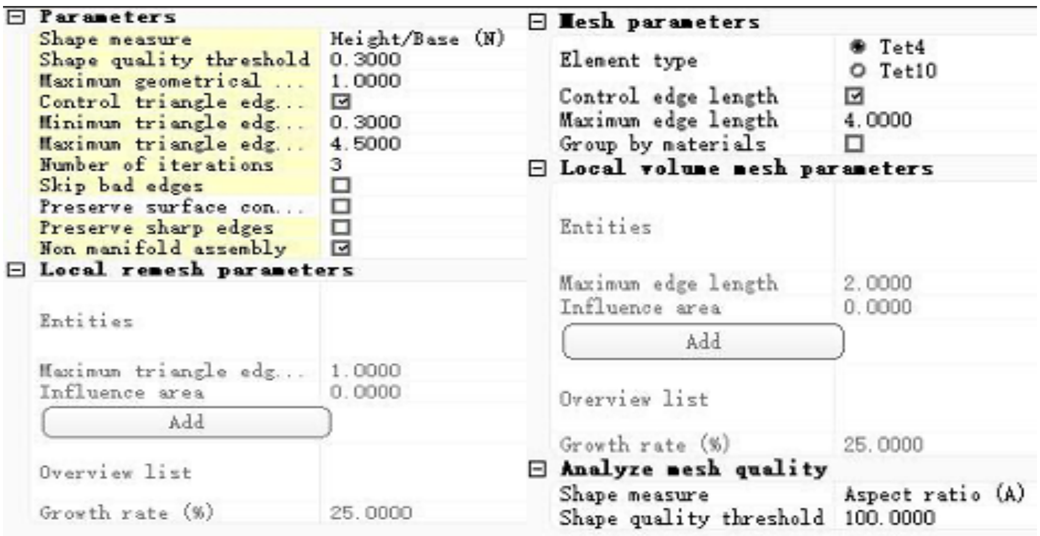

Figure 18. The parameters and details of surface and volume mesh operation in’3-Matic’.

Through the above operations, the processed model was converted and saved as a (.cdb format) file, which was imported into ANSYS™ software for subsequent finite element analysis.

Based on the models, which will be used for further specific analysis, the approximate number of nodes and elements can be summarized as follows:

Frame 02: Nodes: 94,316; Elements: 320,923. Frame 06: Nodes: 95,346; Elements: 323,953. Frame 10: Nodes: 91,693; Elements: 312,160. Frame 14: Nodes: 98,653; Elements: 331,831. Frame 18: Nodes: 96,567; Elements: 326,918

The model required a range of approximately 91,693 to 98,653 nodes and 312,160 to 331,831 elements across the various frames. The inconsistency in the number of elements and nodes for the same model can be roughly attributed to the surface differences resulting from the segmentation of the 4dCT DICOM files and the subsequent model surface processing. During the segmentation process, the anatomical structures of the knee joint are extracted from the CT images. This process is inherently affected by subtle variations in how the boundaries between tissues are defined, depending on factors such as image quality, resolution, and thresholding techniques. In addition, model surface processing in 3-Matic involves smoothing, adjusting, and refining the segmented surface to create a mesh suitable for finite element analysis (FEA). This surface processing can result in subtle variations in mesh density between different frames or stages of the model. As a result, the number of elements and nodes fluctuates from one frame to another as the software automatically adjusts the mesh to accommodate changes in surface complexity.

3.3 Finite Element Analysis

This section elucidates the utilization of finite element analysis (FEA) as the cornerstone computational approach for this investigation, alongside the methodologies employed to achieve the study's objectives. FEA, a sophisticated numerical method, enables the simulation and evaluation of complex biomechanical systems by discretizing continuous structures into discrete elements. This technique provides a robust means to approximate biomechanical responses under varied loading scenarios with high fidelity.

During the FEA phase, the primary aim was to construct a comprehensive computational framework using four-dimensional computed tomography (4dCT) data to investigate knee ligament tension. This framework leverages FEA's capabilities to model the intricate biomechanical interactions within the knee joint. To this end, a detailed finite element model was developed, meticulously capturing the material properties and boundary conditions of the knee ligaments and surrounding anatomical structures. These models facilitated dynamic assessment of ligament tension as it varies with knee flexion angle, while also enabling tracking of patellar and tibial motion across consecutive frames. By incorporating time-dependent kinematic data, the FEA models provided a thorough analysis of ligament behaviour throughout the range of motion, offering critical insights into the biomechanical responses under physiological loading conditions. Initially, the model, including its manually constructed components, was imported into the Ansys™ V19.0 Workbench environment. Within this platform, the model components were reassembled to replicate the knee joint's various positions during flexion, as illustrated in the figure 19 below. This step was crucial in ensuring that the model accurately captured the knee's dynamic motion, providing a reliable foundation for subsequent analysis.

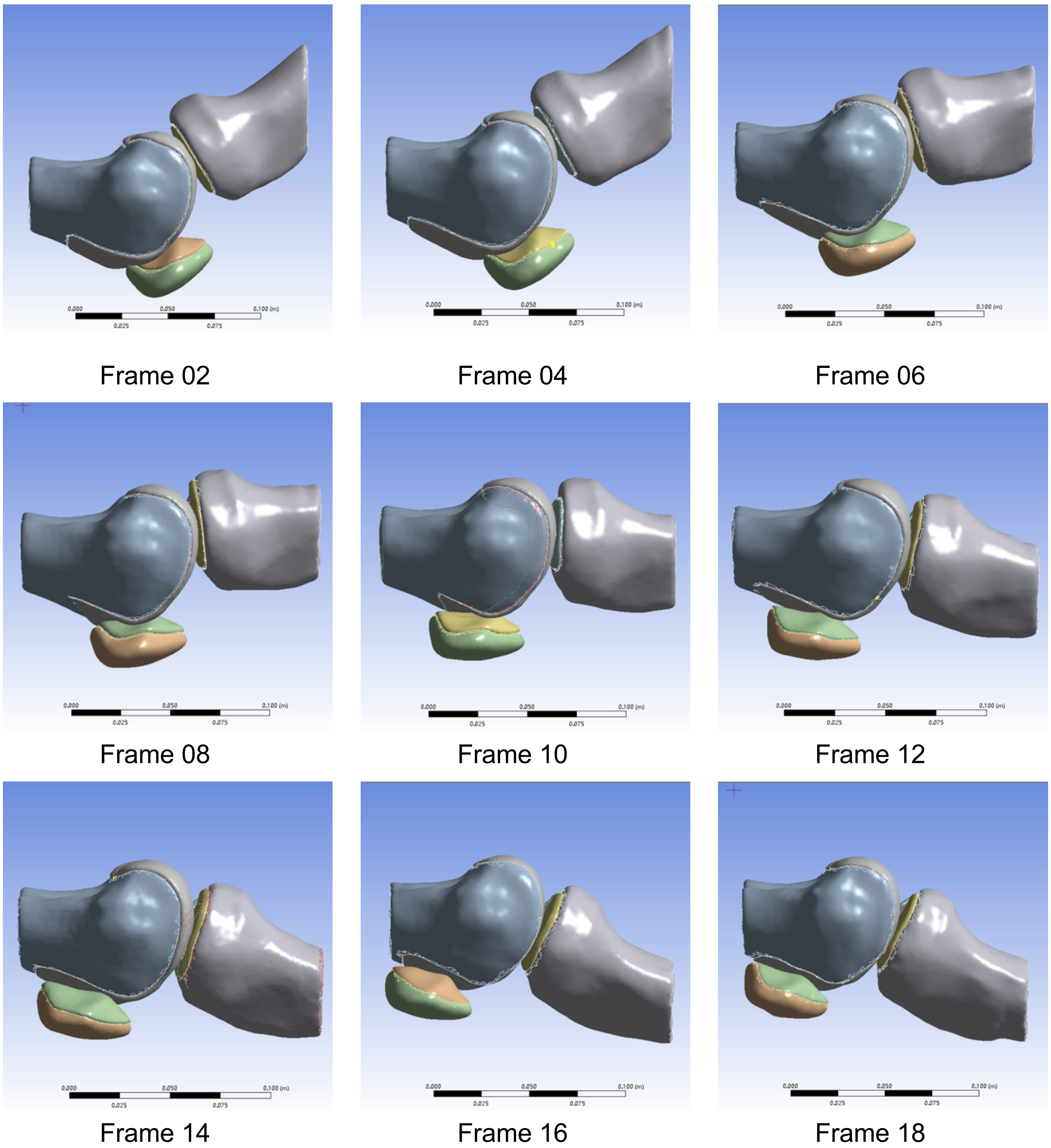

Figure 19. FE model of Knee Joint Range of Motion 65-Degree Flexion Sequence.

This series of frames displayed the dynamic interaction between the femur, tibia, and patella throughout the knee joint's 65-degree range of motion. The frames demonstrate progressive flexion, highlighting tibia tracking and increasing articulation between the femur and tibial plateaus.

3.3.1 Material Properties

The material properties of the model components need to be defined with sufficient accuracy to enable computation of realistic solutions. All tissue is known to have time-dependent and anisotropic behaviours due to their fluid components and microstructure. In the current study, this level of detail was assumed unnecessary where the 1-d stiffness of the ligaments was of primary concern. Both bone and cartilaginous tissues were modelled as isotropic elastic materials and assigned specific values for Young's modulus and Poisson's ratio. The detailed material properties for each component were derived from previous studies. [244-245]

Table 3 (a) provides key material properties for bone tissue, used in finite element analysis (FEA) to simulate its mechanical behaviour.

The Young's Modulus of bone was specified as 11.5 GPa [244], a value that is supported by the referenced document titled “Biomechanical Effects of Different Varus and Valgus Alignments in Medial Unicompartmental Knee Arthroplasty” published in The Journal of Arthroplasty. Their study investigated the effects of different tibial component alignments in noncompartmental knee arthroplasty using a validated finite element model. This Young’s Modulus value is therefore consistent with valiated mechanical characteristics of cortical bone in the context of joint FE modelling.

Poisson's Ratio of bone was defined as 0.31 [244], a dimensionless parameter that describes the bone’s ability to undergo lateral contraction or expansion when stressed longitudinally. A Poisson's ratio of 0.31 suggests that bone exhibits moderate lateral deformation, which is consistent with the mechanical behaviour of biological materials.

Based on these two values, the bulk modulus was calculated as 10.1 GPa and the shear Modulus was provided as 4.39 GPa.

Together, these material properties provide a simple characterisation of bone for FEA. The values indicate that bone tissue is highly stiff, capable of withstanding both compressive and shear stresses, with limited volumetric deformation. These characteristics are essential for accurately modelling bone's mechanical performance under various physiological and loading conditions, such as walking or jumping, within an FEA framework.

Table 3 (b) provides the material properties for the extruded surface mimicking articular cartilage.

The Young's Modulus was defined as 14 MPa [245], which indicates the elastic stiffness of the soft tissue. This paper explores biomechanical effects of uni-compartmental knee arthroplasty (UKA) using finite element analysis (FEA) to model the behaviour of soft tissues such as cartilage under various load conditions. In their study, the articular cartilage was modelled as a linear elastic material with a Young’s modulus ranging from 13 to 15 MPa. Compared to bone, this much lower value reflects the pliability of the tissue, which allows it to deform more easily under stress. Poisson's Ratio was defined as 0.475 [245], which is close to the theoretical limit of 0.5 for incompressible materials. This high Poisson's ratio reflects the high fluid content of the tissue as fluid is usually considered incompressible. The solution, therefore, may only be valid for short time scales in which fluid loss from the tissue is ignored.

As before, bulk modulus and shear modulus were determined to be 93.3 MPa and 4.74MPa respectively.

a

Property	Value	Unit
Young's Modulus	11500.00	MPa
Poisson's Ratio	0.31	-
Bulk Modulus	1.01×10^{10}	Pa
Shear Modulus	4.4×10^{9}	Pa

b

Property	Value	Unit
Young's Modulus	14.00	MPa
Poisson's Ratio	0.48	-
Bulk Modulus	9.3×10^{7}	Pa
Shear Modulus	4.7×10^{6}	Pa

Table 3. Material properties of the model components a.) Bone b.) Cartilage

This assumption neglects the nonlinear, anisotropic behaviour of soft tissues, which could affect accuracy in high-strain scenarios. Future models could incorporate hyperplastic or viscoelastic properties for improved realism.

3.3.2 Ligament and patella tendon insertion

In the field of biomechanical engineering, accurate modelling of ligamentous structures is of paramount importance, especially when it comes to reconciling computer representations with physiological reality. Recent advances have emphasised the importance of identifying and accurately representing biomechanically relevant regions - often referred to as 'nodal points' - where ligaments attach to bone. These areas are critical to ensure that modelling, such as in the Ansys^{TM} Workbench environment, produces results that are not only accurate but also consistent with the complex nature of human biomechanics. In the paper "Automatic detection of knee ligament and tendon attachment sites on CT images" [246], significant progress has been made in the automation and accuracy required to identify these "nodal points". The algorithms proposed in represent a new way to create patient-specific knee joint models. To do so, they consider the different bone surface curvatures and differences in knee joint anatomy that may be observed. Essentially, the localised topology of the bone gives a good indication of the insertion point of the ligament or tendon.

While the method proposed by Yurova et al. [246] is useful and powerful, it was too complex to implement for the biomechanical simulations required for this study. It was felt that manual identification of the insertion area based on localised topology was sufficient for this analysis. This may introduce minor variability between frames as the manual selection of the insertion points had to be made on each frame independently. The errors associated with this approach are deemed insignificant with respect to the other assumptions and sources of errors in the analysis.

The insertion area comprised many mesh nodes

i. Patellar Tendon (PT)

From an anatomical perspective, the patellar tendon is a crucial structure that connects the patella to the tibia, facilitating the transfer of force from the quadriceps muscle to enable knee extension. The attachment areas of the patellar tendon include the distal end of the patella and the tibial tuberosity.

Attachment on the Patella：

The upper part of the patellar tendon attaches to the lower margin of the patella, specifically at the apex of the patella. The patella, a sesamoid bone located at the front of the knee joint, serves as an intermediary between the quadriceps tendon and the patellar tendon.

Attachment on the Tibia

The distal part of the patellar tendon attaches to the tibial tuberosity, a prominent bony structure located on the anterior aspect of the proximal tibia. The tibial tuberosity serves as the primary attachment point for the patellar tendon, bearing the mechanical load generated during knee extension.

ii. Lateral Collateral Ligament (LCL)

Femoral Attachment: The LCL attaches to the lateral epicondyle of the femur, which is a bony prominence on the outer side of the distal femur.

Fibular Attachment: The distal end of the LCL attaches to the head of the fibula, a prominent point on the upper part of the fibula, located on the outer side of the lower leg.

However, in this study, the insertion area on the femur for the lateral collateral ligament (LCL) was altered and based on a simplified geometry of the knee joint. Since the fibula does not directly contact the femur or patella, the fibula was removed from the model to reduce complexity. Although the LCL typically inserts onto the lateral femoral epicondyle and the fibular head, it was assumed that the line of action of the ligament closely follows the lateral aspect of the tibial condyle (see 3.2.1.1). This assumption allows for a reasonable and hopefully justifiable alternative in which the LCL inserts into the lateral tibial epicondyle.

iii. Medial Collateral Ligament (MCL)

Femoral Attachment: The MCL attaches to the medial epicondyle of the femur, a bony prominence on the inner side of the distal femur, close to the joint surface.

Tibial Attachment: The distal end of the MCL attaches to the medial surface of the tibia, extending along a broad area on the proximal medial tibia.

iv. Anterior Cruciate Ligament (ACL)

Femoral Attachment: The ACL attaches to the medial aspect of the lateral femoral condyle, located deep within the joint, posterior to the condyle.

Tibial Attachment: The ACL attaches to the anterior intercondylar area of the tibia, a region at the front centre of the tibial plateau.

v. Posterior Cruciate Ligament (PCL)

Femoral Attachment: The PCL attaches to the lateral aspect of the medial femoral condyle, located posterior to the femur's medial condyle.

Tibial Attachment: The distal end of the PCL attaches to the posterior intercondylar area of the tibia, situated at the back of the tibial plateau.

Using this anatomical information, we were able to accurately delineate the necessary areas for ligament and tendon attachment, ensuring their realistic placement on the bony structures.

Once these anatomical regions were identified from anatomical literature, the next step involved integrating them into the computational mesh of the knee joint model. Specifically, the attachment areas were defined by selecting the nodes that were created during the mesh generation process. These nodes, grouped into node sets, corresponded to the mesh node points covering the attachment regions. Thus, the node sets effectively represented the ligament and patellar tendon attachment points on the bones. Any tensile force in the ligaments and patella tendons would then be equally distributed over the selected nodes.

This integration is critical to maintaining the structural integrity of the FEA model, as it enables the smooth transmission of forces and strains through the ligament and tendon structures, and avoids stress concentrations at single nodes, aiding convergence of the solution.

The connections made between the bony anatomy using spring elements and insertion areas is shown in the figure 20 below.

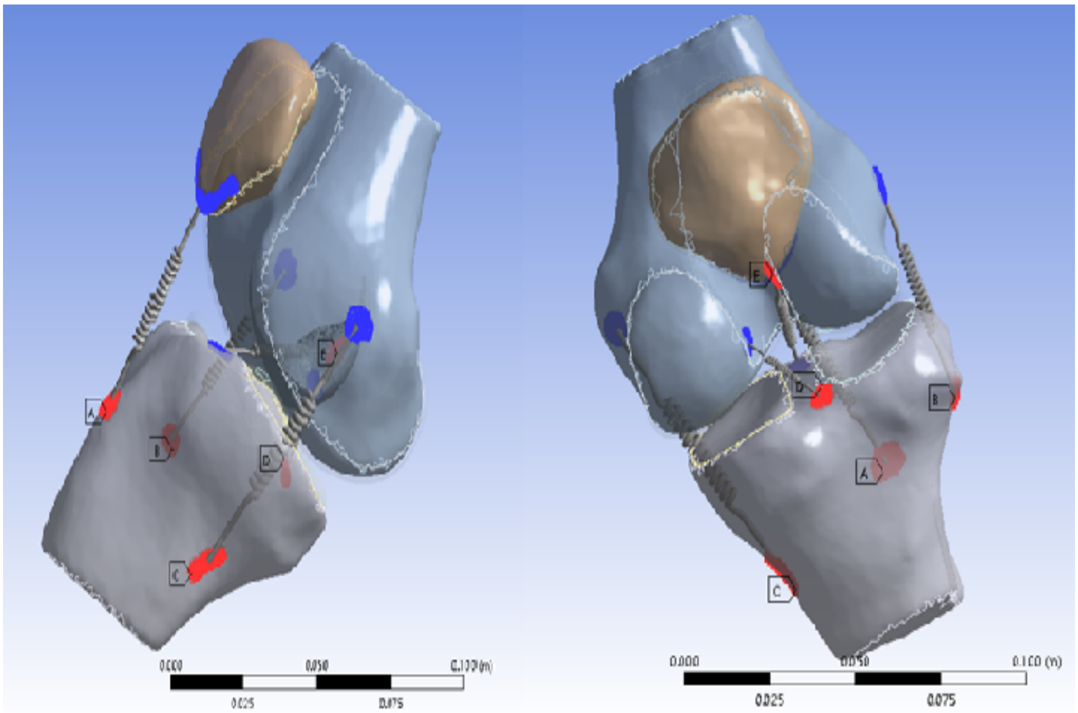

Figure 20. The chosen 'Anchor Region' refers to the specific area on the bone where the ligaments are attached.

3.3.3 Ligament and tendon mechanical properties

The ligaments and tendons in the model were defined as spring elements, as described above, in Ansys. However, the literature has described them as hyperplastic viscoelastic, fibre-reinforced tissues. The current study deemed this behaviour unnecessarily complex given the research questions that the model is designed to answer, and so the ligaments were considered to exhibit simple elastic spring behaviour. As before, this simplification makes the solution more appropriate to short-time understanding of ligament tension in which stress relaxation is ignored.

Ligaments and tendons may maintain a certain degree of preload even when the joint is at rest. Indeed, this is the subject of this thesis. The spring elements in the FEA model allow for the application of this prestress by assigning initial forces to the spring elements, reflecting the physiological tension within these tissues. This preload is crucial for simulating realistic joint behaviour, as it accounts for the natural resistance of ligaments and tendons to mechanical forces. However, with regards to the above diagram, there are an infinite number of combinations of ligament forces and joint contact forces for equilibrium. It is unknown what tensions are in the ligaments, but we are able to guess, and apply some preloads to the spring elements, as described above in section 3.3, which are then modified through the iterative workflow.

Spring elements in Ansys allow for the customisation of key parameters such as stiffness, damping, and preload. This flexibility enables fine-tuning of the mechanical properties of ligaments and tendons in the model, aligning it with experimental observations and biomechanics data. Representing them as springs strikes a balance between computational efficiency and biomechanics fidelity, ensuring the model can simulate large-scale joint mechanics without imposing excessive computational demands.

Damping was not included in the model for ligaments, and so their tensile force, F, was described using Hooke's law:

$$F = kx + F_0$$

Where k is the ligament stiffness (N/m), x is the extension of the ligament, and F_0 is the preload.

3.3.3.1 Spring Material Properties

The material properties of the ligaments, including stiffness, , and maximum tension, were then specified to simulate their mechanical behaviour under load. These parameters ensure that the ligaments respond in a way that reflects their natural biomechanical characteristics during knee joint movements.

The stiffness of the knee ligaments varies according to their specific function and location within the joint. For example, the anterior cruciate ligament (ACL), characterized by a smaller cross-sectional area and shorter length, is stiffer compared to the posterior cruciate ligament (PCL), which has different structural and functional properties.

The Table 4 below present the detailed biomechanical properties of the anterior cruciate ligament (ACL), posterior cruciate ligament (PCL), lateral collateral ligament (LCL), medial collateral ligament (MCL), and patellar tendon (PT) as modelled in finite element analysis (FEA) software. The figure outlines various parameters that define the behaviour of these ligaments, boundary conditions, and coordinates within the simulation environment. In the model, these ligaments are represented as "longitudinal springs" to simulate their biomechanical response to tensile forces along the ligament's length. These springs operate in "tension-only" mode, replicating the physiological behaviour of ligaments, as their primary function is to resist stretching rather than compression.

N/mm	ACL	PCL	LCL	MCL	PT
longitudinal stiffness	91.3	125	91.3	72.2	210

Table 4. Specifications of Stiffness Parameters for Ligaments and Patellar Tendon (PT) Implemented in ANSYS (Units: mm).

The longitudinal stiffness of the ligaments varies, with the ACL modelled at 91.3 N/mm, PCL at 125 N/mm, LCL at 91.3 N/mm, MCL at 72.2 N/mm, and PT at 210 N/mm. These values reflect each ligament's resistance to extension when loaded. For instance, the stiffness of the ACL is consistent with its critical role in stabilizing the knee joint, particularly in preventing anterior translation of the tibia.

Furthermore, the initial lengths of these springs were defined as follows: ACL at 33.14 mm, PCL at 43 mm, LCL at 60 mm, MCL at 18 mm, and PT at 57mm. These initial lengths correspond to the anatomical distances between insertion points in the model [244-245].

3.3.3.2 Ligament Pre-strain Modelling and Iterative Solution Consistency

To replicate the physiological stress state of ligaments in vivo, initial tensile pre-strain was incorporated into the constitutive model before commencing the iterative solution process. The mathematical formulation of this approach is described below.

The tensile force in each ligament bundle was computed based on its engineering strain, defined as:

$$\varepsilon_i = \frac{L_i - L_{0,i}}{L_{0,i}}$$

Where L_i is the current fibre length at iteration i and $L_{0,i}$ is the reference (slack) length. In the pre-strain implementation, $L_{0,i}$ was shortened by a prescribed proportion ε_{pre} to represent the physiological tension at the unloaded reference posture:

$$L_{0,i} = L_{ref} \times \left(1 - \varepsilon_{pre}\right)$$

Here, L_{ref} is the is the anatomically measured ligament length from the neutral position (Frame i). The ligament tensile force was then calculated using the constitutive relation:

$$F_i = k \times \max\left(\varepsilon_i, 0\right)^n$$

where k is the stiffness coefficient derived from the ligament's material modulus and cross-sectional area, and n is a nonlinearity exponent (typically $n \approx 2$ for soft collagenous tissues). The $\max\left(\varepsilon_i, 0\right)^n$ function ensures that the ligament resists only tensile, not compressive, deformation.

During the iterative solution process to determine the quadriceps force F_Q, the global equilibrium equation was solved as:

$$K_{total}\left(F_Q\right) \times \Delta u = F_{ext}\left(F_Q\right) - F_{lig}\left(\varepsilon_{pre}\right)$$

Where:

K_{total} is the combined stiffness matrix (including ligament, cartilage, and bone contributions)

F_{ext} is the applied external force vector (including quadriceps and gravity).

F_{lig} is the internal ligament force vector, already incorporating the pre-strain ε_{pre}.

Δu is the incremental nodal displacement vector.

Because the pre-strain is embedded directly in F_{lig} and not redefined between iterations, the solver maintains the initial physiological stress state throughout the convergence process. This ensures that each iteration step calculates force balance on the true pre-stressed configuration, avoiding artificial relaxation of ligament tension and maintaining consistency between the constitutive model and the numerical solution.

Iteration 1: Initial Test Results

In the initial stage, there is a noticeable difference between the preload and output values for both the 100 N and 200 N preloads.

By the 24th iteration for the 100 N preload and the 36th iteration for the 200 N preload, the error rate between the preload and output values for the patellar tendon (PT) and anterior cruciate ligament (ACL) decreased to less than 1%. The preload and output values for the remaining ligaments (LCL, MCL, PCL) converged close to zero.

Frame 06	Iteration 1		Iteration 24	
	Pre-loading	Output	Pre-loading	Output
PT (N)	100	184.69	208.6267313	208.78
LCL (N)	100	36.199	9.34E-06	0
MCL (N)	100	72.251	9.23E-05	0
PCL (N)	100	43.881	1.41E-05	0
ACL (N)	100	90.613	7.328045673	7.3845
PT % difference	/	84.69	/	0.0734655
LCL % difference	/	-63.801	/	/
MCL % difference	/	-27.749	/	/
PCL % difference	/	-56.119	/	/
ACL % difference	/	-9.387	/	0.7703872

Frame 06	Iteration 1		Iteration 36	
	Pre-loading	Output	Pre-loading	Output
PT (N)	200	166.86	209.1447172	208.92
LCL (N)	200	119.01	1.36E-08	0

MCL (N)	200	159.81	9.04E-07	0
PCL (N)	200	135.48	6.38E-08	0
ACL (N)	200	171.23	5.889950629	5.8844
PT % difference	/	-16.57	/	-0.107446
LCL % difference	/	-40.495	/	/
MCL % difference	/	-20.095	/	/
PCL % difference	/	-32.26	/	/
ACL % difference	/	-14.385	/	-0.094239

Table 5. The frame 06 spring force loaded after multi-iteration test.

3.3.4 Contact specification

Finite element analyses require that surfaces which are in contact in the model to be defined as such. The following figures 21-22 illustrate the bone-cartilage and cartilage-cartilage contact modes, respectively. In both cases, two surfaces are involved in the contact interaction: the contact body is designated as "Entity 1 (External Model)," and the target body is labelled "Entity 2 (External Model)." These bodies represent the surfaces involved in the simulation, specifically bone-cartilage and cartilage-cartilage contact zones.

The bone-cartilage contact is defined as bonded, indicating that no relative motion occurs between the bone and cartilage surfaces during the simulation. In contrast, the cartilage-cartilage contact is characterized as frictional, meaning friction is considered in the interaction between the two cartilage surfaces. In healthy knee joints, the friction coefficient is quite low, usually between 0.001 and 0.02 [247-248]. In cases of osteoarthritis or cartilage wear, the surface of the cartilage may become rougher, leading to an increase in friction [249-250]. When synovial fluid is reduced or becomes less effective (e.g., due to injury or inflammatory conditions), the friction coefficient can also rise [249]. This can raise the friction coefficient to values as high as 0.1 to 0.6

depending on the severity of the damage [251]. Some preliminary analysis of the knee joint was conducted using our model in which friction was specified at 0.002. At some knee angles, this resulted in separation of the tibia and femur, with the tibia sliding completely off the femoral condyles. Clearly, there is significant soft tissue around the knee, which is not included in the model, such as meniscus, joint capsule fascia, fat, muscle, skin etc, all of which may provide resistance to sliding. To represent this resistance to sliding, and to prevent separation of the tibia and femur during the analysis, the minimum friction coefficient was used to ensure no separation occurred at any time frame. Therefore, a friction coefficient of 0.6 was applied, representing a moderate level of resistance between the contacting surfaces. This friction coefficient is appropriate for simulating cartilage-cartilage interactions, where sliding may occur under loading conditions, and is also an upper boundary on literature values [251].

While the applied friction coefficient of 0.6 is within the upper bound of literature values for damaged cartilage surfaces, it is acknowledged that such a high value may artificially increase joint stability in the absence of surrounding soft tissues in the model. In the present study, this parameter was not intended to represent physiological synovial lubrication, but rather to compensate for the missing stabilising effects of structures such as the menisci, joint capsule, and musculature. The high coefficient was therefore a pragmatic choice to maintain joint congruency during simulated motion, with the understanding that stability in this configuration is partly contributed by frictional constraints rather than solely by ligamentous and bony geometry.

The contact behaviour was set to asymmetric, meaning the interaction between the two bodies is not identical from both sides. In this configuration, the target body primarily governs the interaction properties. To enforce the contact constraints within the simulation, the augmented Lagrangian method is employed. This robust algorithm augments the contact stiffness matrix, ensuring precise contact force predictions and improving the accuracy of the model.

Program-controlled, default, options were applied for penetration tolerance, normal stiffness, and tangential stiffness, allowing the software to automatically adjust these parameters to ensure the stability and accuracy of the contact interaction. This automated adjustment enhances the fidelity of the simulation, minimizing the need for manual parameter tuning.

Trimming options were also set to program-controlled, enabling the software to manage potential contact trimming, where excess geometry could interfere with the simulation's accuracy. The Friction Smoothing option is disabled (set to "None"), ensuring that the original geometric characteristics of the contact surfaces are preserved, without the application of additional smoothing algorithms.

Both Contact Geometry Correction and Target Geometry Correction are disabled, meaning that no automatic adjustments are made to the contact surfaces. As a result, the original geometry of the surfaces is maintained throughout the simulation.

The Deflection Method is set to Adjust to Contact, ensuring that the interaction begins only when the bodies come into contact, and that any initial gaps in the geometry are adjusted. Additionally, the Detection Mode is set to Automatic, allowing the software to automatically detect and manage the initiation of contact during the simulation process.

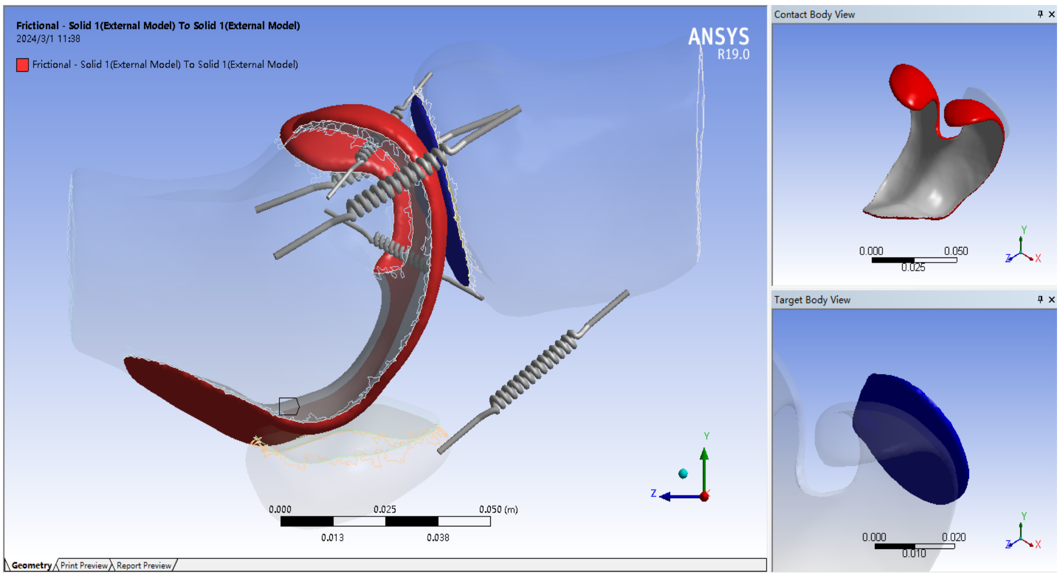

Figure 21. The distal femoral cartilage contacts the lateral meniscus in Ansys$^{TM.}$

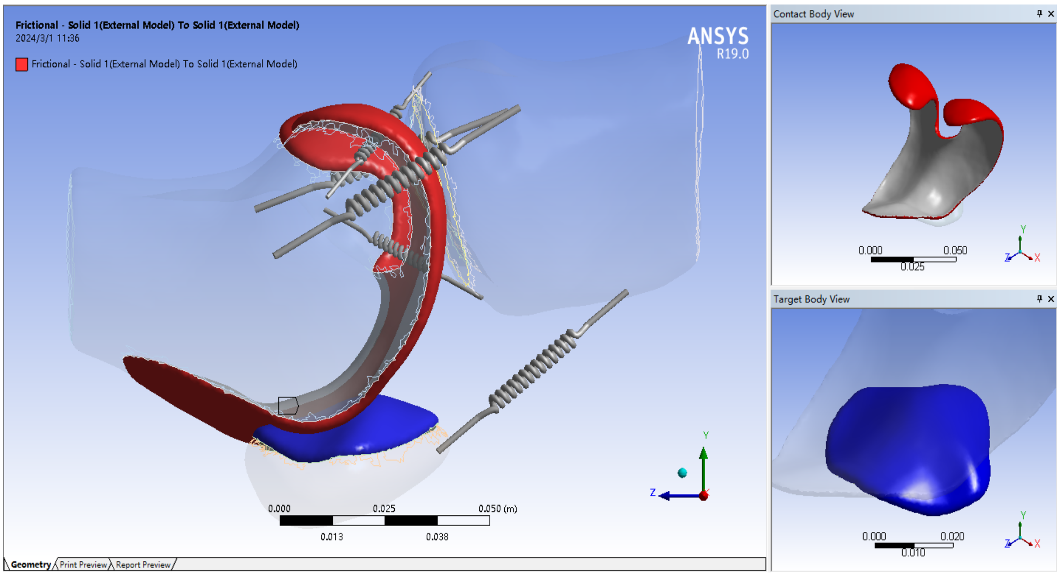

Figure 22. The distal femoral cartilage contacts the patella cartilage in Ansys^{TM}.

3.3.5 Boundary and loading conditions

The kinematic movement of the knee in the experiment was that the thigh remained approximately stationary, and the tibia moved in extension to full extension, with the muscles acting against gravitational weight. Appropriate boundary conditions are required, simulating the experiment and providing necessary model details for a solution to be determined. In each time frame of this movement, the femur and patella were effectively kinematically fixed, preventing rotation and translation. To do this, the distal surface of the femur and the lateral surface of the patella were designated as fixed areas, as illustrated in Figure 23. This implies that no translation or rotation of these fixed areas was allowed during the analysis.

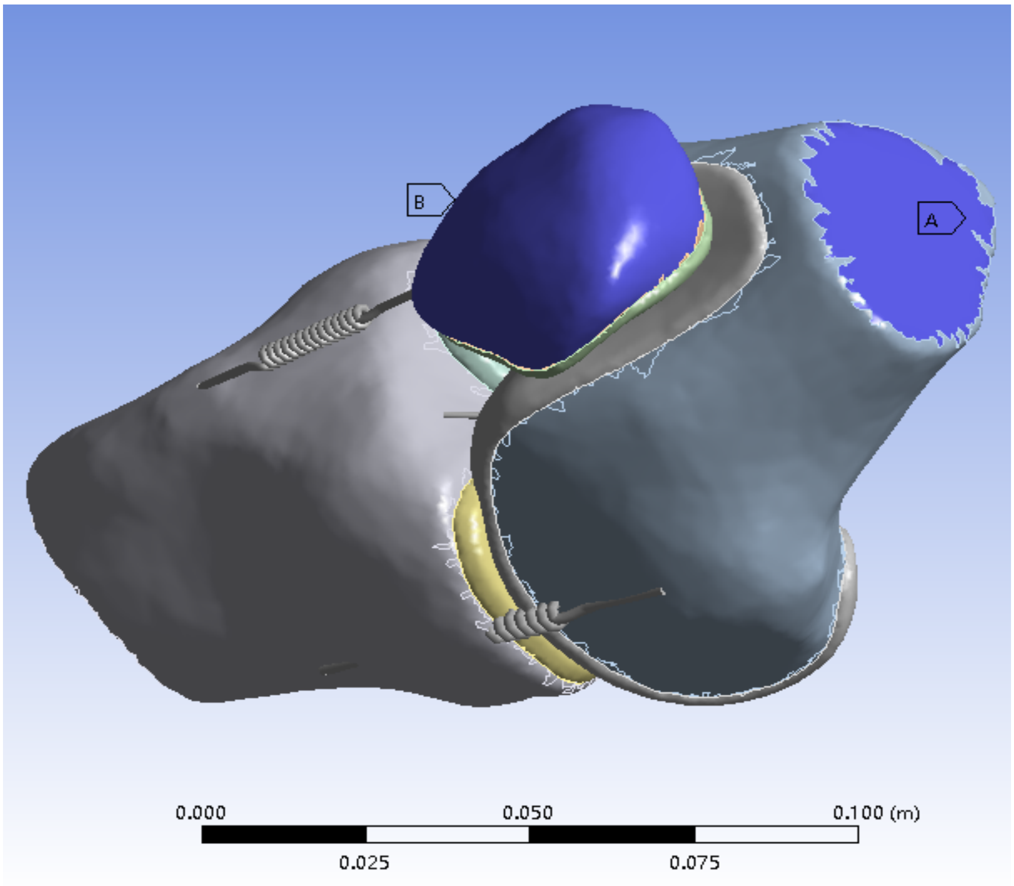

Figure 23. Fixed support conditions applied on the Knee Joint.

As the muscles were acting against gravitational weight, this force needed to be simulated in the model. The mass of the lower limb and foot was estimated to be approximately 4kg, and so a force of 40 N was applied at the centroid of the tibia, which was assumed to be located approximately 20 cm distal to the knee joint, to simulate the weight of the lower leg and foot. This force was directed along the Z-axis (as shown in figure. 24), set by the CT scanner as the vertical direction.

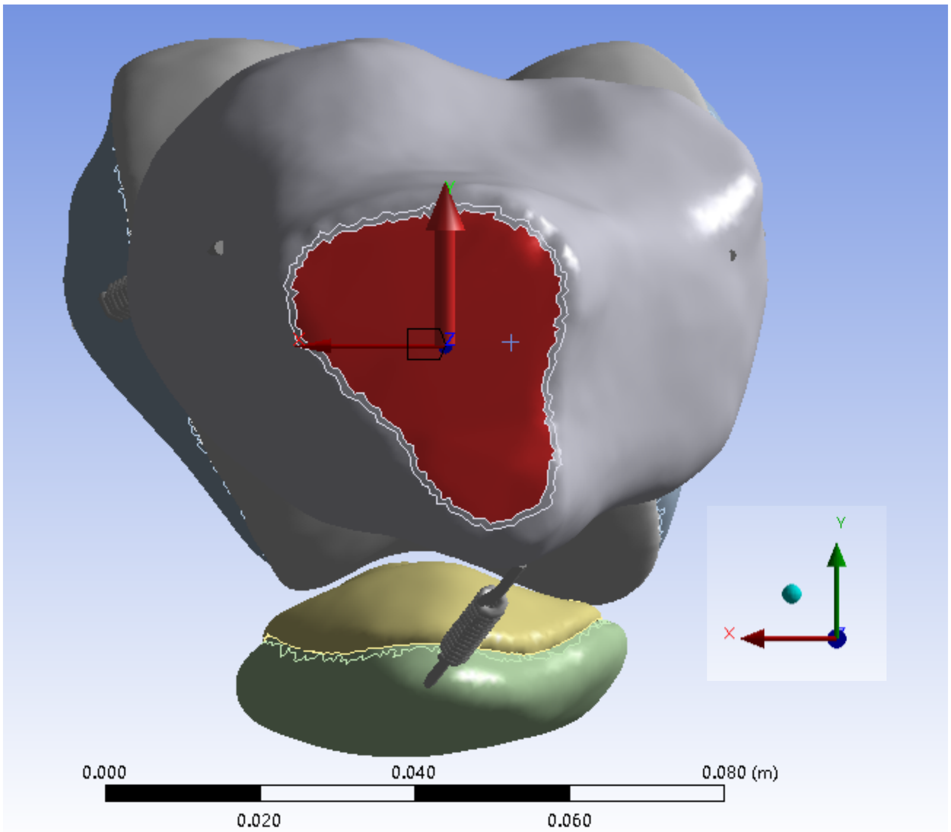

Figure 24. Center of mass on the tibia

Figure 24 shows the finite element model demonstrates the simulation of gravity acting on the lower limb. A force of 40 N is applied at the centre of mass of the tibia, along the Z-axis (defined as vertical by the CT scanner, indicated by the red tip) to simulate the effect of gravity on the muscles.

The assumed point of centre of mass was determined using the model from frame 18 as an example. First, a coordinate system was established at the approximate center of the distal cross-section of the tibia. From this origin, a line was extended along the central axis of the tibia to a distance of 20 cm, as indicated by line segment A in the figure 25 below.

Subsequently, an extension line parallel to the Z-axis (represented as line segment B in the figure 25) was constructed. The angle between line segments A and B was measured, and the lengths of line segments B and C were calculated using the Pythagorean theorem.

Finally, based on this tibial cross-sectional coordinate system, a “Remote Force” application point was created in ANSYS™ to simulate the gravitational force acting on the lower limb. The lengths of line segments B and C were used as coordinate parameters to apply remote forces along the y and z axes, thereby specifying the precise position of the centre of mass.

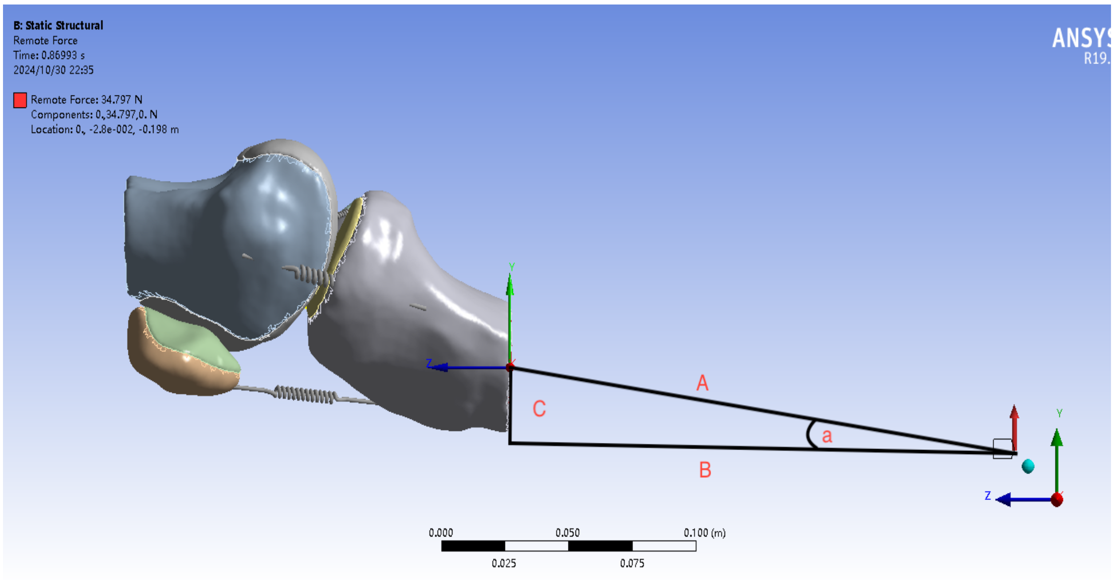

Figure 25. ‘Remote Force’ location

Figure 25. uses Frame 18 as an example, with segments B and C calculated using the Pythagorean theorem defining the "Remote Force" application points along the y and Y axes to simulate gravity.

3.4 Primary research aim: to estimate knee ligament tensions throughout knee flexion/extension

As the literature review has demonstrated, it is very challenging to determine knee ligament tensions simultaneously through cadaveric experimentation. Imaging in vivo methods can only provide relative stresses and strains and not absolute values, since zero stress and strain conditions are unknown. In silico techniques to determine ligament tension is not without difficulty, since the system of forces in the knee joint are indeterminate, meaning there may not be a unique equilibrium solution. Simplistically, in a three-force system of quadriceps force, hamstrings force and a contact force acting at a knee joint, there are an infinite number of solutions to this problem. If two forces are known, then the third may be calculated, but if none or one force is known, then we are unable to directly solve. In the current model, whilst we can estimate the external force acting on the tibia (weight), we have multiple unknowns: the tensions of the ACL, PCL, MCL, LCL and patella tendon, and the contact forces. A methodology therefore needs to be devised to generate an equilibrium solution for the forces in question and then to test the robustness of this solution.

It is proposed in this thesis that an iterative solution methodology may achieve this aim. We can guess the starting tensions in the ligaments, apply an external force, and determine the resulting equilibrium tensions. These tensions can then be used to determine the starting tensions of the subsequent iteration and determine another equilibrium solution. This process can continue until the solution is deemed to have converged. Convergence means that the tibia does not move in the analysis and the difference in tensions between iterations is below some tolerance level.

This methodology will hopefully generate a solution for equilibrium; However, it is still an indeterminate system and other solutions may exist. The robustness of the solution may be assessed by using starting tensions of different values. If the converged solution is independent of these different starting tensions, this gives confidence that the solution achieved is sensible, robust and possibly determinate. The latter will never be known, however.

For each frame of data, initial stage of the analysis involved setting boundary conditions that immobilised the femoral and patellar bone in position while applying a remote force, representing the weight of the lower limb, at the position centre of mass of the tibial bone. To achieve equilibrium in the ligamentous structures, preloading was systematically applied to the ligaments, with initial preload values set either at 100 N or 200 N, as shown in the flowchart below. Additional pre-loads of 0, 300 and 400N were also analysed on some, but not all, models.

The FE model was parameterised by applying material properties to the bone and cartilage components. The ligaments were modelled as spring elements, and their initial preloads were systematically set to a defined pre-load value. Whilst this is a significant simplification [refs saying ligaments need to be modelled well], it allowed for preloads to be applied and for a relative fast computation. The external load was then applied, and the program was run to equilibrium, ascertaining new tensions of the patellar tendon (PT), posterior cruciate ligament (PCL), anterior cruciate ligament (ACL), medial collateral ligament (MCL), and lateral collateral ligament (LCL).

If the relative percent difference between the pre- and post-spring loads exceeded 1%, the simulation was iteratively refined. The average value between the pre- and post-spring loads was set as the new preload value for the subsequent iteration, and the analysis was repeated. This iterative refinement cycle continued until the relative percent difference fell below the difference of 0.1%, ensuring that the mechanical responses of the ligaments closely matched the static force-loading condition. This approach converged to a robust solution for soft tissue tensions in the knee joint.

Given that the movement considered is flexion with the femur and patella fixed, the method is likely finding the force required in the patellar tendon (representing quadriceps activation) to balance the self-weight of the lower leg, rather than establishing a profile of possible tension forces within the ligaments for a complete range of motion of the knee joint. This is because the patella is fixed, preventing direct simulation of active quadriceps contraction, and the iterative process resolves the patellar tendon preload needed for equilibrium under gravity alone. Thus, the calculated tensions primarily reflect the passive balancing required to counteract the applied weight at each discrete flexion angle, rather than a comprehensive dynamic profile across the full ROM under muscle-driven motion. Future work could incorporate active muscle forces or release the patella constraints to better capture quadriceps-driven tension profiles.

3.4.1.1 Ligament and patella tendon under static equilibrium conditions

As previously emphasized, the primary objective of this thesis is to determine the preload required by the ligaments and patellar tendon to maintain knee joint equilibrium under static conditions as per the experiment. Accordingly, the tensile forces acting in the patellar tendon (PT), posterior cruciate ligament (PCL), medial collateral ligament (MCL), and anterior cruciate ligament (ACL) in each frame of the model were calculated through a series of iterative calculations.

Iterative computing is an essential technique for solving complex systems, particularly in cases where the system is indeterminate—that is, when the number of unknowns exceeds the number of governing equations [252-253], making direct calculation impossible. Indeterminate systems, like those found in biomechanical models of the knee joint, require specialized methods to solve for unknown forces, as multiple ligaments and tendons interact and contribute to the overall balance of the joint. The indeterminate nature of this system necessitates iterative techniques because it allows for continuous adjustments, reflecting the interconnected behaviour of the ligaments under load. By repeatedly refining the forces in response to changes in the overall system, the model achieves an equilibrium state that accurately represents the complex interactions at play.

In this study, the knee joint model is treated as an indeterminate system, where the forces exerted by ligaments, such as the patellar tendon (PT), posterior cruciate ligament (PCL), medial collateral ligament (MCL), and anterior cruciate ligament (ACL), must be determined in a way that satisfies static equilibrium under load. Due to the interdependencies among these structures, directly solving for individual ligament forces is not feasible. Instead, iterative methods are employed, which break down the problem into smaller steps and gradually refine the solution.

In this context, iterative operations are used to adjust the ligament preload, a critical component in maintaining the balance of the knee joint under static conditions. The preload in each ligament is adjusted through successive iterations, with each step aiming to minimize the discrepancy between the applied external forces and the resultant internal forces within the ligaments such that the movement of the tibia is zero. This process continues until the difference between iterations in all of the ligament and tendon forces are below a specified threshold—a predefined minimum error percentage that ensures accurate force distribution and biomechanical fidelity. This equilibrium balance of forces results in minimal movement of the tibia in a frame's analysis.

There are many ways in which one can iterate a mathematical process based on the outcome of a previous solution, for example, Newton-Raphson. However, in the current indeterminate system, for determining a step's preload values for ligament tension, it was felt important that this process occurred smoothly, without big jumps in the input values from iteration to iteration. Within an iterative process, it was felt important to converge onto a potentially local solution for the ligament tensions and not jump between possibly different local solutions using a fast iterative scheme. If $F_{pre,i}$ is the initial preload in a solution step i, and $F_{post,i}$ is the ligament tension after the solution has converged to equilibrium in step i, then the preload value for the next solution, $i+1$, step was taken as

$$F_{pre,i+1} = \frac{F_{post,i} + F_{pre,i}}{2}$$

Convergence criteria are defined to determine when the iterative algorithm reaches an acceptable solution. The iteration process is performed until the predefined convergence criteria are met, thus ensuring that the model produces reliable results. In this study, the convergence criteria were set to ensure that the knee joint model reached a state of equilibrium that met the physiological specifications for ligament tension and biomechanical parameters. This approach minimized the risk of model imbalance or instability.

Iterations proceeded as described above until all ligament and patella tendon tension forces satisfied the requirement of less than a 1% difference in tensions during the analysis, or

$$\frac{|F_{post,i} - F_{pre,i}|}{F_{pre,i}} \times 100 \leq 1$$

To ascertain the robustness of the solution for this indeterminate system of forces, different initial preloads were given to the ligaments. They were either given all a preload of 100N, or 200 N. A small subset of frames had starting tension of 0 N.

A critical point to clarify is the relationship between this iterative preload adjustment and the common approach of representing ligaments as springs with pre-strain or pre-stress. In classical spring-based formulations, pre-strain or pre-stress is prescribed explicitly as an initial condition, and the ligament force at any joint position follows directly from the constitutive law. By contrast, the present iterative method does not assume an explicit pre-strain. Instead, it determines the effective preload forces through equilibrium balancing at each discrete flexion position. In other words, the ligament forces emerge as equilibrium requirements rather than as direct outputs of a pre-strained spring model.

It is important to note that, although the self-weight of the lower leg is accounted for in this equilibrium, the quadriceps force is not included in the calculations. This is because the patella was fully fixed in the initial boundary conditions, meaning that quadriceps activation was mechanically excluded from the system. Therefore, the iterative procedure focuses purely on resolving ligament and patellar tendon preloads required for static equilibrium under the specified boundary conditions, rather than simulating active muscle contributions.

3.5 Secondary research aim: Tibia movement tracking and location verification

The second research question is whether the motion of the knee joint from one frame to another can be accurately predicted? If this is the case, with the ligament tensions as found previously, then this would give confidence to these ligament tensions, effectively self-validating the study.

The basic knee joint complex consists of three bones (femur, tibia, and patella), connected by ligaments and tendons. The estimated (already determined knee ligament and patellar tendon tension balance FE model) position of the tibia can be compared to the known (image) position by applying the known motion of the femur and patella from one frame to the next. If the two tibias match well, we can conclude that the interconnecting structures, i.e., the ligaments, are well described in the model.

Quantification of Euclidean displacement variables can reveal subtle changes in the joint mechanics during flexion and extension, such as the movement of motion variables between two frames of the model. This is achieved by calculating the straight-line distance and direction between two points in 3D space, as well as the translational motion (linear motion along the x, y, z axes) and rotational motion (rotation about these axes) of the knee components.

3.5.1 How can the position of the femur and patella be aligned between two frames of the model?

We wish to validate the estimated ligament tensions by determining how well the kinematic position of the tibia matches between two frames separated in time, given those ligament tensions. There are three bones in the knee joint complex that can move: the femur, the patella and the tibia. The femur only moves very slightly due to the experimental protocol and the patella moves in the trochlear groove during knee extension. The tibia moves in extension as a result of the quadriceps muscle force applying itself to the tibia via the patella and patella tendon, anatomical constraints and the any soft tissue constraints (ligament tensions). If we can track the patella and femur between frames, and subsequently compare tibia positions between frames, then we would be in a position to potentially validate the model with regards to the anatomical and soft tissue constraints.

Essentially the workflow of this is as follows.

1. Identify the positions of the femur, patella and tibia in two (nearly) consecutive frames, e.g. frame i and in frame $i + n$.
2. Knowing the position of the femur and patella in frame $i + n$, move the patella and femur in frame i to their frame $i + n$ positions, which will move the tibia in frame i, due to the anatomical and soft tissue constraints.
3. By comparing the resulting position of the tibia in frame i, with that in frame $i + n$, we will be able to assess the appropriateness of model in predicting the knee joint kinematics through the range of motion of the experiment.

To track the femur and patella between frames, one way is to use nodal coordinates. This is done under the assumption that the mesh density of the FE mesh is sufficiently high enabling anatomical landmark loci to be easily and accurately identifiable in two frames, even if the meshes are not the same. As the frames are taken on the same CT machine in the same scan, the global coordinate system is the same between the frames. Three nodes, corresponding to discernible features on the patella and femur are identified in both frame i and frame $i + n$. The vector difference in position between the frames is calculated. In frame i, a prescribed displacement is made to the three nodes identified in frame i, so that they move to their frame $i + n$ position. By using three nodes to define each bone, it is possible to both translate and rotate the femur and patella between frames in 6 degrees of freedom.

Essentially the workflow of this is as follows.

Identify the positions of the femur, patella and tibia in two frames n frames apart, e.g. frame i and in frame i+n.

Knowing the position of the femur and patella in frame i+n, move the patella and femur in frame i to their frame i+n positions, which will move the tibia in frame i, due to the anatomical and soft tissue constraints.

Patella:

$$\Delta P(1,4)_i = P(1,4)_{i+n} - P(1,4)_i$$

Femur:

$$\Delta F(1,4)_i = F(1,4)_{i+n} - F(1,4)_i$$

By comparing the resulting position of the tibia in frame i, with that in frame i+n, we will be able to assess the appropriateness of model in predicting the knee joint kinematics through the range of motion of the experiment. However, the problem is that the nodes in the i+n frame and the nodes in the i frame are not the same: they are not equivalent anatomical positions, and they are not numbered similarly. Therefore, a nearest node approximation needs to be made.

To track the femur and patella between frames, one way is to use nodal coordinates. This is done under the assumption that the mesh density of the FE mesh is sufficiently high enabling anatomical landmark loci to be easily and accurately identifiable in two frames, even if the meshes are not the same. As the frames are taken on the same CT machine in the same scan, the global coordinate system is the same between the frames. Three nodes, corresponding to discernible features on the patella and femur are identified in both frame i and frame i+n. The vector difference in position between the frames is calculated. In frame i, a prescribed displacement is made to the three nodes identified in frame i, so that they move to their frame i+n position. By using three nodes to define each bone, it is possible to both translate and rotate the femur and patella between frames in 6 degrees of freedom.

This approach may induce some minor deformation to the bones, resulting in localised stress and strain, however, since bone stress/strain is not a variable of interest, and the deformation does not affect the articulating surface, this is not a major concern.

The success of this process may be dependent on the choice of anatomical loci used and so this process is repeated another three times using different anatomical loci, and thus different sets of three nodes. An example of this can be seen in Table 6 below which details four sets of three nodes on the patella (P) and femur (F) in frames 2 and 6, and the change in position between them.

Error Analysis Using Comparison Nodes

To validate the accuracy of patellar alignment, three additional comparison nodes, Q_i were selected in the ith frame. These nodes were tracked during the translation of either the patella or femur, with ANSYS outputting their displacement, d_i

$$d_i = \begin{pmatrix} \Delta x \\ \Delta y \\ \Delta z \end{pmatrix} = Q'_{i+n} - Q_i$$

From which the nodal coordinates of Q'_{i+n} are found.

$$Q'_{i+n} = Q_i + d_i$$

This Here, the Q'_{i+n} nodes are in the node numbering of the ith frame. In the i+n frame, manually selected, nearest equivalent nodes for the anatomical landmarks identified in the ith frame are determined, Q_{i+n}. These comparison nodes were treated as independent verification points to quantitatively evaluate the error $Q_{difference}$matching bone positions. The error analysis involved a detailed comparison between the predicted positions of the comparison nodes and their actual positions in the frame, providing a measure of the model's accuracy in aligning anatomical structures.

$$Q_{difference} = \|Q'_{i+n} - Q_{i+n}\|_2$$

The same method was subsequently extended to analyse the positional error of the tibia. This ensured a consistent and comprehensive approach to assessing alignment accuracy across different bones in the knee joint model, reinforcing the robustness of the verification process.

For the patella, four different sets of 3 nodes were used to drive the translation, P1 to P4. The same evaluation nodes, Q, were used to assess the accuracy of the process for nodes other than the driving nodes. The femur was also moved by four different sets of driving nodes on the femur (F1 to F4), however, as the displacements were very small, the accuracy of these movements were not assessed. The effect of using the 16 different node set combinations (different combinations of P and F, e.g. P1 and F3 etc) on the subsequent tibia position was analysed (using the evaluation Q nodes as above) to give an indication as to the importance of selecting the “best” node set.

Units: meter	Frame 2			Frame 6					j=1			j=2			j=3		
Node set	X	Y	Z	X	Y	Z	Euclidean distance	Frame No.	$DX_{j=1}$	$DY_{j=1}$	$DZ_{j=1}$	$DX_{j=2}$	$DY_{j=2}$	$DZ_{j=2}$	$DX_{j=3}$	$DY_{j=3}$	$DZ_{j=3}$
P1A	-0.0989	-0.0716	0.35312	-0.0928	-0.0682	0.36198	0.011318523	F06	-0.09276	-0.068206	0.36198	-0.13876	-0.072998	0.36461	-0.11503	-0.061191	0.3352
P1B	-0.1428	-0.0724	0.35354	-0.1388	-0.073	0.36461	0.011811563	F02	-0.098924	-0.071614	0.35312	-0.14283	-0.072363	0.35354	-0.12048	-0.055221	0.32685
P1C	-0.1205	-0.0552	0.32685	-0.115	-0.0612	0.3352	0.011621786	d'/m	0.006164	0.003408	0.00886	0.00407	-0.000635	0.01107	0.00545	-0.00597	0.00835
P2A	-0.0988	-0.0715	0.34593	-0.0944	-0.0712	0.35745	0.012307007	F06	-0.094425	-0.071175	0.35745	-0.13806	-0.073619	0.36435	-0.11178	-0.064989	0.33784
P2B	-0.142	-0.0733	0.35395	-0.1381	-0.0736	0.36435	0.011121674	F02	-0.0987524	-0.0715281	0.3459343	-0.141984	-0.0732647	0.3539496	-0.115223	-0.058869	0.3282385
P2C	-0.1152	-0.0589	0.32824	-0.1118	-0.065	0.33784	0.011895125	d'/m	0.0043274	0.0003531	0.0115157	0.003924	-0.0003543	0.0104004	0.0034425	-0.00612	0.0096015
P3A	-0.1105	-0.0586	0.35235	-0.1075	-0.0574	0.36167	0.009879108	F06	-0.10752	-0.057364	0.36167	-0.13852	-0.063766	0.35075	-0.12403	-0.062606	0.33671
P3B	-0.1431	-0.0603	0.34274	-0.1385	-0.0638	0.35075	0.009835687	F02	-0.1105356	-0.0586109	0.3523454	-0.143063	-0.0603188	0.3427364	-0.128095	-0.057132	0.3281134
P3C	-0.1281	-0.0571	0.32811	-0.124	-0.0626	0.33671	0.010972294	d'/m	0.0030156	0.0012469	0.0093246	0.0045431	-0.0034472	0.0080136	0.0040651	-0.005474	0.0085966
P4A	-0.1046	-0.08	0.35484	-0.101	-0.0783	0.37004	0.015724786	F06	-0.10096	-0.078256	0.37004	-0.13726	-0.073866	0.36258	-0.11799	-0.06585	0.33701
P4B	-0.1414	-0.0729	0.35157	-0.1373	-0.0739	0.36258	0.011793537	F02	-0.10459	-0.080003	0.35484	-0.14138	-0.072921	0.35157	-0.12211	-0.060863	0.32763
P4C	-0.1221	-0.0609	0.32763	-0.118	-0.0659	0.33701	0.011394252	d'/m	0.00363	0.001747	0.0152	0.00412	-0.000945	0.01101	0.00412	-0.004987	0.00938

Node set	X	Y	Z	X	Y	Z	Euclidean distance		$DX_{j=1}$	$DY_{j=1}$	$DZ_{j=1}$	$DX_{j=2}$	$DY_{j=2}$	$DZ_{j=2}$	$DX_{j=3}$	$DY_{j=3}$	$DZ_{j=3}$
F1A	-0.1075	-0.0123	0.39431	-0.1047	-0.0072	0.39476	0.005858604	F06	-0.073867	-0.0079354	0.38285	-0.1506	-0.0042661	0.38128	-0.1047	-0.007187	0.39476
F1B	-0.1518	-0.0084	0.37996	-0.1506	-0.0043	0.38128	0.004463015	F02	-0.077821	-0.013863	0.38336	-0.15176	-0.0083686	0.37996	-0.10752	-0.012302	0.39431
F1C	-0.0778	-0.0139	0.38336	-0.0739	-0.0079	0.38285	0.007143575	d'/m	0.003954	0.0059276	-0.00051	0.00116	0.0041025	0.00132	0.00282	0.0051155	0.00045
F2A	-0.1148	-0.0449	0.42077	-0.1115	-0.0391	0.42228	0.006862668	F06	-0.069048	-0.021869	0.37544	-0.14847	-0.038084	0.38401	-0.11148	-0.039093	0.42228
F2B	-0.1505	-0.0437	0.38206	-0.1485	-0.0381	0.38401	0.00624496	F02	-0.071781	-0.02898	0.37457	-0.15046	-0.043673	0.38206	-0.11483	-0.044889	0.42077
F2C	-0.0718	-0.029	0.37457	-0.0691	-0.0219	0.37544	0.007667627	d'/m	0.002733	0.007111	0.00087	0.00199	0.005589	0.00195	0.00335	0.005796	0.00151
F3A	-0.1366	-0.0082	0.39692	-0.1333	-0.0034	0.39675	0.005929442	F06	-0.070139	-0.0043061	0.3726	-0.14795	0.0033241	0.37031	-0.13327	-0.003357	0.39675
F3B	-0.1502	-0.002	0.36892	-0.148	0.00332	0.37031	0.005920491	F02	-0.073	-0.00964	0.37207	-0.15023	-0.00196	0.36892	-0.13663	-0.00824	0.39692
F3C	-0.073	-0.0096	0.37207	-0.0701	-0.0043	0.3726	0.006075912	d'/m	0.002861	0.0053339	0.00053	0.00228	0.0052841	0.00139	0.00336	0.0048826	-0.00017
F4A	-0.1061	-0.0095	0.373	-0.1053	-0.0054	0.37405	0.004318876	F06	-0.096501	-0.0091322	0.41265	-0.14212	-0.0030816	0.38667	-0.10526	-0.005398	0.37405
F4B	-0.144	-0.0072	0.38448	-0.1421	-0.0031	0.38667	0.005052965	F02	-0.0979	-0.0141	0.41051	-0.14402	-0.00722	0.38448	-0.10606	-0.00951	0.373
F4C	-0.0979	-0.0141	0.41051	-0.0965	-0.0091	0.41265	0.005587114	d'/m	0.001399	0.0049678	0.00214	0.0019	0.0041384	0.00219	0.0008	0.0041122	0.00105

Table 6. Single frame model tested based on the combinations of different random set nodes.

Units in metres (m); 0.001 m = 1 mm.

3.5.2 Tibia position analysis using direct node analysis

3.5.3 Bony position analysis using CloudCompare™

After the manually displacing the femur and tibia, CloudCompare™ was used to analyse the positional similarity of the entire knee model. CloudCompare allows for a detailed comparison of the two-frame model states. Initially the patella-femur alignment accuracy is considered, as this is our driving displacement, and then the tibial alignment is evaluated.

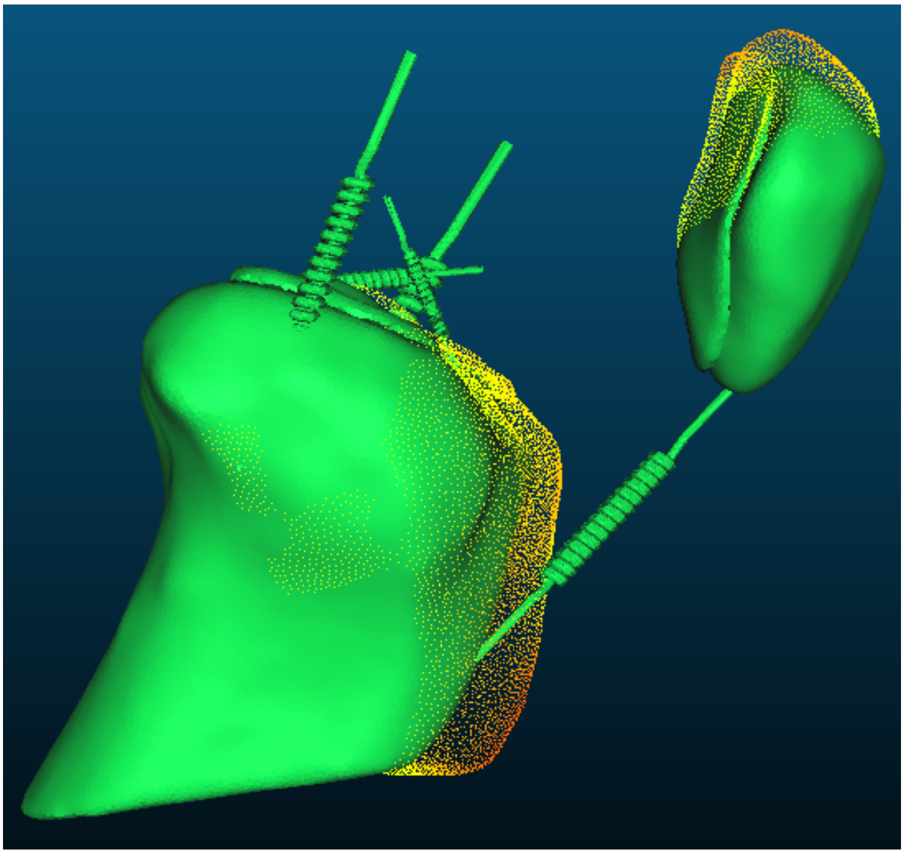

Figure 26. Relative distance analysis of cloud compares

The figure 26 shows the model is indicating displacement between these locations and the model surface by showing geometric changes in three dimensions between two models.

In order to analyse the two coupled knee models, it is necessary to understand how CloudCompare calculates distances to identify positional differences between these models. The introduction gives an overview of the two main types of distances that

CloudCompare can calculate: cloud-to-cloud and cloud-to-grid distances.

When the mesh vertices are densely and consistently sampled, the point clouds themselves can be used directly to calculate distances. In this approach, the vertices of one mesh are treated as a set of points and distances to another mesh are calculated. This greatly simplifies the calculation of distances between a point cloud and a grid. The nearest-neighbour calculation in CloudCompare™ involves the following steps:

1. CloudCompare™ determines the nearest point to the reference model (cloud or grid) for each point in the compared cloud (or grid vertices/sampled points).
2. The spatial discrepancy is estimated by calculating the Euclidean distance between each pair of compared and reference points.

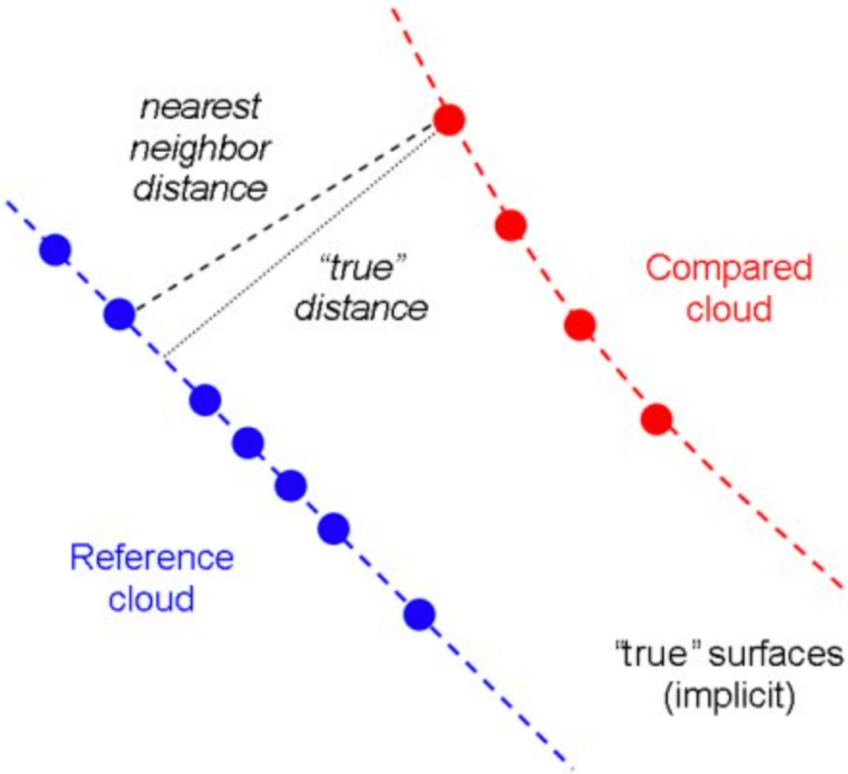

Figure 27. The nearest neighbour distance Vs. true distance between compared cloud and reference cloud.

However, if the reference model is not dense enough, this approach may not accurately represent the real distance between surfaces. To solve this problem, CloudCompare can use a more sophisticated approach that involves applying a mathematical model to a specific surface of the reference model. Cloud-Compare identifies the nearest point in the reference frame and then builds the local surface by determining a mathematical representation of the surface model in the vicinity of this location. Then, instead of calculating the distance to the nearest point, the distance is determined by calculating the shortest distance to this local surface model. This approach provides a more accurate measure of distance that is less affected by the density of the reference frame, although it is more computationally demanding.

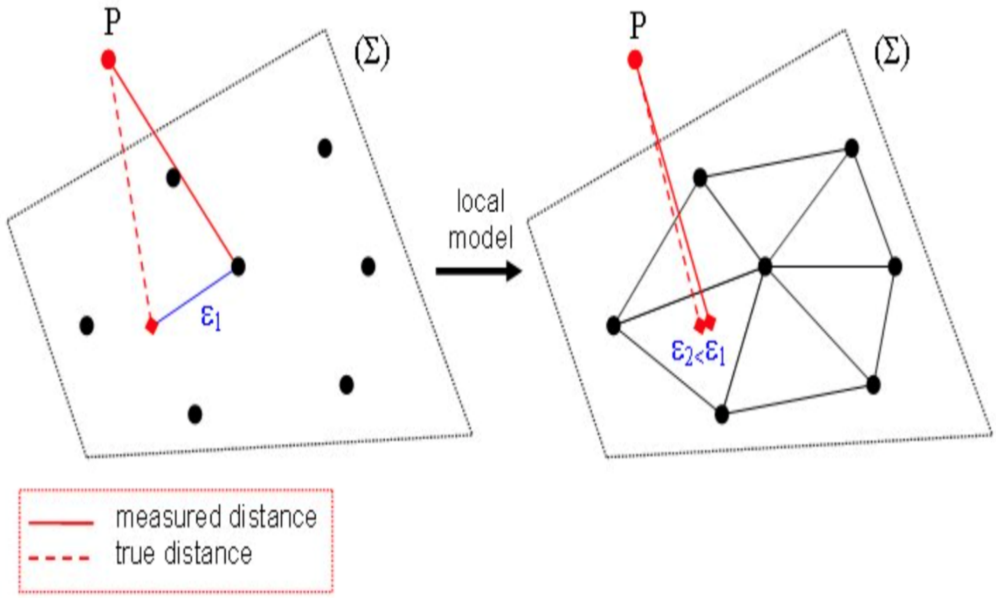

Figure 28. Enhancing Distance Accuracy in Cloud-Compare: From Nearest Points to Mathematical Surface Modelling.

3.5.4 Bony position workflow using Cloud-Compare™

Firstly, all the nodal coordinates of the two knee models to be compared are exported by Ansys and imported into Cloud-Compare. When two models created within a unified coordinate system are imported into Cloud-Compare, they are well-aligned because they share the same global coordinate system.

However, the CloudCompare software contains a point cloud registration tool, enabling an automatic alignment of two-point clouds. Conducting this point cloud registration enabled both further enhanced the alignment of the patella and femur between frames and also allowed us to quantify any residual errors between the manually matched nodes on the patella and femur. In doing so, this would verify the consistency of the node-based displacement calculation.

After verifying patella-femoral alignment, CloudCompare's M3C2 (Multiscale Model-to-Model Cloud Comparison) algorithm was used to map the overall displacement of the knee joint, with a particular focus on tibial position. The M3C2 algorithm accurately measures the distance between corresponding points on the tibia between frames, providing a comprehensive understanding of differences in tibial position. This analysis assessed how well the predicted tibial displacement matches the actual tibial kinematics.

4 Results

In this chapter, we present the results of the in silico experiment as described in Chapter 3. Central to our study is the analysis of a time-sequence of different models, derived and processed from the original 4dCT DICOM datasets. Through a systematic and rigorous approach, the DICOM data were transformed into three-dimensional models of bony anatomy and, together with estimated soft tissue structures, finite element models were constructed. These models were simulated in ANSYS™, under a simple loading scenario.

This study aims to quantify in situ ligament tension across the flexion range of motion of the knee joint, by incorporating an initial ligament pretension and iteratively changing these in order to converge on equilibrium solutions. Following this, the frame-to-frame kinematics of the knee are explored in order to self-validate the models. To do this, the patella and femur underwent a prescribed displacement in space, and the relative tibia position between two frames was assessed using point clouds.

This novel approach aims to provide proof-of-concept for a way to determine knee ligament tensions in situ via computational modelling thereby establishing a foundational basis for future developments in biomechanical modelling and clinical applications.

4.1 Finite Element Model Accurately Segmented and Generated from 4D CT Data

Utilizing the research methodologies delineated in Chapter 3, we successfully segmented the 4d computed tomography (CT) DICOM data pertaining to knee flexion motion into nine discrete frame models, spanning approximately 65 degrees of extension. Each model was processed individually, which involved the conversion of DICOM data into three-dimensional solid models, the construction of soft tissue architectures, and the application of mesh subdivision techniques. This methodical processing was pivotal in preserving the integrity of anatomical structures and optimizing the models for subsequent biomechanical analyses. To facilitate a comparative study, we selected 5 frames: frame numbers 02, 06, 10, 14, and 18, which correspond to approximately 65 degrees of flexion to 0 degrees respectively (Figure 29.). These frames capture key phases of knee extension, allowing for analysis of ligament behaviour during transitions from mid-flexion to full extension, which is critical for understanding load distribution in activities like standing or walking.

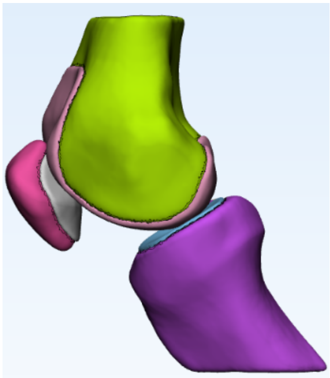

a.

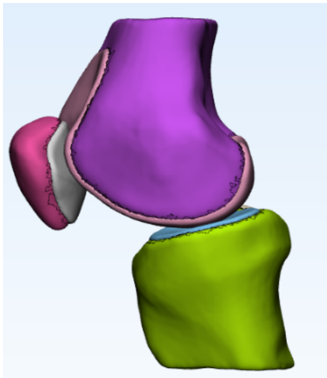

b.

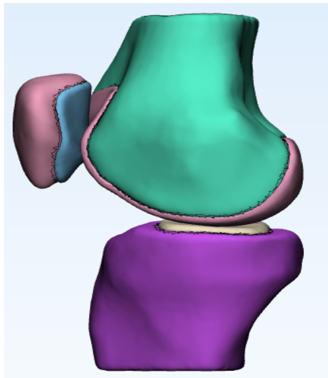

c.

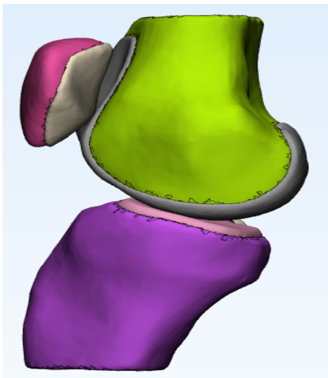

d.

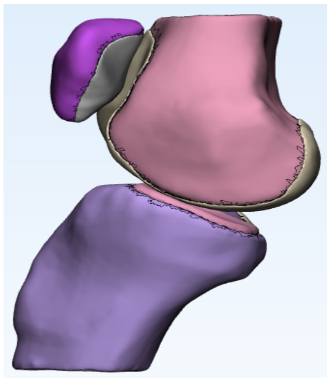

e.

Figure 29. Frame of simulation model from 02-18, a) Frame 02, b) Frame 06, c) Frame 10, d) frame 14, e) Frame 18

4.2 Estimation and Balancing of Ligament Tension

The computational model achieved consistent convergence through iterative calculations, yielding minimal tibial translation and thus converging on estimations of ligament tension across the entire flexion curve (Figure 30 and Figure 31.). Initial ligament pre-tensions were initialized at 100N and 200N and they converged toward near-identical final tension values, giving confidence that the final ligament tensions are robust estimations of the global solution within the defined model parameters. Interestingly, the posterior cruciate ligament (PCL) and lateral collateral ligament (LCL) consistently demonstrated tensions of 0N across all flexion angles. The final values for the ligament tensions are provided in table 7, corresponding to 100 and 200 N starting tensions. These zero tensions in PCL and LCL suggests they are lax during the unloaded flexion simulated here, which aligns with their roles in restricting posterior and varus motions, respectively—motions not prominent in this passive extension scenario. In contrast, the patellar tendon (PT) bore the majority of load, reflecting its primary function in transmitting quadriceps force, while the ACL and MCL showed tension peaks around 20°-35° flexion, consistent with their stabilization during early stance phases of gait.

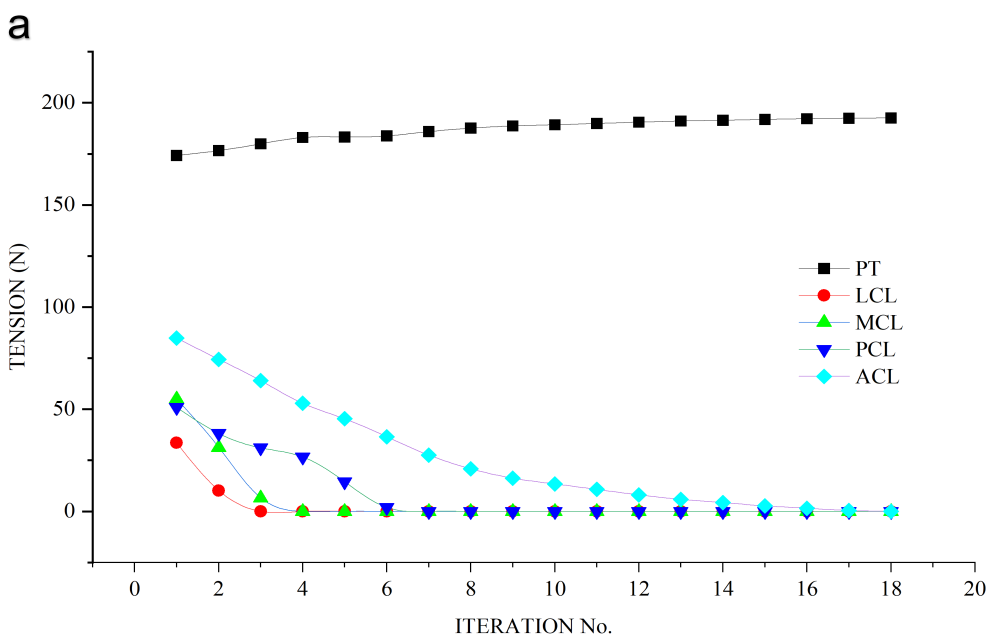

b

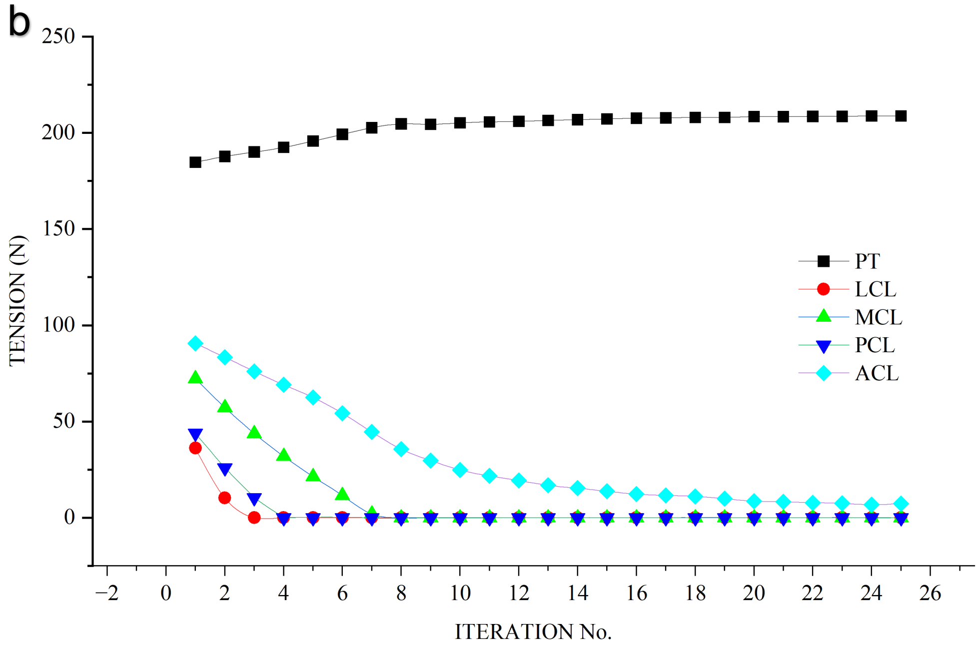
250
200
150
100
50
0
TENSION (N)
−2
0
2
4
6
8
10
12
14
16
18
20
22
24
26
ITERATION No.
PT
LCL
MCL
PCL
ACL

c

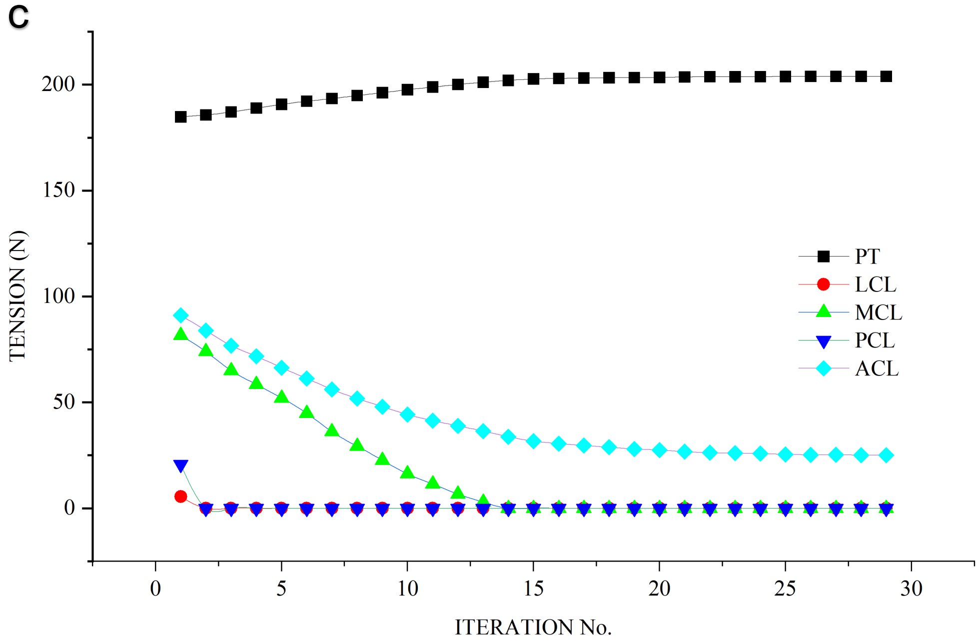
200
150
100
50
0
TENSION (N)
0
5
10
15
20
25
30
ITERATION No.
PT
LCL
MCL
PCL
ACL

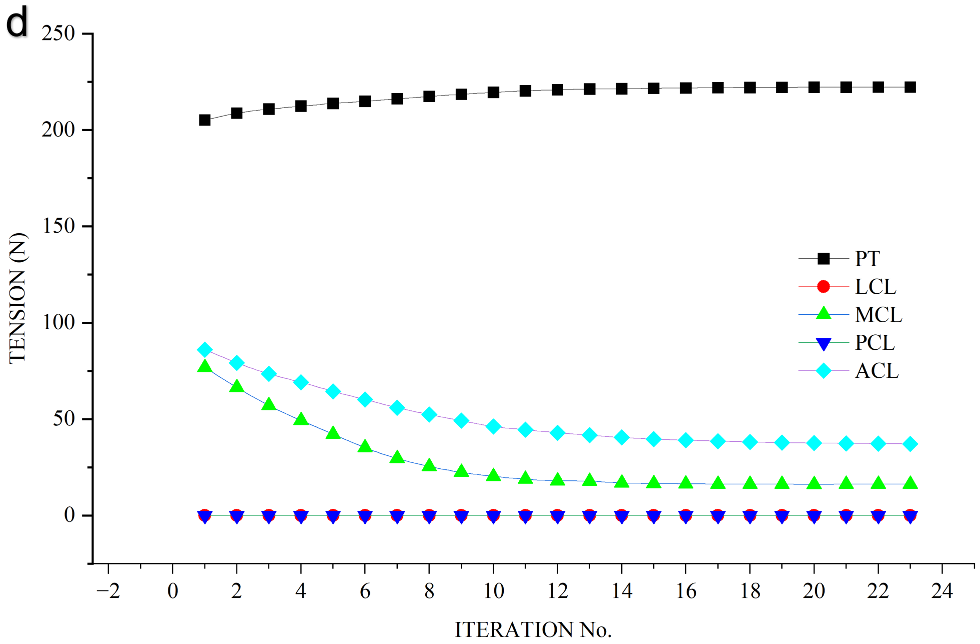

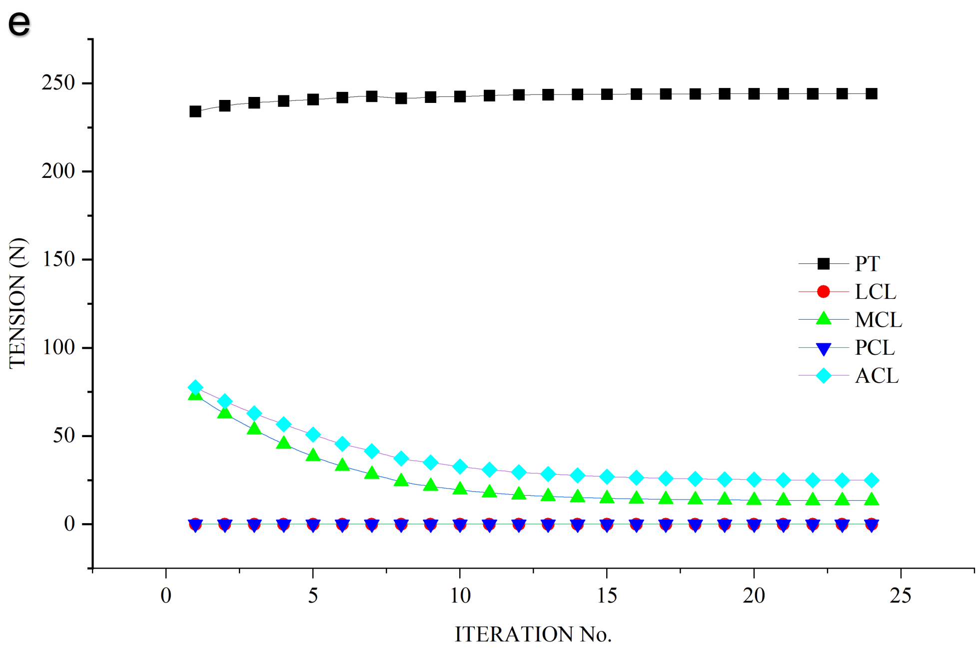

Figure 30. The Frame 02–18 models were used to iteratively calculate the tension curves. Specifically, the models from a) Frame 02, b) Frame 06, c) Frame 10, d) Frame 14, and e) Frame 18 iteratively calculated the tension curves of all ligaments (ACL, PCL, LCL, and MCL) and the patellar tendon (PT) under an initial preload of 100 N.

a

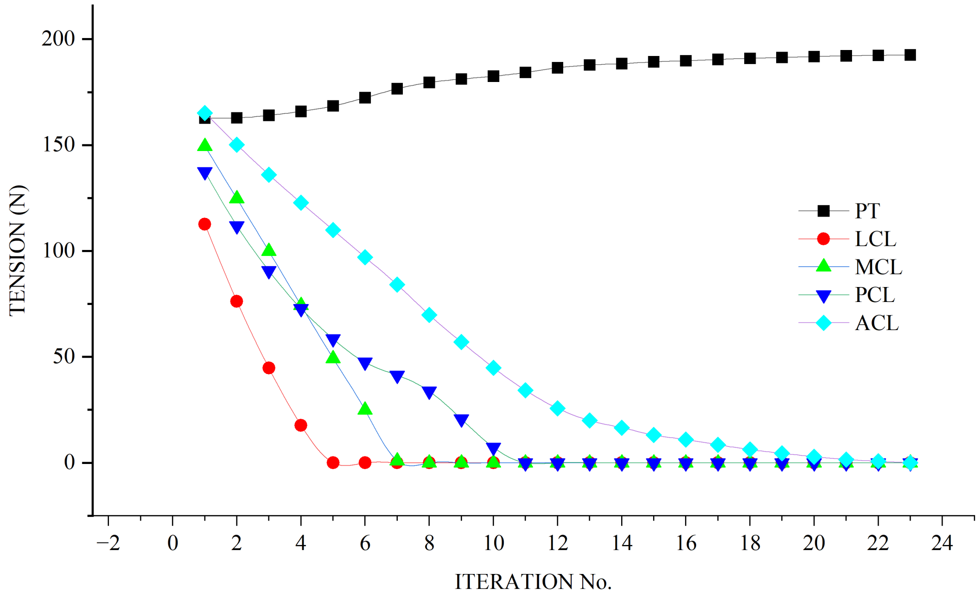

TENSION (N)
ITERATION No.
PT
LCL
MCL
PCL
ACL

b

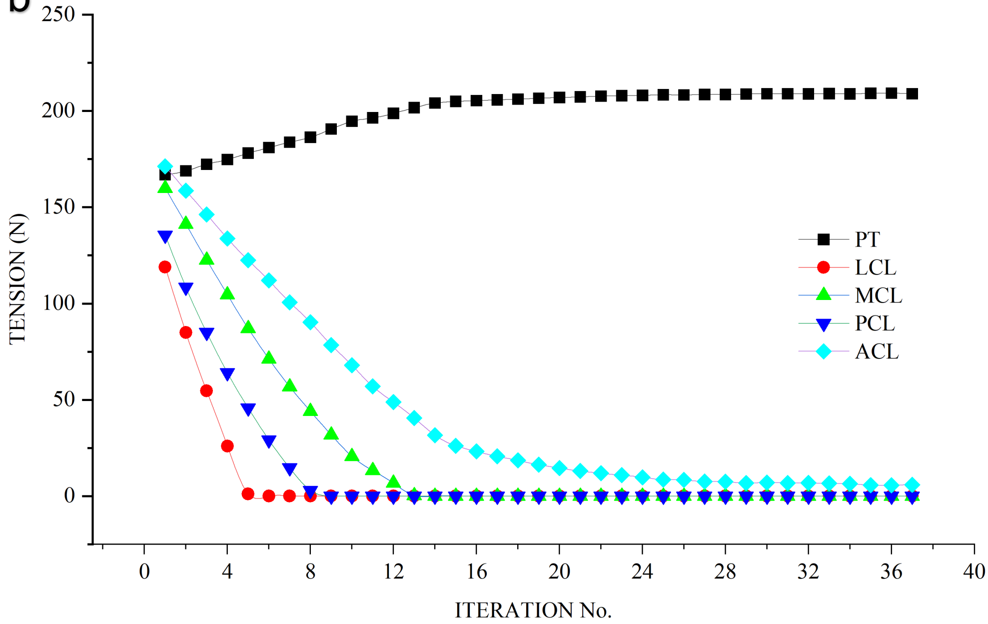

TENSION (N)
ITERATION No.
PT
LCL
MCL
PCL
ACL

c

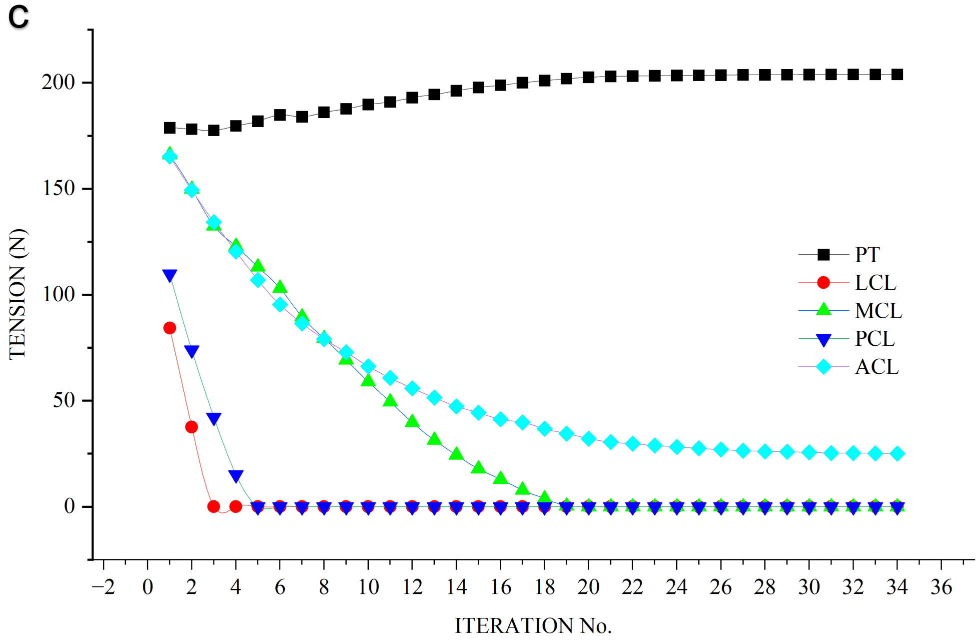
TENSION (N)
200
150
100
50
0
−2
0
2
4
6
8
10
12
14
16
18
20
22
24
26
28
30
32
34
36
ITERATION No.
PT
LCL
MCL
PCL
ACL

d

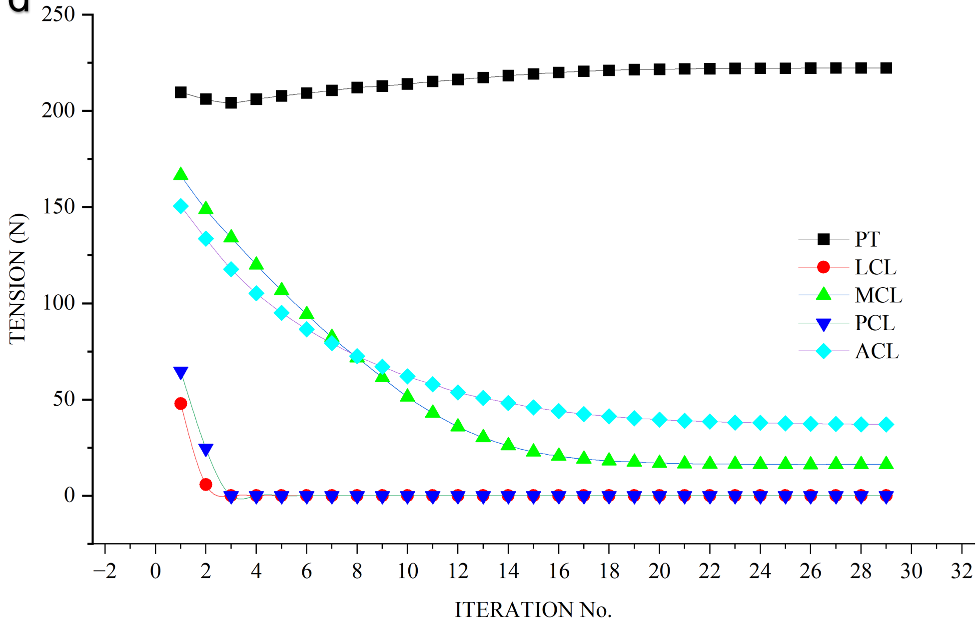
TENSION (N)
250
200
150
100
50
0
−2
0
2
4
6
8
10
12
14
16
18
20
22
24
26
28
30
32
ITERATION No.
PT
LCL
MCL
PCL
ACL

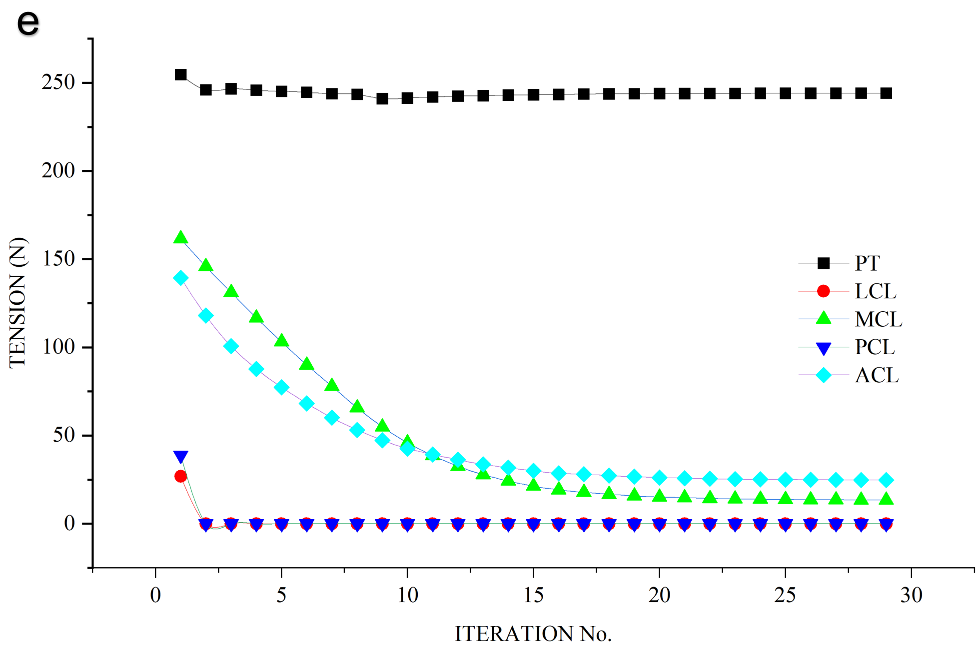

Figure 31. The Frame 02–18 models were used to iteratively calculate the tension curves. Specifically, the models from a) Frame 02, b) Frame 06, c) Frame 10, d) Frame 14, and e) Frame 18 iteratively calculated the tension curves of all ligaments (ACL, PCL, LCL, and MCL) and the patellar tendon (PT) under an initial preload of 200 N.

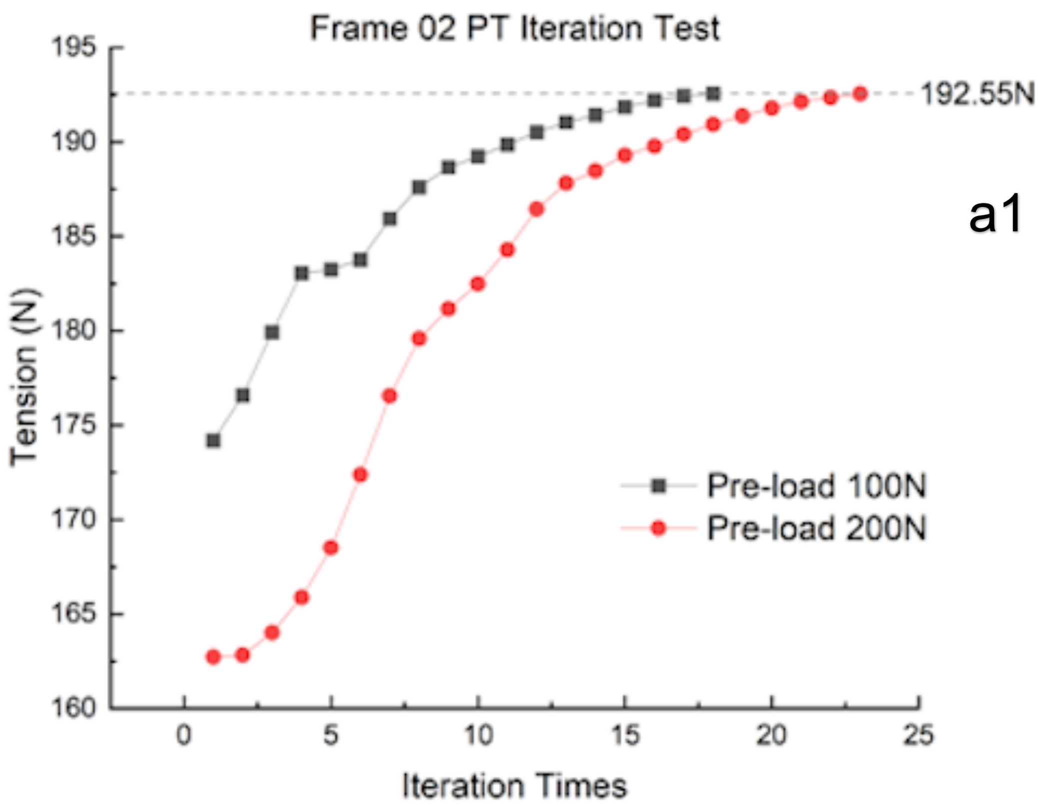
Frame 02 PT Iteration Test
192.55N
a1
Tension (N)
Iteration Times
Pre-load 100N
Pre-load 200N

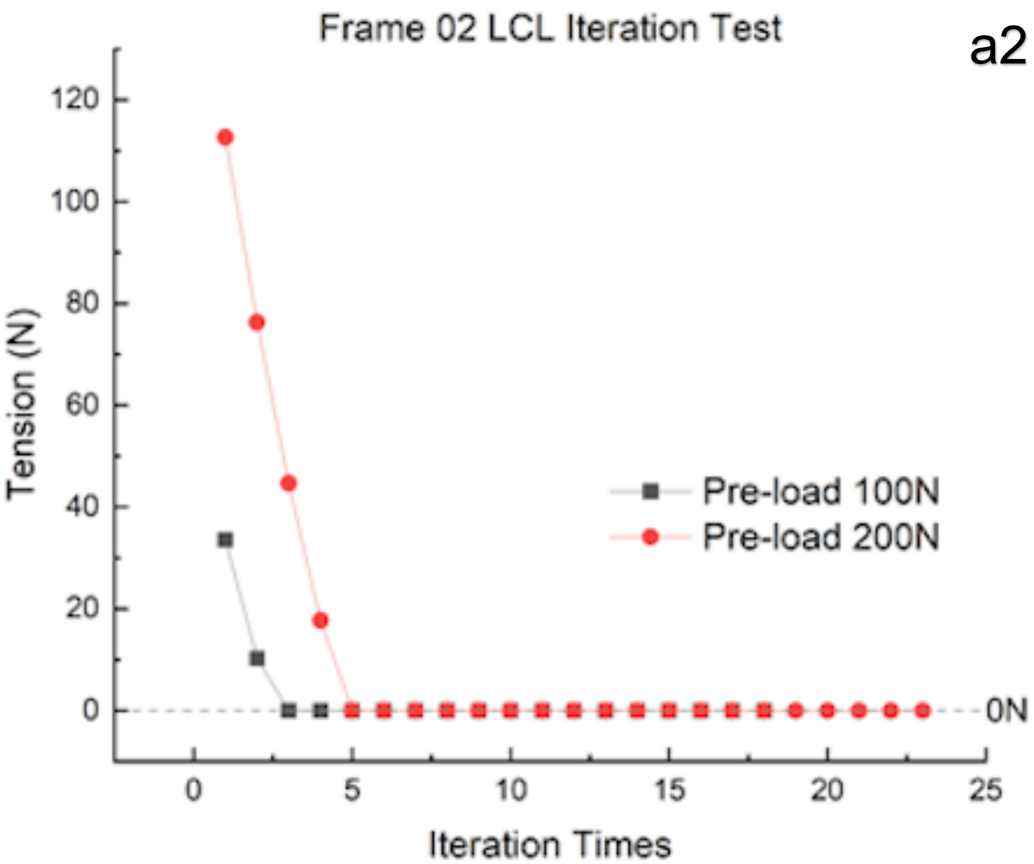
Frame 02 LCL Iteration Test
a2
0N
Tension (N)
Iteration Times
Pre-load 100N
Pre-load 200N

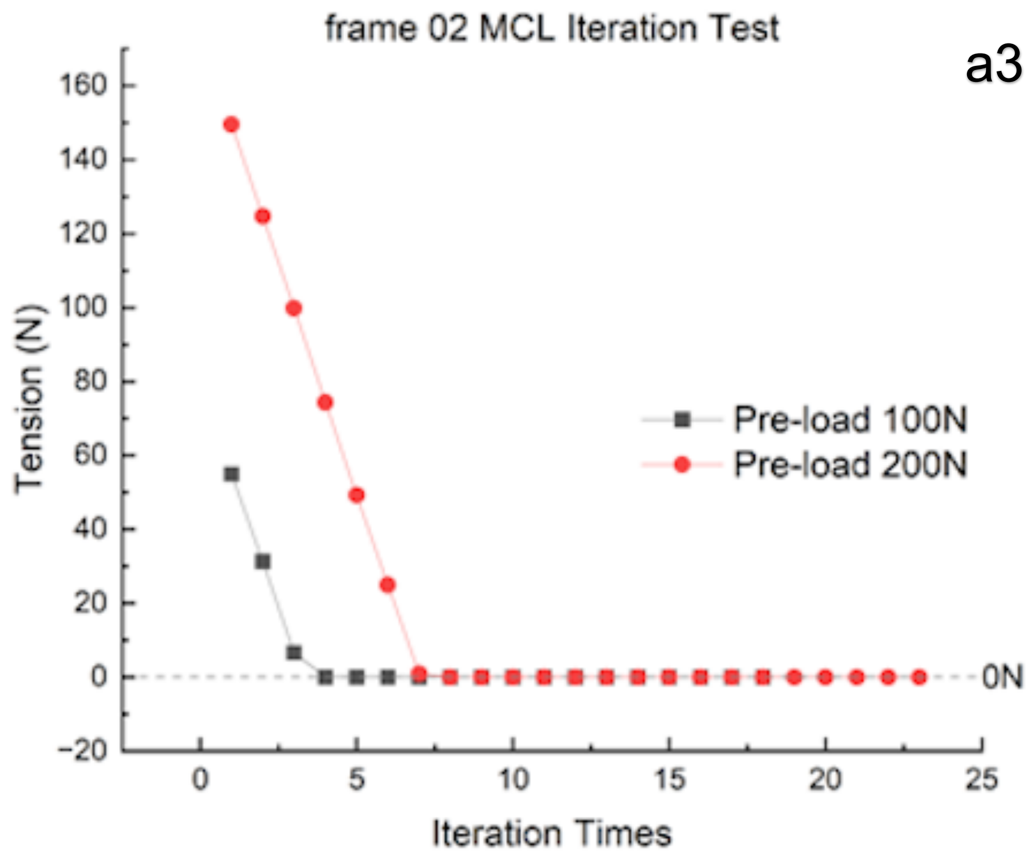
frame 02 MCL Iteration Test
a3
Tension (N)
Iteration Times
Pre-load 100N
Pre-load 200N
0N

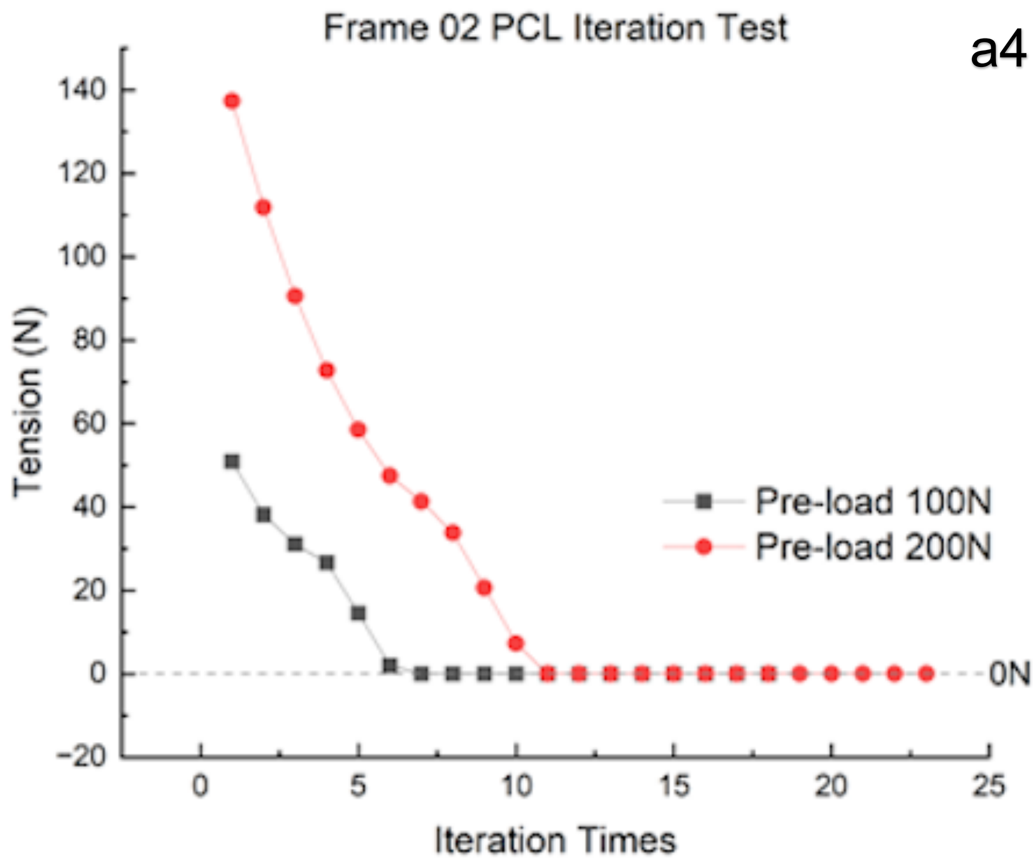
Frame 02 PCL Iteration Test
a4
Tension (N)
Iteration Times
Pre-load 100N
Pre-load 200N
0N

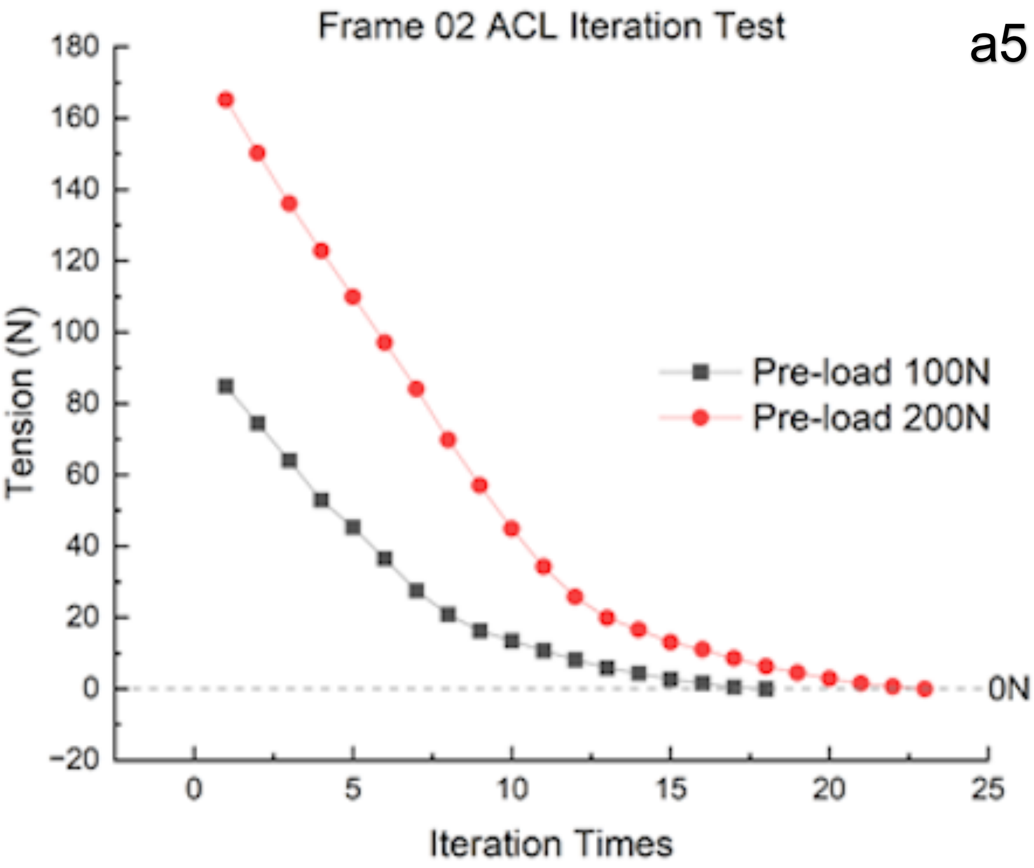
Frame 02 ACL Iteration Test
a5
Tension (N)
180
160
140
120
100
80
60
40
20
0
−20
Pre-load 100N
Pre-load 200N
0N
0
5
10
15
20
25
Iteration Times

a.

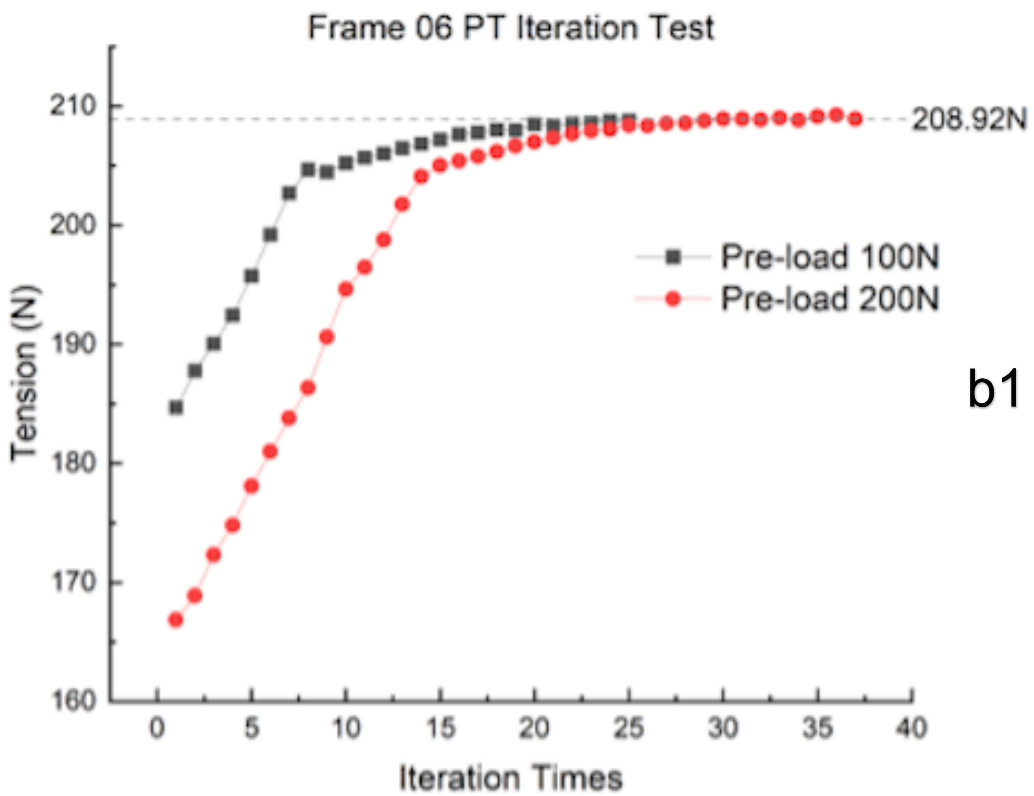
Frame 06 PT Iteration Test
210
200
190
180
170
160
Tension (N)
208.92N
Pre-load 100N
Pre-load 200N
b1
0
5
10
15
20
25
30
35
40
Iteration Times

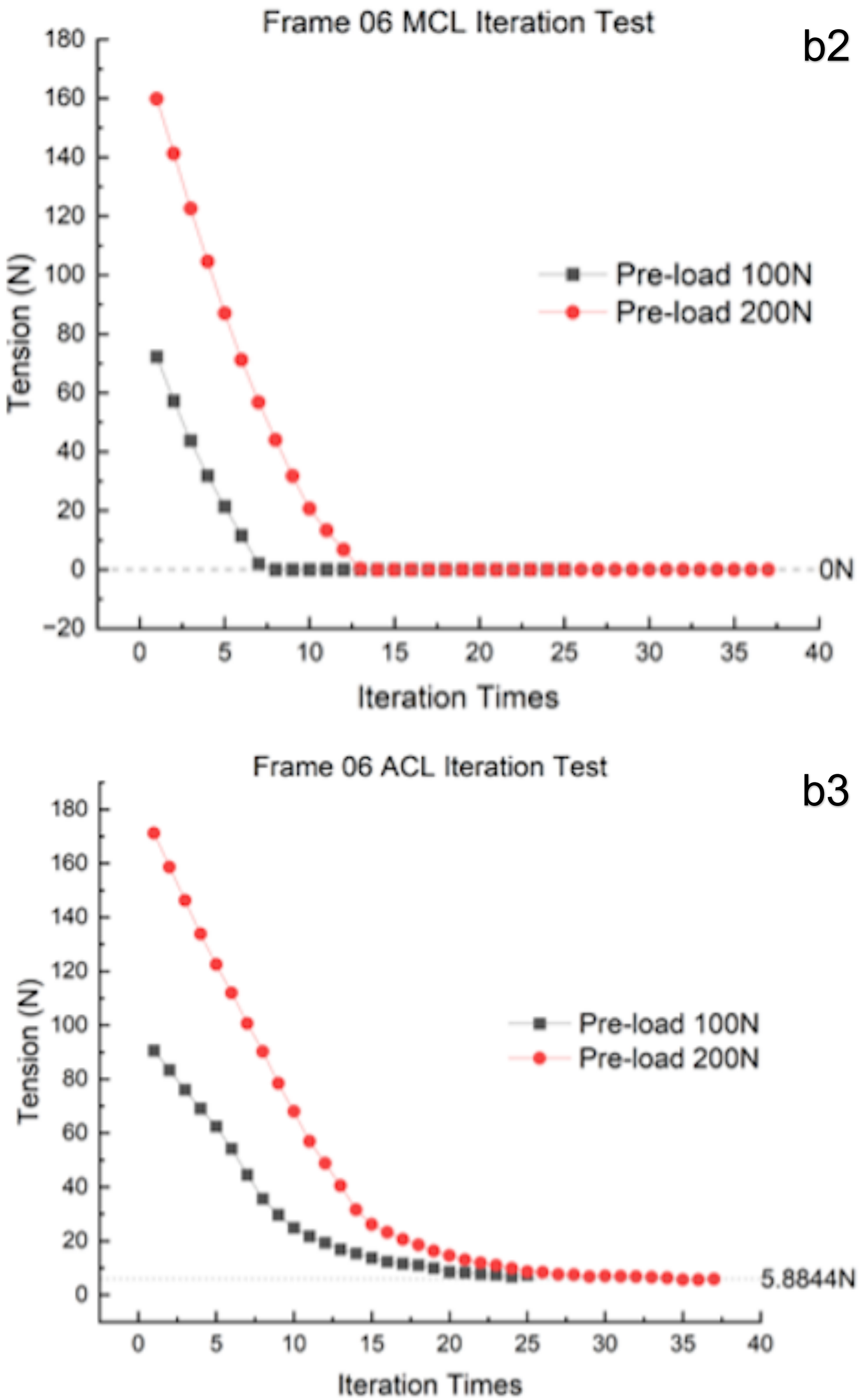
Frame 06 MCL Iteration Test
b2
Tension (N)
Iteration Times
Pre-load 100N
Pre-load 200N
0N
Frame 06 ACL Iteration Test
b3
Pre-load 100N
Pre-load 200N
5.8844N

b.

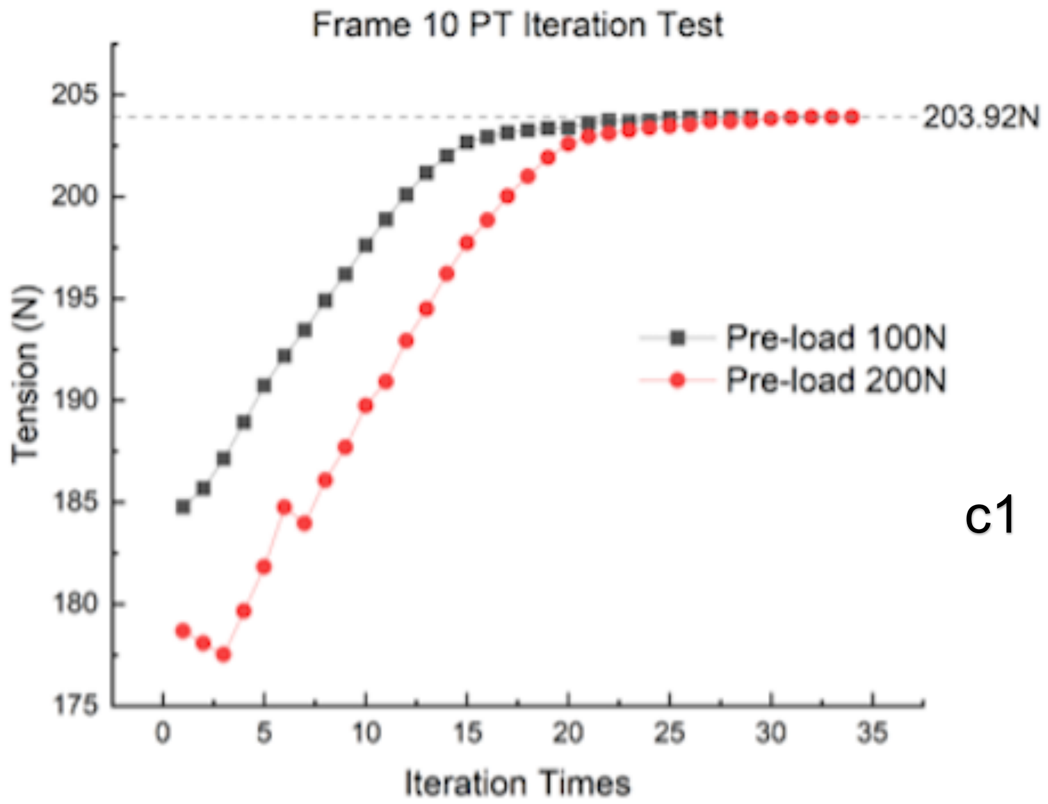
Frame 10 PT Iteration Test
203.92N
Pre-load 100N
Pre-load 200N
c1
Tension (N)
Iteration Times

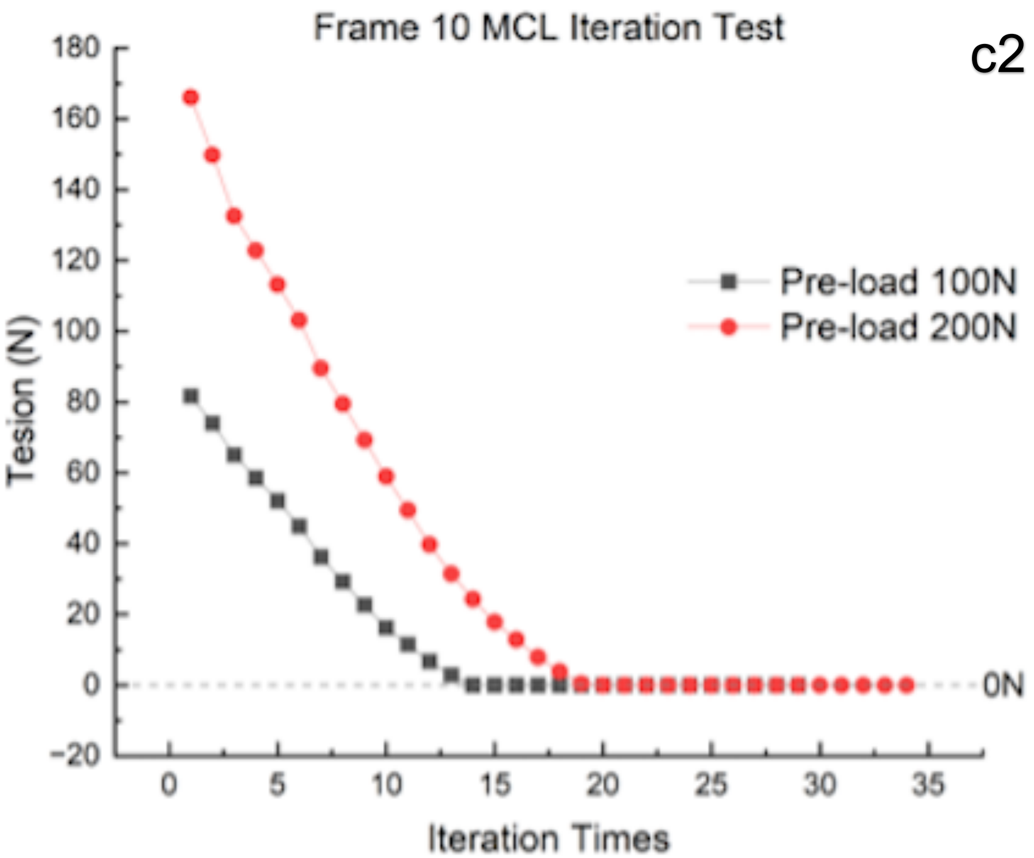
Frame 10 MCL Iteration Test
c2
Pre-load 100N
Pre-load 200N
0N
Tesion (N)
Iteration Times

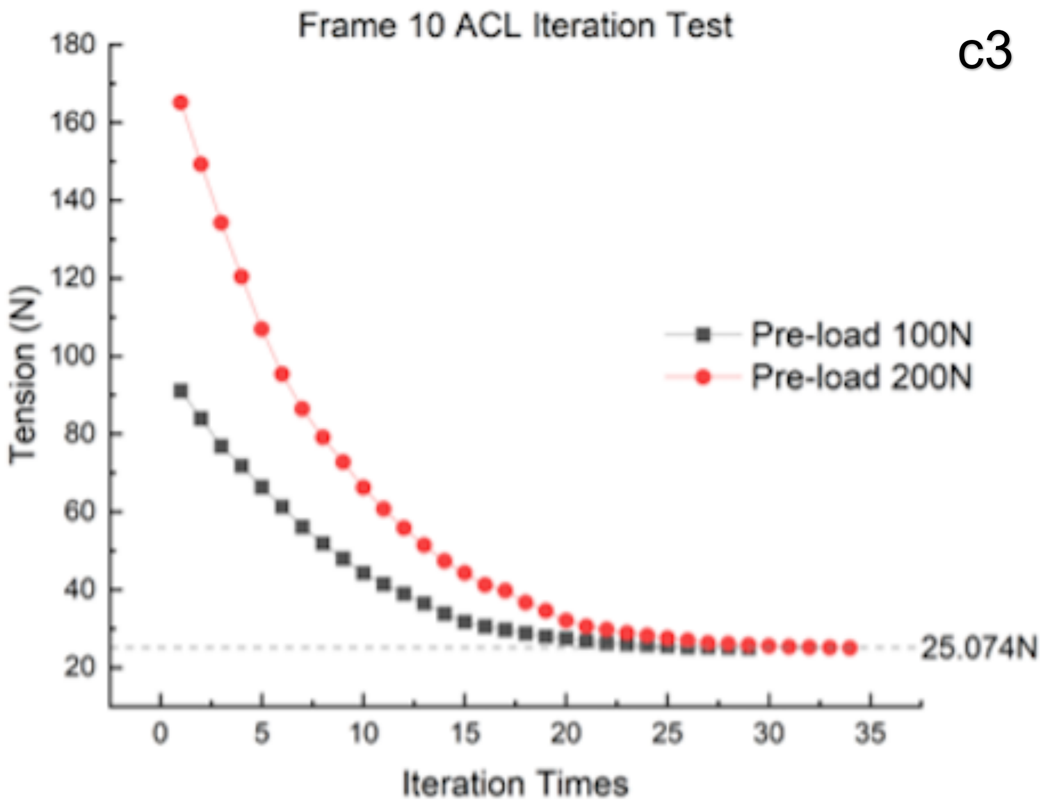
Frame 10 ACL Iteration Test
c3
Tension (N)
Iteration Times
Pre-load 100N
Pre-load 200N
25.074N
180
160
140
120
100
80
60
40
20
0
5
10
15
20
25
30
35

c.

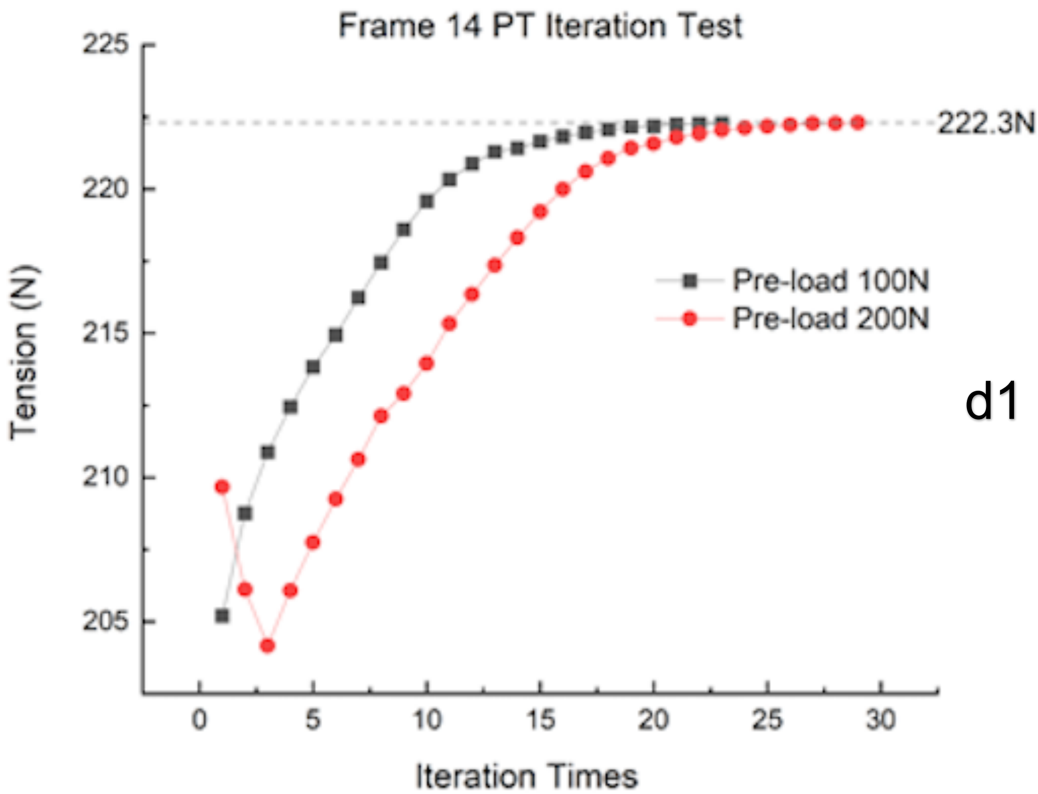
Frame 14 PT Iteration Test
d1
Tension (N)
Iteration Times
Pre-load 100N
Pre-load 200N
222.3N
225
220
215
210
205
0
5
10
15
20
25
30

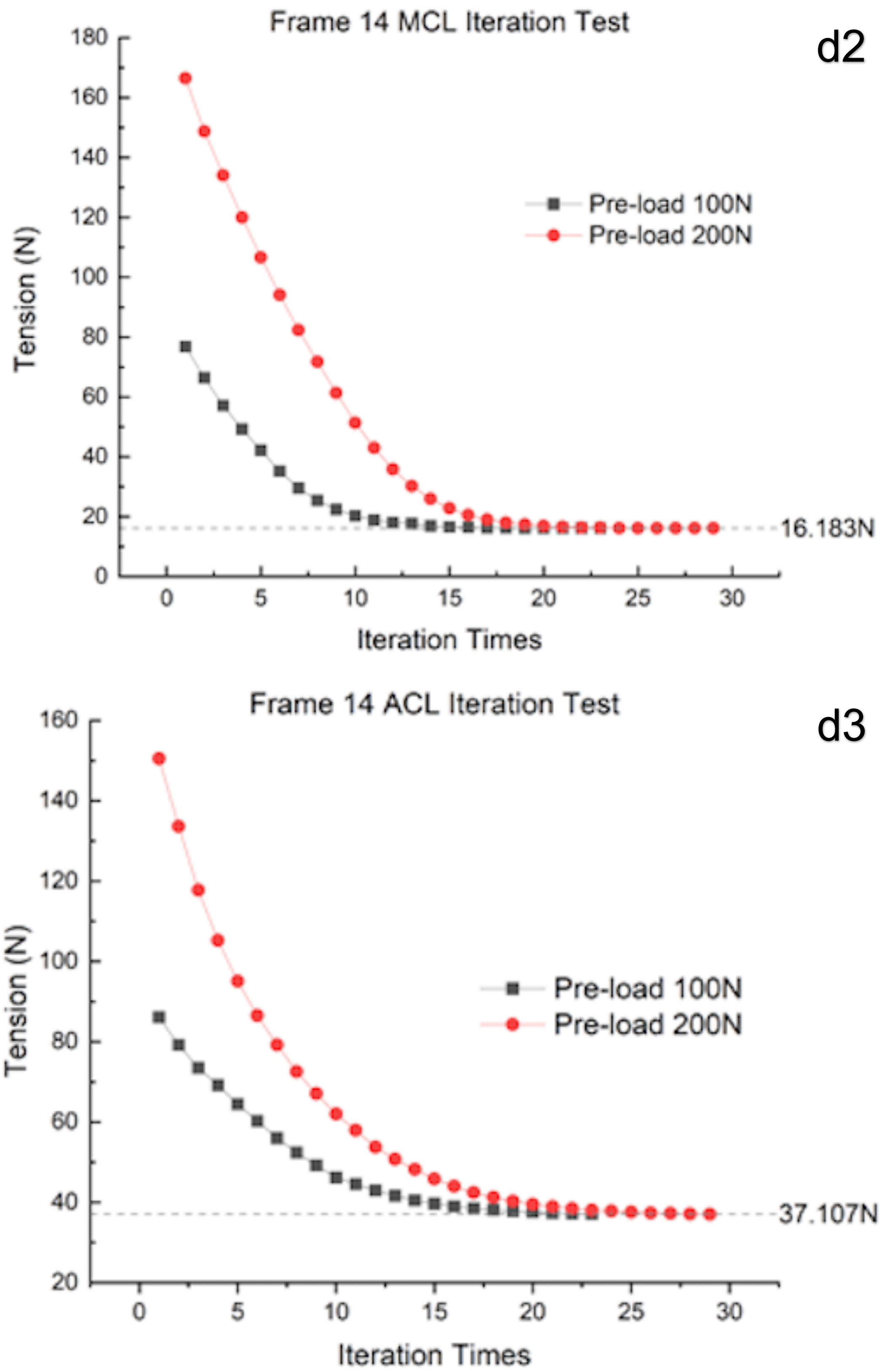
Frame 14 MCL Iteration Test
d2
Pre-load 100N
Pre-load 200N
16.183N
Tension (N)
Iteration Times
Frame 14 ACL Iteration Test
d3
Pre-load 100N
Pre-load 200N
37.107N
Tension (N)
Iteration Times

d.

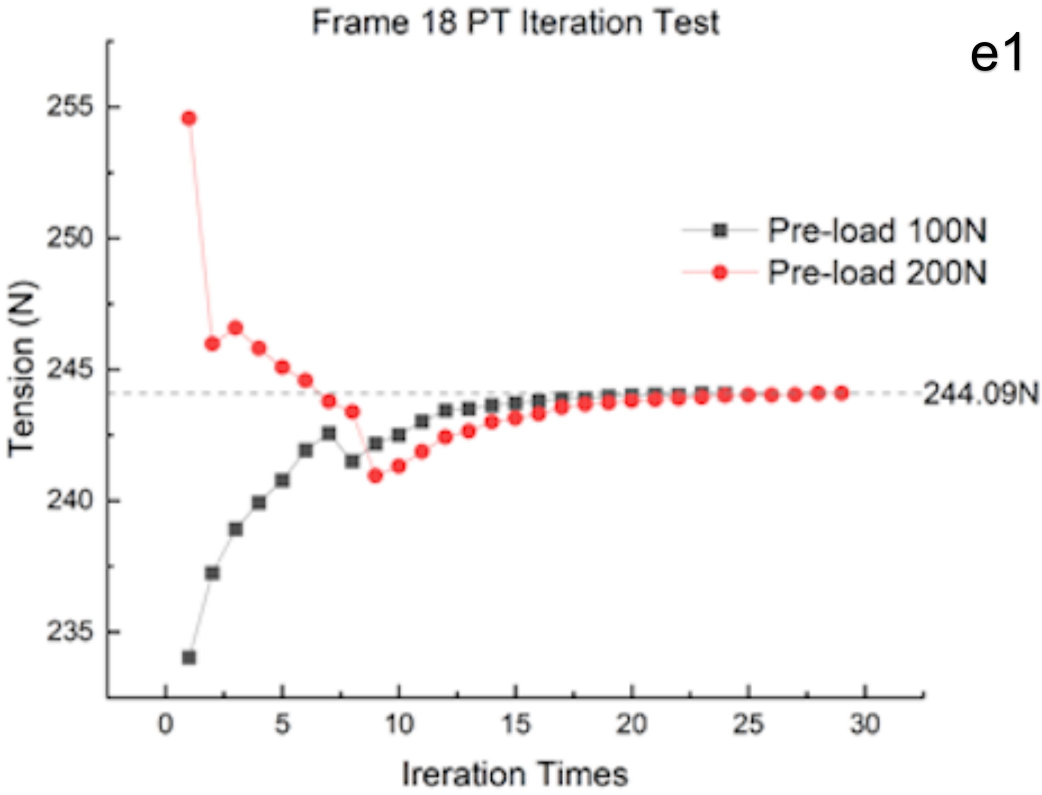
Frame 18 PT Iteration Test
e1
Tension (N)
255
250
245
240
235
0
5
10
15
20
25
30
Ireration Times
Pre-load 100N
Pre-load 200N
244.09N

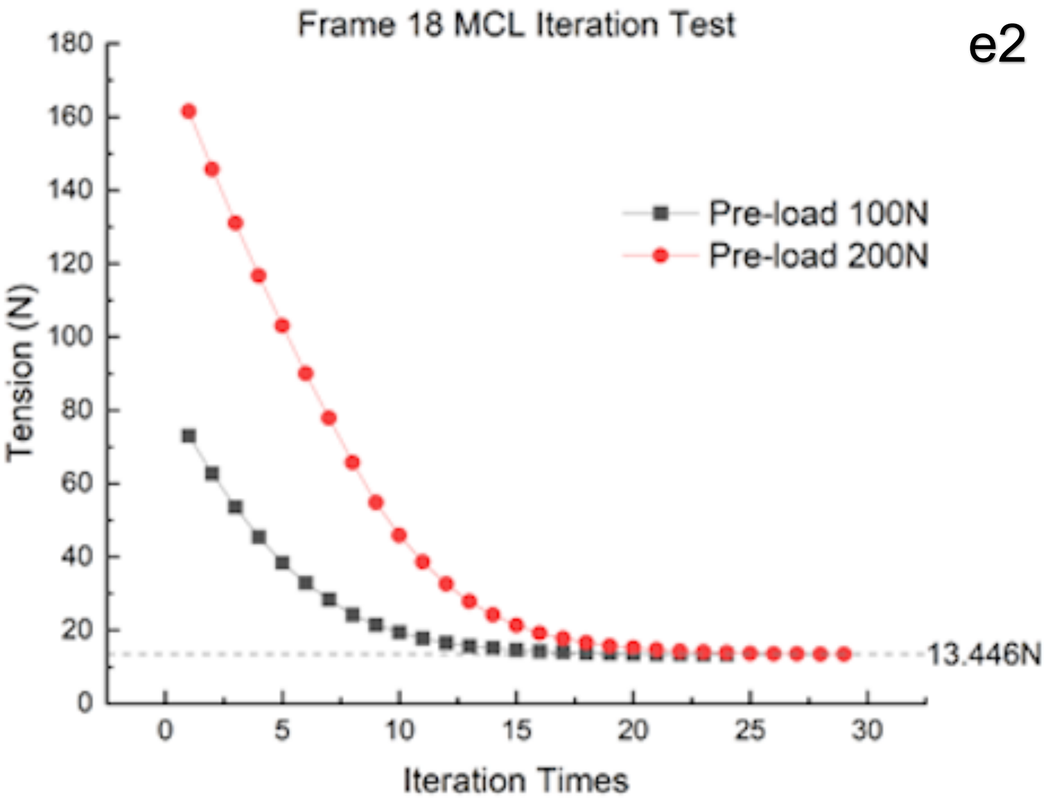
Frame 18 MCL Iteration Test
e2
Tension (N)
180
160
140
120
100
80
60
40
20
0
0
5
10
15
20
25
30
Iteration Times
Pre-load 100N
Pre-load 200N
13.446N

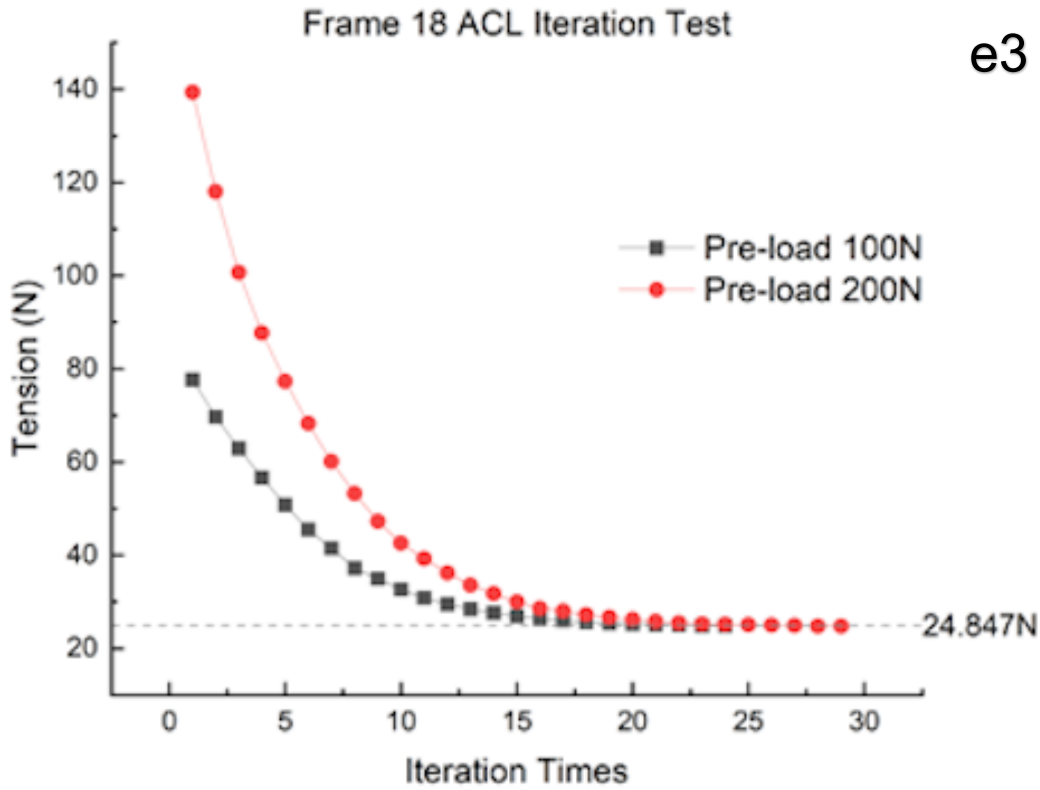

e.

Figure 32. Comparative analysis of the iterative test results for the knee joint model is presented in panels (a) to (e). Panel (a) shows the tension profiles of the patellar tendon (PT; a1), lateral collateral ligament (LCL; a2), medial collateral ligament (MCL; a3), posterior cruciate ligament (PCL; a4), and anterior cruciate ligament (ACL; a5) under two initial pre-tension conditions (100 N, black line; and 200 N, red line) for Frame 02. Panels (b–e) present the corresponding iterative results for Frames 06 (b1–b3), 10 (c1–c3), 14 (d1–d3), and 18 (e1–e3), respectively, focusing on the PT, MCL, and ACL under the same pre-tension conditions (100N and 200N). It is noteworthy that both LCL and PCL exhibit zero tension during the iterative tests for Frames 06–18; therefore, their results are not displayed in panels (b–e).

c

	Frame 02				Frame 06				Frame 10				Frame 14				Frame 18			
Iteration times	Iteration 0		Iteration 22		Iteration 0		Iteration 36		Iteration 0		Iteration 33		Iteration 0		Iteration 28		Iteration 0		Iteration 28	
Units (N)	Pre-loading	Output	Pre-loading	Output	Pre-loading	Output	Pre-loading	Output	Pre-loading	Output	Pre-loading	Output	Pre-loading	Output	Pre-loading	Output	Pre-loading	Output	Pre-loading	Output
PT	200.00	162.73	181.37	192.54	200.00	166.86	209.14	208.92	200.00	178.68	189.34	203.91	200.00	209.67	204.84	222.30	200.00	254.57	227.29	244.09
LCL	200.00	112.64	156.32	0.00	200.00	119.01	0.00	0.00	200.00	84.32	142.16	0.00	200.00	47.85	123.93	0.00	200.00	26.82	113.41	0.00
MCL	200.00	149.44	174.72	0.00	200.00	159.81	0.00	0.00	200.00	166.02	183.01	0.00	200.00	166.45	183.23	16.18	200.00	161.55	180.78	13.45
PCL	200.00	137.36	168.68	0.00	200.00	135.48	0.00	0.00	200.00	109.67	154.84	0.00	200.00	64.75	132.38	0.00	200.00	38.78	119.39	0.00
ACL	200.00	165.18	182.59	0.00	200.00	171.23	5.89	5.88	200.00	165.16	182.58	25.07	200.00	150.54	175.27	37.00	200.00	139.38	169.69	24.78
PT % difference	/	-18.64		0.26	/	-16.57	/	-0.11	/	-10.66		0.01	/	4.83		0.02	/	27.29		0.01
LCL % difference	/	-43.68		/	/	-40.50	/	/	/	-57.84		/	/	-76.08		/	/	-86.59		/
MCL % difference	/	-25.28		/	/	-20.10	/	/	/	-16.99		/	/	-16.78		-0.09	/	-19.23		-0.69
PCL % difference	/	-31.32		/	/	-32.26	/	/	/	-45.17		/	/	-67.62		/	/	-80.61		/
ACL % difference	/	-17.41		/	/	-14.39	/	-0.09	/	-17.42		-0.88	/	-24.73		-0.72	/	-30.31		-0.39

b

	Frame 02				Frame 06				Frame 10				Frame 14				Frame 18			
Iteration times	Iteration 0		Iteration 17		Iteration 0		Iteration 24		Iteration 0		Iteration 28		Iteration 0		Iteration 22		Iteration 1		Iteration 24	
Units (N)	Pre-loading	Output	Pre-loading	Output	Pre-loading	Output	Pre-loading	Output	Pre-loading	Output	Pre-loading	Output	Pre-loading	Output	Pre-loading	Output	Pre-loading	Output	Pre-loading	Output
PT	100.00	174.19	137.10	192.55	100.00	184.69	208.63	208.78	100.00	184.78	142.39	203.92	100.00	205.20	152.60	222.28	100.00	234.03	167.02	244.08
LCL	100.00	33.56	66.78	0.00	100.00	36.20	0.00	0.00	100.00	5.50	52.75	0.00	100.00	0.00	50.00	0.00	100.00	0.00	50.00	0.00
MCL	100.00	54.93	77.47	0.00	100.00	72.25	0.00	0.00	100.00	81.66	90.83	0.00	100.00	76.82	88.41	16.18	100.00	73.06	86.53	13.40
PCL	100.00	50.93	75.46	0.00	100.00	43.88	0.00	0.00	100.00	20.67	60.33	0.00	100.00	0.00	50.00	0.00	100.00	0.00	50.00	0.00
ACL	100.00	84.86	92.43	0.00	100.00	90.61	7.33	7.38	100.00	91.06	95.53	25.04	100.00	86.09	93.05	37.11	100.00	77.65	88.82	24.85
PT % difference	/	74.19		0.23	/	84.69	/	0.07	/	84.78		0.01	/	105.20		0.03	/	134.03		0.01
LCL % difference	/	-66.44		/	/	-63.80	/	/	/	-94.50		/	/	-100.00		/	/	-100.00		/
MCL % difference	/	-45.07		/	/	-27.75	/	/	/	-18.34		/	/	-23.18		-0.22	/	-26.94		-0.35
PCL % difference	/	-49.07		/	/	-56.12	/	/	/	-79.33		/	/	-100.00		/	/	-100.00		/
ACL % difference	/	-15.14		/	/	-9.39	/	0.77	/	-8.94		-0.83	/	-13.91		-0.87	/	-22.36		-0.57

a

	Frame 02				Frame 06				Frame 10				Frame 14				Frame 18			
Iteration times	Iteration 0		Iteration 4		Iteration 0		Iteration 11		Iteration 0		Iteration 5		Iteration 0		Iteration 5		Iteration 1		Iteration 7	
Units (N)	Pre-loading	Output	Pre-loading	Output	Pre-loading	Output	Pre-loading	Output	Pre-loading	Output	Pre-loading	Output	Pre-loading	Output	Pre-loading	Output	Pre-loading	Output	Pre-loading	Output
PT	0	187.88	192.34	192.56	0	204.4	209.07	209.21	0	201.83	203.95	203.95	0	222.73	222.52	222.44	0	239.19	243.667969	243.78
LCL	0	0	0	0	0	0	0	0	0	0	0	0	0	0	0	0	0	0	0.15625	0
MCl	0	0	0	0	0	0	0	0	0	0	0	0	0	14.297	16.32	16.265	0	8.4999	13.6052031	13.692
PCL	0	0	0	0	0	0	0	0	0	0	0	0	0	0	0	0	0	0	0.15625	0
ACL	0	12	0.70349	0	0	16.636	5.3856	5.4899	0	20.807	24.45	24.655	0	24.72	35.741	36.166	0	17.601	23.7240938	23.831
PT % difference	/	/	/	0.1144	/	/	/	0.067	/	/	/	0	/	/	/	-0.036	/	/	/	0.046
LCL % difference	/	/	/	/	/	/	/	/	/	/	/	/	/	/	/	/	/	/	/	/
MCL % difference	/	/	/	/	/	/	/	/	/	/	/	/	/	/	/	-0.337	/	/	/	0.638
PCL % difference	/	/	/	/	/	/	/	/	/	/	/	/	/	/	/	/	/	/	/	/
ACL % difference	/	/	/	/	/	/		1.936	/	/	/	0.8384	/	/	/	1.1891	/	/	/	0.4506

Table 7. a) The model can always achieve convergence through the iterative calculation process, with Pre-load at 0N; b) The model can always achieve convergence through the iterative calculation process, with Pre-load at 100N; c) The model can always achieve convergence through the iterative calculation process, with Pre-load at 200N. Ligament and patellar-tendon tensions are reported in Newtons (N), and knee angle is reported in degrees (°).

In each frame of the model, the initial pre-tension applied to the ligaments and the patellar tendon (PT) is established at 0N (Table 7a). Subsequent adjustments yielded variations in tension of less than 1% after numerous iterations. These findings indicate that the models consistently achieve convergence through iterative computational processes.

In each frame of the model, the initial pre-tension applied to the ligaments, and the patellar tendon (PT) is established at 100N (Table 7b). Subsequent adjustments yielded variations in tension of less than 1% after numerous iterations. These findings indicate that the models consistently achieve convergence through iterative computational processes. Similar to Table 7(a), PT dominates (244.08N), with ACL and MCL patterns mirroring unloaded conditions, but initial preload accelerates convergence.

In each frame of the model, the initial pre-tension applied to the ligaments, and the patellar tendon (PT) is established at 200N (Table 7c). Subsequent adjustments yielded variations in tension of less than 1% after numerous iterations. These findings indicate that the models consistently achieve convergence through iterative computational processes. Convergence is robust, with final tensions nearly identical to lower preloads (e.g., PT at 244.09N in Frame 18), confirming the method's stability and potential for clinical application in predicting patient-specific ligament balance.

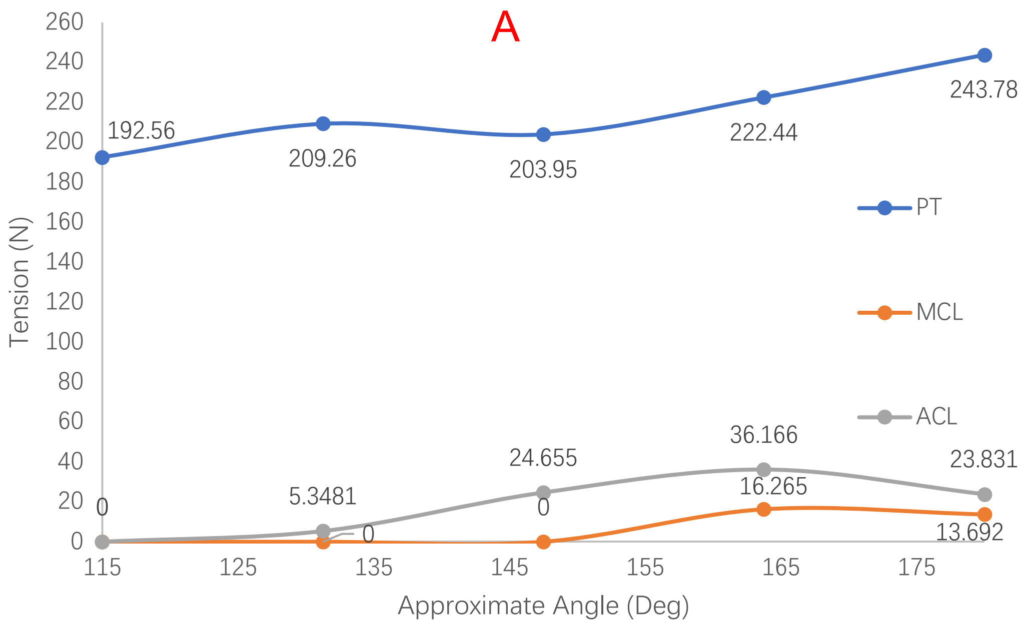
A
Tension (N)
Approximate Angle (Deg)
PT
MCL
ACL
192.56
209.26
203.95
222.44
243.78
0
5.3481
0
24.655
0
36.166
16.265
23.831
13.692

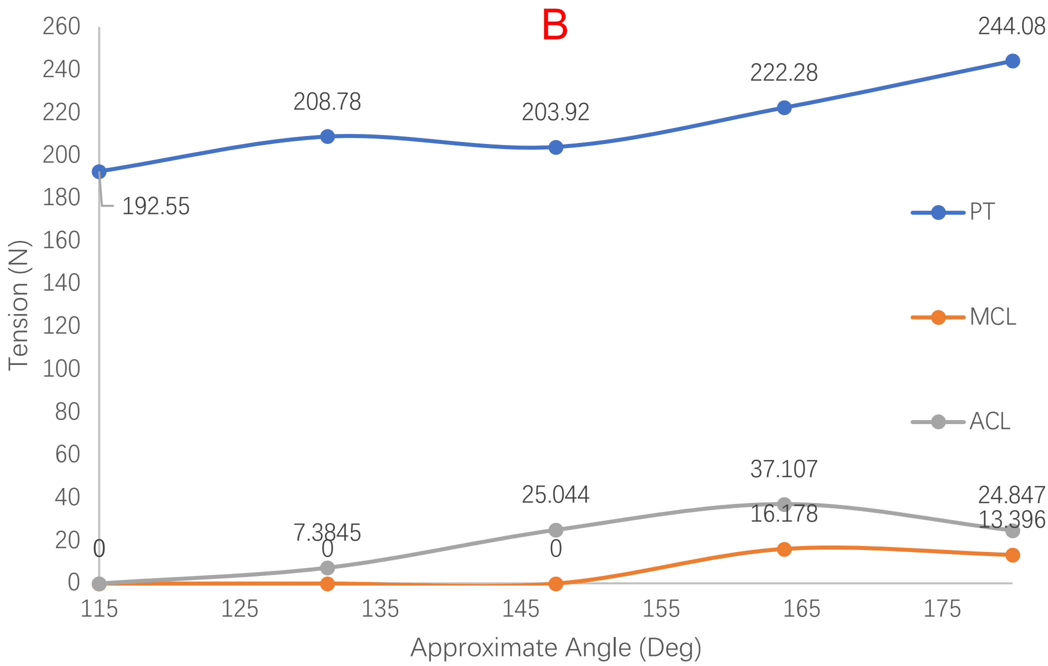
B
Tension (N)
Approximate Angle (Deg)
PT
MCL
ACL
192.55
208.78
203.92
222.28
244.08
0
7.3845
0
25.044
0
37.107
16.178
24.847
13.396

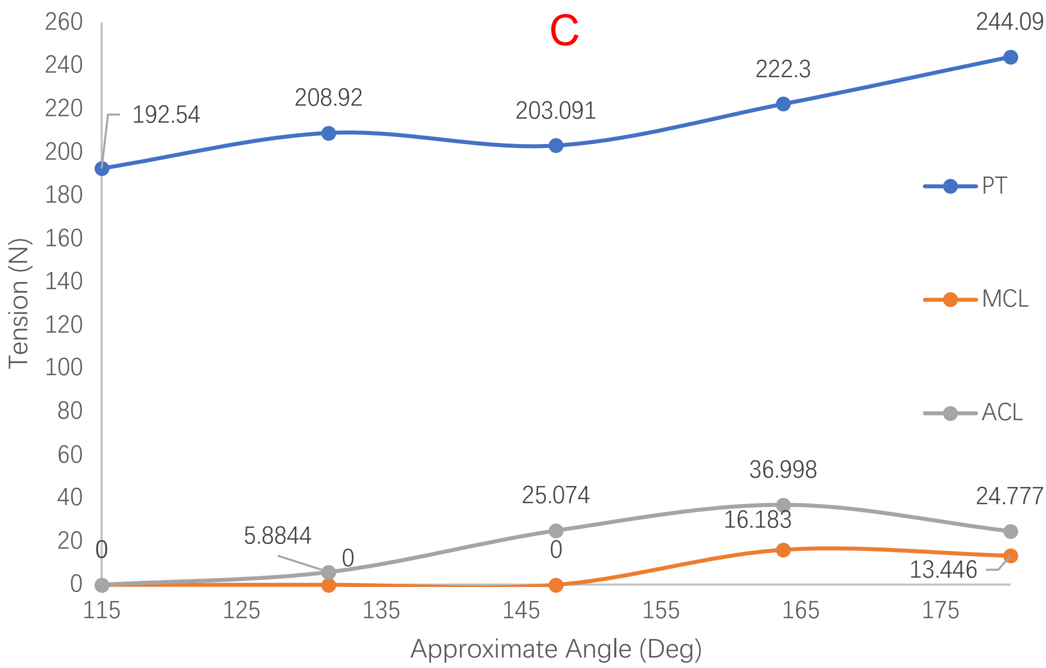

Figure 33. Ligament tension along the flexion curve has been systematically estimated under initial pre-tension (0N, 100N and 200N).

Figure 33 A.) Ligament tension along the flexion curve has been systematically estimated under initial pre-tension at 0N; B.) Ligament tension along the flexion curve has been systematically estimated under initial pre-tension at 100N; C.) Ligament tension along the flexion curve has been systematically estimated under initial pre-tension at 200N.

Figures 33 A, B and C show the converged ligament tensions as a function of estimated knee angle (180 degrees = full extension). The patella tendon, as expected, carries most load, with the ACL increasing in tension to 20 degrees of flexion and then decreases again towards full extension. The MCL has no tension until 35 degrees of flexion. There is a suggestion, again, that this ligament tension also peaks around 20 degrees of flexion. Comparing Figure 33 A, B and C, it is clear that these two converged solutions are effectively the same, irrespective of the initial tension.

20 degrees corresponds to the maximum knee flexion in the stance phase of gait and possibly the passive structures of the knee are so designed to maximise ACL tension at this point to assist the body in the weight acceptance phase.

Biomechanical Optimization of ACL Function at 20° Knee Flexion

During the weight acceptance phase of gait, the knee flexes to approximately 20°, a critical angle where passive anatomical structures synergistically maximize ACL tension to stabilize the joint.

At 20° flexion, the ACL's orientation aligns it to directly oppose anterior forces generated by ground reaction forces (GRFs) and quadriceps contraction. The quadriceps, acting through the patellar tendon, induces an anterior pull on the tibia, while GRFs exert a posteriorly directed femoral force. These combined vectors create a shear force that increases ACL tension, positioning the ligament as the dominant stabilizer against ATT.

The medial tibial spine and intercondylar notch guide femoral rollback, maintaining ACL tautness by preventing excessive anterior femoral displacement. At 20° flexion, the posterior cruciate ligament (PCL) becomes relatively lax, redistributing load-bearing responsibility to the ACL. This passive "handover" ensures the ACL bears peak tension when shear forces are highest during weight acceptance.

Studies demonstrate that ACL strain peaks between 10–20° flexion during dynamic tasks (Mizuno et al., 2009; Weinhandl et al., 2016) [254-255], coinciding with the angle of maximum GRF absorption in gait. This correlation reinforces the hypothesis that passive knee structures—particularly ACL orientation, bony geometry, and ligamentous interplay—are biomechanically optimized to exploit ACL tension at 20 degrees, ensuring efficient energy dissipation and joint stability during weight acceptance.

4.3 Secondary aim: comparison

4.3.1 Patella and femur tracking results

This section describes the procedure used to match the positions of the patella and femur between different frame-specific models (e.g., F02 and F06), such that the patellar displacement could be calculated manually from nodal coordinates and then applied in ANSYS as a remote displacement. Establishing this inter-frame alignment provides the kinematic input required to drive the knee model consistently across frames. Using this approach, the patella exhibits an average inter-frame displacement of 12 ± 1mm per tracked node, whereas the femur shows a smaller average displacement of 6 ± 1mm, indicating substantially less femoral motion over the same frame transitions. Given the comparatively small magnitude of femoral displacement and its limited influence on the subsequent analyses presented in this chapter, femoral motion is not discussed separately in the sections that follow; instead, subsequent results focus primarily on the patella- and tibia-related tracking outcomes.

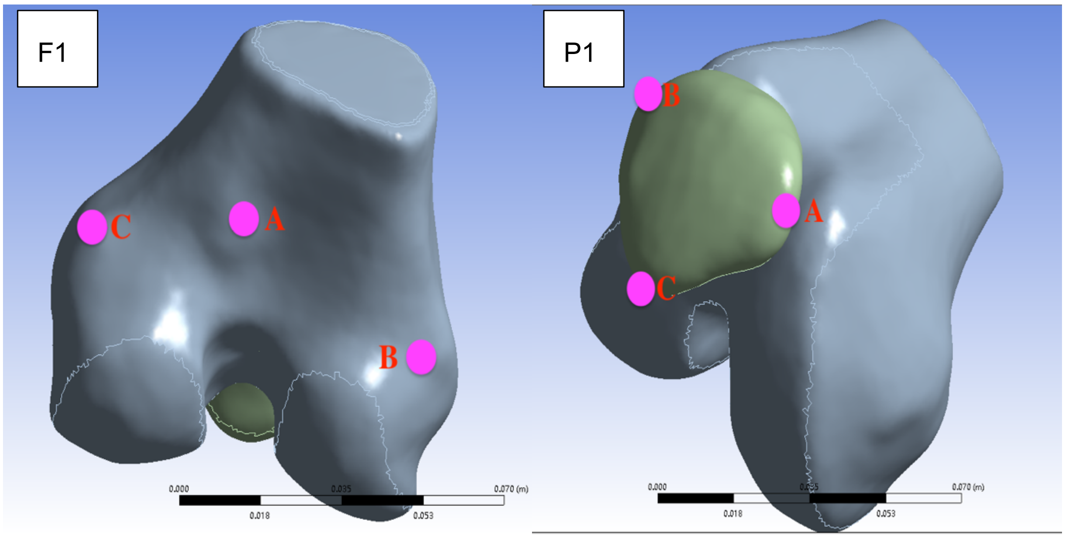

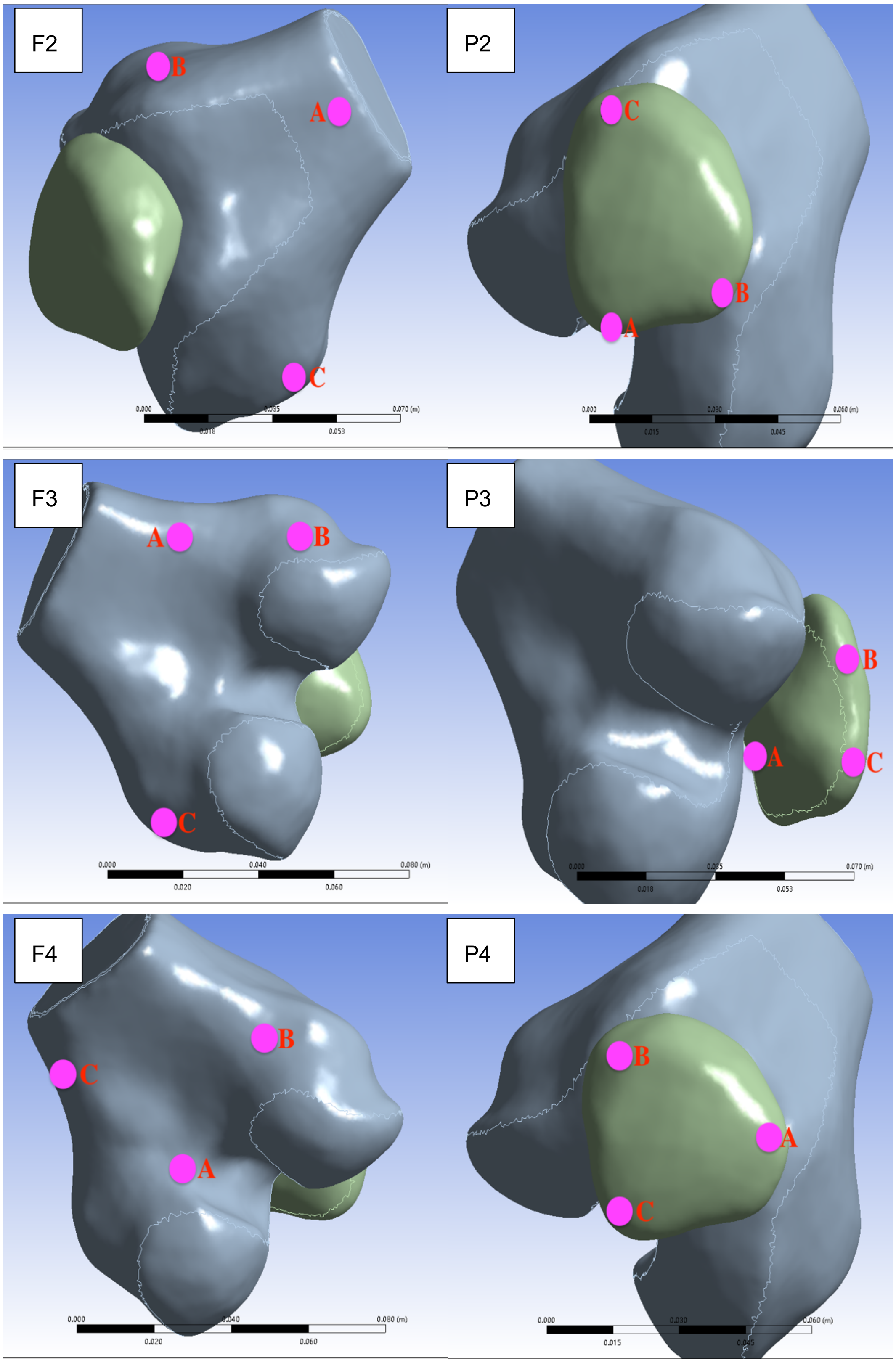

Figure 34. Definition of the femoral and patellar tracking node sets used to drive inter-frame alignment of the knee joint model in ANSYS (F1–P1 to F4–P4). Pink-highlighted regions indicate the selected mesh nodes and are presented in magnified views to clearly show the node locations.

The node sets shown in Figure 34 were applied to drive the knee joint model in ANSYS, enabling rigid-body alignment of the patella and distal femur between consecutive frames. Representative ANSYS renderings (Frame F02) illustrate the anatomical locations of the tracked node sets on the distal femur (grey) and patella (green). In the figure, F# denotes the femoral node set and P# denotes the corresponding patellar node set.

On the patella, three landmarks were defined and are referenced throughout the thesis as the medial border (Patella-MED), the lateral region (Patella-LAT), and the patellar apex (Patella-APEX). Node sets P1, P3, and P4 were selected on the anterior patellar surface. For these three sets, labels A, B, and C correspond to Patella-MED, Patella-LAT, and Patella-APEX, respectively. In contrast, node set P2 was defined on the posterior patellar surface, with the three points (A, B, and C) lying predominantly on the articular/posterior region. Accordingly, in P2, labels A, B, and C correspond to Patella-APEX, Patella-MED, and Patella-LAT, respectively.

On the femur, nodes were selected on anatomically distinct regions of the distal femur. In F1, label A is located on the distal popliteal surface (Femur-POP-DIST), B on the lateral epicondyle (Femur-LEPI), and C on the medial epicondyle (Femur-MEPI). In F2, B and C identify the lateral and medial epicondyles (Femur-LEPI and Femur-MEPI), while A marks the superior rim above the patellofemoral contact surface (Femur-TROCH-SUPRIM). In F3, B and C again denote the lateral and medial epicondyles, and A lies in the supracondylar region above the lateral condyle (Femur-LCOND-SUP). In F4, C lies on the popliteal surface in the proximal–medial region (Femur-POP-MED), while A and B are located superior to the medial and lateral condyles, respectively (Femur-MCOND-SUP and Femur-LCOND-SUP).

For traceability, the corresponding mesh node numbers for each node set, together with the inter-frame distances used as the remote displacement input to ANSYS, are reported in Appendix Tables A1–A4. Equivalent nodes were selected at Frames 06, 10, 14, and 18 to maintain the same anatomical correspondence as the landmarks illustrated here.

4.3.1.1 Repeat analysis

In knee joint finite element models, validating estimated ligament tensions requires precise and repeatable alignment of bony positions across frames. However, because each frame is generated independently, the meshes differ in node numbering and local surface discretisation. Therefore, a method is required to establish node correspondences between frames so that the same anatomical locations can be compared and used to compute displacement inputs.

To achieve this, a nearest-node approximation strategy was adopted to identify equivalent nodes across frames—i.e., nodes that represent the same anatomical landmark within a high-density mesh, despite differences in mesh topology. For example, a node in F02 can be paired with a node in F06 when the two nodes occupy nearly identical spatial locations on the corresponding anatomical surface; such a pair is then treated as an equivalent-node correspondence. The high mesh density facilitates reliable identification of these anatomically consistent locations and supports repeatable matching across alternative node sets.

The repeatability of the method is reflected by the consistency of the calculated Euclidean displacements obtained across different node-set selections, with mean values of approximately 0.012 m (12mm) for the patella and 0.006 m (6 mm) for the femur. These displacement vectors—computed from manu ally extracted nodal coordinates—were then applied in ANSYS to reproduce the patellar motion between frames. This patella–femur alignment subsequently provides the kinematic basis for driving the tibial displacement so that the tibia can be repositioned to match its corresponding location between frame-specific models (The inter-frame remote displacement components applied in ANSYS (X-, Y- and Z-directions) are provided in Appendix A1–A4 for completeness and traceability).

4.3.1.2 Patella matching error verification

This section reports the actual patellar displacement achieved after the remote displacement was applied and evaluates how accurately the driven patella matches its target position across the analysed frame pairs (F02–F06, F06–F10, F10–F14, and F14–F18). The verification focuses on the performance of the nodal coordinate–based driving method. Specifically, four alternative sets of driving nodes (P1–P4) were used to prescribe patellar motion, and the resulting (driven) patella position was assessed using three independent comparison nodes for each frame pair. These comparison nodes were not used to drive the motion; instead, they provide an objective measure of the residual positional mismatch between the driven configuration and the corresponding target frame.

For each frame, the three comparison nodes were selected to represent distinct anatomical regions of the patella (superior, medial, and lateral), thereby providing comprehensive spatial coverage for error assessment. Their X-, Y-, and Z-coordinates were extracted from the initial frame of each pair (frame i; e.g., F02 for the F02–F06 transition) and compared with the coordinates obtained after the patella had been driven towards the subsequent frame. In the global coordinate system used in this study, Y corresponds to the anterior–posterior (AP) axis, X to the medial–lateral (ML) axis, and Z to the superior–inferior (SI) axis. Accordingly, this analysis captures the realised inter-frame patellar translation along anatomically meaningful directions and quantifies any remaining discrepancies attributable to the driving procedure, thereby providing a direct verification of patellar alignment accuracy.

Before presenting the results, it is essential to clearly define all tracked nodes and their correspondence across frames. This section therefore documents the anatomical location of each tracking point and provides an explicit mapping between the mesh node identifiers and the standardised landmark labels used throughout the thesis. Establishing this information at the outset ensures that subsequent displacement, error, and trajectory results can be interpreted in anatomically meaningful terms, rather than as arbitrary node numbers, while maintaining full mesh-level traceability. Accordingly, anatomically representative equivalent nodes were selected on the patella and proximal tibia and labelled using a consistent nomenclature (Patella-SUP/MED/LAT and Tibia-ANT/LAT/MED). These definitions and node-to-landmark correspondences provide a transparent and reproducible reference framework for the results presented in the following sections.

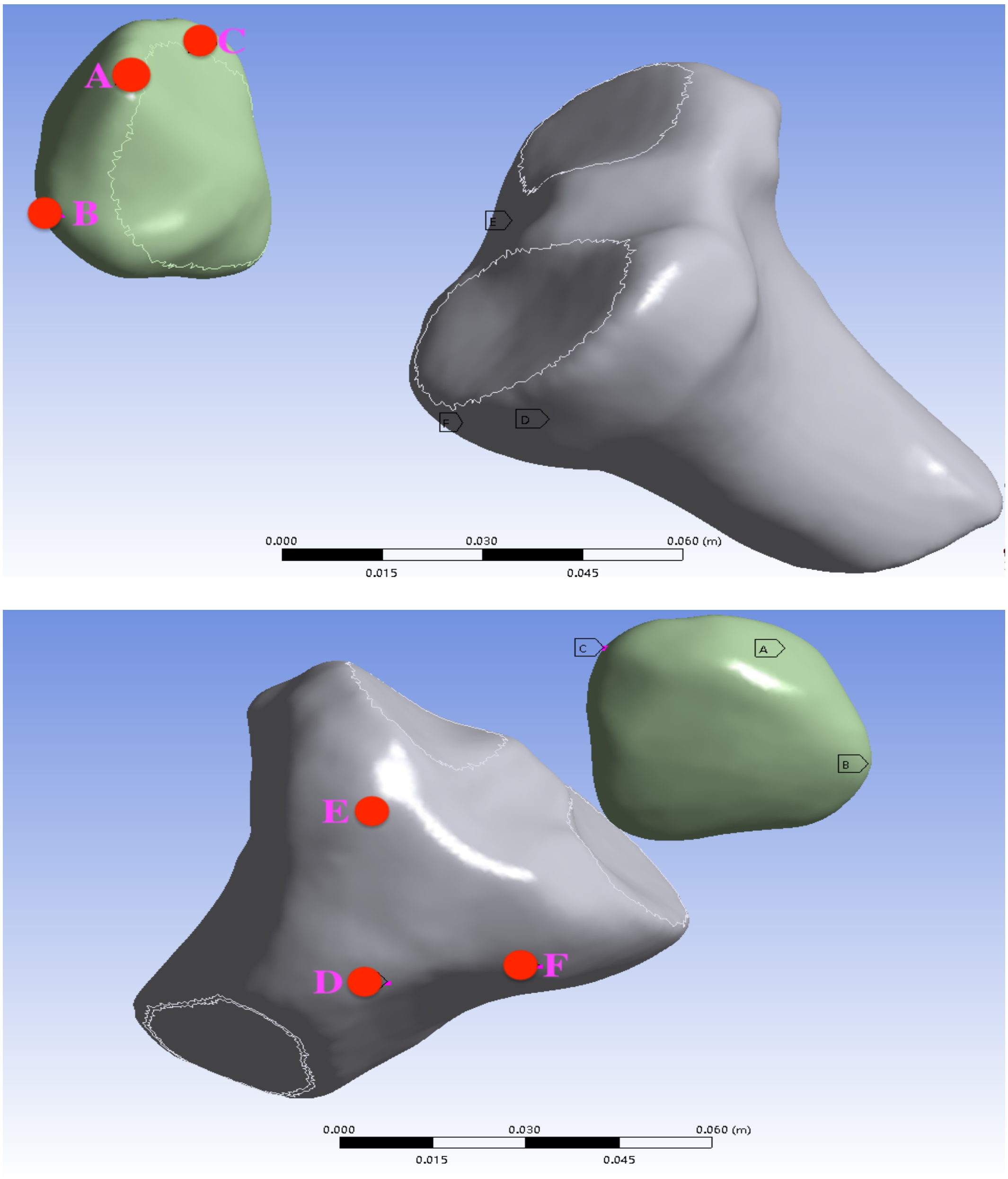

Figure 35. Example from Frame 06: anatomical locations of the tracked equivalent landmarks on the patella and tibia. Red-highlighted regions indicate the selected mesh nodes and are shown in magnified views to provide a clearer illustration of the node locations.

Three equivalent anatomical landmarks were defined on the patella (A–C) and three on the proximal tibia (D–F) to support landmark-based kinematic tracking and subsequent validation (As shown in Figure 35.). On the patella, A (Patella-SUP) represents a superior patellar articular landmark located on the posterior surface at the superior base, immediately proximal to the median vertical ridge (patellar crest). B (Patella-MED) corresponds to a medial patellar articular landmark on the medial border, whereas C (Patella-LAT) denotes a lateral patellar articular landmark on the lateral border. On the tibia, D–F represent three anatomically meaningful proximal tibial landmarks (Tibia-ANT, Tibia-LAT, and Tibia-MED, respectively); these tibial landmark definitions are described in detail in Section 4.3.2.

Crucially, the landmark nodes defined here constitute a separate, independent landmark set, selected specifically for tracking/verification and independent of the previously established frame-matching node sets used to align meshes between frames. For each landmark label (Patella-SUP, Patella-MED, Patella-LAT, and D–F on the tibia), frame-specific surface nodes were chosen to represent the same anatomical locations throughout the motion sequence. Although mesh topology and node numbering vary between frames, the selected points were maintained as anatomically equivalent. This independent landmark set was applied consistently across all frames from F02 to F18, providing a dedicated set of equivalent validation nodes for assessing landmark-based kinematic tracking across the full flexion–extension range

Using the tracked patellar landmark coordinate data, the inter-frame displacements in the medial–lateral (ML, X), anterior–posterior (AP, Y), and superior–inferior (SI, Z) directions were manually calculated for each landmark. Full details of the calculation procedure and the resulting values are provided in Appendix B1–B4. For visual interpretation of inter-frame kinematics, the landmark motion is presented as three-dimensional trajectories in the global coordinate system (Figure 36) and as two-dimensional planar projections in the sagittal (Y–Z) and coronal (X–Z) planes (Figure 37). These plots complement the Euclidean error metrics by illustrating both the direction and the relative magnitude of landmark motion across the flexion sequence.

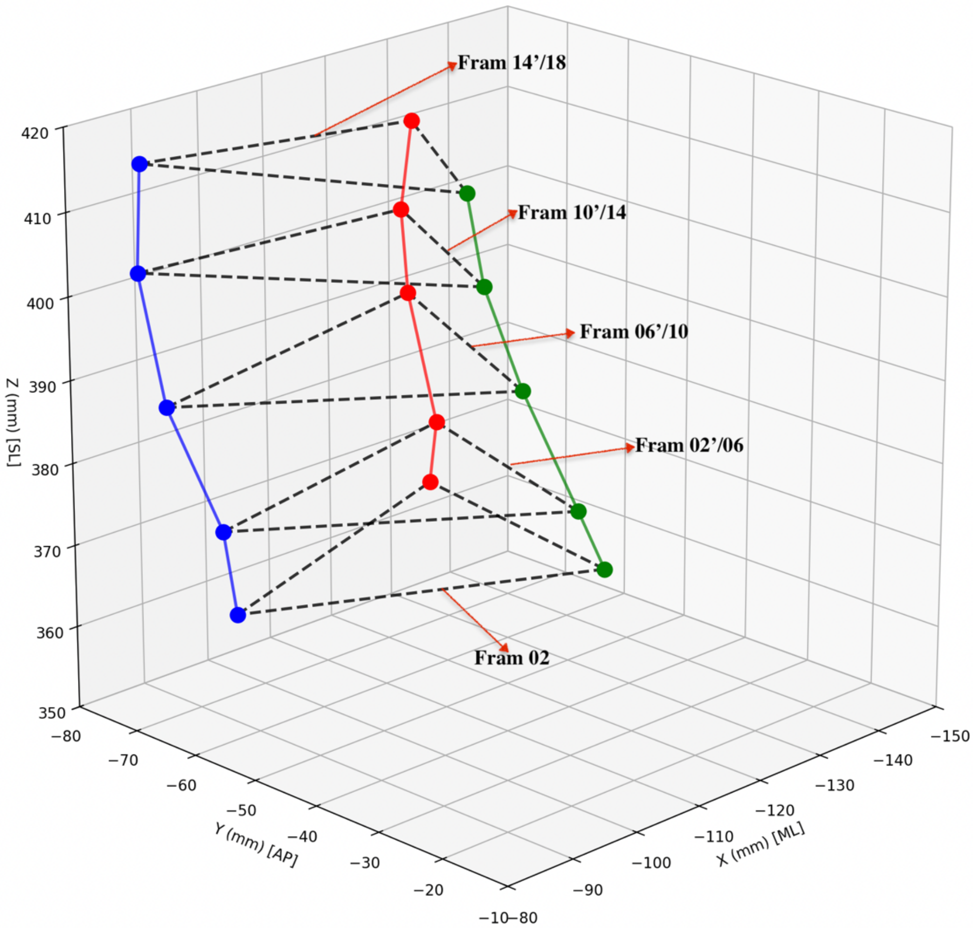

Figure 36. Patella 3D motion trajectories across all frames (F02–F18). Three-dimensional trajectories of the tracked patellar landmarks Patella-LAT (green), Patella-MED (blue), and Patella-SUP (red) are plotted in the global coordinate system (X: mediolateral, ML; Y: anteroposterior, AP; Z: superoinferior, SI;). Solid lines connect the same landmark between consecutive frames to visualise frame-to-frame displacement throughout the extension sequence (≈65° flexion at F02 to 0° at F18). Dashed lines link the three landmarks within each frame, illustrating the instantaneous triangular configuration of the patella and its evolution across the motion cycle. The annotated inter-frame tracking intervals (e.g., F02′/06) denote the displacement-driving step that maps the patellar configuration from F02 to F06; similarly, F06′/10, F10′/14, and F14′/18 represent the corresponding driving displacements from F06 to F10, F10 to F14, and F14 to F18. These interval-specific displacements were used as inputs for subsequent model alignment and FE-driven analyses. (Units: mm)

Figure 36 summaries the patellar landmark kinematics across the full extension sequence (F02 to F18). The 3D plot visualises the tracked trajectories of Patella-SUP (red), Patella-MED (blue), and Patella-LAT (green) in the global coordinate system (X-ML, Y-AP, Z-SI). Solid line segments join the same landmark across frames, while the dashed interconnecting segments illustrate the instantaneous triangular configuration of the three landmarks at each frame, providing an intuitive view of both translation and the preservation of landmark geometry over time.

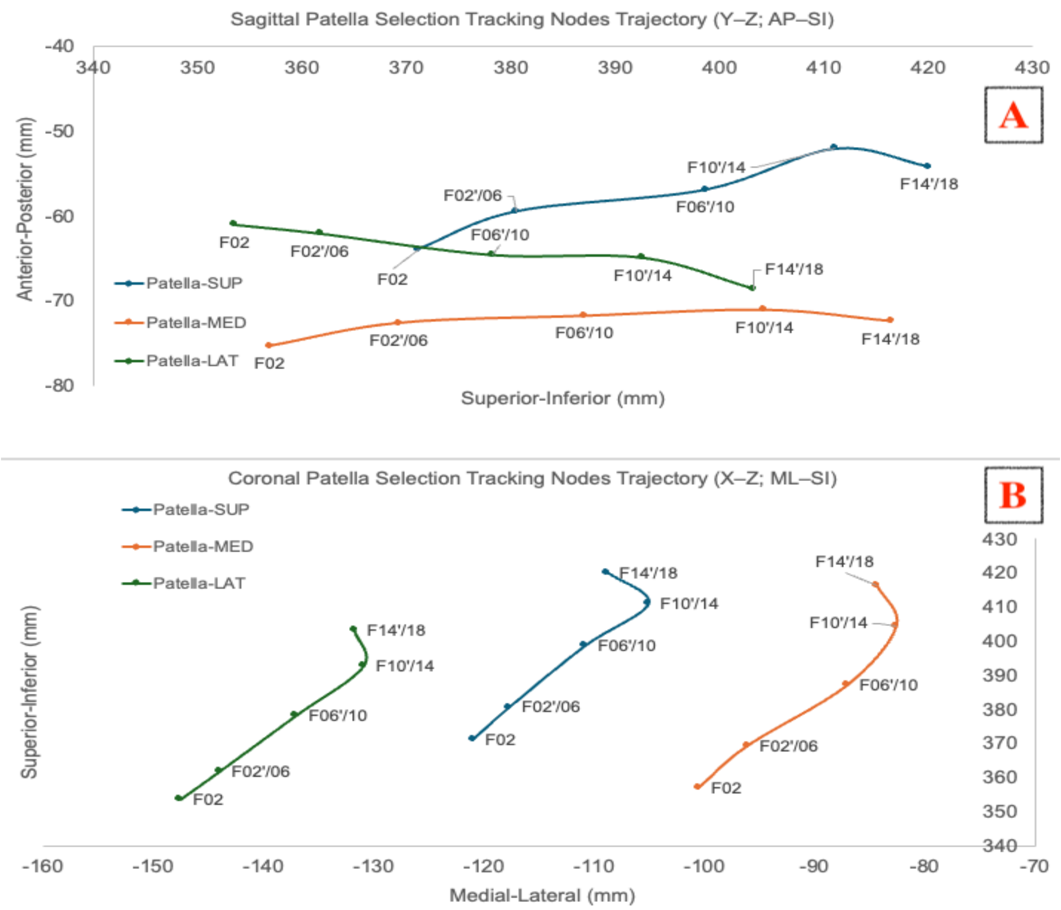

Figure 37. Two-dimensional sagittal- and coronal-plane projections of patellar landmark trajectories. This figure shows the patellar landmark motion obtained from 3D tracking, projected onto the 2D sagittal and 2D coronal planes to visualise the dominant in-plane displacement patterns during knee extension. (A) 2D sagittal-plane (Y–Z) projection: AP (mm) versus SI (mm) trajectories for Patella-SUP (blue), Patella-MED (orange), and Patella-LAT (green). (B) 2D coronal-plane (X–Z) projection: ML (mm) versus SI (mm) trajectories for the same three patellar landmarks (units: mm).

In the sagittal plane (Y–Z; AP versus SI, as shown in Figure. 37 (A)), all three landmarks translate superiorly as the knee extends from ~65° (F02) towards 0° (F18), consistent with the monotonic increase in SI (Z) reported in Table 8. The accompanying AP behavior is landmark-dependent. Patella-SUP exhibits a pronounced anterior shift (i.e., AP becoming less posterior/less negative) through most of the extension pathway, reaching its most anterior position around mid-to-late extension (approximately F10/14), followed by a small return towards posterior translation in the final interval (F14/18). Patella-MED shows comparatively limited AP excursion, with its trajectory dominated by superior translation and only minor AP variation. By contrast, Patella-LAT demonstrates a progressive posterior shift across the sequence (increasing posterior translation), indicating a posterior displacement component that becomes more evident towards terminal extension.

The coronal-plane representation (X–Z; ML versus SI, as shown in Figure. 37 (B)) likewise confirms a consistent superior translation for all three landmarks and shows that the relative ML ordering is maintained throughout the motion: Patella-LAT remains the most lateral, Patella-MED the most medial, and Patella-SUP intermediate. In addition, the trajectories indicate an interval-dependent ML adjustment that mirrors Table 8: a reduction in lateral displacement through mid-to-late extension (up to approximately F10/14), followed by a modest increase in lateral displacement near terminal extension (F14/18). Overall, the smooth, continuous trajectories and the consistent frame-wise landmark configuration (as indicated by the dashed connections) support systematic and repeatable tracking across the extension cycle, with ML changes occurring in a more stage-dependent manner than the largely monotonic superior progression.

Frames	Landmark	Mean difference (mm)			± Standard deviation (mm)		
		Medial–lateral (ML-X)	Anterior–posterior (AP-Y)	Superior–inferior (SI-Z)	Medial–lateral (ML-X)	Anterior–posterior (AP-Y)	Superior–inferior (SI-Z)
F02/06	Patella-SUP	-117.7436	-59.4344	380.6127	1.5041	0.3362	0.6392
	Patella-MED	-96.1389	-72.5913	369.2795	1.2303	0.6181	1.6652
	Patella-LAT	-144.0453	-62.0488	361.7280	0.8875	0.1549	0.3306
F06/10	Patella-SUP	-110.8412	-56.8756	398.6773	1.9682	3.8496	1.0822
	Patella-MED	-87.0894	-71.7541	387.0778	1.6312	3.8665	1.7597
	Patella-LAT	-137.0709	-64.5853	378.2210	1.2487	1.2840	1.0225
F10/14	Patella-SUP	-105.1522	-51.9988	411.0345	1.1101	1.4208	0.8080
	Patella-MED	-82.6286	-71.0521	404.3378	0.5028	1.6052	1.0321
	Patella-LAT	-130.9520	-64.9074	392.6795	0.5844	0.5028	0.6554
F14/18	Patella-SUP	-108.9035	-54.1479	420.0958	1.2826	1.0306	0.3425
	Patella-MED	-84.4061	-72.3788	416.4303	0.6639	0.5716	0.4426
	Patella-LAT	-131.7713	-68.5660	403.2110	0.1980	0.6403	1.7784

Table 8. Segment-wise mean inter-frame coordinate differences for the tracked patellar landmarks. For each tracking segment (F02–06, F06–10, F10–14, and F14–18), the mean translational differences and corresponding standard deviations are reported along the medial–lateral (ML–X), anterior–posterior (AP–Y), and superior–inferior (SI–Z) directions for Patella-SUP, Patella-MED, and Patella-LAT. All values are in millimetres (mm).

Table 8 summarises the mean differences (mm) and associated standard deviations (±SD, mm) for three patellar tracking landmarks (Patella-SUP, Patella-MED, Patella-LAT) across four adjacent frame intervals (F02/06, F06/10, F10/14, F14/18) in the global medial–lateral (ML-X), anterior–posterior (AP-Y) and superior–inferior (SI-Z) directions. Importantly, frames F02 to F18 span the knee motion from approximately 65° flexion to full extension (0°); therefore, the reported interval-wise differences describe how the patellar landmarks evolve progressively during extension.

The variability (±SD) is generally low, supporting good repeatability of the estimated differences across the extension sequence. Most SD values remain within ~0.2–2.0 mm for ML-X and ~0.3–1.8 mm for SI-Z. A notable exception occurs in the F06/10 interval, where AP-Y variability increases for Patella-SUP (SD = 3.85 mm) and Patella-MED (SD = 3.87 mm), suggesting that, during this mid-range portion of extension, the AP component is more variable for these landmarks. In the terminal interval (F14/18), Patella-LAT shows particularly low ML-X dispersion (SD = 0.20 mm) but a higher SI-Z dispersion (SD = 1.78 mm), indicating direction-specific variability near full extension.

To complement the ML/AP/SI component differences, overall tracking accuracy was assessed using the Euclidean distance. Table 9 summarises the mean ± SD Euclidean displacement errors (mm) for each node-set combination, while Figure 38 shows how these errors evolve for Patella-SUP/MED/LAT across F02–F18. For comparison, Figure 39 presents average Euclidean error trends for grouped tibial nodes across Frames F02–F14, highlighting region-dependent tracking accuracy (mm).

Units: mm	P1	P2	P3	P4
Patella-SUP	2.624	1.921	1.592	2.329
Patella-MED	1.02	4.262	4.385	5.586
Patella-LAT	1.689	1.481	1.583	1.784
Ave.	1.778	2.555	2.52	3.233
S. deviation	0.805	1.495	1.615	2.056
Patella-SUP	1.986	3.92	9.268	8.45
Patella-MED	3.493	6.202	4.09	3.24
Patella-LAT	1.965	2.364	3.523	3.251
Ave.	2.481	4.162	5.627	4.98
S. deviation	0.877	1.931	3.166	3.005
Patella-SUP	2.628	2.749	4.431	1.725
Patella-MED	2.51	1.552	2.654	2.75
Patella-LAT	1.078	1.434	0.482	0.848
Ave.	2.072	1.912	2.522	1.775
S. deviation	0.863	0.728	1.978	0.952
Patella-SUP	2.194	1.991	2.842	3.383
Patella-MED	3.794	5.232	3.944	4.644
Patella-LAT	0.75	1.559	2.266	2.213
Ave.	2.246	2.927	3.017	3.413
S. deviation	1.523	2.008	0.852	1.215

Table 9. Set of nodes Euclidean displacement error, average and standard deviation results. (Units: mm)

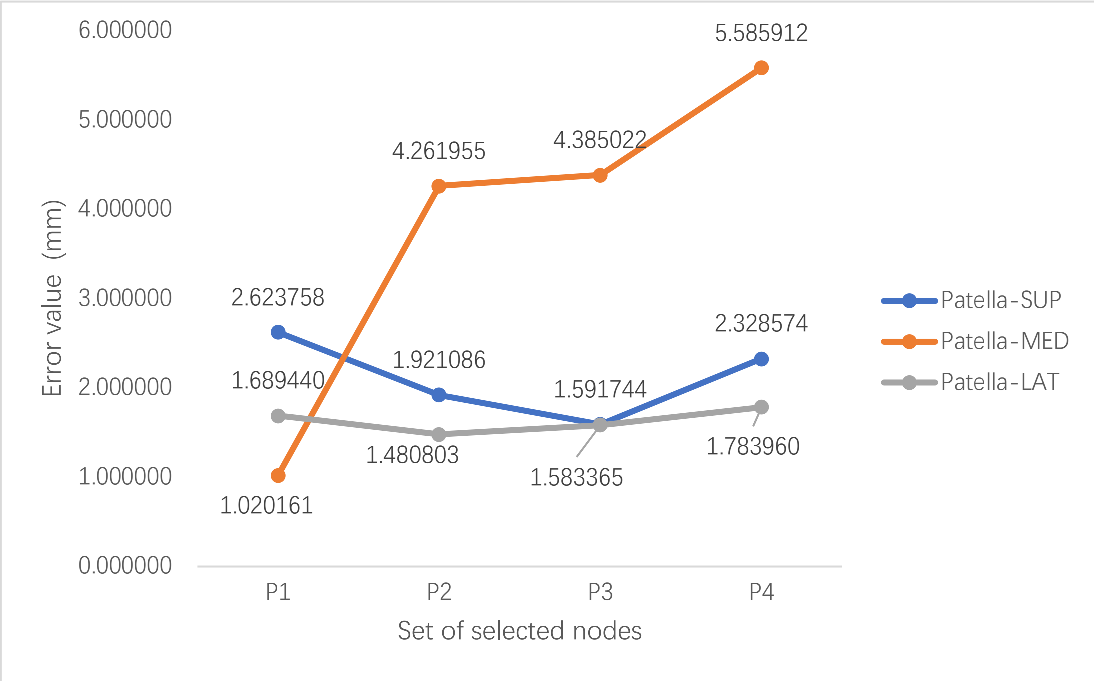
6.000000
5.000000
4.000000
3.000000
2.000000
1.000000
0.000000
Error value (mm)
5.585912
4.261955
4.385022
2.623758
2.328574
1.921086
1.689440
1.591744
1.480803
1.583365
1.783960
1.020161
P1
P2
P3
P4
Set of selected nodes
Patella-SUP
Patella-MED
Patella-LAT

a.

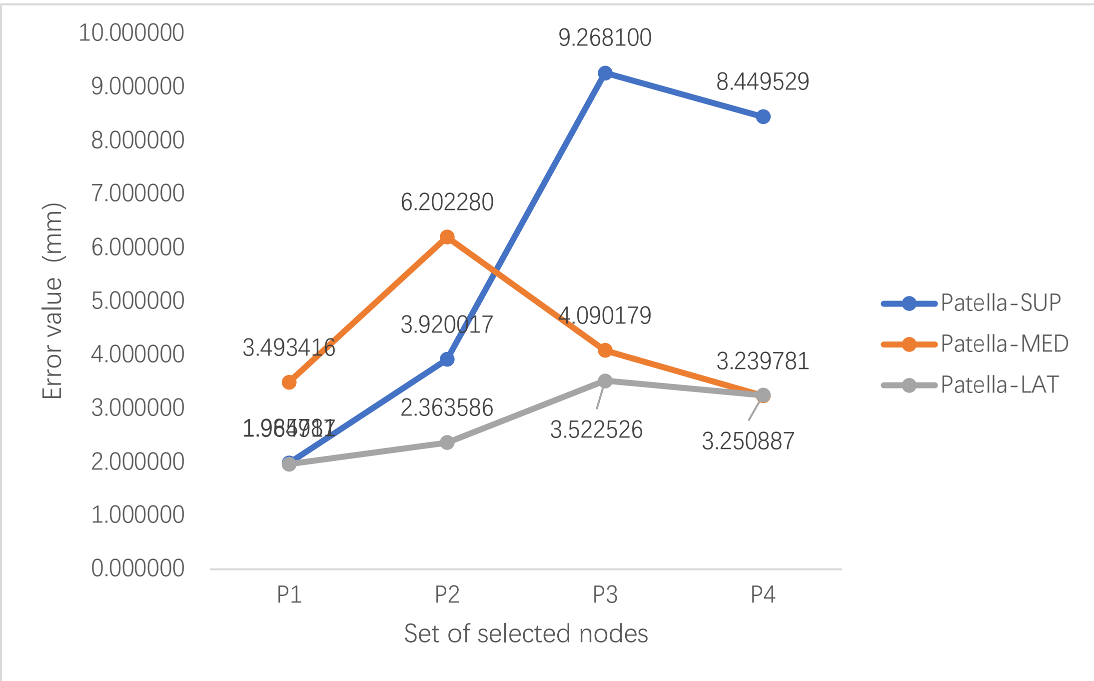
10.000000
9.000000
8.000000
7.000000
6.000000
5.000000
4.000000
3.000000
2.000000
1.000000
0.000000
Error value (mm)
9.268100
8.449529
6.202280
3.493416
3.920017
4.090179
3.239781
2.363586
3.522526
3.250887
P1
P2
P3
P4
Set of selected nodes
Patella-SUP
Patella-MED
Patella-LAT

b.

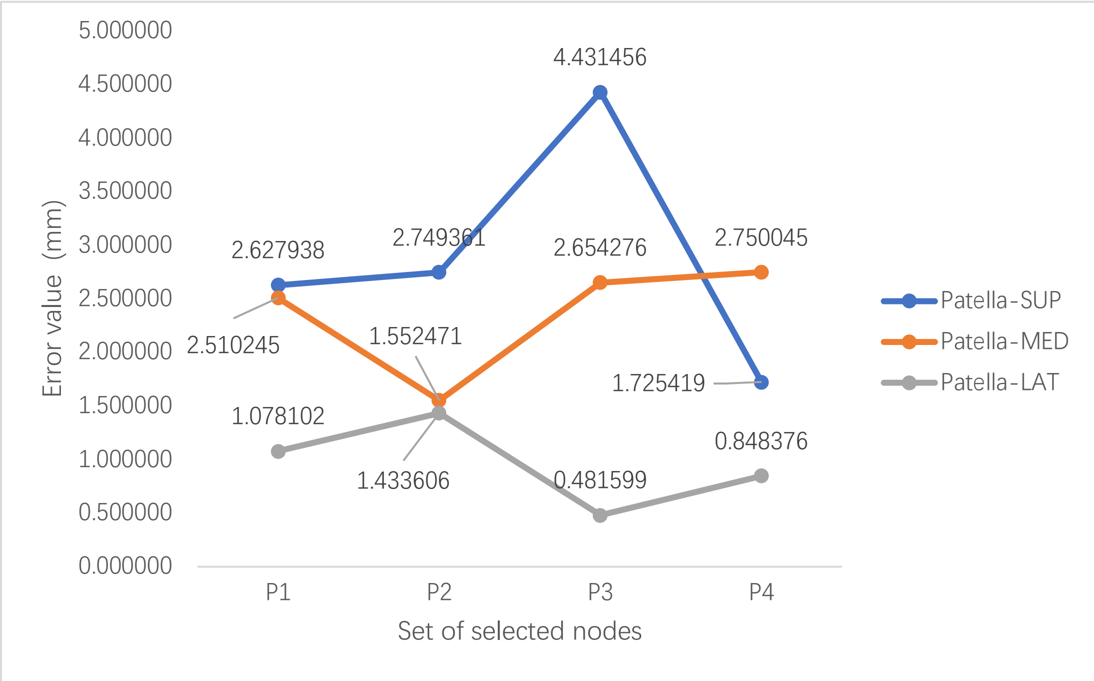

c.

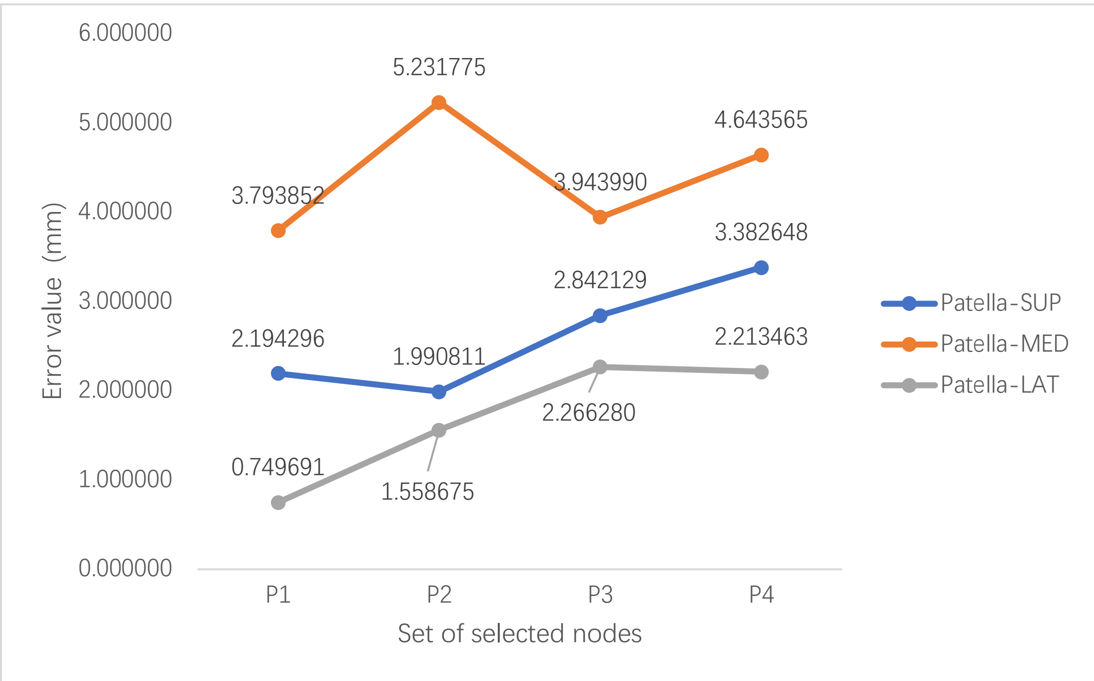

d.

Figure 38. Euclidean distance trends for the tracked patellar landmarks across the flexion–extension sequence (F02–F18). Curves show the Euclidean discrepancy between finite element model–predicted landmark positions and the corresponding locations from the 4dCT-

derived reference geometry, reported for the anatomically defined landmarks Patella-SUP, Patella-MED, and Patella-LAT (maintained as equivalent anatomical locations across frames). Panel (a) shows the F02–F06 transition, (b) F06–F10, (c) F10–F14, and (d) F14–F18. (Units: mm)

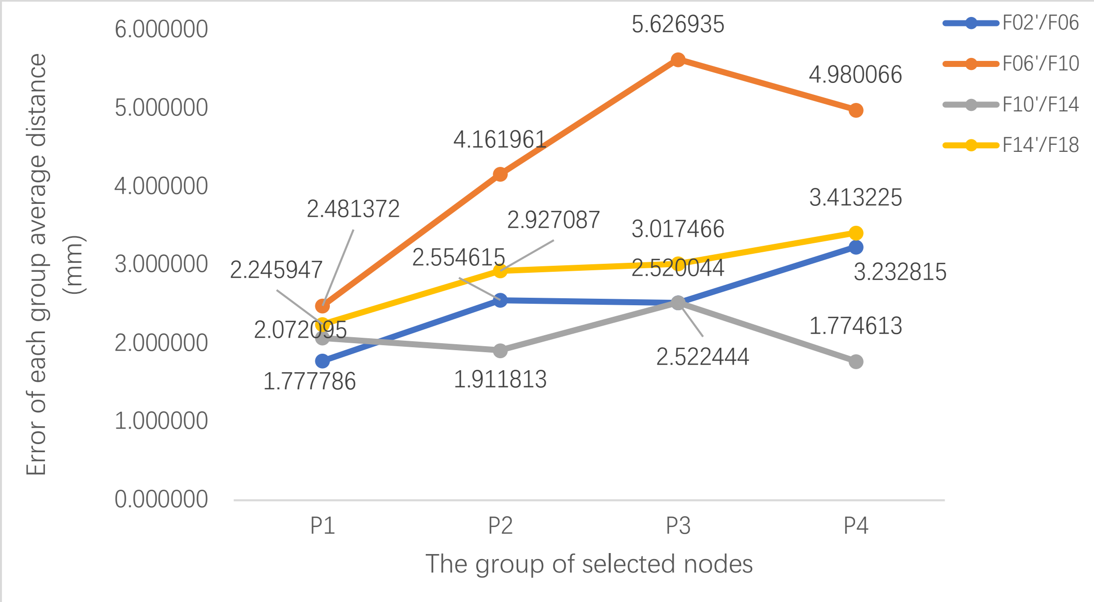

Figure 39. Average Euclidean distance trends for grouped tibial nodes across flexion Frames 02–14. The figure shows mean displacement errors for each predefined node group, providing a summary measure of tibial tracking performance and highlighting differences in positional accuracy among anatomical regions. (Units: mm).

The results indicate that most patellar matching errors are small, typically ranging from 1 to 9 mm. Overall, these values suggest that the nodal coordinate driving method can align the patella between frames with reasonable precision, although the accuracy is sensitive to the choice of driving landmark set (P1–P4).

Frame 02: Mean errors range from 1.778 mm (P1) to 3.233 mm (P4), with standard deviations of 0.805–2.056 mm, indicating modest variability across the comparison landmarks (Patella-SUP / Patella-MED / Patella-LAT).

Frame 06: Errors are higher overall, with a maximum error of 9.268 mm observed for Patella-SUP under the P3 driving set. Mean errors span 2.481 mm (P1) to 5.627 mm (P3).

Frames 10 and 14: Errors remain low, with mean values of approximately 1.775–3.413 mm, and in some cases tighter dispersion (e.g., 0.728 mm standard deviation for P2 in Frame 10) across the three anatomical verification landmarks.

Across frames, P1 frequently produces the lowest mean errors (e.g., 1.778 mm in Frame 02 and 2.072 mm in Frame 10), highlighting that alignment accuracy is influenced by the selected driving landmark set. Nevertheless, occasional outliers—such as the 9.268 mm discrepancy at Patella-SUP in Frame 06—suggest that frame-specific motion complexity and/or landmark selection challenges can lead to localised inconsistencies in the driven patellar alignment.

4.3.2 Tibia tracking results

Tibial tracking was done in two ways: using direct analysis of a few node positions and also by analysing point clouds using CloudCompare™. This dual approach provides both localized (node) and global (cloud) validation, enhancing confidence in tibial kinematics. It is worth noting that, in this section, the CloudCompare/ANSYS output reports distances in metres; for example, 0.01 m is equivalent to 10 mm.

4.3.2.1 Tibia position analysis using direct node analysis

To enable a comprehensive and precise comparison of tibial displacement variables across different simulation scenarios, three nodes were selected at key anatomical locations on the proximal tibia within each simulation group. These landmarks form the basis of the displacement reference system and ensure that tibial motion is evaluated in a consistent, repeatable, and directly comparable manner across all model configurations, thereby strengthening the rigour of the analysis.

Following the tracking and validation workflow described in Section 4.3.1.2, the tibia was analysed using three anatomically defined landmarks: Tibia-ANT (anterior tibial plateau margin), Tibia-LAT (lateral tibial plateau peripheral/articular region), and Tibia-MED (medial tibial plateau peripheral/articular region). For each frame-to-frame comparison, these landmarks were identified on the surface mesh of both frames as anatomically equivalent points. Although node numbering varies between frame-specific meshes due to topology changes, the selected nodes represent the same anatomical locations, enabling robust displacement comparisons between frames.

For the Frame 02–06 comparison, Tibia-ANT/LAT/MED were defined on both meshes to support direct positional evaluation. The same landmark-mapping procedure was then applied consistently to subsequent transitions (Frame 06–10, Frame 10–14, and Frame 14–18). In each case, Tibia-ANT, Tibia-LAT, and Tibia-MED were re-identified as anatomically equivalent nodes on the two frame-specific meshes, providing a continuous and traceable basis for tibial displacement assessment across the full motion sequence from F02 to F18. Importantly, this tibial landmark set is used here within the independent tracking/validation framework (Section 4.3.1.2), ensuring that displacement trends observed across simulation groups reflect genuine biomechanical behaviour rather than inconsistencies in landmark identification or mesh-dependent node numbering.

Using the coordinate data of the tracked tibial landmarks defined above, the inter-frame displacements of each landmark were manually calculated along the global mediolateral (ML, X), anteroposterior (AP, Y), and superoinferior (SI, Z) directions. Full details of the calculation procedure and the corresponding results are reported in Appendix B4–B7 to ensure transparency and traceability.

To complement these component-wise displacement comparisons and to aid interpretation of tibial kinematics, landmark motion is additionally visualised as trajectory plots. The overall tibial landmark motion is first summarised as three-dimensional trajectories across all frames (F02–F18) in the global coordinate system (Figure 40; X–ML, Y–AP, Z–SI; mm). For direct interpretation in clinically meaningful anatomical planes, the same landmark motion is also presented as two-dimensional planar projections in the sagittal (Y–Z) and coronal (X–Z) planes (Figure 41). Together, these visualisations provide a clear representation of both the direction and the relative magnitude of landmark motion across the flexion–extension sequence.

Building on this framework, Figure 40 depicts three-dimensional trajectories in which solid lines connect each landmark between consecutive frames to show stepwise displacement from approximately 65° flexion at F02 to 0° at F18, while dashed lines link the three landmarks within each frame to illustrate the instantaneous triangular configuration and its evolution throughout the motion cycle.

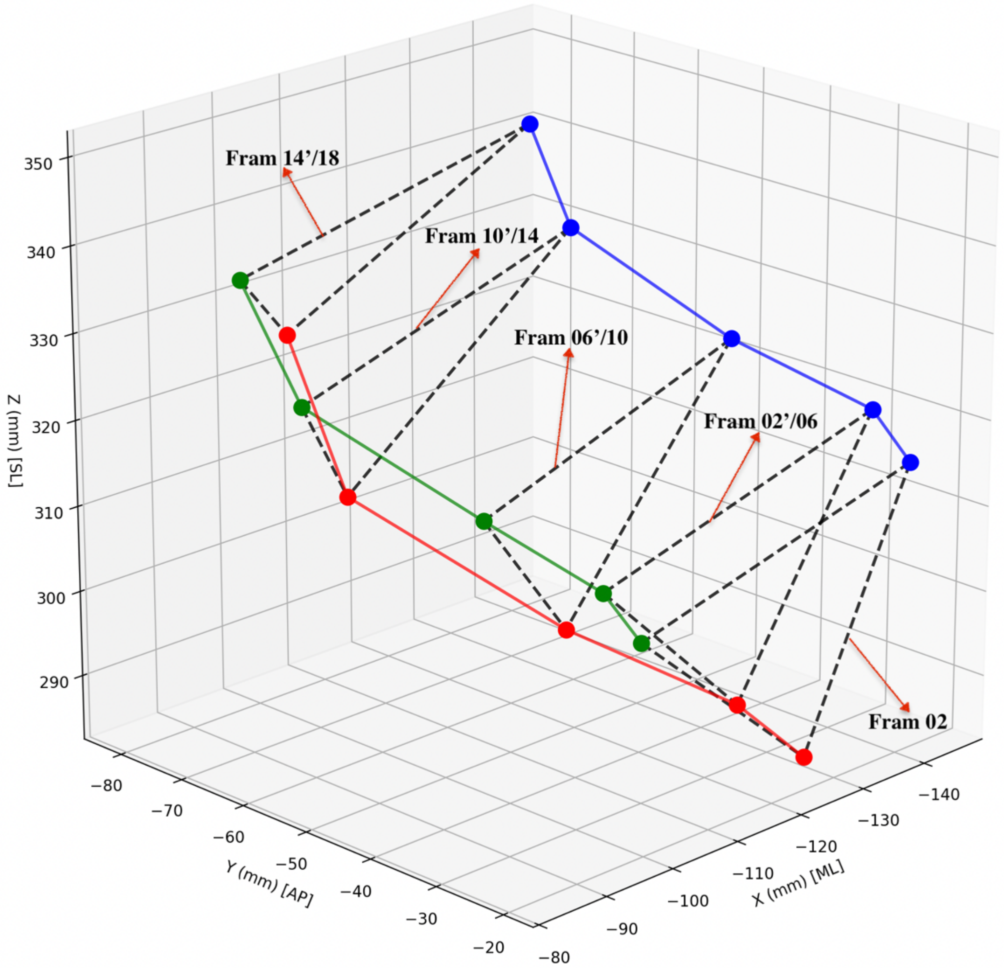

Figure 40. Tibia 3D motion trajectories across all frames (F02–F18). Three-dimensional trajectories of the tracked tibial landmarks Tibia-LAT (blue), Tibia-MED (green), and Tibia-ANT (red) are plotted in the global coordinate system (X: mediolateral, ML; Y: anteroposterior, AP; Z: superoinferior, SI; mm). Solid lines connect the same landmark between consecutive frames to visualise frame-to-frame displacement throughout the extension sequence (≈65° flexion at F02 to 0° at F18). Dashed lines link the three landmarks within each frame, illustrating the instantaneous triangular configuration and its evolution across the motion cycle. The annotated inter-frame tracking intervals (e.g., F02′/06) denote the displacement-driving step that maps the tibial configuration from frame F02 to frame F06; similarly, F06′/10, F10′/14, and F14′/18

represent the corresponding driving displacements from F06 to F10, F10 to F14, and F14 to F18, respectively. These interval-specific displacements were used as inputs for subsequent model alignment and FE-driven analyses.

Figure 40 summarises the tibial landmark kinematics across the full extension sequence (F02 to F18) using a 3D trajectory representation in the global coordinate system (X-ML, Y-AP, Z-SI; mm). The trajectories of Tibia-LAT (blue), Tibia-MED (green), and Tibia-ANT (red) are shown as solid line segments connecting consecutive frames, while the dashed connections indicate the instantaneous triangular configuration formed by the three landmarks at each frame, providing a visual check of geometric consistency throughout the motion.

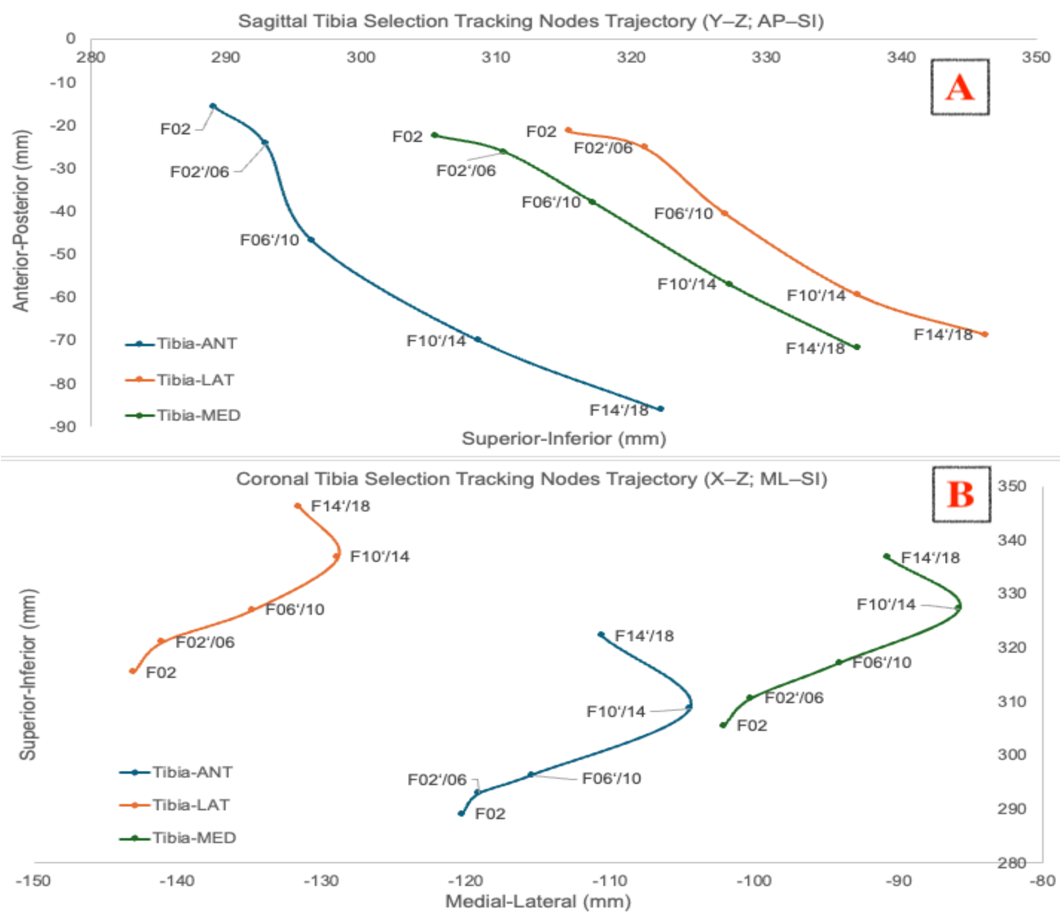

Figure 41. Two-dimensional sagittal- and coronal-plane projections of tibial landmark trajectories. This figure presents the tibial landmark motion obtained from 3D tracking, projected onto the 2D sagittal and coronal planes to visualise the dominant in-plane displacement patterns during

knee extension. (A) 2D sagittal-plane (Y–Z) projection: AP (mm) versus SI (mm) trajectories for Tibia-ANT (blue), Tibia-LAT (orange), and Tibia-MED (green). (B) 2D coronal-plane (X–Z) projection: ML (mm) versus SI (mm) trajectories for the same three tibial landmarks (units: mm).

In the sagittal-plane projection (Y–Z; AP versus SI, as shown in Figure 41 (A)), all three landmarks follow a consistent coupled pattern during extension from ~65° (F02) to ~0° (F18): superior translation increases monotonically (SI increases), accompanied by a progressive posterior shift (AP becomes more negative). This produces smooth, continuous trajectories in the AP–SI projection and is consistent with the monotonic trends reported in Table 10, indicating a coherent posterior–superior coupling of tibial motion during extension. Among the landmarks, Tibia-ANT exhibits the largest posterior excursion (approximately −24.36 mm to −86.18 mm), whereas Tibia-LAT and Tibia-MED show a more uniform posterior progression over the same interval.

The coronal-plane projection (X–Z; ML versus SI, as shown in Figure 41 (B)) similarly confirms a consistent increase in superior translation for all three landmarks. The ML behaviour is more phase-dependent, reflecting the interval trends reported in Table 10: lateral translation reduces through mid-to-late extension (up to approximately F10/14), followed by a modest increase near terminal extension (F14/18). Importantly, the trajectories preserve the same lateral ordering throughout the cycle, with Tibia-LAT remaining the most lateral, Tibia-MED the most medial, and Tibia-ANT intermediate, supporting the robustness and internal consistency of the selected tracking landmarks across all frames.

		Mean difference (mm)			± Standard deviation (mm)		
Frames	Landmark	Medial–lateral (ML-X)	Anterior–posterior (AP-Y)	Superior–inferior (SI-Z)	Medial–lateral (ML-X)	Anterior–posterior (AP-Y)	Superior–inferior (SI-Z)
F02/06	Tibia-ANT	-119.0750	-24.3607	292.9260	2.6923	0.8691	0.6049
	Tibia-LAT	-141.0466	-25.2285	321.0579	1.9054	1.8054	0.8238
	Tibia-MED	-100.1848	-26.2477	310.6144	2.1679	1.1981	0.9610
F06/10	Tibia-ANT	-115.4057	-46.7693	296.3615	4.2227	1.9002	1.2346
	Tibia-LAT	-134.8073	-40.5645	327.0013	2.8572	5.0413	1.4595
	Tibia-MED	-94.0910	-37.9639	317.2072	3.2825	3.1113	1.4629
F10/14	Tibia-ANT	-104.4672	-69.9907	308.7055	1.9797	2.2055	0.3662
	Tibia-LAT	-128.9113	-59.5160	336.8396	1.1942	0.4953	1.0745
	Tibia-MED	-85.7788	-56.9511	327.2689	1.4121	1.8572	0.7121
F14/18	Tibia-ANT	-110.5615	-86.1780	322.2409	0.9357	0.8493	0.9263
	Tibia-LAT	-131.6361	-68.6819	346.2497	0.8485	0.5847	0.8318
	Tibia-MED	-90.7180	-71.8768	336.7785	0.8696	0.7557	1.1158

Table 10. Segment-wise mean inter-frame coordinate differences for the tracked tibial landmarks. For each tracking segment (F02–06, F06–10, F10–14, and F14–18), the mean translational differences and corresponding standard deviations are reported along the medial–lateral (ML–X), anterior–posterior (AP–Y), and superior–inferior (SI–Z) directions for Tibia-ANT, Tibia-LAT, and Tibia-MED. All values are in millimetres (mm).

Table 10 summarises the mean differences (mm) and standard deviations (±SD, mm) of three tibial tracking landmarks (Tibia-ANT, Tibia-LAT, and Tibia-MED) across four adjacent frame intervals (F02/06, F06/10, F10/14, and F14/18) along the global medial–lateral (ML-X), anterior–posterior (AP-Y), and superior–inferior (SI-Z) directions. As frames F02–F18 represent progressive knee extension from approximately 65° flexion to 0°, the trends reported below characterise how these directional differences evolve as the knee approaches full extension.

Overall, a clear separation in magnitude is evident across the three components. The SI-Z component dominates (approximately 292.93–346.25 mm), substantially exceeding the ML-X component (approximately −85.78 to −141.05 mm) and the AP-Y component (approximately −24.36 to −86.18 mm). This indicates that, over the extension cycle represented by F02–F18, the relative coordinate differences are driven primarily by the superior–inferior direction, whereas ML and AP components are smaller in magnitude but exhibit systematic temporal evolution.

Across all intervals, the reported SDs are generally low (SI-Z: 0.37–1.46 mm; ML-X: 0.85–4.22 mm; AP-Y: 0.50–5.04 mm), indicating good stability of the estimates within each interval. Notably, the F06/10 interval exhibits the largest dispersion, including an AP-Y SD of 5.04 mm for Tibia-LAT and an ML-X SD of 4.22 mm for Tibia-ANT, suggesting increased variability during this mid-extension phase. In contrast, SDs in the final interval (F14/18) are consistently lower (approximately 0.85–1.12 mm), indicating tighter clustering as the motion approaches 0°.

Using nodal coordinate data, displacement components along the global X, Y, and Z (medial–lateral (ML), anterior–posterior (AP), and superior–inferior (SI)) axes were calculated (see Appendix Tables B5-B8 for full details). For each tracking segment, the Euclidean distance between corresponding nodal pairs in the two coordinate systems was then computed to quantify the residual positional bias. This workflow was repeated systematically across multiple nodal sets (i.e., alternative landmark selections), yielding 16 nodal-set combinations per segment. Comparison of the resulting Euclidean errors provides an objective basis for assessing the relative performance of different landmark/nodal-set selections and identifying the combinations that deliver the most accurate and repeatable tracking.

Table 11 summarises the mean Euclidean bias (mm) for each nodal-set combination within a given tracking segment, thereby providing a statistical characterisation of tracking accuracy. The component-wise displacement results indicate that the largest positional differences between corresponding nodes occur predominantly in the Y and Z directions, whereas the bias in the X direction is comparatively smaller. For each tracking segment, an overall estimate of the coordinate-system difference was obtained by averaging the Euclidean errors across all nodal-set combinations, as reported in Tables 12, 13, 14, and 15.

Importantly, the larger discrepancies reported in this section (e.g., Frame 06–10: 9.3 ± 3.3 mm) should be interpreted as mean errors associated with a given nodal-set selection, rather than as isolated outliers at individual nodes. This interpretation is supported by the Frame 06–10 trajectory results, where the P4–F1 configuration yields a tracking error of 5.648 ± 0.062 mm, indicating a consistently elevated mean mismatch but very low variability across the evaluated landmarks. Such a pattern suggests that, for this configuration, the residual error is dominated by a systematic offset between the driven and reference positions—likely reflecting the specific landmark selection and its sensitivity to inter-frame kinematics—rather than sporadic or unstable node correspondences.

Tracking frame segments	Mean difference (mm) between equivalent nodes in 16 different node sets
Frames 2-6 (65°–48°)	4.63+/-1.69 mm
Frames 6-10 (48°–32°)	9.3+/-3.3 mm
Frames 10-14 (32°–16°)	8.61+/-2.6 mm
Frames 14-18 (16°–0°)	4.9+/-1.59 mm

Table 11. Mean difference (Units: mm) between equivalent nodes of 16 different sets of nodes for a given tracking frame segment.

Upon obtaining the displacement components for each selected tibial landmark along the global X, Y, and Z axes, the resultant (total) displacement for each landmark was calculated manually. These manually derived resultant values were then compared with the corresponding total deformation reported by ANSYS™. The comparison is presented in the Table 12.

The Table 12 and accompanying statistical summary quantify the errors in total deformation between the manual calculations and the ANSYS™ outputs for the Frame 02–06 transition at three anatomically defined tibial landmarks: Tibia-ANT, Tibia-LAT, and Tibia-MED. The mean errors were 7.23 mm for Tibia-ANT, 4.9 mm for Tibia-LAT and 5.19 mm for Tibia-MED. The corresponding standard deviations were 2.08 mm, 1.99 mm, and 1.68 mm, respectively.

Inspection of Figure 42 indicates that the displacement error profiles for test scenarios P2–F2, P2–F3, P2–F4, and P3–F4 show the closest agreement with the ANSYS™-derived values. This agreement suggests a strong correspondence between the manual resultant displacement calculations and the computational outputs under these specific test configurations, supporting the reliability of the manual approach for the simulated evaluation. For the Frame 02–06 comparison, the mean positional errors across the 16 node-set combinations ranged from 2.21 mm to 6.16 mm. The P4–F1 combination produced the lowest mean error (2.21 mm; Tibia-ANT: 4.45 mm, Tibia-LAT: 2.17 mm, Tibia-MED: 2.55 mm), with a standard deviation of 1.22 mm, indicating relatively consistent accuracy across the tibial landmarks. In contrast, the P3–F1 combination exhibited the highest mean error (6.16 mm; Tibia-ANT: 10.01 mm, Tibia-LAT: 8.48 mm, Tibia-MED: 6.96 mm), with a standard deviation of 1.52 mm, indicating greater variability. Overall, the mean error across all combinations was approximately 5.77 mm (Tibia-ANT: 7.23 mm, Tibia-LAT: 4.89 mm, Tibia-MED: 5.19 mm), with corresponding standard deviations of 2.08 mm, 1.99 mm, and 1.68 mm, respectively.

Distance Units: mm	**Tibia-ANT**	**Tibia-LAT**	**Tibia-MED**	**Average**	**S. deviation**
P1-F1	5.731485499	3.28303353	4.443227306	3.00483968	1.224784051
P2-F1	4.853594846	2.809283	3.365797954	2.55429262	1.056918429
P3-F1	10.00852994	8.47773201	6.964671875	6.16208732	1.521937647
P4-F1	4.447918546	2.17039381	2.553019422	2.20610412	1.219573967
P1-F2	7.39403225	4.858136	5.920860742	4.08405608	1.273472155
P2-F2	9.510149644	7.45832361	7.152143	5.65615775	1.282181214
P3-F2	6.754211879	4.99341221	5.214581304	3.9158747	0.959148366
P4-F2	6.769601529	4.98986967	5.234219426	3.91982373	0.964758217
P1-F3	6.391968464	4.19722206	4.924917419	3.52973018	1.117936423
P2-F3	10.33177078	7.04845219	7.40542461	5.79340766	1.801439801
P3-F3	5.65913367	3.68139507	4.266791119	3.11350958	1.015936044
P4-F3	5.664417775	3.25309679	4.437177447	2.97250485	1.205724868

P1-F4	6.213753325	3.37464362	3.498451672	3.19613231	1.604614982
P2-F4	10.11940643	7.2404826	7.355825837	5.78662968	1.629871373
P3-F4	10.16747599	7.26841837	7.386673001	5.81196479	1.64070028
P4-F4	5.583272921	3.20014464	2.905351808	2.92780585	1.468415513
Average	7.225045217	4.89400245	5.189320871		
S. deviation	2.081359169	1.99014422	1.680670155		

Table 12. The table shows the distance error (Units: mm) of the equivalent nodes on Frame 02-06, as well as the average and standard deviation of the equivalent node combination and each equivalent node across all tests. Summary: P4-F1 best (2.21mm average), P3-F1 worst (6.16mm), with anterior node most variable. (P1–P4 and F1–F4 are the patellar and femoral driving node sets defined in Figure 34.)

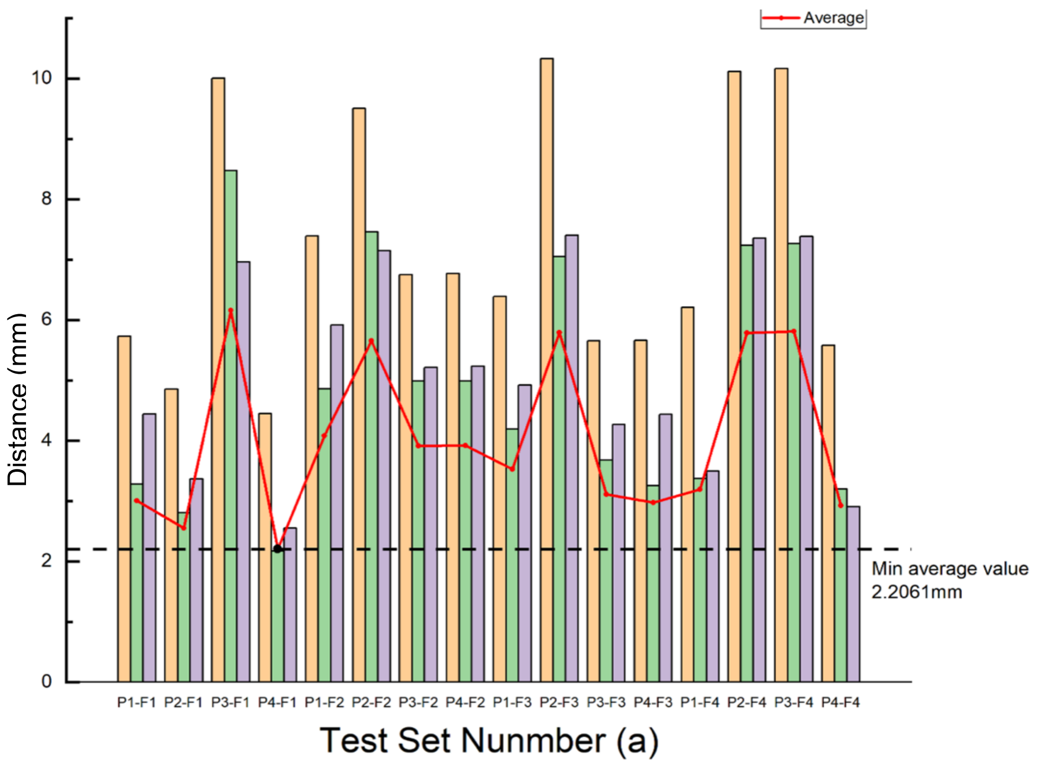

Figure 42. Frame 02–06 comparison showing the translational errors of equivalent tibial nodes. Errors are reported for Tibia-ANT (orange), Tibia-LAT (green), and Tibia-MED (purple), with a mean line indicating the average translational error across the three nodes included in each test (units: mm).

After obtaining the displacement components for each selected tibial landmark along the global X, Y, and Z axes, the resultant (total) displacement for each landmark was computed manually. These manually calculated resultant values were then compared with the corresponding total deformation values reported by ANSYS™, and the comparative results are presented in the Table 13 and Figure 43 below. The plot and statistical summary provide an overview of the errors in total deformation between the manual calculations and ANSYS™ outputs for the Frame 06–10 transition at Tibia-ANT, Tibia-LAT, and Tibia-MED.

Across the sampling intervals, Tibia-ANT exhibits a fluctuating error profile, with several pronounced peaks indicating higher discrepancies at specific points, suggestive of a quasi-cyclical rise-and-fall pattern. Tibia-LAT (shows a less volatile trend than Tibia-ANT, but still displays intermittent peaks, indicating occasional elevated mismatch. Tibia-MED generally maintains lower error magnitudes overall, but includes a sharp negative excursion at one interval, which may represent an outlier or a local measurement/processing anomaly.

For the Frame 06–10 comparison, mean positional errors across the 16 node-set combinations were higher overall, ranging from 5.65 mm to 13.44 mm. The P4–F1 configuration again produced the best agreement (Figure 43), with a mean error of 5.65 mm (Tibia-ANT: 5.58 mm, Tibia-LAT: 5.68 mm, Tibia-MED: 5.69 mm) and a notably low standard deviation of 0.06 mm, indicating highly consistent performance across the three tibial landmarks. The largest error was observed for P1–F3, with a mean of 13.44 mm (Tibia-ANT: 12.34 mm, Tibia-LAT: 10.65 mm, Tibia-MED: 16.90 mm) and a standard deviation of 3.23 mm, reflecting substantial variability. Overall, the mean error across all combinations was approximately 9.63 mm (Tibia-ANT: 8.36 mm, Tibia-LAT: 8.22 mm, Tibia-MED: 11.31 mm), with standard deviations of 2.52 mm, 2.80 mm, and 3.67 mm, respectively.

Distance Units: mm	Tibia-ANT	Tibia-LAT	Tibia-MED	Average	S. deviation
P1-F1	6.832240614	7.969202518	9.042818635	7.948087256	1.105440268
P2-F1	8.131137682	7.149475993	8.00156464	7.760726105	0.533307901
P3-F1	10.12950242	10.43354439	17.47750686	12.68018456	4.157383354
P4-F1	5.576518486	5.681045306	5.687720022	5.648427938	0.062364773
P1-F2	8.457523652	10.70949837	11.27108433	10.14603545	1.489009322
P2-F2	10.42917148	11.45133714	12.5485529	11.47635384	1.059912155
P3-F2	7.457785586	8.021672898	11.53380447	9.004420986	2.208580504
P4-F2	8.53676842	10.16790745	11.83800336	10.18089308	1.650655778
P1-F3	12.34267213	10.65037287	16.89621131	13.29641877	3.230301679
P2-F3	12.86808226	11.18184099	16.2629641	13.43762912	2.587999366
P3-F3	3.894217905	9.221197094	6.635487699	6.583634233	2.663868129
P4-F3	5.64361924	9.097740595	7.370058644	7.370472826	1.727060715
P1-F4	9.253565335	5.472196238	9.64952073	8.125094101	2.305991212
P2-F4	9.649416368	2.844455022	13.39381159	8.629227661	5.34816041
P3-F4	6.253308847	3.317346405	11.99487955	7.188511602	4.413711424
Average	8.363702028	8.224588885	11.30693259		
S. deviation	2.518601751	2.80258113	3.667216022		

Table 13. The table shows the distance error (Units: mm) of the equivalent nodes on Frame 06-10, as well as the average and standard deviation of the equivalent node combination and each equivalent node across all tests. Summary: P4-F1 best (5.65mm), P1-F3 worst (13.44mm), with medial node most variable. (P1–P4 and F1–F4 are the patellar and femoral driving node sets defined in Figure 34.)

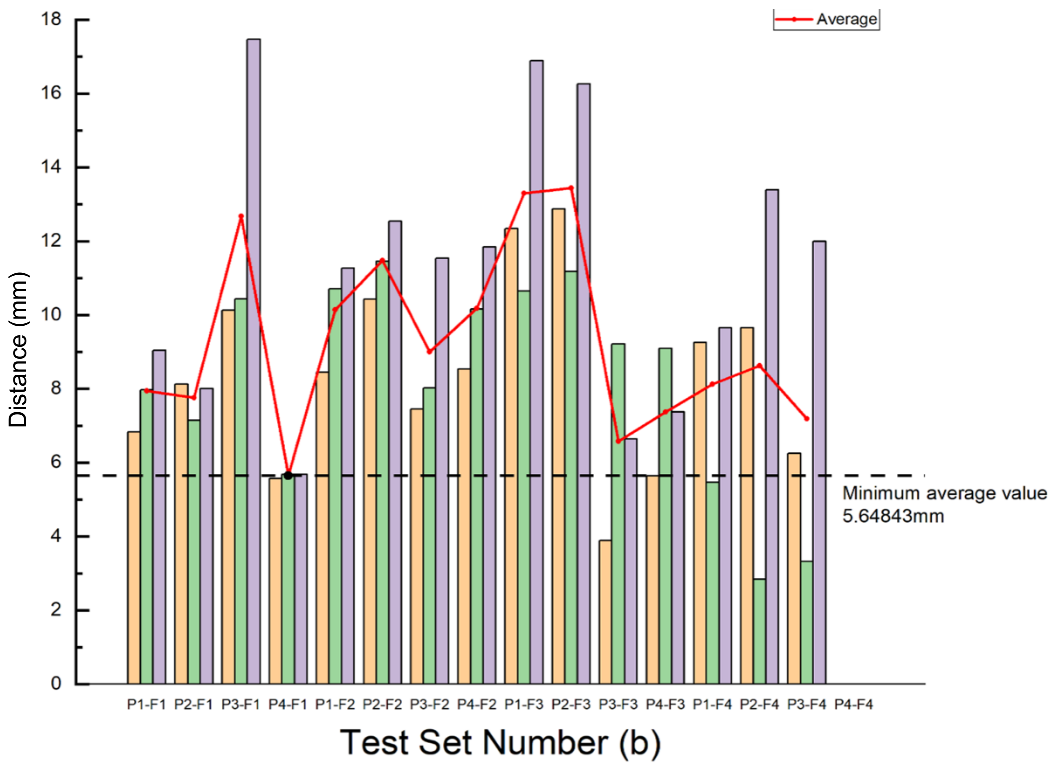

Figure 43. Frame 06–10 comparison showing the translational errors of equivalent tibial nodes. Errors are reported for Tibia-ANT (orange), Tibia-LAT (green), and Tibia-MED (purple), with a mean line indicating the average translational error across the three nodes included in each test (units: mm).

After obtaining the displacement components for each selected tibial landmark along the global X, Y, and Z axes, the resultant (total) displacement for each landmark was computed manually. These manually calculated resultant values were then compared against the corresponding total deformation values reported by ANSYS™, with the comparative results illustrated in the Table 14 and Figure 44 below. The plot and statistical summary provide an overview of the errors in total deformation between the manual calculations and ANSYS™ outputs across Frames 10–14 for Tibia-ANT, Tibia-LAT, and Tibia-MED.

Across the sampled test cases, Tibia-ANT exhibits a relatively high mean error with moderate variability, and the error range indicates appreciable fluctuation in discrepancy magnitude. Tibia-LAT shows the highest mean error among the three landmarks, but with the lowest variability (smallest standard deviation and range), implying more consistent mismatch levels. In contrast, Tibia-MED presents the lowest mean error, yet its larger standard deviation and range indicate substantial fluctuations in agreement between the manual and ANSYS™ estimates.

For the Frame 10–14 comparison, mean errors across the 16 node-set combinations ranged from 6.82 mm to 10.68 mm. The P2–F3 configuration produced the lowest mean error (Figure 44) of 6.82 mm (Tibia-ANT: 7.34 mm; Tibia-LAT: 4.54 mm; Tibia-MED: 8.59 mm), with a standard deviation of 2.07 mm. The highest mean error was observed for P3–F4, averaging 10.68 mm (Tibia-ANT: 12.40 mm; Tibia-LAT: 8.11 mm; Tibia-MED: 11.54 mm), with a standard deviation of 2.27 mm. Overall, the mean error across all combinations was approximately 8.61 mm (Tibia-ANT: 9.90 mm; Tibia-LAT: 5.72 mm; Tibia-MED: 10.20 mm), with standard deviations of 1.86 mm, 1.32 mm, and 1.64 mm, respectively. Notably, errors for Tibia-LAT were consistently lower than those for Tibia-ANT and Tibia-MED, suggesting a potential directional or landmark-dependent bias in the alignment procedure, possibly influenced by the tibial kinematics and the distribution of applied constraints.

Distance Units: mm	Tibia-ANT	Tibia-LAT	Tibia-MED	Average	S. deviation
P1-F1	8.97359876	4.980625537	8.50513724	7.486453845	2.182715208
P2-F1	8.4069186	4.903333289	7.99172472	7.100658867	1.91422994
P3-F1	9.04197825	5.422253401	8.79985047	7.754694039	2.023577516
P4-F1	8.77720809	4.72481877	8.06181014	7.187945666	2.162913345
P1-F2	9.70417711	5.373624067	12.1932664	9.090355872	3.45100897
P2-F2	9.28468473	5.551135272	12.0912085	8.975676167	3.280968482
P3-F2	9.24244919	5.524013524	11.9165405	8.894334402	3.210449841
P4-F2	9.79521373	5.30562724	12.2387538	9.113198273	3.516521001

P1-F3	7.9607794	4.536093836	9.14218063	7.213017956	2.392356427
P2-F3	7.33942068	4.543430922	8.59181719	6.824889596	2.072658804
P3-F3	7.97689422	5.084233709	9.56973814	7.543622024	2.273924165
P4-F3	13.0368955	4.224158513	8.78285811	8.681304043	4.407246108
P1-F4	12.4467366	7.897643379	11.4719304	10.60543681	2.395134809
P2-F4	11.89854	7.705935202	11.0927309	10.23240204	2.224771471
P3-F4	12.3963648	8.107794626	11.5355298	10.67989641	2.26870887
P4-F4	12.1816365	7.596770981	11.1639966	10.31413471	2.40768498
Average	9.90396852	5.717593267	10.1968171		
S. deviation	1.85683888	1.316276647	1.6365089		

Table 14. The table shows the distance error (Units: mm) of the equivalent nodes on Frame 10-14, as well as the average and standard deviation of the equivalent node combination and each equivalent node across all tests. Summary: P2-F3 best (6.82mm), P3-F4 worst (10.68mm), with anterior node most variable. (P1–P4 and F1–F4 are the patellar and femoral driving node sets defined in Figure 34.)

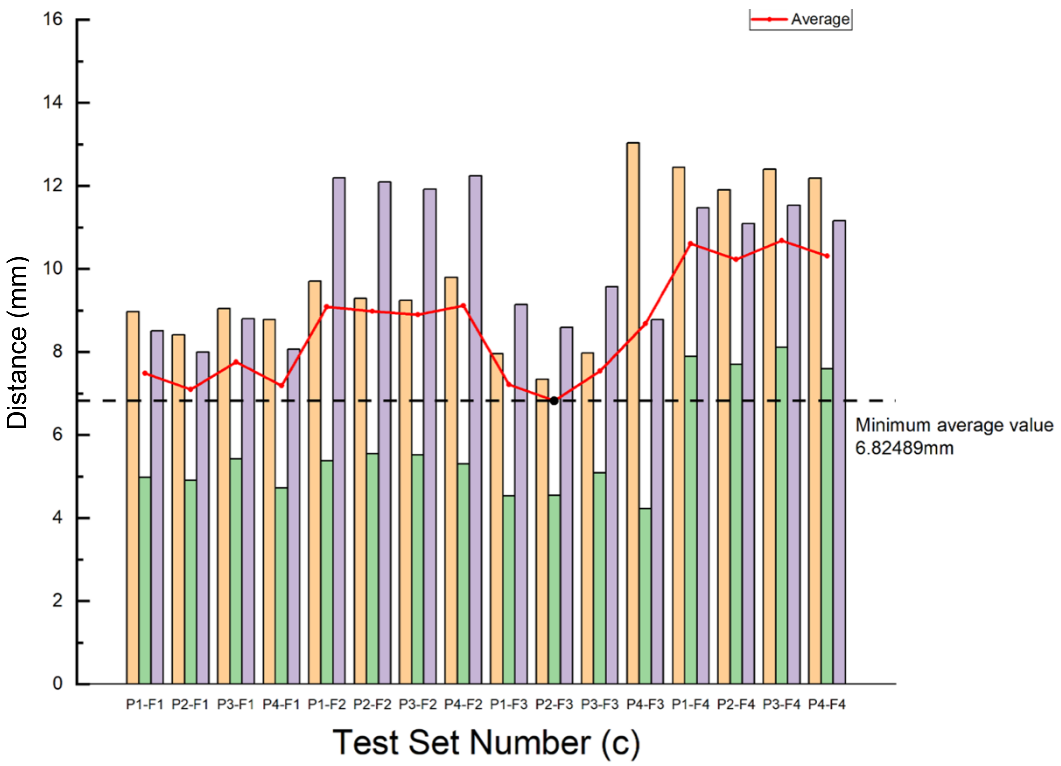

Figure 44. Frame 10–14 comparison showing the translational errors of equivalent tibial nodes. Errors are reported for Tibia-ANT (orange), Tibia-LAT (green), and Tibia-MED (purple), with a mean line indicating the average translational error across the three nodes included in each test (units: mm).

After obtaining the displacement components for each selected tibial landmark along the global X, Y, and Z axes, the resultant (total) displacement was computed manually and compared with the total deformation reported by ANSYS™. Table 15 and Figure 45 below summarises the total-deformation error between the manual calculations and ANSYS™ outputs for the Frame 14–18 transition at Tibia-ANT, Tibia-LAT, and Tibia-MED. Overall, Tibia-LAT shows a high mean error comparable to Tibia-ANT but with lower variability (smaller standard deviation and narrower range), indicating more consistent discrepancy magnitudes. In contrast, Tibia-MED exhibits a substantially lower mean error than the other two landmarks, although its larger standard deviation and wider range indicate notable fluctuations in agreement between manual and ANSYS™ estimates.

Among the tested frame pairs, the Frame 14–18 comparison produced the lowest errors overall, with mean errors across the 16 node-set combinations ranging from 4.13 mm to 6.36 mm. The P2–F3 configuration yielded the smallest mean error (Figure 45) of 4.13 mm (Tibia-ANT: 4.30 mm; Tibia-LAT: 2.49 mm; Tibia-MED: 5.59 mm), with a standard deviation of 1.56 mm. The largest mean error was observed for P4–F1, averaging 6.36 mm (Tibia-ANT: 6.05 mm; Tibia-LAT: 4.15 mm; Tibia-MED: 8.89 mm), with a standard deviation of 2.38 mm. Overall, the mean error across all combinations was approximately 4.90 mm (Tibia-ANT: 5.08 mm; Tibia-LAT: 3.26 mm; Tibia-MED: 6.38 mm), with corresponding standard deviations of 0.57 mm, 0.82 mm, and 1.28 mm, respectively.

Distance Units: mm	Tibia-ANT	Tibia-LAT	Tibia-MED	Average	S, deviation
P1-F1	6.032350279	4.123202994	8.781834349	6.312462541	2.341913467
P1-F2	5.525547329	2.379157803	6.507995755	4.804233629	2.156860172
P1-F3	4.496843227	2.42878716	6.152829324	4.35948657	1.865816885
P1-F4	4.934950088	3.062672106	5.341225974	4.446282723	1.215338956
P2-F1	5.496104676	4.038449135	7.886558062	5.807037291	1.942805933
P2-F2	5.288526608	2.457495174	6.197518947	4.64784691	1.950588966
P2-F3	4.298117053	2.491752143	5.594538392	4.128135862	1.558361586
P2-F4	4.674753231	3.078069478	5.499966143	4.417596284	1.23125673
P3-F1	5.432880482	4.789626418	7.692780224	5.971762374	1.524752693
P3-F2	4.989161655	3.178749158	4.998935521	4.388948778	1.048075008
P3-F3	4.199472806	3.57826571	4.948961687	4.242233401	0.686347738
P3-F4	4.883455795	4.35752361	4.978976234	4.739985213	0.334647123
P4-F1	6.054858284	4.15081463	8.886877872	6.364183595	2.383135617

P4-F2	5.460932072	2.396247377	6.422162039	4.759780496	2.102547828
P4-F3	4.472633991	2.407088625	6.186373372	4.35536533	1.892369481
P4-F4	4.976140377	3.16891433	5.96493186	4.703328856	1.417832184
Average	5.076045497	3.255425991	6.37765411		
S,deviation	0.570403898	0.818592482	1.284462107		

Table 15. The table shows the distance error (Units: mm) of the equivalent nodes on Frame 14-18, as well as the average and standard deviation of the equivalent node combination and each equivalent node across all tests. Summary: P2-F3 best (4.13mm), P4-F1 worst (6.36mm), with medial node most variable. (P1–P4 and F1–F4 are the patellar and femoral driving node sets defined in Figure 34.)

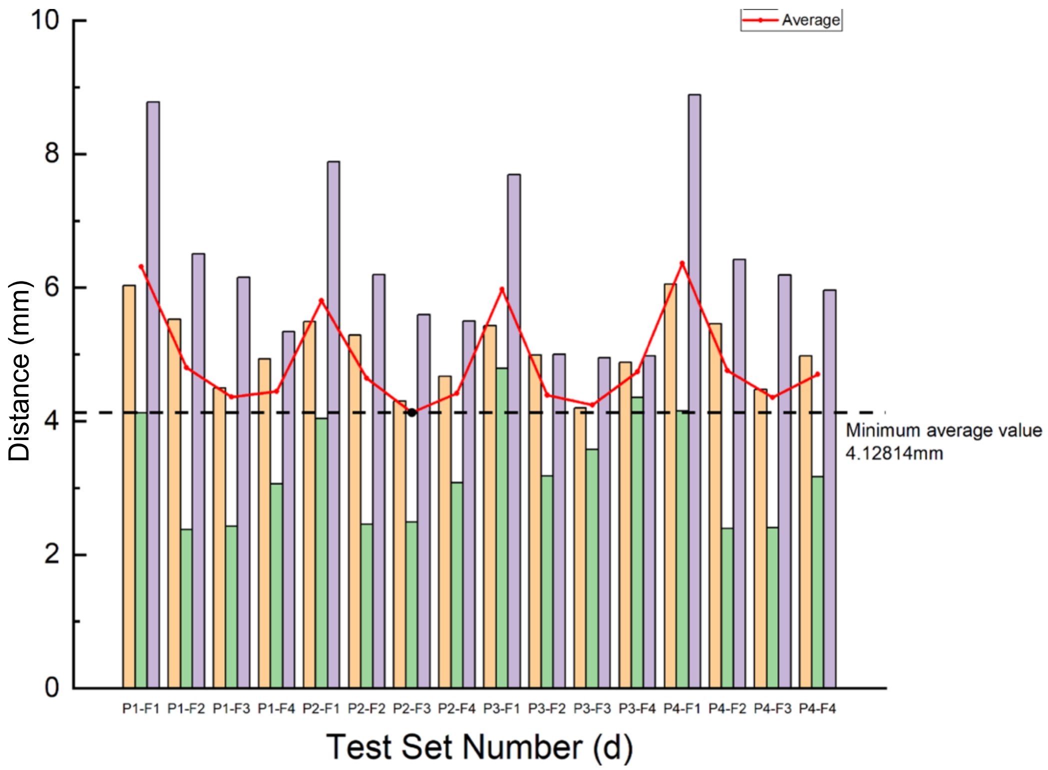

Figure 45. Frame 14–18 comparison showing the translational errors of equivalent tibial nodes. Errors are reported for Tibia-ANT (orange), Tibia-LAT (green), and Tibia-MED (purple), with a mean line indicating the average translational error across the three nodes included in each test (units: mm).

The experimental results of the nodal coordinate-based alignment method for knee joint models, which involve aligning the femur, patella, and tibia between two frames, rely on a manual testing approach that has a notable limitation: it only analyses the matching error of manually selected equivalent nodes. This method selects three nodes on the patella and femur in each frame, calculates the vector difference in their positions, and applies a prescribed displacement to align the bones. The accuracy is then assessed by comparing the predicted position of the tibia in one frame to its actual position in the second frame using three additional nodes. While this approach provides useful insights, it falls short of evaluating the full alignment accuracy across the entire bone structure. To address this limitation and provide a more comprehensive evaluation, the cloud compare method is proposed. Considers All Surface Points: It compares the entire point cloud of the bone structures between the two frames, assessing alignment across every available data point rather than just a handful of nodes.

4.4 Cloud-to-Mesh Signed Distance Analysis of Patellofemoral Tracking

To comprehensively evaluate the accuracy of patellofemoral tracking, Cloud-to-Mesh (C2M) signed distance analysis was performed across the entire flexion range from 65° down to 0°. All analyses were consistently based on the selected set nodes group P1-F1, thereby ensuring that deviations were quantified within a uniform reference framework throughout the full motion sequence. C2M measures signed distances (positive/negative for over/under-alignment), providing spatial signed distance map to identify misalignment regions. CloudCompare reports signed distances in metres; however, for clinical/biomechanical interpretation, all values are converted to millimetres (e.g., 0.001 m = 1 mm), and the results are reported in millimetres throughout the remainder of this section.

In the early flexion phase (frames 02–06, 65°–48°), deviations were generally small (–0.020 m to +0.012 m, i.e., –20 to +12 mm). Localised errors appeared primarily on the anterior patellar surface and at the peripheral regions of the tibial plateau (Figure 46), reflecting the sensitivity of these regions to segmentation resolution and registration.

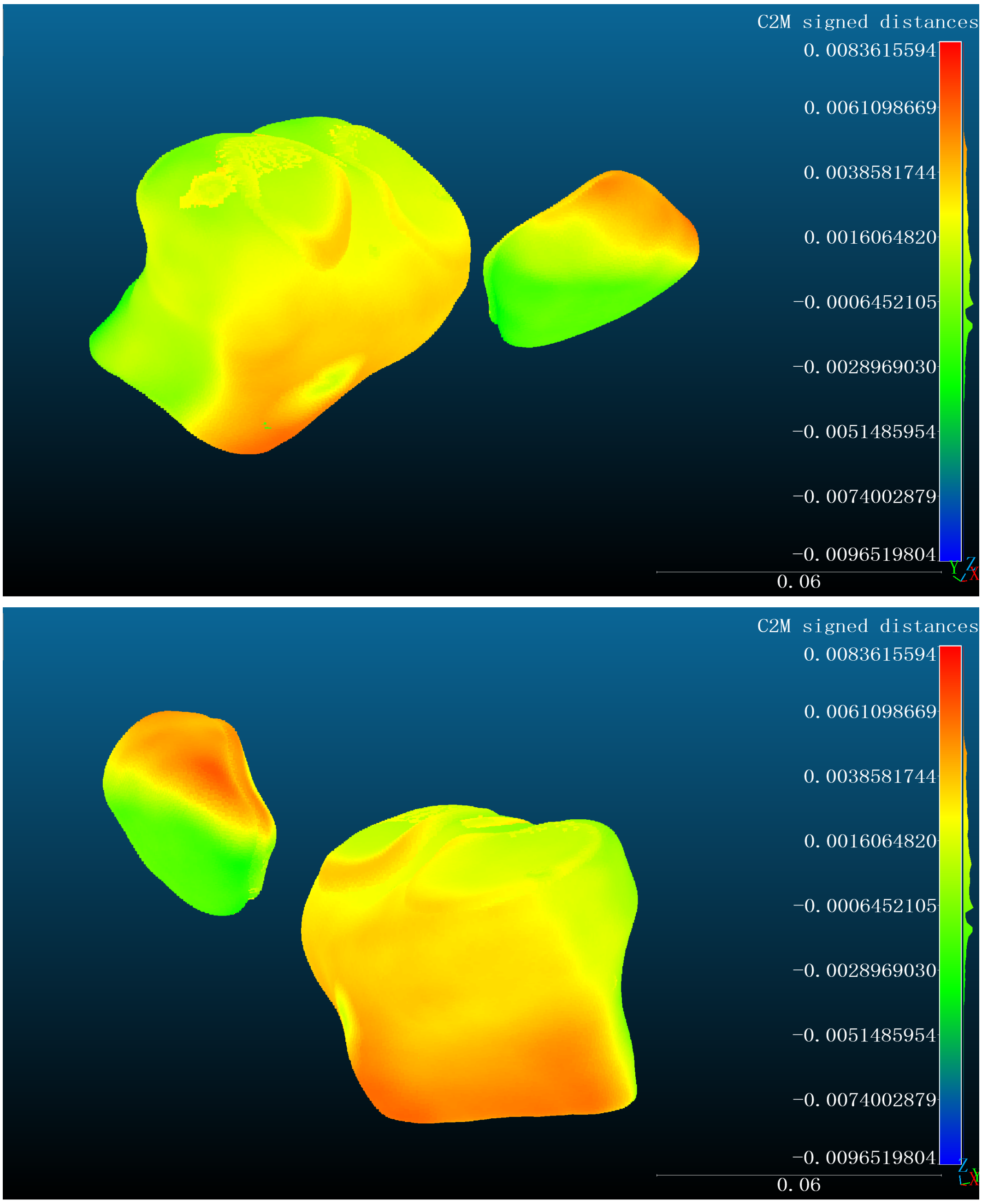

Figure 46. Cloud-to-Mesh Signed Distance Analysis of Patellofemoral Tracking (Frames 02–06, Flexion 65°–48°). Top: Patella view showing anterior errors (red positive deviations); Bottom: Tibia view with peripheral plateau discrepancies (blue negative deviations). (CloudCompare C2M signed distances; units in metres; 0.001 m = 1 mm)

During mid-flexion (frames 06–10, 48°–32°), the deviation range broadened (–0.024 m to +0.018 m, i.e., –24 to +18 mm), with errors concentrated on the anterior–inferior tibial surface and the superior aspect of the patella (Figure 47). This indicates that as flexion progresses into the transitional mid-range, misalignments become more pronounced in regions subject to complex patellofemoral articulation.

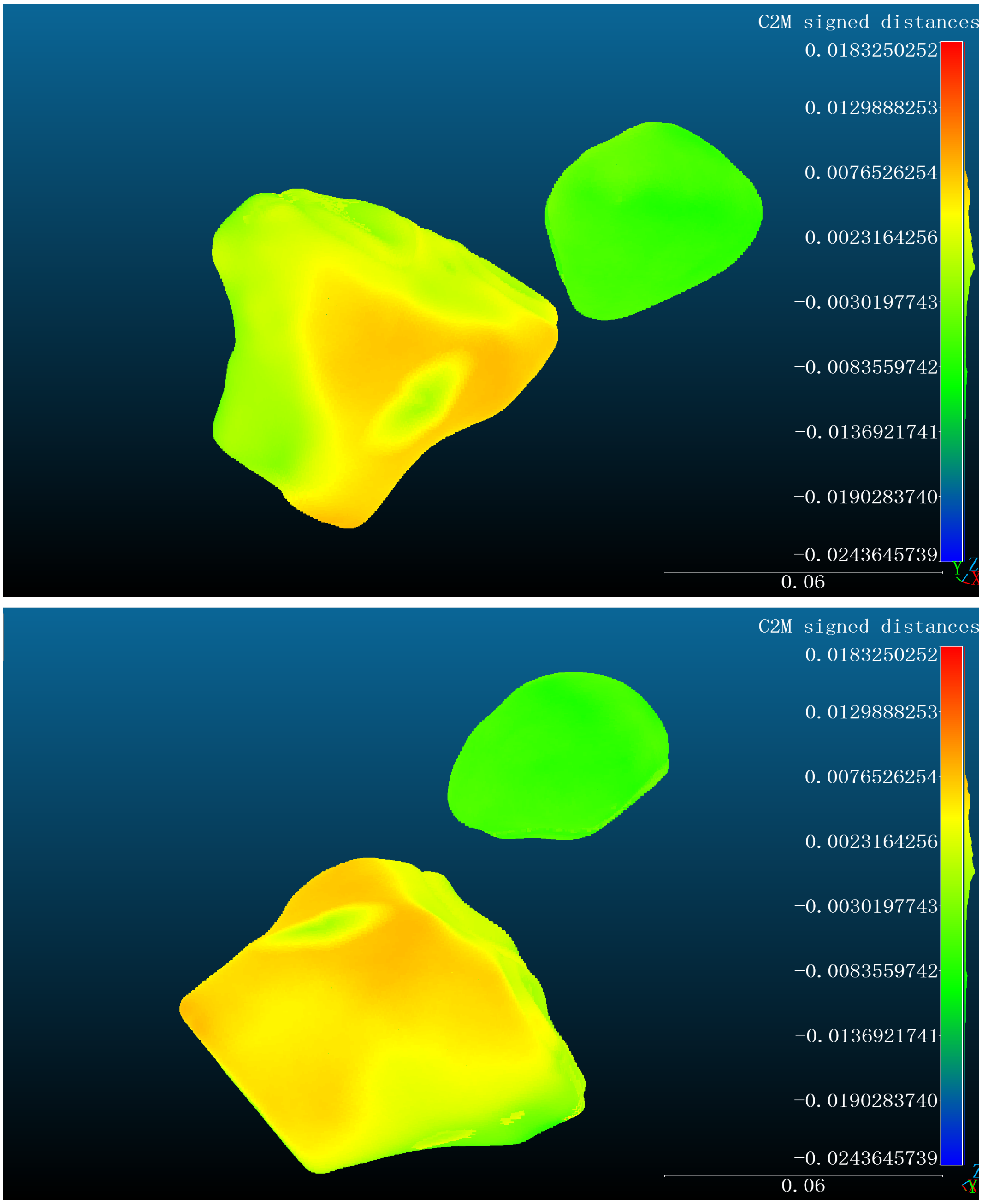

Figure 47. Cloud-to-Mesh Signed Distance Analysis of Patellofemoral Tracking (Frames 06–10, Flexion 48°–32°). Top: Patella with superior deviations; Bottom: Tibia showing anterior-inferior errors. (CloudCompare C2M signed distances; units in metres; 0.001 m = 1 mm)

In the subsequent phase (frames 10–14, 32°–16°), the overall deviation range reduced slightly (–0.020 m to +0.014 m, i.e., –20 to +14 mm). The patella displayed relatively uniform deviations, whereas the tibia showed higher discrepancies at its distal and posterior aspects (Figure 48). This suggests that the patella maintained stable tracking, while the tibial surface experienced localised deviations in regions subject to increased load transfer.

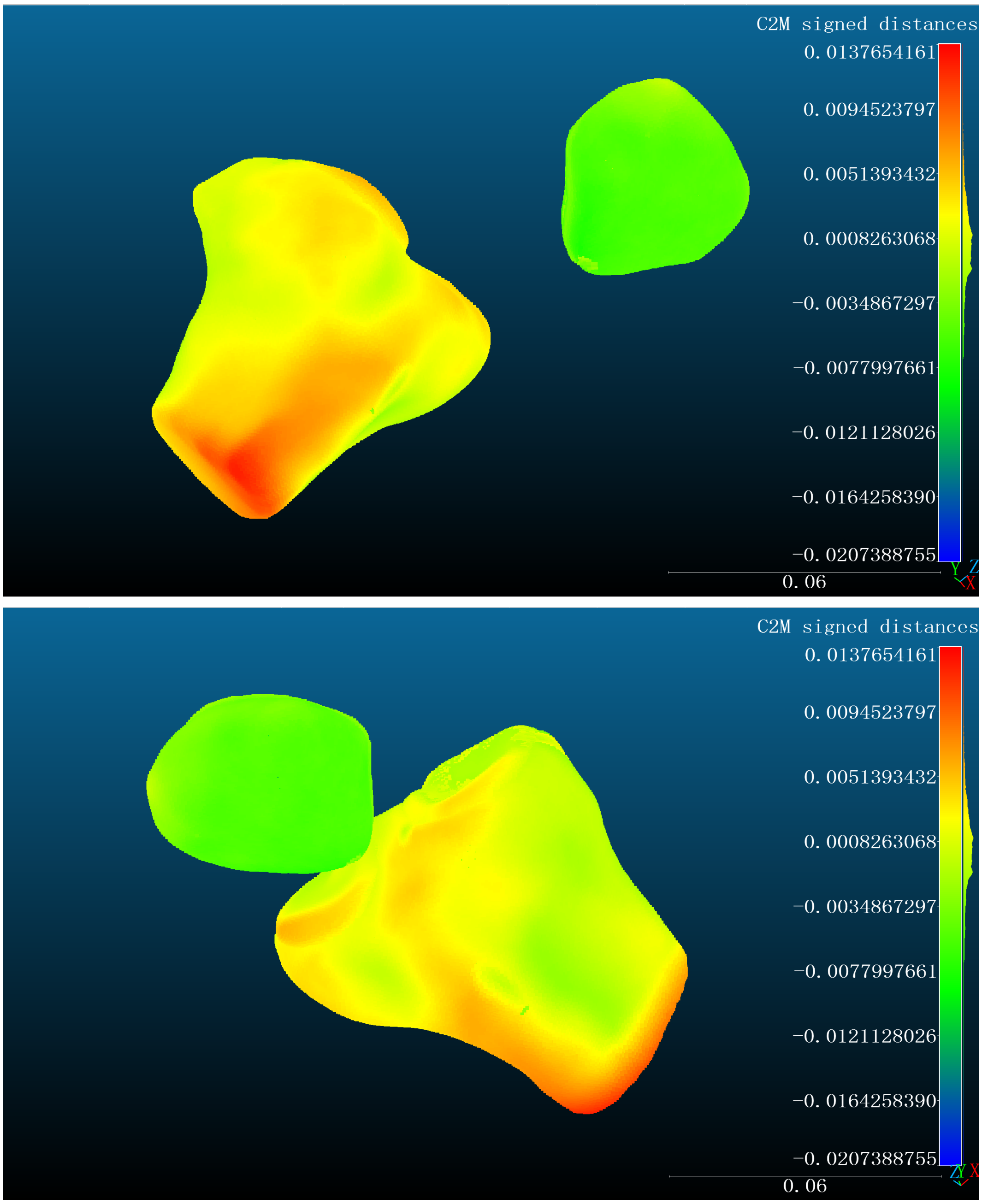

Figure 48. Cloud-to-Mesh Signed Distance Analysis of Patellofemoral Tracking (Frames 10–14, Flexion 32°–16°). Top: Uniform patella alignment; Bottom: Tibia with distal/posterior discrepancies. (CloudCompare C2M signed distances; units in metres; 0.001 m = 1 mm)

In the terminal flexion phase (frames 14–18, 16°–0°), deviations further decreased (–0.017 m to +0.014 m, i.e., –17 to +14 mm). The patella exhibited a consistent correspondence with only minor local variations, while the tibial errors were mainly confined to distal extremities (Figure 49). This reflects a stabilisation of patellofemoral alignment as the joint approaches full extension.

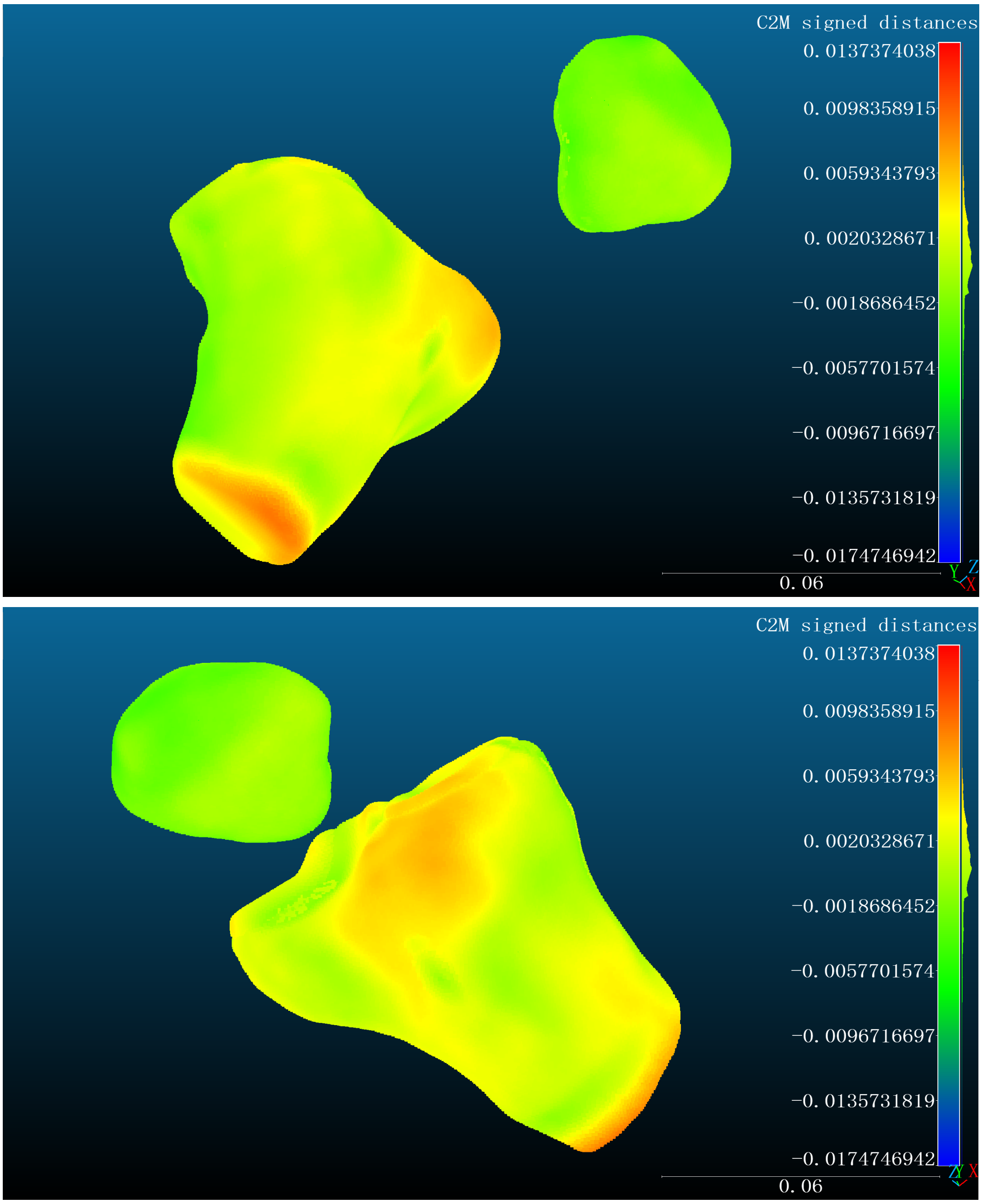

Figure 49. Cloud-to-Mesh Signed Distance Analysis of Patellofemoral Tracking (Frames 14–18, Flexion 16°–0°). Top: Consistent patella matching; Bottom: Tibia with distal errors. (CloudCompare C2M signed distances; units in metres; 0.001 m = 1 mm)

Taken together, the C2M analysis based on the P1-F1 node group reveals a clear trend across flexion: deviations are initially low, increase in magnitude and localisation during mid-flexion, and then gradually diminish toward late flexion. Regionally, the anterior patella and the distal/posterior tibia consistently exhibited the highest deviations, whereas the remaining articular surfaces maintained closer correspondence. These findings confirm the robustness of the tracking methodology and ensure the reliability of the reconstructed kinematics for subsequent finite element modelling and biomechanical validation.

4.5 Patellar matching analysis results based on cloud comparison

Comparison with literature is difficult given the different adopted boundary conditions and loading scenarios applied. Based on the above factors, Cloud-compare was used for further comparative analysis of displacement variables.

Four sets of reference nodes were positioned on the surface of the patella to function as anchor points for the manual alignment of the patellar position. Subsequently, the Cloud Compare software was utilized to evaluate the degree of congruence and to analyse discrepancies. Figures 50–65 present CloudCompare C2M signed distance maps comparing the driven patellar geometry with the corresponding target frames for each inter-frame transition (F02–F06, F06–F10, F10–F14, and F14–F18) and for each patellar reference node set (P1–P4). CloudCompare reports signed distances in metres; for clinical/biomechanical interpretation, all values are converted and reported in millimetres (mm), and millimetres are used throughout the remainder of this section. For each comparison, the C2M output samples the full set of available surface points (typically ~11k–12k points for the patella), allowing the overall spatial agreement to be assessed across the entire patellar surface rather than at a small number of discrete nodes. The findings are presented as follows.

As shown in Figure 50, the spatial distribution of signed distance across the articular surface, the selected set nodes group P1 (Figure 50.), there are 11,473 node points, meaning this number of point distances was compared. It is roughly distributed within the plus or minus 7.5 mm threshold range. Among them, 75% are roughly distributed within the range of plus or minus 2.8mm of the threshold.

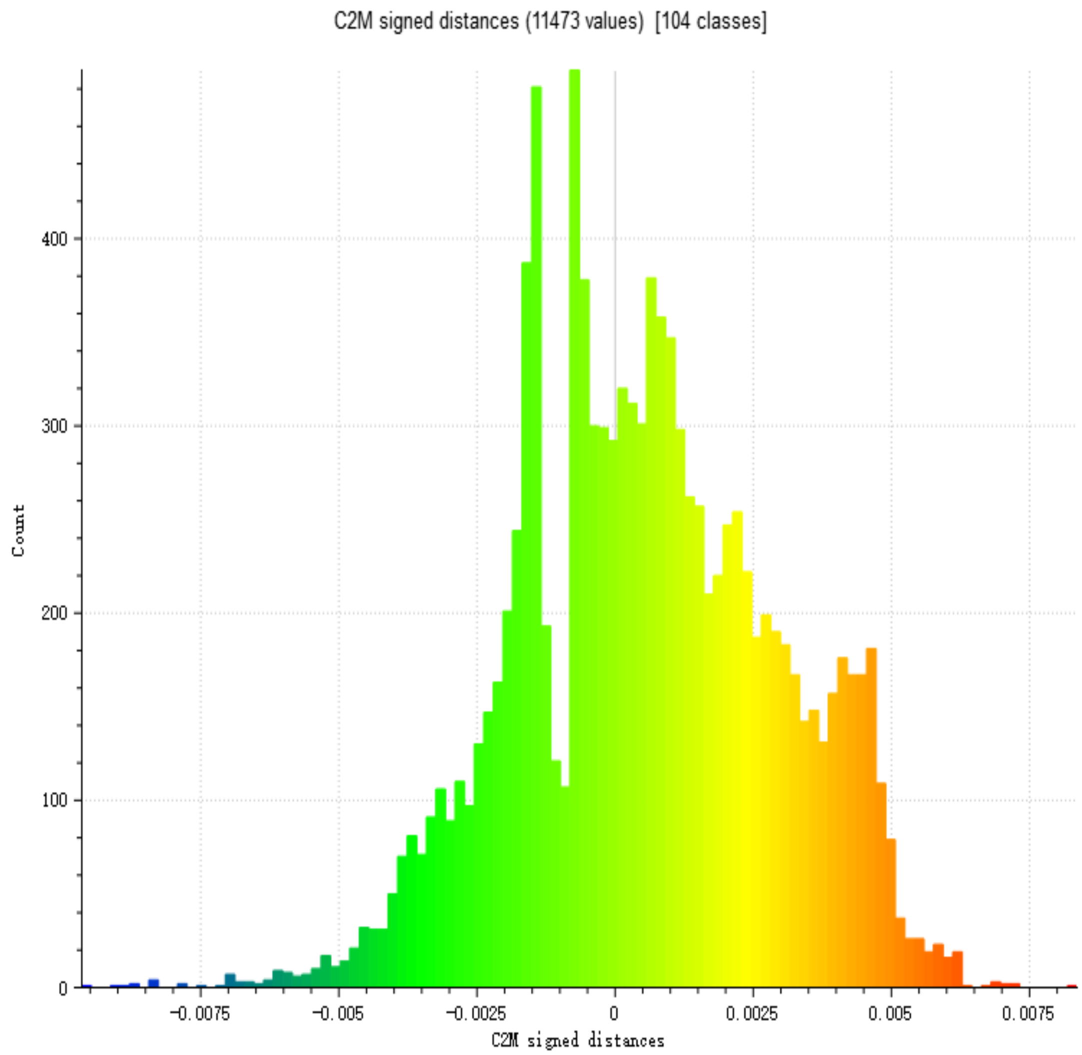

Figure 50. Patella displacement between frames 02 to 06 (CloudCompare; C2M signed distances; node set P1). Frame 02 is the driven frame and frame 06 is the target frame; the green→yellow→orange ramp indicates increasing magnitude (Units in metres (m); 0.001 m = 1 mm).

As shown in Figure 51, for the selected set nodes group P2, it is roughly distributed within the plus or minus 7 mm threshold range. Among them, 86% are roughly distributed within the range of plus or minus 4mm of the threshold.

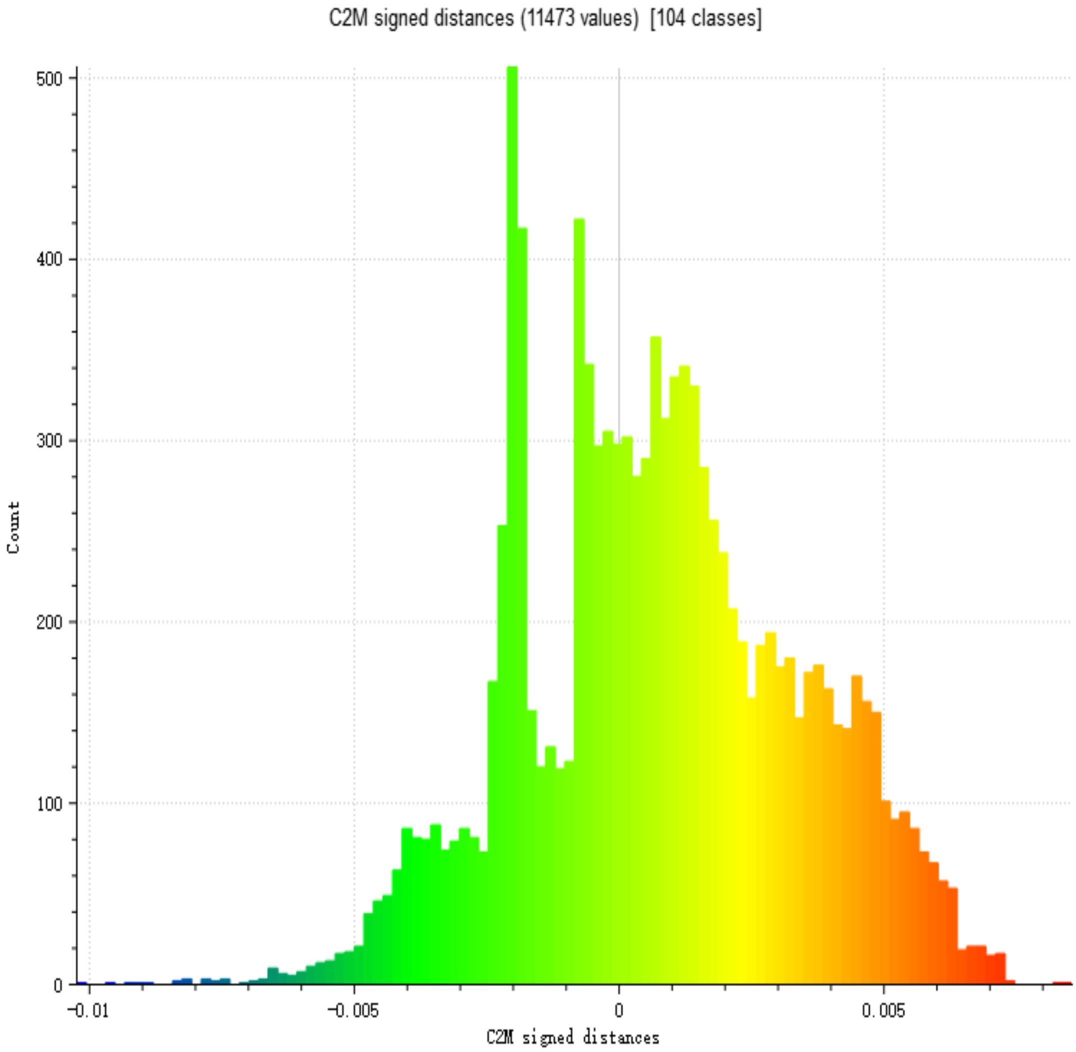

Figure 51. Patella displacement between frames 02 to 06 (CloudCompare; C2M signed distances; node set P2). Frame 02 is the driven frame and frame 06 is the target frame; the green→yellow→orange ramp indicates increasing magnitude (Units in metres (m); 0.001 m = 1 mm).

As shown in Figure 52, for the selected set nodes group P3, it is roughly distributed within the plus or minus 7 mm threshold range. Among them, 80% are roughly distributed within the range of plus or minus 3.2mm of the threshold.

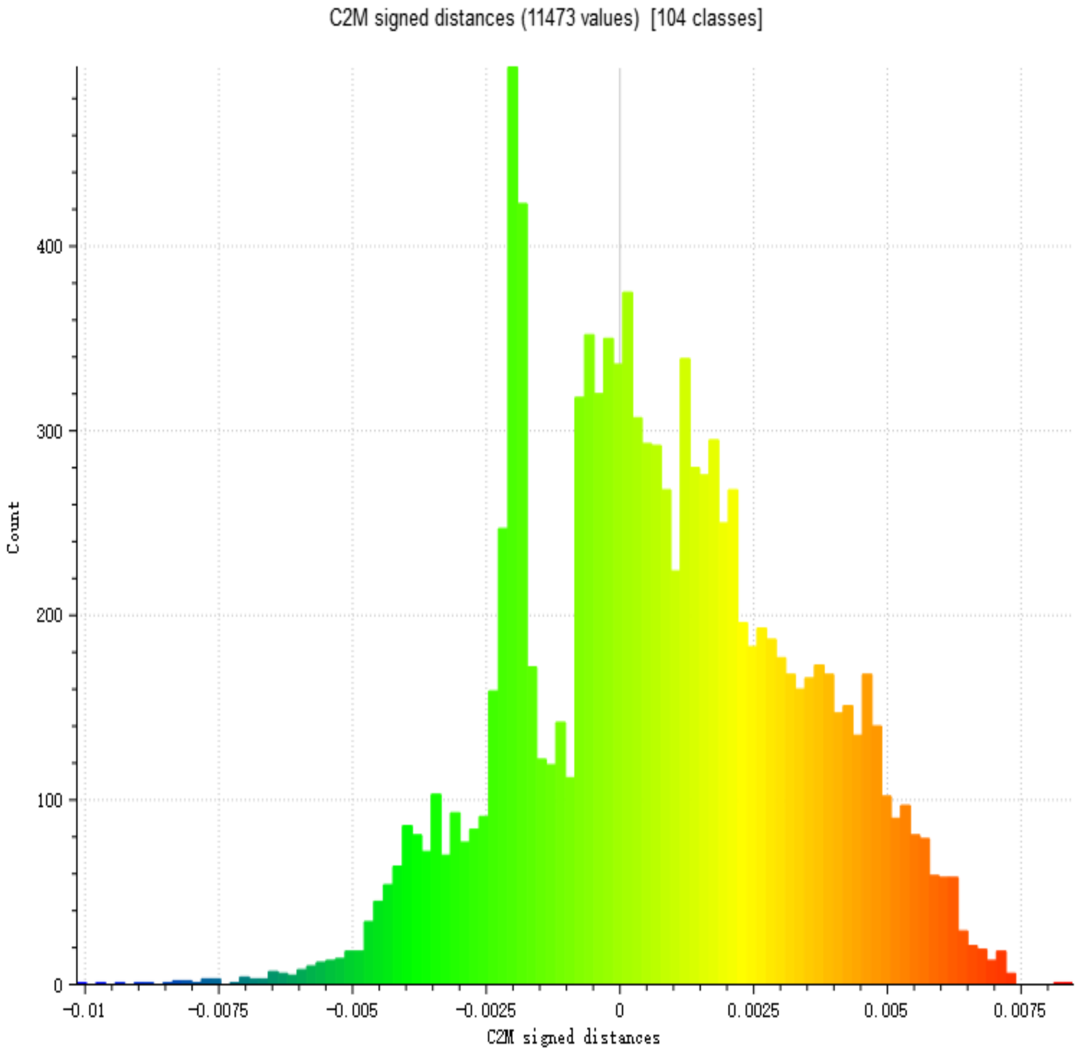

Figure 52. Patella displacement between frames 02 to 06 (CloudCompare; C2M signed distances; node set P3). Frame 02 is the driven frame and frame 06 is the target frame; the green→yellow→orange ramp indicates increasing magnitude (Units in metres (m); 0.001 m = 1 mm).

As shown in Figure 53, for the selected set nodes group P4, it is roughly distributed within the plus or minus 7 mm threshold range. Among them, 80% are roughly distributed within the range of plus or minus 3.3mm of the threshold.

P2 and P4 show higher percentages within tighter thresholds, suggesting superior node selection for medial/lateral patella regions.

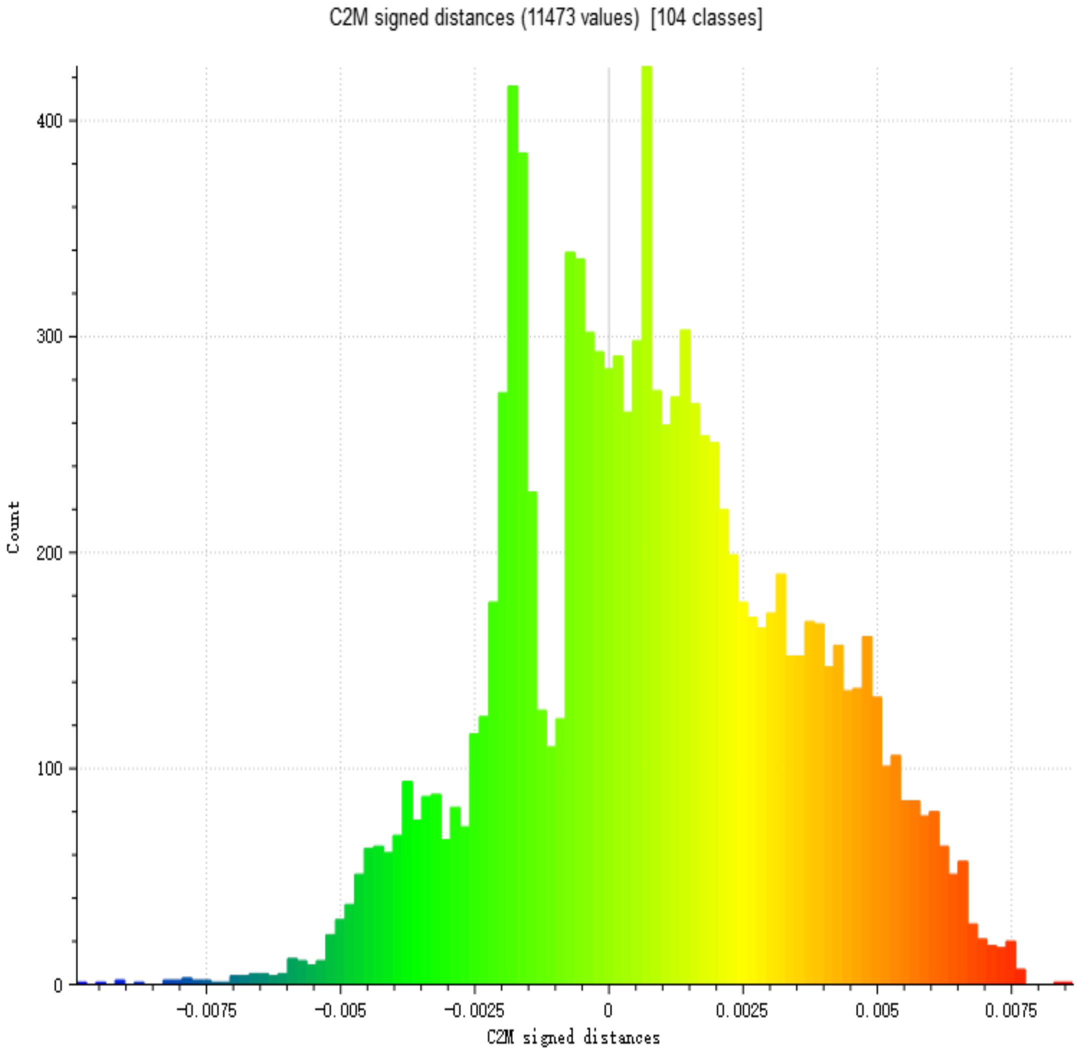

Figure 53. Patella displacement between frames 02 to 06 (CloudCompare; C2M signed distances; node set P4). Frame 02 is the driven frame and frame 06 is the target frame; the green→yellow→orange ramp indicates increasing magnitude (Units in metres (m); 0.001 m = 1 mm).

As shown in Figure 54, the spatial distribution of signed distance across the articular surface, the selected set nodes group P1 there are 11,401 node points, meaning this number of point distances was compared. It is roughly distributed within the plus or minus 3 mm threshold range. Among them, 97% are roughly distributed within the range of plus or minus 1mm of the threshold.

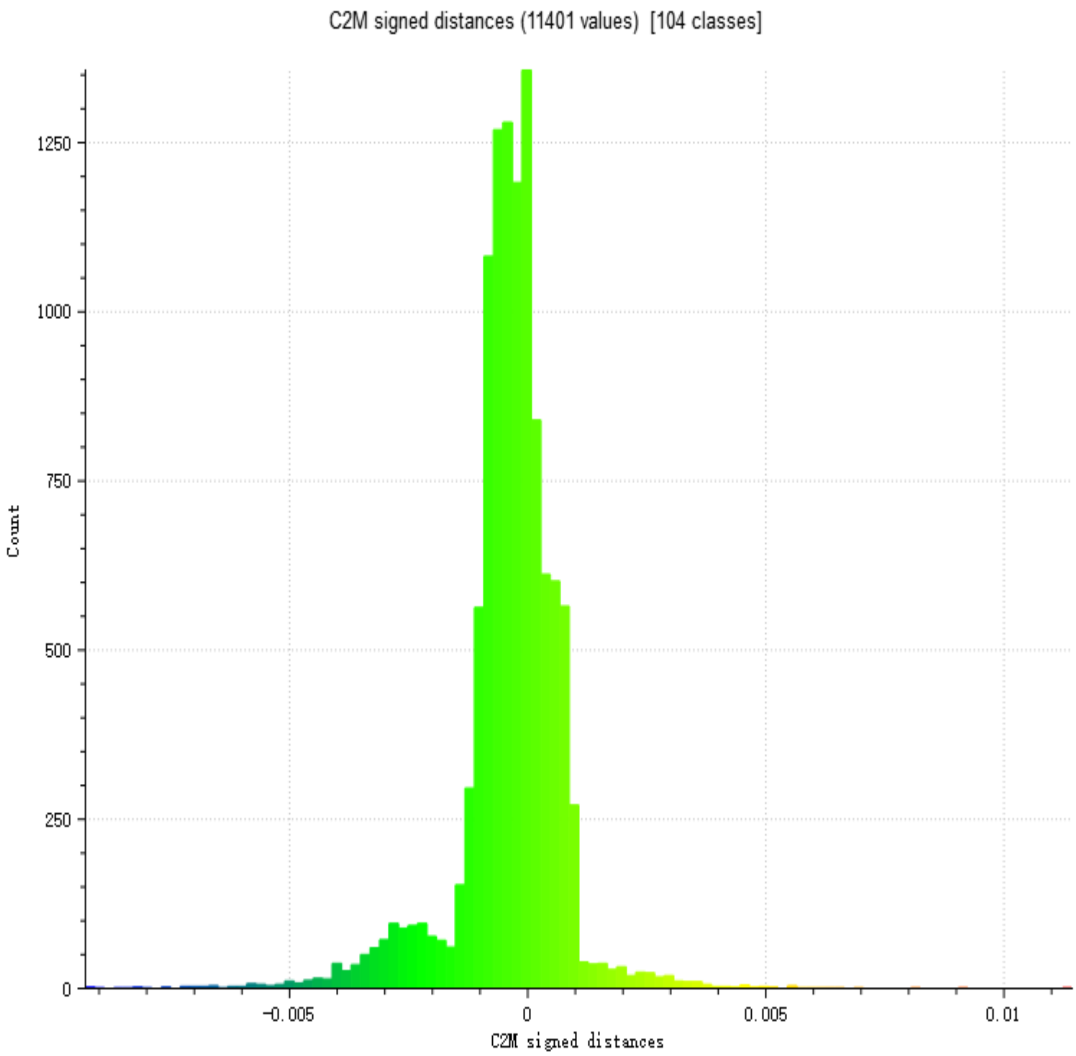

Figure 54. Patella displacement between frames 06 to 10 (CloudCompare; C2M signed distances; node set P1). Frame 06 is the driven frame and frame 10 is the target frame; the green→yellow→orange ramp indicates increasing magnitude (Units in metres (m); 0.001 m = 1 mm).

As shown in Figure 55, for the selected set nodes group P2, it is roughly distributed within the plus or minus 5mm threshold range. Among them, 94% are roughly distributed within the range of plus or minus 2.6mm of the threshold.

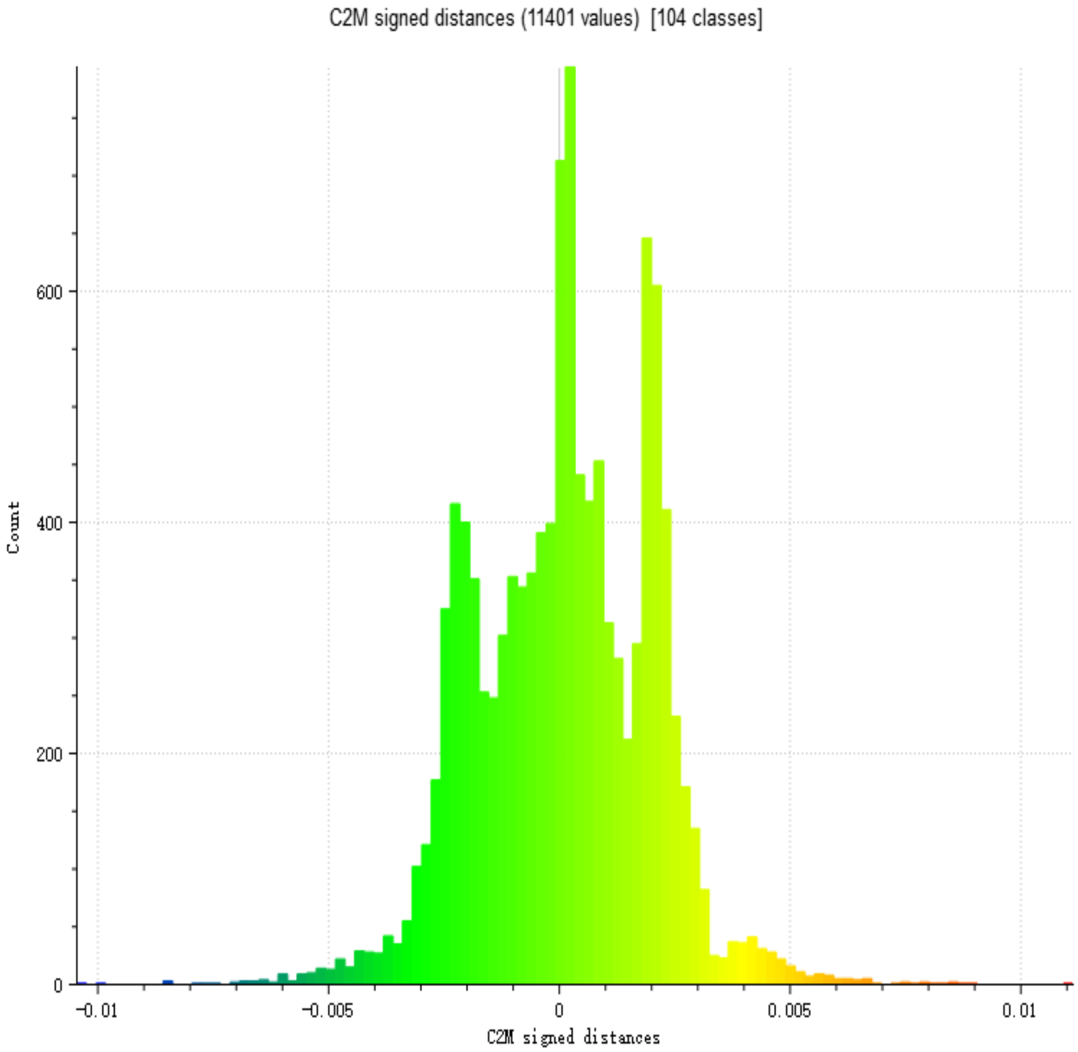

Figure 55. Patella displacement between frames 06 to 10 (CloudCompare; C2M signed distances; node set P2). Frame 06 is the driven frame and frame 10 is the target frame; the green→yellow→orange ramp indicates increasing magnitude (Units in metres (m); 0.001 m = 1 mm).

As shown in Figure 56, for the selected set nodes group P3, it is roughly distributed within the plus or minus 6 mm threshold range. Among them, 93% are roughly distributed within the range of plus or minus 3.6mm of the threshold.

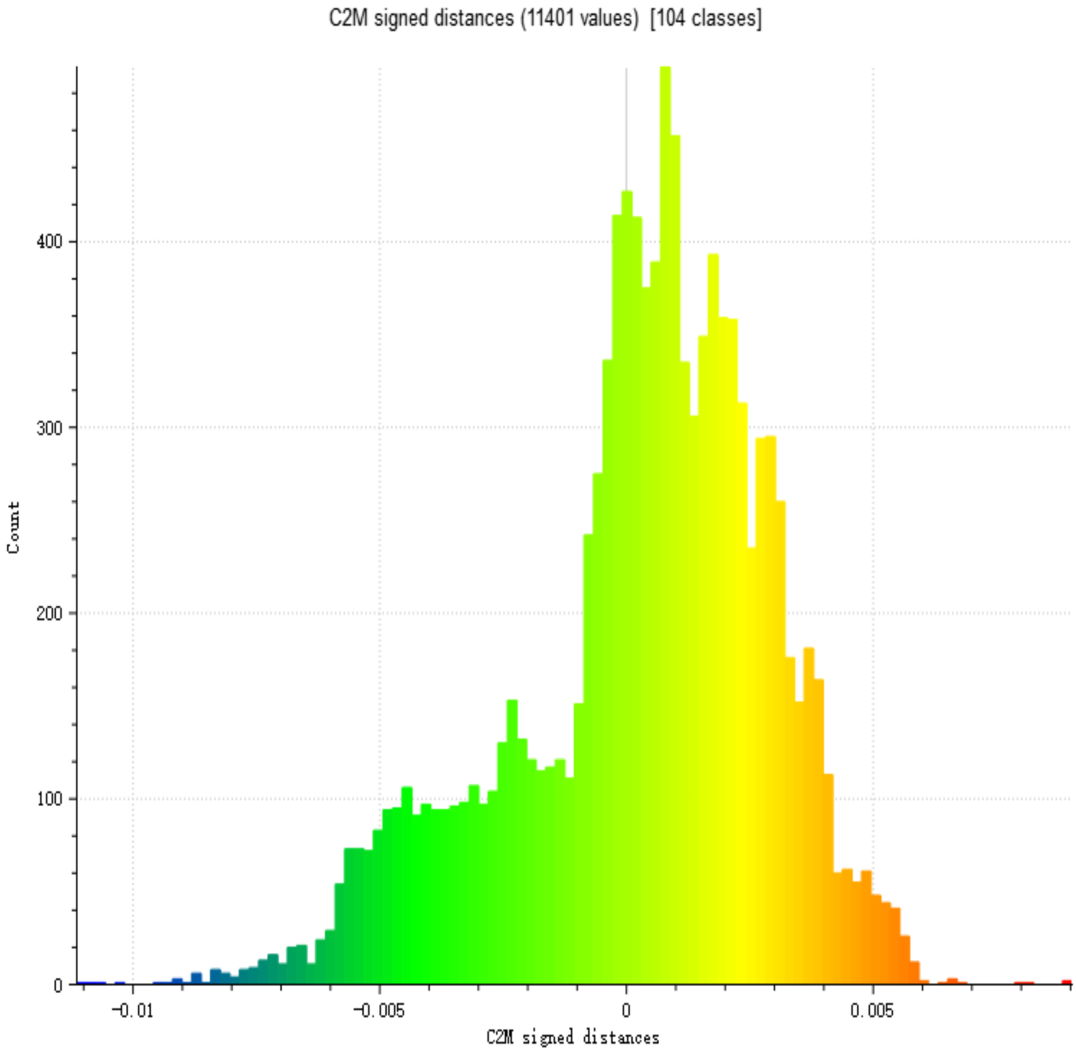

Figure 56. Patella displacement between frames 06 to 10 (CloudCompare; C2M signed distances; node set P3). Frame 06 is the driven frame and frame 10 is the target frame; the green→yellow→orange ramp indicates increasing magnitude (Units in metres (m); 0.001 m = 1 mm).

As shown in Figure 57, for the selected set nodes group P4, it is roughly distributed within the plus or minus 5 mm threshold range. Among them, 97% are roughly distributed within the range of plus or minus 2.4mm of the threshold.

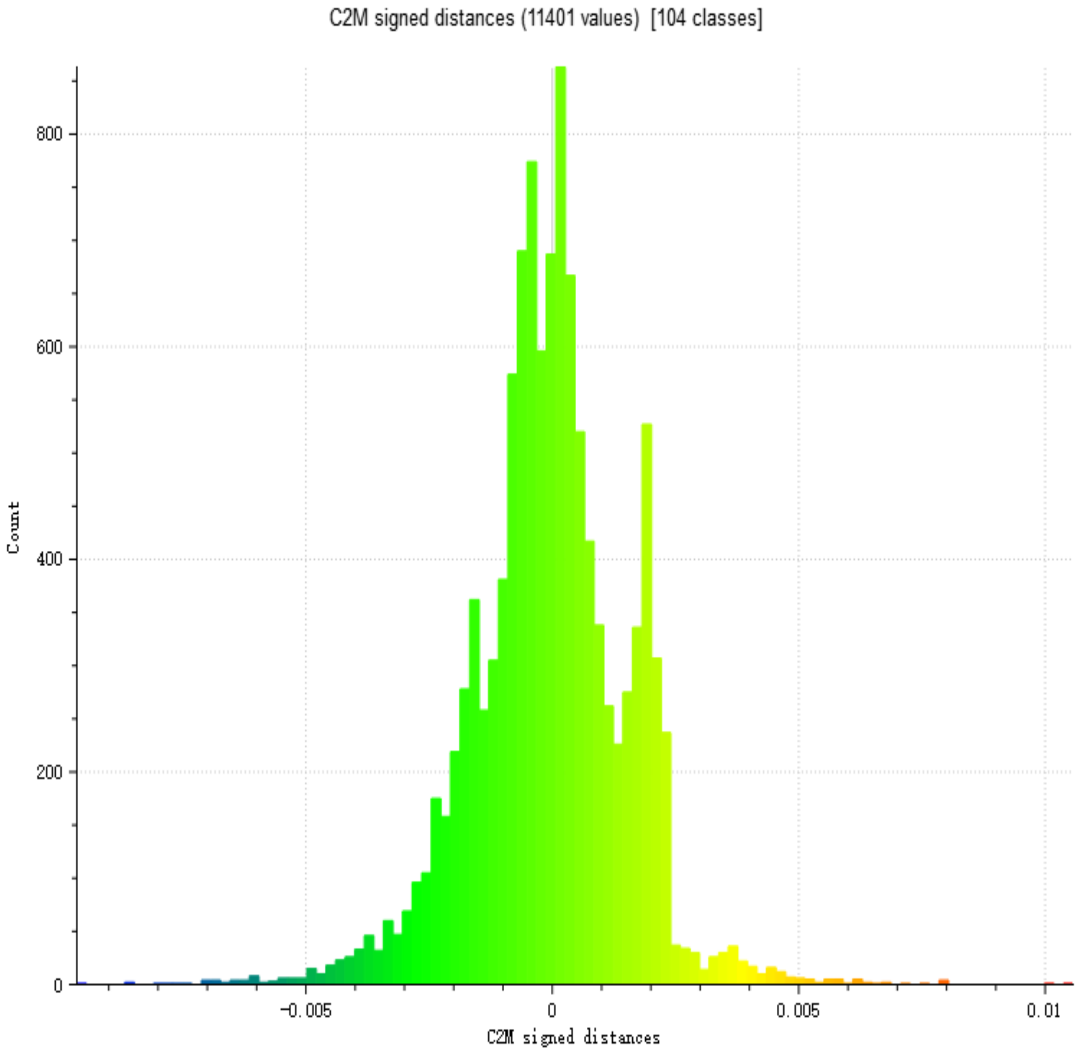

Figure 57. Patella displacement between frames 06 to 10 (CloudCompare; C2M signed distances; node set P4). Frame 06 is the driven frame and frame 10 is the target frame; the green→yellow→orange ramp indicates increasing magnitude (Units in metres (m); 0.001 m = 1 mm).

As shown in Figure 58, the spatial distribution of signed distance across the articular surface, the selected set nodes group P1 there are 12,061 node points, meaning this number of point distances was compared. It is roughly distributed within the plus or minus 2.3mm threshold range. Among them, 97% are roughly distributed within the range of plus or minus 1.4mm of the threshold.

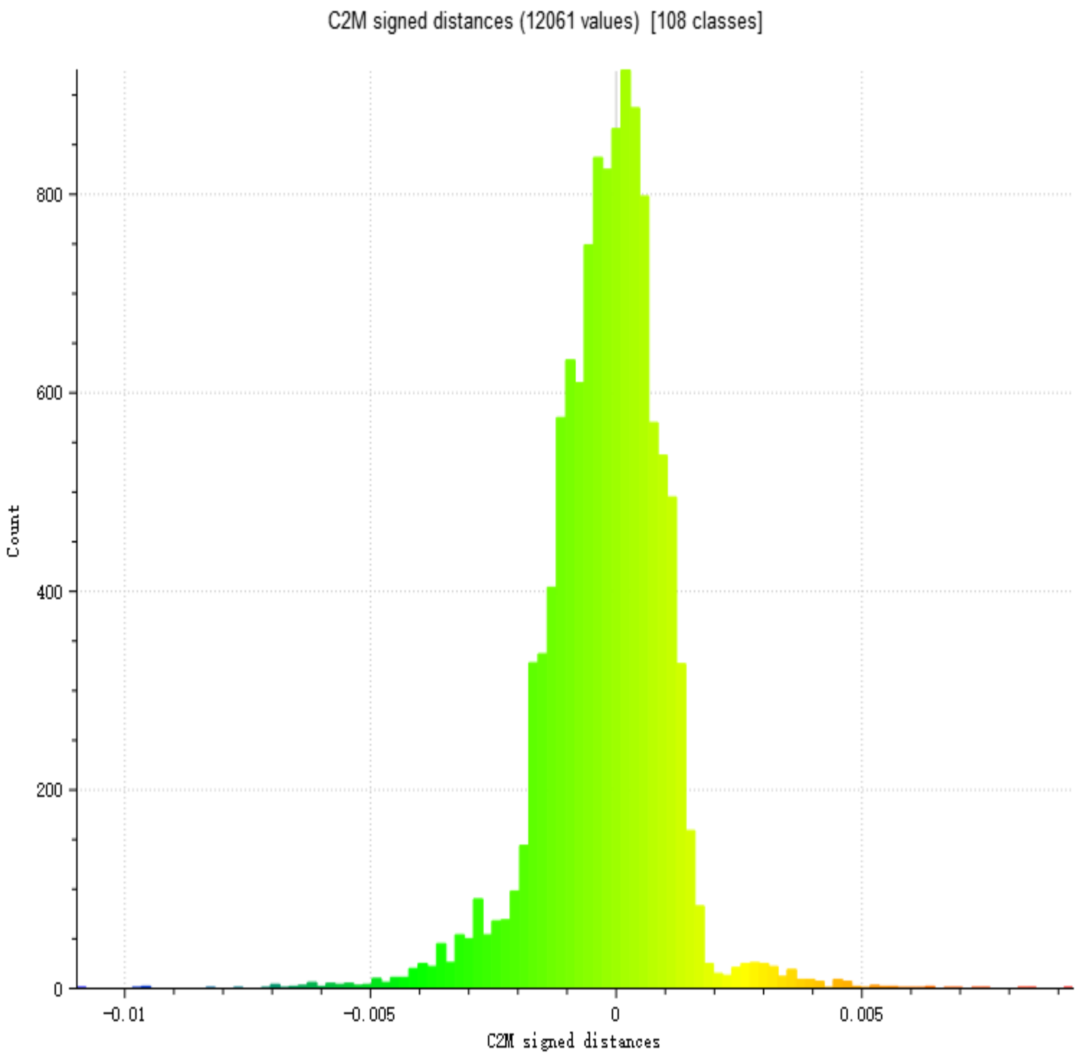

Figure 58. Patella displacement between frames 10 to 14 (CloudCompare; C2M signed distances; node set P1). Frame 10 is the driven frame and frame 14 is the target frame; the green→yellow→orange ramp indicates increasing magnitude (Units in metres (m); 0.001 m = 1 mm).

As shown in Figure 59, for the selected set nodes group P2, it is roughly distributed within the plus or minus 3.8mm threshold range. Among them, 97% are roughly distributed within the range of plus or minus 1.8mm of the threshold.

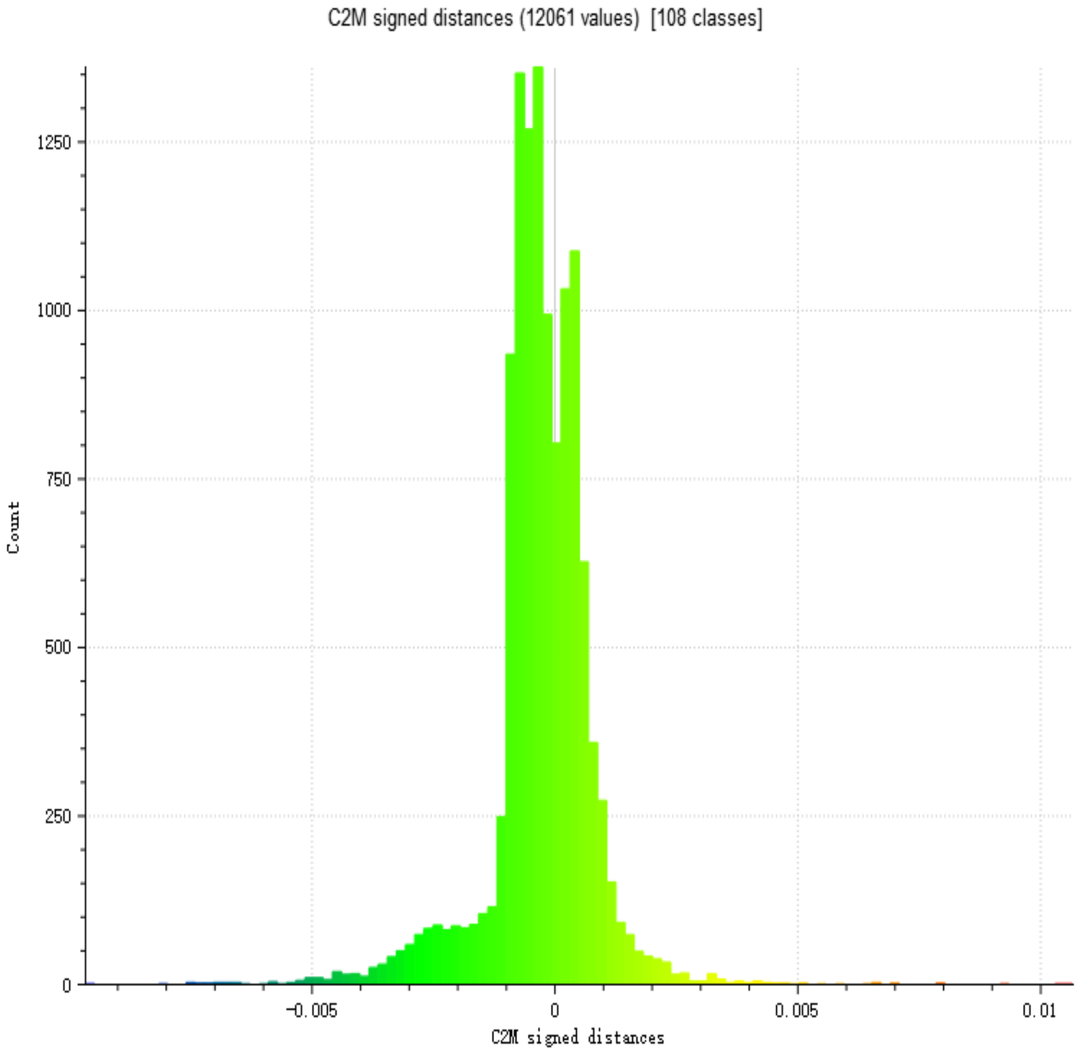

Figure 59. Patella displacement between frames 10 to 14 (CloudCompare; C2M signed distances; node set P2). Frame 10 is the driven frame and frame 14 is the target frame; the green→yellow→orange ramp indicates increasing magnitude (Units in metres (m); 0.001 m = 1 mm).

As shown in Figure 60, for the selected set nodes group P3, it is roughly distributed within the plus or minus 2 mm threshold range. Among them, 98% are roughly distributed within the range of plus or minus 1.7mm of the threshold.

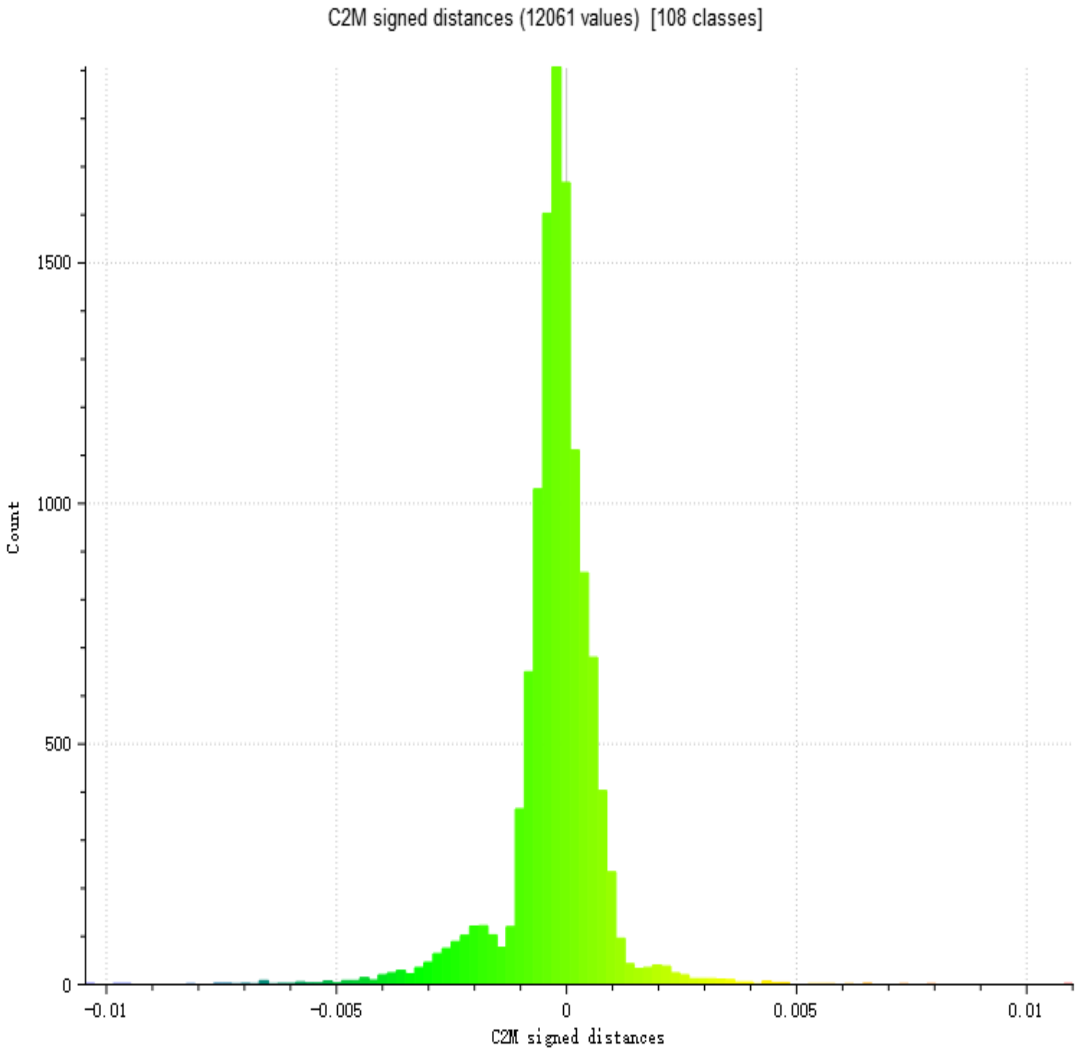

Figure 60. Patella displacement between frames 10 to 14 (CloudCompare; C2M signed distances; node set P3). Frame 10 is the driven frame and frame 14 is the target frame; the green→yellow→orange ramp indicates increasing magnitude (Units in metres (m); 0.001 m = 1 mm).

As shown in Figure 61, for the selected set nodes group P4, it is roughly distributed within the plus or minus 2.8 mm threshold range. Among them, 97% are roughly distributed within the range of plus or minus 1.2mm of the threshold.

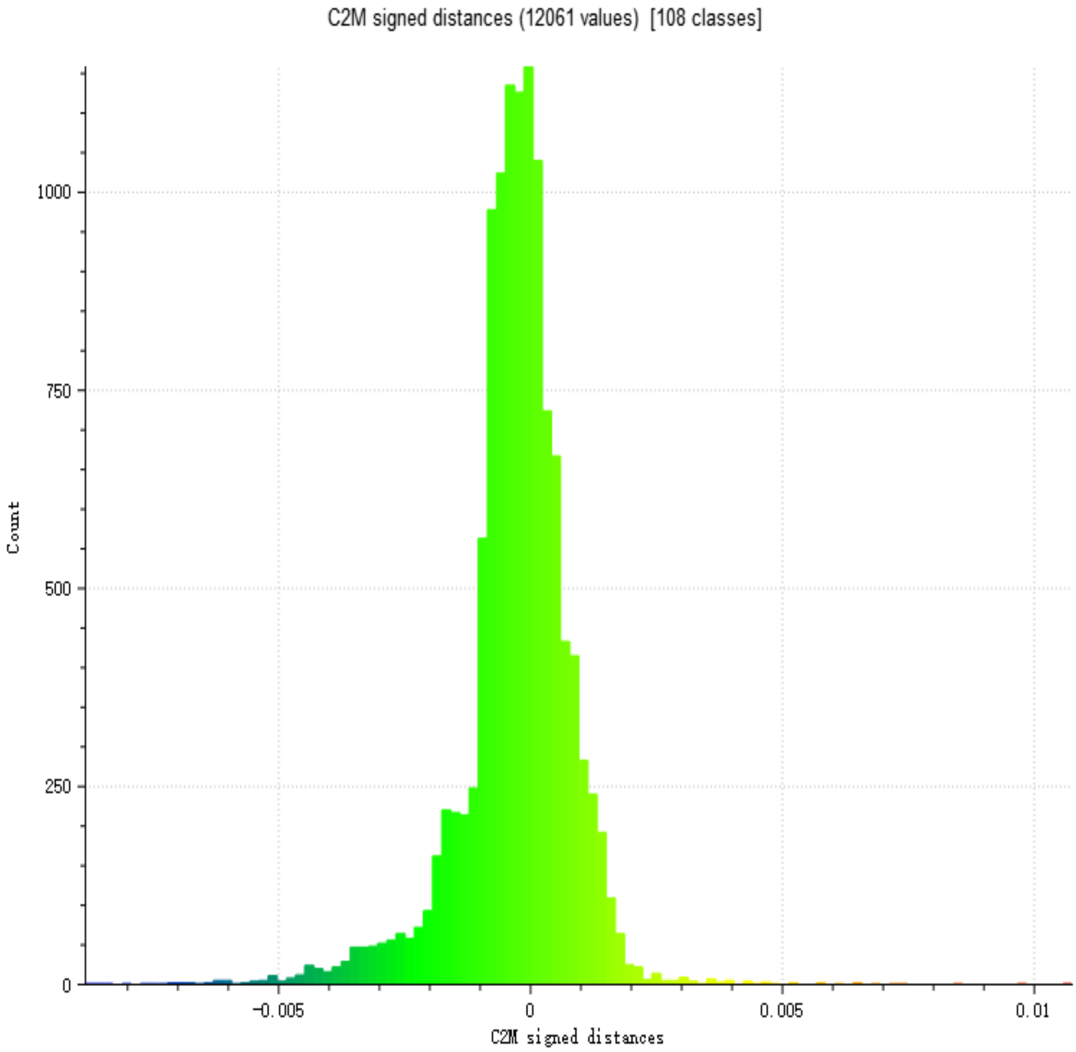

Figure 61. Patella displacement between frames 10 to 14 (CloudCompare; C2M signed distances; node set P4). Frame 10 is the driven frame and frame 14 is the target frame; the green→yellow→orange ramp indicates increasing magnitude (Units in metres (m); 0.001 m = 1 mm).

As shown in Figure 62, the spatial distribution of signed distance across the articular surface, the selected set nodes group P1 there are 10,996 node points, meaning this number of point distances was compared. It is roughly distributed within the plus or minus 3mm threshold range. Among them, 97.5% are roughly distributed within the range of plus or minus 1.6mm of the threshold.

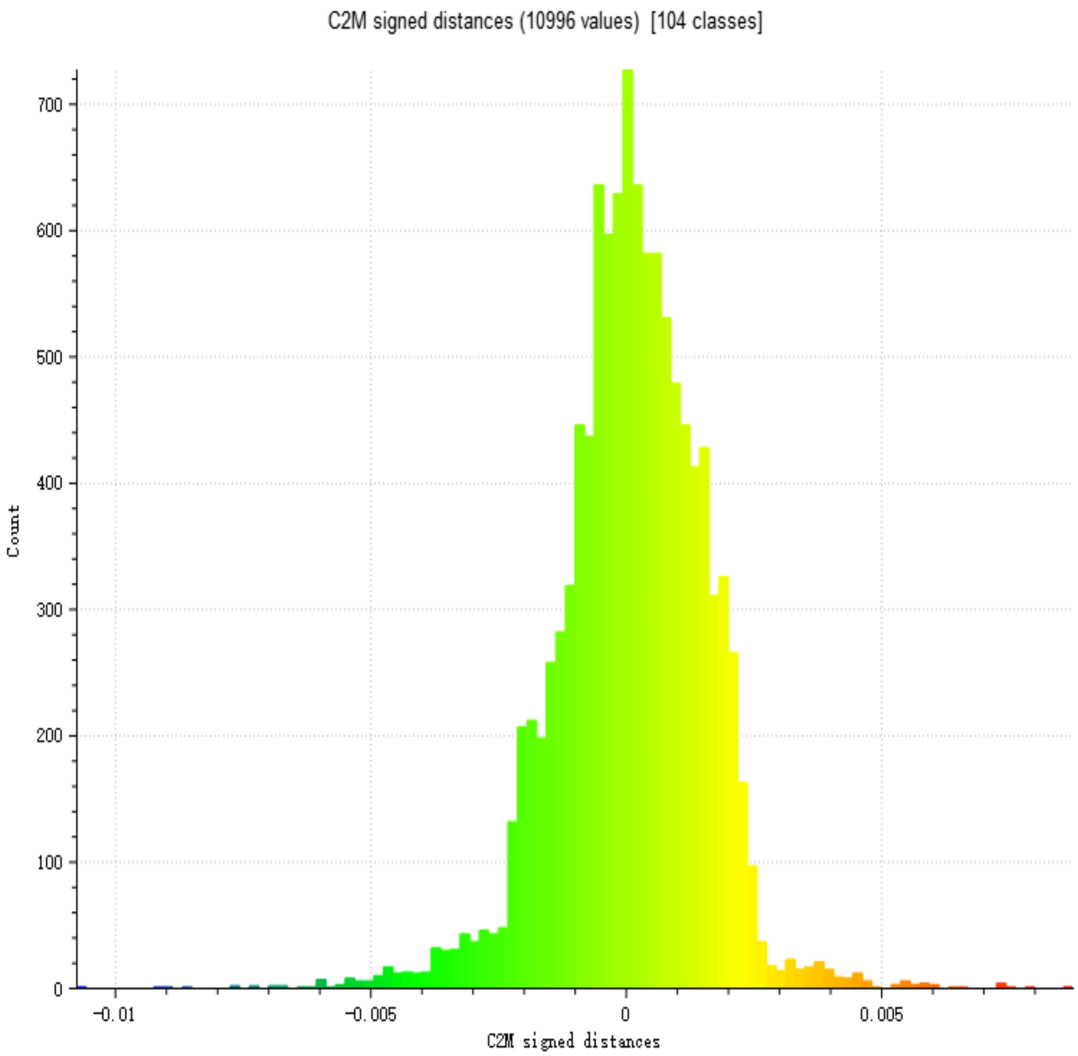

Figure 62. Patella displacement between frames 14 to 18 (CloudCompare; C2M signed distances; node set P1). Frame 14 is the driven frame and frame 18 is the target frame; the green→yellow→orange ramp indicates increasing magnitude (Units in metres (m); 0.001 m = 1 mm).

As shown in Figure 63, for the selected set nodes group P2, it is roughly distributed within the plus or minus 3.8mm threshold range. Among them, 96% are roughly distributed within the range of plus or minus 2mm of the threshold.

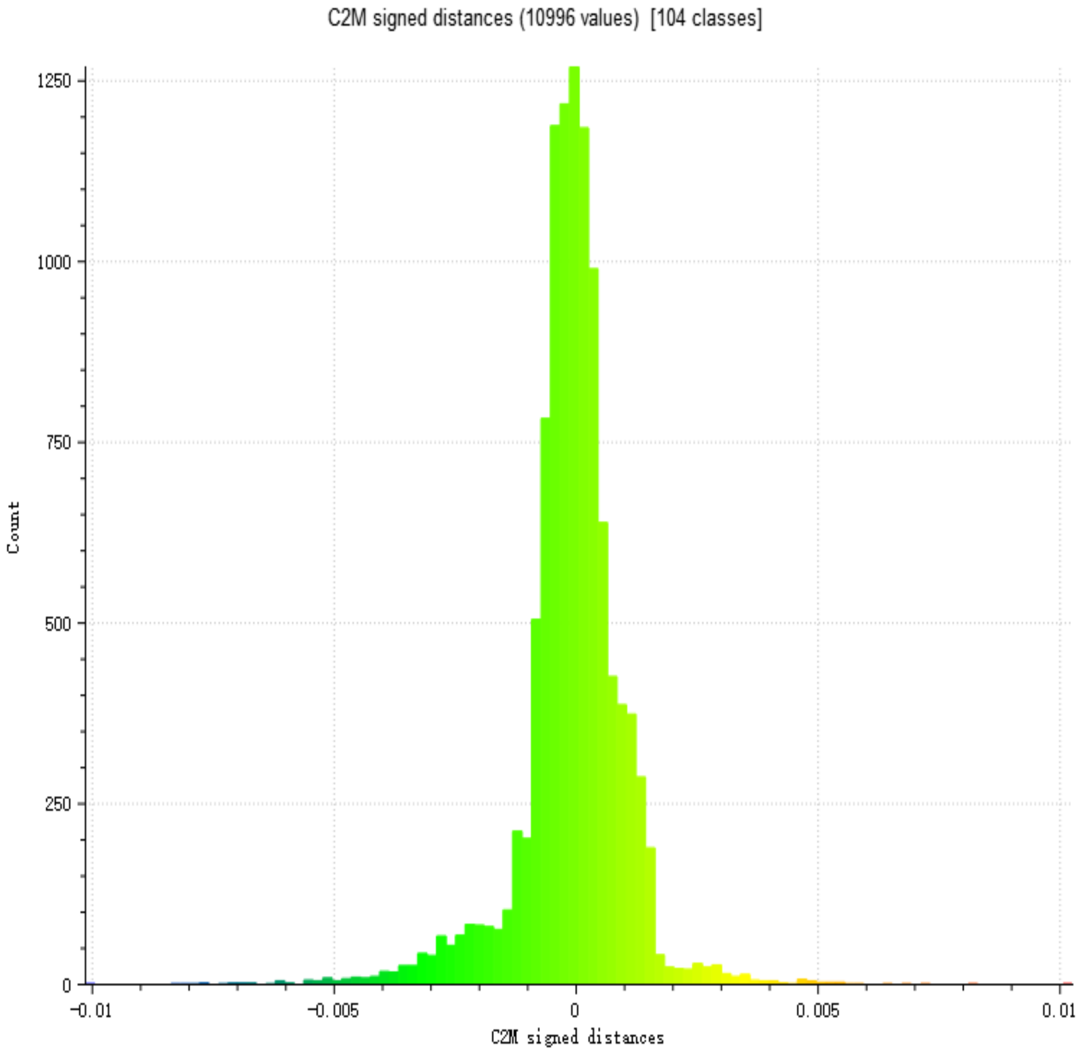

Figure 63. Patella displacement between frames 14 to 18 (CloudCompare; C2M signed distances; node set P2). Frame 14 is the driven frame and frame 18 is the target frame; the green→yellow→orange ramp indicates increasing magnitude (Units in metres (m); 0.001 m = 1 mm).

As shown in Figure 64, for the selected set nodes group P3, it is roughly distributed within the plus or minus 3.5 mm threshold range. Among them, 98% are roughly distributed within the range of plus or minus 1.9mm of the threshold.

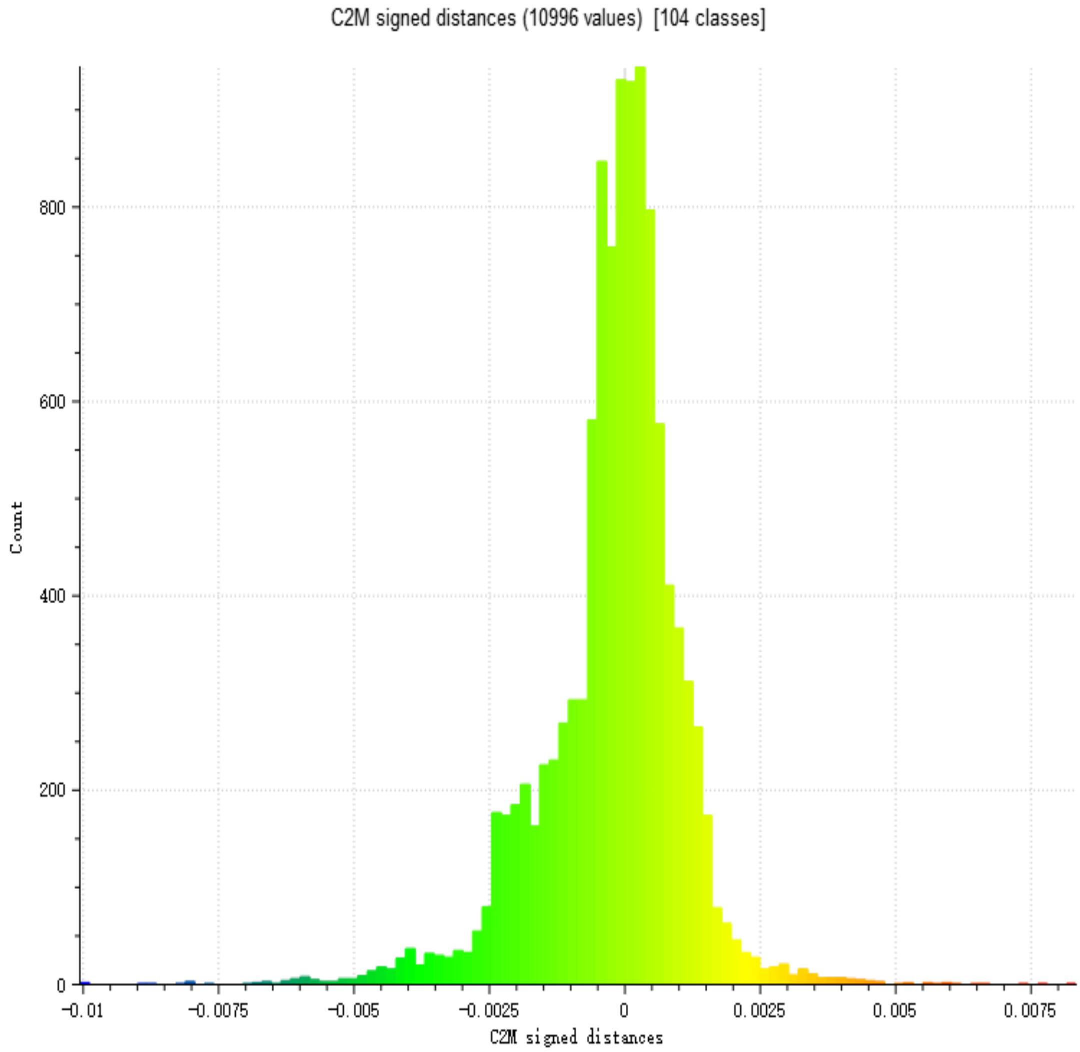

Figure 64. Patella displacement between frames 14 to 18 (CloudCompare; C2M signed distances; node set P3). Frame 14 is the driven frame and frame 18 is the target frame; the green→yellow→orange ramp indicates increasing magnitude (Units in metres (m); 0.001 m = 1 mm).

As shown in Figure 65, for the selected set nodes group P4, it is roughly distributed within the plus or minus 2.9 mm threshold range. Among them, 97% are roughly distributed within the range of plus or minus 1.5mm of the threshold.

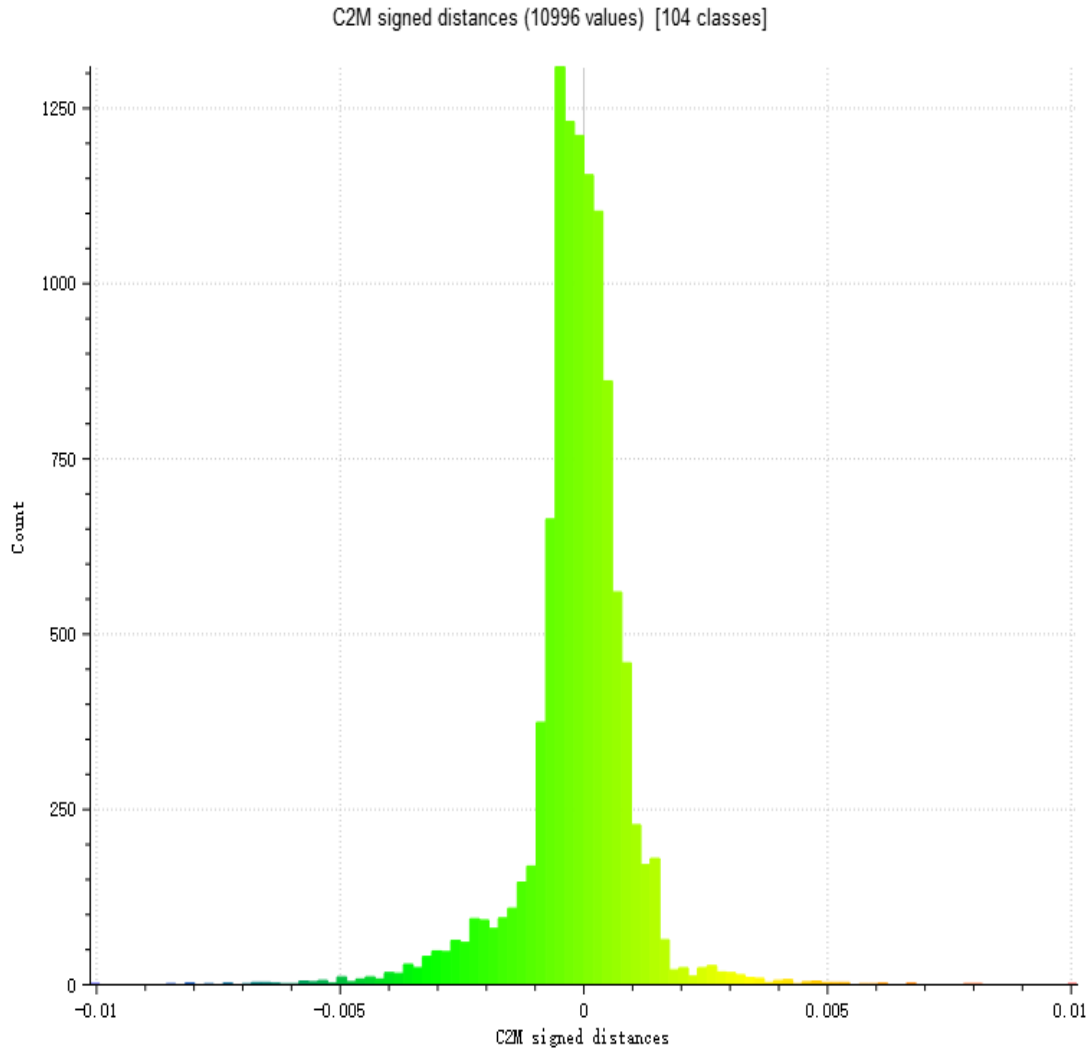

Figure 65. Patella displacement between frames 14 to 18 (CloudCompare; C2M signed distances; node set P4). Frame 14 is the driven frame and frame 18 is the target frame; the green→yellow→orange ramp indicates increasing magnitude (Units in metres (m); 0.001 m = 1 mm).

Across all transitions, the signed-distance distributions indicate that the majority of surface points lie within a few millimetres, demonstrating broadly consistent agreement between the driven and target configurations. In the early transition (F02–F06), distances are generally contained within approximately ±7–7.5 mm, with the bulk of points concentrated within tighter bounds (e.g., ~75–86% within ±2.8–4.0 mm, depending on the node set). In subsequent transitions (F06–F10 and F10–F14), the distributions tighten further, with most points falling within ±2–5 mm, and a high proportion clustered within ~±1–3.6 mm. In the terminal transition (F14–F18), distances remain comparably constrained (approximately ±2.9–3.8 mm overall, with ~96–98% of points within ~±1.5–2.0 mm, depending on the node set). Collectively, these maps confirm that the residual mismatch is spatially heterogeneous—dominated by localised surface regions—rather than reflecting a uniform global offset, and they provide an objective basis for comparing the relative performance of the patellar node sets (P1–P4) across the extension sequence.

4.6 Tibia matching analysis results based on cloud comparison

In the biomechanical analysis, tibial tracking was characterised using a node-based approach, in which discrete mesh nodes collectively represent the tibial spatial configuration. A matching strategy based on 16 node-set combinations distributed across the femur and patella was implemented to quantify tibial displacement behaviour during dynamic patellofemoral interactions. This workflow incorporated a temporal dimension by performing pairwise comparisons between successive frame-specific models. Each neighbouring frame pair represents a discrete time step along the flexion–extension continuum, enabling a detailed assessment of tibial displacement trajectories across the full motion sequence.

For the interval spanning frames 02–06 (65°–48°), a total of 30,873 nodes were compared. For the P1-F1 to P1-F4 series, deviations were predominantly confined within −11 mm to +8.7 mm, with an average of 85% of values within ±5 mm. The P2-F1 to P2-F4 series showed a comparable distribution (−11 mm to +8.6 mm), with 86.5% of values within ±5 mm. For P3-F1 to P3-F4, the range widened slightly (−13 mm to

+13 mm), although 88.3% of values still fell within ±5 mm. The P4-F1 to P4-F4 series yielded a distribution similar to P2 (−11 mm to +8.6 mm), with 87.2% of values within ±5 mm.

During frames 06–10 (48°–32°), 29,755 nodes were compared. The P1-F1 to P1-F4 series showed deviations between −18 mm and +12 mm, with 68% of values within ±5 mm. The P2-F1 to P2-F4 series exhibited a broader range (−18 mm to +15 mm), with 65.9% of values within ±5 mm. The P3-F1 to P3-F4 series produced the widest distribution (−19 mm to +16 mm), with 63.9% of values within ±5 mm. By contrast, P4-F1 to P4-F3 demonstrated a narrower range (−13 mm to +9.6 mm) and the highest proportion, with 74.8% of values within ±5 mm.

For frames 10–14 (32°–16°), 33,445 nodes were analysed. The P1-F1 to P1-F4 series exhibited deviations between −11 mm and +12 mm, with 83.3% of values within ±5 mm. The P2-F1 to P2-F4 series showed a range of −12 mm to +12 mm, with 84.25% of values within ±5 mm. For P3-F1 to P3-F4, deviations extended from −11 mm to +13 mm, with 82.1% within ±5 mm. The P4-F1 to P4-F4 series demonstrated similar results (−10 mm to +13 mm), with 82.8% of values within ±5 mm.

Finally, for frames 14–18 (16°–0°), 34,542 nodes were compared. The P1-F1 to P1-F4 series exhibited deviations between −10 mm and +10 mm, with 91% of values within ±5 mm. For P2-F1 to P2-F4, the range was −9 mm to +10 mm, with 91.7% of values within ±5 mm. The P3-F1 to P3-F4 series showed a comparable distribution (−9 mm to +10 mm) and the highest proportion within ±5 mm (92.1%). The P4-F1 to P4-F4 series displayed deviations from −11 mm to +10 mm, with 91% of values within ±5 mm.

Overall, these results demonstrate that the spatial distribution of node-based tibial tracking deviations varies across the sequential flexion intervals. The initial interval (65°–48°) exhibits relatively constrained deviations with a high proportion of nodes within ±5 mm. In contrast, the mid-range interval (48°–32°) shows the broadest deviation ranges, indicating increased sensitivity during this transitional phase of patellofemoral articulation. The subsequent interval (32°–16°) demonstrates a partial reduction in deviation spread, whereas the terminal interval (16°–0°) presents the most constrained distributions and the highest proportion of nodes within ±5 mm. Across all intervals, however, the majority of nodal deviations remain tightly centred around zero, supporting the robustness of the node-based workflow for capturing tibial kinematics during dynamic patellofemoral interactions.

For completeness, the detailed CloudCompare cloud-to-mesh (C2M) signed-distance analysis, including the full distribution outputs and associated summary statistics for each flexion interval (Frames 02–06, 06–10, 10–14, and 14–18), is reported in Appendix C1–C4. The tibial C2M signed distance maps are interpreted using the same convention as in Section 4.5. CloudCompare outputs distances in metres (m).

Flexion Interval	Node Count	Threshold Range (mm)	Within ±5 mm (%)
Frame 02-06(65°–48°)	30873	-13 to +13	85 -88.3
Frame 06-10(48°–32°)	29755	-19 to +16	63.9 – 74.8
Frame 10-14(32°–16°)	33445	-12 to +13	82.1 – 84.25
Frame 14-18(16°–0°)	34542	-11 to +10	91 – 92.1

Table 16. Tibia node-based tracking error summary (Units: mm)

5 Discussion and Conclusion

This study presents a comprehensive exploration of knee biomechanics by integrating four-dimensional computed tomography (4dCT) with finite element analysis (FEA). This innovative methodology captures ligament mechanics and knee joint dynamics across a full range of motion, using sequential 4dCT imaging at five frames (02, 06, 10, 14, and 18) to cover approximately 65 degrees of extension. By enabling detailed analysis of ligament displacement and tension, this approach provides insights into ligament strain distribution and joint loading patterns during movement and serves as a proof-of-concept for in-situ force estimation in a living knee.

Previous work by Attard [241] demonstrated the feasibility of using 4dCT to extract knee kinematics, including six-degrees-of-freedom motion, contact point trajectories, and the axial centre of rotation in both healthy and replaced knees. While this represented an important step forward in applying dynamic imaging to orthopaedics, the study was confined to describing kinematic behaviour. It did not quantify the underlying ligament tensions or model the internal load transfer mechanisms that fundamentally determine knee stability. Moreover, the use of bespoke MATLAB-based software, though efficient for extracting motion patterns, was not designed to incorporate the mechanical properties of soft tissues or simulate cartilage-cartilage interactions.

The present work advances this line of research by integrating 4dCT imaging with finite element analysis (FEA) to provide a deeper biomechanical interpretation. Unlike Attard's rigid-body and kinematic description, the FEA-based model developed here accounts for subject-specific bone and cartilage geometries, anatomically defined ligament insertion regions, and iterative tension-balancing simulations. This enables the estimation of in vivo ligament forces alongside the observed joint motion. Importantly, the current model captures cartilage contact mechanics, producing spatially resolved stress distributions that cannot be obtained from simplified rigid-body or spring-based approaches.

What a simpler model would (and wouldn't) provide. A considerably simplified pipeline e.g., rigid-body bones driven by measured motion with linear spring ligaments and low/zero friction could reproduce the gross kinematics observed in 4dCT and yield qualitative trends in constraint forces. However, such a model cannot provide credible cartilage contact pressures or stress distributions, is prone to non-physiological separation or drift without additional stabilising constraints and offers limited insight into how small changes in alignment or soft-tissue balance redistribute joint loads. By contrast, the present 4dCT-informed FEA captures deformable contact and load transfer across the joint surfaces, allowing spatially resolved interpretations.

This distinction highlights a fundamental difference in scope: Attard's [241] model provides insight into "how" the knee moves, whereas the present study addresses both "how" and "why" the knee moves by linking motion to the mechanical contributions of individual ligaments and soft tissues. In doing so, the methodology not only advances the fidelity of computational knee models but also offers clinically relevant outputs that can inform ligament balancing strategies in total knee replacement (TKR). Compared to previous frameworks, this approach provides a more comprehensive and physiologically realistic representation of native knee function.

The primary aim of this research is to advance methodologies for estimating ligament tension and ensuring joint stability. While these goals have clear relevance to clinical and biomechanical research, any direct clinical claims should be considered preliminary given that the data derive from a single healthy participant and under simplified loading. By quantifying dynamic ligament behaviour, the study establishes a methodological paradigm that future work may build upon to inform soft tissue balancing in total knee replacement (TKR) and to support predictive modelling for orthopaedic interventions.

This work develops and validates an FEA model that goes beyond conventional static models and traditional soft-tissue management techniques (e.g., gap and force balancing). Unlike historical approaches that rely on fixed pre-tension assumptions, the integration of dynamic 4dCT enables frame-to-frame assessment of knee motion.

This captures interactions between ligament strain and joint stability under the given physiological scenario, addressing limitations of static and overly simplified models. Importantly, although simplified models with ligaments represented as linear elastic springs may reproduce coarse trends in force–flexion relationships, such models generally cannot resolve intra-articular contact pressures/stress distributions at cartilage and meniscal surfaces. The benefits of the FEA approach extend beyond tension estimation to deriving spatially resolved contact pressures, which are essential for analysing cartilage wear, predicting osteoarthritis progression, and evaluating implant longevity in TKR scenarios. The anatomically informed FEA used here therefore provides added value by enabling analysis of contact mechanics—critical for understanding degeneration, pain mechanisms, and implant wear.

The iterative methodology aligns simulated knee movements with 4dCT-derived kinematics, enhancing internal validation. Final ligament tensions were consistent across initial pre-tension estimates (100 N and 200 N), demonstrating numerical robustness. Notably, the posterior cruciate ligament (PCL) and lateral collateral ligament (LCL) exhibited near-zero tension across the sampled flexion range under the specific boundary conditions tested, which differs from some reports that apply alternative loads or muscle forces. This highlights the sensitivity of ligament forces to boundary conditions and activity context.

The study segmented 4dCT data into nine discrete frame models, covering 65 degrees of extension. DICOM data were processed into three-dimensional solid models, incorporating soft-tissue architectures and mesh subdivision techniques to preserve anatomical integrity. Five frames (02, 06, 10, 14, and 18), corresponding to flexion angles from ~65° to 0° (full extension), were selected for detailed analysis. This pipeline ensures high fidelity in capturing dynamic anatomical changes.

The FEA model achieved consistent convergence through iterative calculations, estimating ligament tensions with minimal tibial translation. The anterior cruciate ligament (ACL) peaked at ~20° of flexion, the medial collateral ligament (MCL) engaged beyond ~35°, and the patellar tendon consistently carried the highest load, underscoring its central role in stability. Convergence with <1% variation across additional preloads supports the model's reliability and insensitivity to starting conditions.

The study systematically examines factors affecting displacement associated with passive tibial traction, revealing interactions between joint anatomy, ligament properties, and external forces. Section 3.5.1 details the methodology for modelling passive knee motion and aligning the patella and femur using node-specific selection to ensure high accuracy. This contributes to the model's predictive credibility.

The biomechanical optimization of the ACL at 20 degrees of flexion is a key finding, aligning with the weight acceptance phase of gait. At this angle, the ACL counters anterior tibial translation induced by ground reaction forces and quadriceps contraction, supported by the medial tibial spine and intercondylar notch, while the PCL remains lax. This is in agreement with other literature (Mizuno et al., 2009; Weinhandl et al., 2016) giving confidence to our methods [254-255].

The novelty of the present study lies in its simultaneous estimation of tensile forces across five knee ligament structures, a significant advancement over cadaveric assessments, which are typically confined to evaluating single ligaments. The results of this study are compared with existing literature [165] [256-259], as illustrated in the accompanying Figure 66. This comparison highlights that the current approach (Figure 66-f) more comprehensively elucidates the relationships between in the situ forces and flexion angles for the PT, LCL, MCL, ACL, and PCL under conditions of ligament and patellar tendon preload.

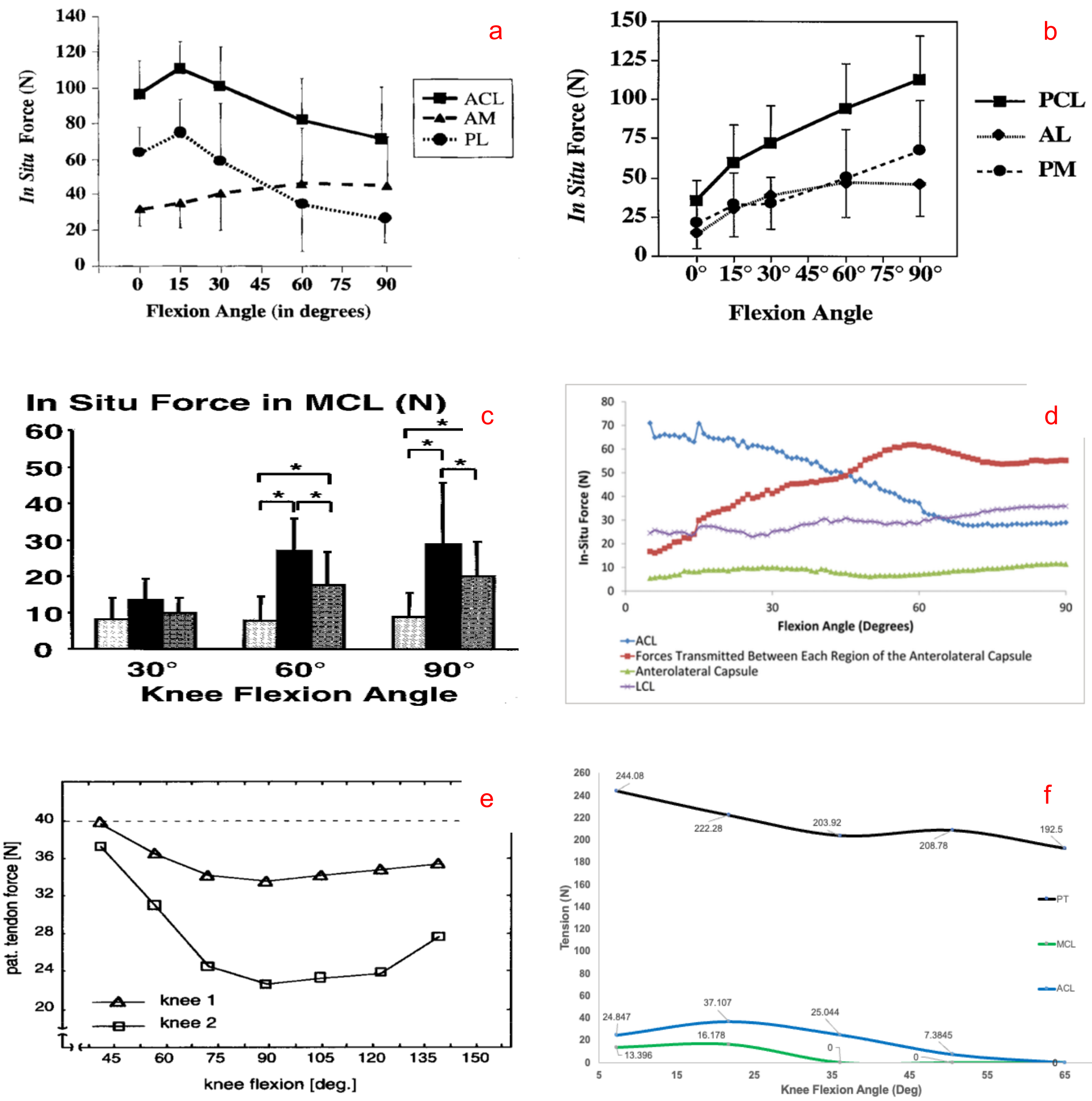

Figure 66. Comparison of previous research results with the results of this study.

In the Figure 66, a)Magnitude of in situ force in the intact anterior cruciate ligament (ACL), anteromedial bundle (AM), and posterolateral bundle (PL) under 110 N of applied anterior tibial load [256]; b) In situ force in the PCL and in the anterolateral (AL) and posteromedial (PM) bundles under 110 N of posterior tibial load with respect to flexion angle [165]; c) In situ forces in MCL in response to an anterior 67N tibial load at 30°, 60°, and 90° of knee flexion (mean ±SD). Light Gray – intact, black – ACL deficient, and dark Gray – ACL reconstructed. [257]; d) The in-situ force in the LCL and ACL and the anterolateral structures throughout the range of flexion for the intact knee.

[258]; e) Patellar tendon tension as a function of knee flexion, for knee 1 (triangles) and for knee 2 (squares). The dotted line corresponds to the applied 40 N quadriceps force [259]; f) The results provided by this study, ligament tension along the flexion curve was systematically estimated with an initial pretension of 100N.

Patellar and femoral displacements were tracked across frames 02 to 18 using the nearest node approximation method. Patellar nodes showed average Euclidean displacements of 0.012 ± 0.001 m between frames 02 and 06, compared to 0.006 ± 0.001 m for femoral nodes, reflecting greater patellar mobility. Matching errors across frame pairs (F02–F06, F06–F10, F10–F14, F14–F18) ranged from 1.775 mm to 9.268 mm, with the P1 node set often yielding the lowest errors (e.g., 1.778 mm in F02). Higher errors in F06 (e.g., 9.268 mm for P3) suggest frame-specific complexities, possibly due to motion dynamics or node selection challenges. Cloud Compare analysis of patellar point clouds showed 75–86% of nodes within ±2.8–4 mm for F02–F06, improving to 93–98% within ±1–3.6 mm in later frames, indicating enhanced alignment accuracy as flexion progresses.

Tibial displacement analysis combined direct node analysis and Cloud Compare. Direct analysis computed displacements for three nodes per frame, with mean errors between manual calculations and ANSYS simulations ranging from 1.86 mm to 2.66 mm for F02–F06. Frame F06–F10 exhibited the highest errors (5.65–13.44 mm), while F14–F18 showed the lowest (4.13–6.36 mm). Cloud Compare analysis of tibial point clouds revealed broader error distributions: 85–88.3% of nodes within ±5 mm for F02–F06, dropping to 63.9–74.8% for F06–F10, and improving to 91–92.1% for F14–F18. These findings highlight the limitations of nodal analysis for complex tibial kinematics and the superiority of point cloud methods for comprehensive alignment evaluation.

The 4dCT acquisition parameters are given in Section 3.1.1 (e.g., voxel/slice thickness ≈ 0.625 mm, 512 × 512 matrix, FOV ≈ 320 mm). These settings govern spatial sampling and partial-volume effects. Compared with central regions, the scan periphery or motion extremes tend to show larger registration and distance-map errors owing to lower SNR and anisotropy. With fixed acquisition, single boundary-location uncertainty can be conservatively treated as voxel-scale, and aggregate uncertainty increases after smoothing, discretisation, and contact computation. Accordingly, differences near the voxel scale should be interpreted cautiously, whereas effects well above it are more likely to reflect genuine kinematic/contact behaviour. Overall, DICOM resolution in this study principally bounds the confidence intervals of geometric and mechanical quantities and motivates future work on higher resolution or reconstruction optimisation, multi-modal registration, and resolution-sensitivity analyses with local mesh refinement to quantify and reduce uncertainty.

The low errors in patellar and tibial tracking demonstrate the model's high fidelity, particularly for proximal joint structures. However, larger distal tibial errors suggest areas for refinement, such as improving 4dCT resolution or incorporating soft tissue deformation models. Three factors contribute to these errors: (1) the greater distance from the joint centre amplifies minor angular misalignments; (2) soft tissue deformations near the distal tibia introduce imaging artifacts; and (3) 4dCT resolution degrades at the scan periphery, reducing segmentation accuracy (Liang et al., 2018) [200].These findings align with the literature, which acknowledges that 100% accuracy kinematic matching remains elusive due to anatomical variability and computational constraints (Dastgerdi et al., 2023; Navacchia et al., 2016). [158][232]

The 4dCT-FEA model's segmentation and tension estimation exhibit high computational reliability, with converged ligament tensions aligning with biomechanical expectations. Patellar tracking errors are lower than tibial errors due to simpler motion dynamics. Cloud Compare's point cloud approach enhances alignment evaluation, exposing limitations in nodal methods for complex tibial kinematics. The ACL's optimization at 20 degrees links passive knee structures to functional stability during gait. While this methodology advances biomechanical modelling, distal tibial errors underscore the need for further refinements to achieve closer kinematic matching, a challenge unmet in existing research.

Collectively, the node-specific analyses and surface-wide consistency provide a quantitative foundation for subject-specific biomechanics. Crucially, because this framework can be extended to compute intra-articular contact pressures and stress maps, it has clear potential for research on joint contact stress and related clinical questions (e.g., overload, wear, and pain).

5.1 Implications for Knee Biomechanics and Orthopaedic Applications

The proposed methodology represents a computational biomechanical model designed to estimate ligament tension with high accuracy under patient-specific conditions. Unlike traditional methods that rely on static cadaveric models or generalized in vivo estimates, this approach is dynamic and personalized. It integrates patient-specific data—such as anatomical measurements, joint kinematics, and imaging—into a predictive model that simulates ligament behaviour under various loading conditions. The use of iterative kinematic predictions indicates a computational framework, likely involving finite element analysis (FEA), musculoskeletal modelling, or machine learning algorithms, to iteratively simulate joint mechanics and optimize tension estimates. This framework holds particular potential to enhance understanding of joint contact mechanics by modelling force distributions and pressure patterns at articular surfaces.

The model's emphasis on dynamic accuracy enables real-time or near-real-time simulation capabilities, potentially allowing researchers and clinicians to visualize how ligaments respond to forces during knee motion. For example, it could predict how the medial collateral ligament (MCL) or lateral collateral ligament (LCL) behaves during flexion or extension under different implant alignments or tensioning scenarios, while also simulating joint contact forces, such as tibiofemoral or patellofemoral interactions, to reveal how these influence overall biomechanical stability.

Traditional approaches to soft tissue balancing in knee arthroplasty, such as cadaveric studies and in vivo assessments, have significant limitations. Cadaveric models cannot account for patient-specific factors like ligament elasticity, muscle activation, or joint wear. In vivo assessments, often based on intraoperative manual testing or gap-balancing techniques, lack precision due to their subjectivity and inability to simulate dynamic joint behaviour under physiological loads. In contrast, this methodology achieves a paradigm shift by prioritizing individualized analysis. It employs advanced computational tools to integrate patient-specific data, providing a nuanced understanding of ligament tension and its interplay with joint contact mechanics. For instance, it may utilize 3D reconstructions of a patient's knee to simulate ligament-implant interactions under diverse loading conditions, such as standing, walking, or stair climbing, mitigating the "one-size-fits-all" limitations that contribute to instability, stiffness, or implant failure, and highlighting potential insights into optimizing contact force distribution to minimize wear and improve load-bearing efficiency.

The model's validation through iterative kinematic predictions ensures reliability. This process involves comparing predictions with experimental or clinical data, such as intraoperative measurements, motion capture data, or postoperative outcomes. The iterative nature of validation, where discrepancies refine model parameters, enhances predictive accuracy, including in aspects of joint contact mechanics like pressure mapping across cartilage surfaces. For example, the model can simulate ligament tension changes across a full range of motion (0° to 120° flexion) and adjust predictions based on validation datasets, offering deeper insights into how these tensions affect contact stresses and joint congruence. This rigor is critical for potential clinical adoption, distinguishing the methodology from traditional approaches that often lack systematic testing due to reliance on static or generalized data.

In practice, this methodology could transform the knee arthroplasty workflow by providing powerful preoperative and intraoperative tools. Preoperatively, the model might simulate various surgical scenarios—such as different implant sizes, alignments, or tensioning strategies—to identify optimal approaches for achieving soft tissue balance, with a strong emphasis on predicting joint contact mechanics to forecast how implants alter force transmission and reduce peak pressures. For instance, it could enable input of a patient's knee anatomy to test how a prosthesis affects ligament tension during weight-bearing activities, facilitating data-driven decision-making and potentially reducing intraoperative trial-and-error. Intraoperatively, the model might guide real-time adjustments, potentially through integration with surgical navigation systems or augmented reality platforms. For example, model outputs could inform fine-tuning of PCL tension during TKR, ensuring balanced femoral-tibial gaps and highlighting opportunities to optimize contact mechanics for reduced complications like aseptic loosening or patellofemoral pain.

The methodology's ability to provide personalized analysis has far-reaching implications for knee biomechanics and orthopaedic applications. By improving soft tissue balance, it could enhance joint function, reduce pain, and promote longer implant longevity, particularly by advancing knowledge of joint contact mechanics to address challenges like uneven load distribution in TKR, where minor imbalances can lead to significant morbidity. A key contribution of this study lies in its implications for ligament balancing in total knee replacement (TKR). By quantifying native ligament tensions in vivo, the model provides reference values that can directly inform intraoperative decision-making. The iterative FEA approach not only estimates absolute ligament forces but also reveals how imbalances between medial and lateral compartments manifest dynamically during flexion. Such insights go beyond the capabilities of simplified kinematic analyses, positioning this methodology as a valuable tool for improving patient-specific soft tissue balancing strategies. The model's predictive capabilities may also reduce variability in biomechanical outcomes, standardizing approaches across research and practice. Beyond TKR, the methodology could be adapted for other procedures requiring precise soft tissue management, such as hip or shoulder replacements, with potential to deepen insights into contact force dynamics in multi-joint systems. Its computational framework could integrate with emerging technologies, such as robotics or artificial intelligence, to further enhance precision in modelling joint mechanics. However, challenges remain, including the need for robust validation in biomechanical studies, user-friendly interfaces, and cost-effective implementation across diverse settings.

It may be argued that similar outcomes could be obtained using rigid body models with spring elements to represent ligaments. While such simplifications are valuable for gross kinematic simulations, they cannot replicate the anatomical detail or contact mechanics incorporated in the present FEA-based approach. Specifically, this methodology was easily implemented from 4dCT data, and simplifying the data would have been a challenge in its own right. The method captured cartilage-cartilage interactions and can be easily enhanced to focus on providing insight into localised stress distributions and tissue loading in these tissues. Furthermore, ligament insertions were simply defined at the node level based on imaging data, ensuring anatomical fidelity. These features justify the additional numerical complexity of the current method and highlight its advantage over rigid body simplifications. Finally, since solutions took little more than 10 minutes to numerically solve, the additional complexity of the approach did not add a major computational limitation.

5.2 Limitations

Despite its promising results, this study has several limitations that warrant consideration. The reliance on 4dCT data from a single individual limits the generalizability of findings. Variations in knee anatomy—such as ligament thickness, bone morphology, and muscle attachment points—can significantly influence joint mechanics, and these nuances were not addressed in the current model. To enhance robustness, future studies should incorporate data from a diverse sample to capture a broader spectrum of knee biomechanics. Indeed, ideally models should be patient specific.

A limitation arises from the spatial resolution of the 4dCT DICOM data. As described in the Chapter 3, the voxel size constrained the fidelity of bone and cartilage surface reconstruction, particularly at curved geometries and soft tissue regions. This inherent limitation introduced surface irregularities during segmentation, which subsequently propagated into the meshing process and finite element model generation. The impact of this resolution dependency is twofold: first, it influences the precision of defining ligament insertion sites at a node-to-node level; and second, it affects the accuracy of contact mechanics calculations, including cartilage-cartilage and cartilage-meniscus interactions. Although smoothing and remeshing techniques were employed to minimise artefacts, these steps may also compromise the exact anatomical representation. Consequently, while the iterative FEA approach was able to achieve convergence and produce physiologically plausible ligament tensions, the quantitative accuracy of the tension values should be interpreted considering the resolution limitations of the input DICOM data.

The knee joint is stabilized and mobilized by numerous tendinous insertions, including, but not limited to, the quadriceps tendon, hamstring tendons (biceps femoris, semitendinosus, semimembranosus), pes anserinus (conjoined tendon of sartorius, gracilise, and semitendinosus), popliteus tendon, iliotibial band, and gastrocnemius tendons. These structures play critical roles in facilitating knee flexion, extension, and rotational stability. However, the present study did not incorporate these additional tendinous insertions in its analysis. The current methodology, nonetheless, provides a robust framework for systematically integrating these structures to evaluate their contributions to the indeterminate biomechanical problem. To estimate the unknown forces in ligaments and tendons, it may be necessary to establish a relationship between muscle activation and coactivation, such as assuming coactivation forces constitute approximately 10% of the primary active force. This approach could enhance the precision of force estimations in future investigations.

The meniscus plays a crucial role in optimizing tibiofemoral contact mechanics by increasing contact area and decreasing contact stress [260]. Meniscal tears and partial meniscectomies lead to increased peak compressive and shear stresses on articular cartilages and meniscus, particularly in the medial compartment [261]. While the meniscofemoral ligaments contribute to reducing contact stresses in the lateral compartment [262], the anterior intercensal ligament does not significantly affect tibiofemoral contact pressures [263]. This suggests that the medial and lateral menisci function independently in converting axial loads into circumferential hoop stresses, likely due to their individual root attachments to the tibia [263]. Since the meniscus plays an important role in contact stresses, the model should be updated if contact stresses are the main outcome variable of interest. However, this would increase complexity of the model by significantly increasing the number and extent of contact surfaces in the model with knock-on negative consequences for model solution.

Additionally, while the model accurately simulates ligament mechanics, replicating the complex properties of soft tissues, particularly tendons and cartilage, remains challenging. Ligaments and tendons exhibit nonlinear and anisotropic behaviour, which the elastic material properties used here do not fully capture. This limitation may affect the precision of load distribution predictions, especially under varying physiological loads or complex motion sequences. Future iterations could incorporate advanced material properties, such as viscoelastic and time-dependent characteristics, to improve simulation fidelity.

Boundary conditions also pose a limitation. The model was based on kinematic data at full knee extension with anterior tibial loading, relevant for specific injury mechanisms but less comprehensive for capturing the full range of ACL loading scenarios. The absence of compressive, bending, and rotational loads reduces the model's applicability for simulating complex, multi-planar movements, such as pivoting or cutting manoeuvres common in dynamic sports settings.

The exercise was done supine, with only the weight of the leg estimated as the load. Future work on designing rigs to load the knee in a similar fashion to walking, whilst being imaged in 4dCT, would increase the application of this method.

5.3 Future Research Directions

Future research should expand the model's capabilities to simulate injury mechanisms and assess repair strategies. Incorporating injury-specific parameters, such as partial or complete ligament tears, could enable examination of biomechanical effects on joint stability and inform targeted rehabilitation protocols. Such a model could help clinicians predict recovery timelines and identify optimal therapeutic interventions based on specific injury profiles.

Additionally, leveraging machine learning algorithms to analyse large datasets across multiple knee models could enhance predictive capabilities. Machine learning could identify patterns in ligament strain distribution, bone density, and joint kinematics, laying the groundwork for personalized orthopaedic solutions. Integrating the model with real-time motion capture data would further extend its applications, enabling in situ biomechanical assessments in sports science and injury prevention.

Parameter sensitivity analysis should also be conducted to evaluate the impact of variables such as ligament insertion point variability and muscle co-contraction on ligament tension outcomes. This approach could determine the extent to which these factors affect model accuracy and stability, enhancing its utility for both research and clinical applications.

To address the single-subject limitation, future studies should validate the methodology across a larger cohort, including patients with varying demographics, pathologies, and activity levels, to better substantiate its potential for informing joint replacement techniques, individualized treatment plans, and injury prevention strategies.

5.4 Conclusion

This dissertation has developed a sophisticated methodology combining FEA with 4dCT, offering a dynamic and anatomically precise model of knee biomechanics. By capturing ligament mechanics across movement phases, the model enables robust estimates of ligament tensions and predictions of joint kinematics throughout the range of motion. The ability to validate model predictions—demonstrated by the node displacement results in different frame comparisons, where the majority of patellar displacement errors remained within ±3.25 mm for Frames 02–06—exemplifies the reliability and clinical applicability of this approach.

This model provides valuable clinical insights for improving knee arthroplasty outcomes, offering detailed, patient-specific analyses of soft tissue behaviour that can inform surgical planning and postoperative rehabilitation. Although the model has certain limitations in its current form, it lays a strong foundation for subsequent research aimed at informing joint replacement techniques, developing individualized treatment plans, and enhancing injury prevention strategies in which knee ligament tension is an important, yet unknown, parameter.

In conclusion, this thesis introduces a validated methodology that surpasses prior simplified models, such as that of Attard [241], by integrating 4dCT imaging with finite element analysis to achieve anatomically precise and biomechanically rich predictions of knee ligament tensions. Beyond advancing fundamental understanding of knee biomechanics, the work establishes a framework that can be translated to clinical practice, particularly for guiding ligament balancing in TKR. Future developments may extend this methodology to pathological knees and patient-specific surgical planning, thereby bridging the gap between computational modelling and personalised orthopaedic care.

Reference

[1] Regenerative Spine and Joint. (2023, February 23). Knee anatomy & regenerative treatment options. https://regenerativespineandjoint.com/2023/02/23/knee-anatomy-regenerative-treatment-options/

[2] Von Rehlingen-Prinz, F., Leiderer, M., Dehoust, J., Dust, T., Kowald, B., Frosch, K. H., Izadpanah, K., Henes, F. O., & Krause, M. (2023). Association of medial collateral ligament complex injuries with anterior cruciate ligament ruptures based on posterolateral tibial plateau injuries. Sports medicine - open, 9(1), 70. https://doi.org/10.1186/s40798-023-00611-6

[3] Niknam, K., Goldberg, D., Markes, A. R., Feeley, B. T., Zhang, A. L., Ma, C. B., & Lansdown, D. A. (2025). Concomitant medial collateral ligament injury increases the risk of revision anterior cruciate ligament reconstruction. Arthroscopy: The Journal of Arthroscopic & Related Surgery, 41(5), 1423-1433.

[4] Nukuto, K., Gale, T., Yamamoto, T., Musahl, V., & Anderst, W. (2023). Bone morphology features associated with knee kinematics may not be predictive of ACL elongation during high-demand activities. Knee Surgery, Sports Traumatology, Arthroscopy, 31, 5096 - 5103.

[5] Li, C., Chen, J., Yang, Y., Jin, Y., Wang, C., Tsai, T., & Li, P. (2022). Asymmetry of Posterior Condyles in Resection Plane and Axial Curvature for Total Knee Arthroplasty. Orthopaedic Surgery, 14, 3340 - 3348.

[6] Hodel, S., Postolka, B., Flury, A., Schütz, P., Taylor, W.R., Vlachopoulos, L., & Fucentese, S. (2022). Influence of Bone Morphology on In Vivo Tibio-Femoral Kinematics in Healthy Knees during Gait Activities. Journal of Clinical Medicine, 11.

[7] Jensen, C., Walser, R.F., Gothard, M.D., Holmes, T.A., & Raskey, R. (2021). Morphological Variances on the Anterior Surface of the Patella: A Cadaveric Study. The FASEB Journal, 35.

[8] Vahabi, A., Biçer, E.K., Kayıkçı, K., Şahin, F., Kavakli, K., Tamsel, I"., & Aydoğdu, S. (2024). Morphological analysis of patellofemoral joint in haemophilic arthropathy: A case-control study. Haemophilia : the official journal of the World Federation of Hemophilia.

[9] Marisami, P., & Venkatachalam, R. (2023). Design and experimental validation of a high-performance polycentric prosthetic knee joint for transfemoral amputees in developing countries. Journal of the Brazilian Society of Mechanical Sciences and Engineering, 45, 1-16.

[10] Reddie, M., Bedi, S., Vaidya, M., Griffin, A., Petelina, N. T., & Winter, A. G. (2023, August 20–23). Achieving high performance and low cost: Development of a high-performing passive prosthetic knee for emerging markets. In *Proceedings of the ASME 2023 International Design Engineering Technical Conferences and Computers and Information in Engineering Conference (IDETC/CIE 2023)* (Vol. 3B: 49th Design Automation Conference, V03BT03A021). Boston, MA: ASME. https://doi.org/10.1115/DETC2023-116478

[11] Rasheed, F., Martin, S.“., & Tse, K.M. (2023). Design, Kinematics and Gait Analysis, of Prosthetic Knee Joints: A Systematic Review. Bioengineering, 10.

[12] Gehweiler, D., Styger, U., Gueorguiev, B., Colcuc, C., Vordemvenne, T., & Wähnert, D. (2022). Local bone quality measure and construct failure prediction: A biomechanical study on distal femur fractures. *Archives of Orthopaedic and Trauma Surgery, 142*, 1055–1061. https://doi.org/10.1007/s00402-021-03782-7

[13] Mishra, R. N. et al. “Biomechanical Analysis of Human Femur using Finite Element Method: A Review Study.” Materials Today: Proceedings (2022)

[14] Babacan, S., & Deniz, M. (2022). Femur morphometry and correlation between proximal and distal parts. *Cukurova Medical Journal, 47*(1), 50–61. https://doi.org/10.17826/cumj.994863

[15] Petrescu, Relly Victoria Virgil et al. “News in Bone Modeling for Customized Hybrid Biological Prostheses Development.” Journal of Biological Sciences 21 (2021):

285-316.

[16] Murray, A.A., MacKinnon, M., Carswell, T.M., & Giles, J.W. (2023). Anterior diaphyseal curvature of the femur and tibia has biomechanical consequences during unloaded uphill locomotion. Frontiers in Ecology and Evolution.

[17] Preuschoft, H., & Tardieu, C. (1996). Biomechanical reasons for the divergent morphology of the knee joint and the distal epiphyseal suture in hominoids. Folia primatologica; international journal of primatology, 66 1-4, 82-92.

[18] Moore, S.R., Milz, S., & Knothe Tate, M.L. (2014). The Linea Aspera: A Virtual Case Study Testing Emergence of Form and Function. The Anatomical Record, 297.

[19] Cristofolini, L. (2015). In vitro evidence of the structural optimization of the human skeletal bones. Journal of biomechanics, 48 5, 787-96.

[20] Swan, K.R., Ives, R., Wilson, L.A., & Humphrey, L.T. (2020). Ontogenetic changes in femoral cross-sectional geometry during childhood locomotor development. American journal of physical anthropology, e24080.

[21] McCabe, K., Henderson, K., Pantinople, J., Richards, H.L., & Milne, N. (2017). Curvature reduces bending strains in the quokka femur. PeerJ, 5.

[22] Yashina, I.N., Ivanov, A.V., & Klochkova, S.V. (2019). Morphological Manifestations of Human Locomotor Bipedality in Femur. Journal of Anatomy and Histopathology.

[23] Francis, A., Shrivastava, A., Masih, C., Dwivedi, N., Tiwari, P., Nareliya, R., & Kumar, V.B. (2012). Biomechanical Analysis of Human Femur: A Review.

[24] Gdoutos, E.E., Raftopoulos, D.D., & Baril, J. (1982). A critical review of the biomechanical stress analysis of the human femur. Biomaterials, 3 1, 2-8.

[25] Dye, S.F. (2003). Functional morphologic features of the human knee: an evolutionary perspective. Clinical orthopaedics and related research, 410, 19-24.

[26] Eckhoff, D.G., Bach, J.M., Spitzer, V.M., Reinig, K., Bagur, M.M., Baldini, T.H.,

Rubinstein, D., & Humphries, S.M. (2003). Three-Dimensional Morphology and Kinematics of the Distal Part of the Femur Viewed in Virtual Reality: Part II. The Journal of Bone & Joint Surgery, 85, 97–104.

[27] Eckhoff, D.G., Bach, J.M., Spitzer, V.M., Reinig, K., Bagur, M.M., Baldini, T.H., & Flannery, N. (2005). Three-dimensional mechanics, kinematics, and morphology of the knee viewed in virtual reality. The Journal of bone and joint surgery. American volume, 87 Suppl 2, 71-80.

[28] Fox, J.C., & Keaveny, T.M. (2001). Trabecular eccentricity and bone adaptation. Journal of theoretical biology, 212 2, 211-21.

[29] Geraldes, D.M., Modenese, L., & Phillips, A.T. (2015). Consideration of multiple load cases is critical in modelling orthotropic bone adaptation in the femur. Biomechanics and Modeling in Mechanobiology, 15, 1029 - 1042.

[30] Za︠t︡siorskiĭ, V.M., & Prilutsky, B.I. (2012). Biomechanics of Skeletal Muscles.

[31] Sperber, G.H. (2006). Clinically Oriented Anatomy. Journal of Anatomy, 208, 393.

[32] Fox, A.J., Wanivenhaus, F., & Rodeo, S.A. (2012). The Basic Science of the Patella: Structure, Composition, and Function. The Journal of Knee Surgery, 25, 127 - 142.

[33] Palmieri-Smith, R. M., & Lepley, L. K. (2015). Quadriceps strength asymmetry after ACL reconstruction alters knee joint biomechanics and increases knee joint loading: A proof-of-concept study. *The American Journal of Sports Medicine, 43*(7), 1662–1669. https://doi.org/10.1177/0363546515578252

[34] Paolo, S.D., Grassi, A., Lucidi, G.A., Macchiarola, L., Fabbro, G.D., & Zaffagnini, S. (2021). Biomechanics of the lateral meniscus: evidences from narrative review. Annals of Joint.

[35] Linus, A., Tanska, P., Sarin, J.K., Nippolainen, E., Tiitu, V., Mäkelä, J.T., Töyräs, J., Korhonen, R.K., Mononen, M.E., & Afara, I.O. (2023). Visible and Near-Infrared Spectroscopy Enables Differentiation of Normal and Early Osteoarthritic Human

Knee Joint Articular Cartilage. Annals of Biomedical Engineering, 51, 2245 - 2257.

[36] Kumar V, D., Sontakke, Y.A., & Murugharaj, S. (2020). Truly Existing or Hyped up? Unravelling the Current Knowledge Regarding the Anatomy, Radiology, Histology and Biomechanics of the Enigmatic Anterolateral Ligament of the Knee Joint. The archives of bone and joint surgery, 8 3, 332-342.

[37] Eckstein, F., Wluka, A. E., Wirth, W., & Cicuttini, F. (2024). 30 Years of MRI-based cartilage & bone morphometry in knee osteoarthritis: From correlation to clinical trials. Osteoarthritis and Cartilage, 32(4), 439-451.

[38] Meister, B.R., Michael, S.P., Moyer, R.A., Kelly, J.D., & Schneck, C.D. (2000). Anatomy and Kinematics of the Lateral Collateral Ligament of the Knee. The American Journal of Sports Medicine, 28, 869 - 878.

[39] Wilson, W.T., Deakin, A.H., Payne, A.P., Picard, F., & Wearing, S.C. (2012). Comparative analysis of the structural properties of the collateral ligaments of the human knee. The Journal of orthopaedic and sports physical therapy, 42 4, 345-51.

[40] Andrews, K.A., Lu, A., Mckean, L., & Ebraheim, N.A. (2017). Review: Medial collateral ligament injuries. Journal of orthopaedics, 14 4, 550-554.

[41] Juneja, P., & Hubbard, J.B. (2018). Anatomy, Bony Pelvis and Lower Limb, Knee Medial Collateral Ligament.

[42] Wierer, G., Schroedter, R., Hoser, C., & Milinkovic, D. D. (2024). Trilogy of isolated deep medial collateral ligament injuries of the knee: A set of three cases and overview of the literature. Journal of ISAKOS, 9(5), 100296. https://doi.org/10.1016/j.jisako.2023.12.005

[43] Griffith, C.J., LaPrade, R.F., Johansen, S., Armitage, B.M., Wijdicks, C.A., & Engebretsen, L. (2009). Medial Knee Injury: Part 1, Static Function of the Individual Components of the Main Medial Knee Structures. The American Journal of Sports Medicine, 37, 1762 - 1770.

[44] Warren, L.A., Marshall, J., & Girgis, F.G. (1974). The prime static stabilizer of the medical side of the knee. The Journal of bone and joint surgery. American volume, 56 4, 665-74.

[45] Cleveland Clinic. (2021, November 16). Knee ligament. Cleveland Clinic. https://my.clevelandclinic.org/health/body/21596-knee-ligament

[46] Willinger, L., Balendra, G., Pai, V., Lee, J.C., Mitchell, A., Jones, M., & Williams, A. (2021). High incidence of superficial and deep medial collateral ligament injuries in 'isolated' anterior cruciate ligament ruptures: a long overlooked injury. Knee Surgery, Sports Traumatology, Arthroscopy, 30, 167 - 175.

[47] Lee, J., Ihle, S.J., Pellegrino, G.S., Kim, H., Yea, J., Jeon, C., Son, H., Jin, C., Eberli, D., Schmid, F.A., Zambrano, B.L., Renz, A.F., Forró, C., Choi, H., Jang, K., Küng, R., & Vörös, J. (2021). Stretchable and suturable fibre sensors for wireless monitoring of connective tissue strain. Nature Electronics, 4, 291 - 301.

[48] Soda, Y., Ohkawa, S., Kano, T., Nakamura, M., & Adachi, N. (2022). Isolated Lateral Collateral Ligament Injury of the Knee in a Judo Athlete: A Surgical Case Report. Journal of Orthopaedic Case Reports, 12, 84 - 87.

[49] Karunathilaka, C. (2023). The lateral stability of the knee, A review of the clinical Anatomy of the Popliteal hiatus and its clinical pathologies. Sri Lanka Journal of Surgery.

[50] Kurtys, K., Gonera, B., Olewnik, Ł., Karauda, P., Tubbs, R.S., & Polguj, M. (2020). Case report of a bifurcated fibular (lateral) collateral ligament: which band is the dominant one? Folia morphologica.

[51] LaPrade, R. F., Bollom, T. S., Wentorf, F. A., Wills, N. J., & Meister, K. (2005). Mechanical properties of the posterolateral structures of the knee. The American journal of sports medicine, 33(9), 1386–1391. https://doi.org/10.1177/0363546504274143

[52] Ardern, C.L., Ekås, G.R., Grindem, H., Moksnes, H., Anderson, A.F., Chotel, F., Cohen, M., Forssblad, M., Ganley, T.J., Feller, J.A., Karlsson, J., Kocher, M.S.,

LaPrade, R.F., McNamee, M., Mandelbaum, B.R., Micheli, L.J., Mohtadi, N.G., Reider, B.J., Roe, J.P., Seil, R., Siebold, R., Silvers-Granelli, H.J., Soligard, T., Witvrouw, E., & Engebretsen, L. (2018). 2018 International Olympic Committee consensus statement on prevention, diagnosis and management of paediatric anterior cruciate ligament (ACL) injuries. Knee Surgery, Sports Traumatology, Arthroscopy, 26, 989 - 1010.

[53] Myer, G.D., Ford, K.R., Di Stasi, S., Foss, K.D., Micheli, L.J., & Hewett, T.E. (2014). High knee abduction moments are common risk factors for patellofemoral pain (PFP) and anterior cruciate ligament (ACL) injury in girls: Is PFP itself a predictor for subsequent ACL injury? British Journal of Sports Medicine, 49, 118 - 122.

[54] Amis, A.A. (2012). The functions of the fibre bundles of the anterior cruciate ligament in anterior drawer, rotational laxity and the pivot shift. Knee Surgery, Sports Traumatology, Arthroscopy, 20, 613-620.

[55] Makris, C.A., Georgoulis, A.D., Papageorgiou, C.D., Moebius, U.G., & Soucacos, P.N. (2000). Posterior cruciate ligament architecture: evaluation under microsurgical dissection. Arthroscopy: the journal of arthroscopic & related surgery: official publication of the Arthroscopy Association of North America and the International Arthroscopy Association, 16 6, 627-32.

[56] Duthon, V.L., Barea, C., Abrassart, S., Fasel, J.H., Fritschy, D., & Menetrey, J. (2006). Anatomy of the anterior cruciate ligament. Knee Surgery, Sports Traumatology, Arthroscopy, 14, 204-213.

[57] Logterman, S., Wydra, F., & Frank, R.M. (2018). Posterior Cruciate Ligament: Anatomy and Biomechanics. Current Reviews in Musculoskeletal Medicine, 11, 510-514.

[58] Race, A., & Amis, A.A. (1994). The mechanical properties of the two bundles of the human posterior cruciate ligament. Journal of biomechanics, 27 1, 13-24.

[59] Garcia, S.A., Johnson, A.K., Brown, S.R., Washabaugh, E.P., Krishnan, C., & Palmieri-Smith, R.M. (2022). Dynamic knee stiffness during walking is increased

in individuals with anterior cruciate ligament reconstruction. Journal of biomechanics, 146, 111400.

[60] McNally, T., Edwards, S., Halaki, M., O'Dwyer, N., Pizzari, T., & Blyton, S. (2023). Quantifying demands on the hamstrings during high-speed running: A systematic review and meta-analysis. Scandinavian Journal of Medicine & Science in Sports, 33(12), 2423-2443.

[61] Musculoskeletal Key. (n.d.). Basic sciences. https://musculoskeletalkey.com/basic-sciences/

[62] Latash, M. L. (2018). Muscle coactivation: definitions, mechanisms, and functions. Journal of neurophysiology, 120(1), 88-104.

[63] Martins, E. C., Ruschel, C., Roesler, E. M., Silvano, G. A., de Castro, M. P., Herzog, W., & de Brito Fontana, H. (2022). Tensor fascia latae and gluteal muscles myoelectric responses to increasing levels of hip medial rotation torque. Journal of Biomechanics, 132, 110944.

[64] Aagaard, P., Simonsen, E. B., Andersen, J. L., Magnusson, S. P., Bojsen-Møller, F., & Dyhre-Poulsen, P. (2000). Antagonist muscle coactivation during isokinetic knee extension. Scandinavian journal of medicine & science in sports, 10(2), 58–67. https://doi.org/10.1034/j.1600-0838.2000.010002058.x

[65] Lee, J. H., Kim, S., Heo, J., Park, D. H., & Chang, E. (2022). Differences in the muscle activities of the quadriceps femoris and hamstrings while performing various squat exercises. BMC Sports Science, Medicine and Rehabilitation, 14(1), 12.

[66] Marshall, R. N., Morgan, P. T., Martinez-Valdes, E., & Breen, L. (2020). Quadriceps muscle electromyography activity during physical activities and resistance exercise modes in younger and older adults. Experimental gerontology, 136, 110965. https://doi.org/10.1016/j.exger.2020.110965

[67] Draganich, L. F., Jaeger, R. J., & Kralj, A. R. (1989). Coactivation of the hamstrings and quadriceps during extension of the knee. The Journal of bone and joint

surgery. American volume, 71(7), 1075–1081.

[68] Veeck, F., de Vargas, J. S., Godinho, R. A. T., Wilhelm, E. N., Pinto, M. D., & Pinto, R. S. (2024). Hamstring-to-quadriceps activation ratio during lower-limb strengthening exercises. Research in Sports Medicine, 32(5), 843-856. https://doi.org/10.1080/15438627.2023.2286355

[69] Sanchez-Gomez, R., Carrión, Á. G., Ortuño Soriano, I., Sanz Wozniak, P., Zaragoza García, I., Waer, F. B., Alexe, C. I., & Alexe, D. I. (2025). Iliotibial Band Behavior Assessed Through Tensor Fasciae Latae Electromyographic Activity with Different Foot Orthoses in Recreational Runners According to Foot Type: A Cross-Sectional Study. Journal of functional morphology and kinesiology, 10(3), 237. https://doi.org/10.3390/jfmk10030237

[70] The Knee Doc. (n.d.). Muscles and tendons. The Knee Doc. https://www.thekneedoc.co.uk/medical-resources/muscles-and-tendons/

[71] Ristaniemi, A., Stenroth, L., Mikkonen, S., & Korhonen, R.K. (2018). Comparison of elastic, viscoelastic and failure tensile material properties of knee ligaments and patellar tendon. Journal of biomechanics, 79, 31-38.

[72] Pavlik, A., Hidas, P.I., Czigány, T., & Berkes, I. (2004). Biomechanical evaluation of press-fit femoral fixation technique in ACL reconstruction. Knee Surgery, Sports Traumatology, Arthroscopy, 12, 528-533.

[73] Sylvester, A.D., Mahfouz, M.R., & Kramer, P.A. (2011). The Effective Mechanical Advantage of A.L. 129-1a for Knee Extension. The Anatomical Record: Advances in Integrative Anatomy and Evolutionary Biology, 294.

[74] Seynnes, O.R., Erskine, R.M., Maganaris, C.N., Longo, S., Simoneau, E.M., Grosset, J., & Narici, M.V. (2009). Training-induced changes in structural and mechanical properties of the patellar tendon are related to muscle hypertrophy but not to strength gains. Journal of applied physiology, 107 2, 523-30.

[75] Scheffler, S.U., Südkamp, N.P., Göckenjan, A., Hoffmann, R.F., & Weiler, A. (2002). Biomechanical comparison of hamstring and patellar tendon graft anterior cruciate ligament reconstruction techniques: The impact of fixation level and fixation method under cyclic loading. Arthroscopy : the journal of arthroscopic & related surgery : official publication of the Arthroscopy Association of North America and the International Arthroscopy Association, 18 3, 304-15 .

[76] Akbarshahi, M., Fernandez, J.W., Schache, A.G., & Pandy, M.G. (2014). Subject-specific evaluation of patellofemoral joint biomechanics during functional activity. Medical engineering & physics, 36 9, 1122-33.

[77] Lee, T., Sandusky, M.D., Adeli, A., & McMahon, P.J. (2014). Effects of simulated vastus medialis strength variation on patellofemoral joint biomechanics in human cadaver knees. Journal of rehabilitation research and development, 39 3, 429-38.

[78] Brazaitis, A., Tamošiūnas, A.E., & Tutkuviene, J. (2015). Patellofemoral joint biomechanics in the females with anterior knee pain applying full weight bearing kinematic MRI. Acta Medica Lituanica, 22.

[79] Zhou, Y., Li, L., Chen, X., Zhao, Q., Qu, N., Zhang, B., Jin, X., & Xia, C. (2023). Impaired autophagy contributes to the aggravated deterioration of osteoarthritis articular cartilage by peroxisome proliferator-activated receptor α deficiency, associated with decreased ERK and Akt activation. European Journal of Medical Research, 28.

[80] Thrive Now Physio. (n.d.). Meniscus: The gasket of the knee. https://thrivenowphysio.com/meniscus-the-gasket-of-the-knee/

[81] Walker, P.S. and Erkman, M.J., 1975. The role of the menisci in force transmission across the knee. Clinical Orthopaedics and Related Research, 109, pp.184–192. DOI: 10.1097/00003086-197506000-00027.

[82] Seedhom, B.B. and Hargreaves, D.J., 1979. Transmission of the load in the knee joint with special reference to the role of the menisci: Part II—Experimental results. Engineering in Medicine, 8(4), pp.220–228. DOI:

10.1243/EMED_JOUR_1979_008_041_02.

[83] Markolf, K.L., Bargar, W.L., Shoemaker, S.C. and Amstutz, H.C., 1981. The role of joint load in knee stability. The Journal of Bone and Joint Surgery, 63(4), pp.570–585. DOI: 10.2106/00004623-198163040-00007.

[84] Paletta, G.A., Crane, D.M., Koníček, J., Piepenbrink, M., Higgins, L.D., Milner, J.D., & Wijdicks, C.A. (2020). Surgical Treatment of Meniscal Extrusion: A Biomechanical Study on the Role of the Medial Meniscotibial Ligaments With Early Clinical Validation. Orthopaedic Journal of Sports Medicine, 8.

[85] Chung, J.Y., Song, H., Jung, M.K., Oh, H., Kim, J.H., Yoon, J., & Min, B.H. (2016). Larger medial femoral to tibial condylar dimension may trigger posterior root tear of medial meniscus. Knee Surgery, Sports Traumatology, Arthroscopy, 24, 1448-1454.

[86] Ghosh, P., & Taylor, T.K. (1987). The knee joint meniscus. A fibrocartilage of some distinction. Clinical orthopaedics and related research, 224, 52-63.

[87] Diermeier, T., Beitzel, K., Bachmann, L., Petersen, W., Esefeld, K., Wörtler, K., Imhoff, A. B., & Achtnich, A. (2019). Mountain ultramarathon results in temporary meniscus extrusion in healthy athletes. Knee surgery, sports traumatology, arthroscopy : official journal of the ESSKA, 27(8), 2691–2697. https://doi.org/10.1007/s00167-018-5303-x

[88] Ishii, Y., Hashizume, T., Okamoto, S., Iwamoto, Y., Ishikawa, M., Nakashima, Y., Hashiguchi, N., Okada, K., Takagi, K., Adachi, N., & Takahashi, M. (2023). Cumulative knee adduction moment during jogging causes temporary medial meniscus extrusion in healthy volunteers. Journal of medical ultrasonics (2001), 50(2), 229–236. https://doi.org/10.1007/s10396-023-01288-w

[89] OrthoVirginia. (2020, August 12). Meniscus tears: Why are some repaired and others removed? https://www.orthovirginia.com/blog/meniscus-tears-why-are-some-repaired-and-others/

[90] Fox, A. J., Wanivenhaus, F., Burge, A. J., Warren, R. F., & Rodeo, S. A. (2015).

The human meniscus: a review of anatomy, function, injury, and advances in treatment. Clinical anatomy (New York, N.Y.), 28(2), 269–287. https://doi.org/10.1002/ca.22456

[91] Makris, E. A., Hadidi, P., & Athanasiou, K. A. (2011). The knee meniscus: structure-function, pathophysiology, current repair techniques, and prospects for regeneration. Biomaterials, 32(30), 7411–7431. https://doi.org/10.1016/j.biomaterials.2011.06.037

[92] Seedhom, B.B. and Hargreaves, D.J., 1979. Transmission of the load in the knee joint with special reference to the role of the menisci. Engineering in Medicine, 8(4), pp.220–228. DOI: 10.1243/EMED_JOUR_1979_008_041_02.

[93] Jerosch, J., Prymka, M. and Castro, W.H.M., 1996. Proprioception of knee joints with a lesion of the medial meniscus. Acta Orthopaedica Belgica, 62(1), pp.41–45. PMID: 8669276.

[94] Baratz, M.E., Fu, F.H. and Mengato, R., 1986. Meniscal tears: The effect of meniscectomy and of repair on intraarticular contact areas and stress in the human knee. The American Journal of Sports Medicine, 14(4), pp.270–275. DOI: 10.1177/036354658601400405.

[95] McNicholas, M.J., Rowley, D.I., McGurty, D., Adalberth, T., Abdon, P., Lindstrand, A. and Lohmander, L.S., 2000. Total meniscectomy in adolescence: A thirty-year follow-up. The Journal of Bone and Joint Surgery. British Volume, 82(2), pp.217–221. DOI: 10.1302/0301-620X.82B2.9942.

[96] Kung, M.S., Markantonis, J.E., Nelson, S.D., & Campbell, P.A. (2015). The Synovial Lining and Synovial Fluid Properties after Joint Arthroplasty. Lubricants, 3, 394-412.

[97] Galandáková, A., Ulrichová, J., Langová, K., Hanakova, A., Vrbka, M., Hartl, M., & Gallo, J. (2017). Characteristics of synovial fluid required for optimization of lubrication fluid for biotribological experiments. Journal of biomedical materials research. Part B, Applied biomaterials, 105 6, 1422-1431.

[98] Levick, J.R., & McDonald, J.N. (1995). Fluid movement across synovium in healthy joints: role of synovial fluid macromolecules. Annals of the Rheumatic Diseases, 54, 417 - 423.

[99] García-Manrique, M., Calvet, J., Orellana, C., Berenguer-Llergo, A., Garcia-Cirera, S., Llop, M., Albiñana-Giménez, N., Galisteo-Lencastre, C., & Gratacós, J. (2021). Synovial fluid but not plasma interleukin-8 is associated with clinical severity and inflammatory markers in knee osteoarthritis women with joint effusion. Scientific Reports, 11.

[100] Jansen, M.P., Salzlechner, C., Barnes, E., Difranco, M.D., Custers, R., Watt, F.E., Vincent, T., Lafeber, F., & Mastbergen, S.C. (2023). Joint Repair Evaluated on Radiographs Is Associated with Pain and Synovial Fluid Marker Changes After Knee Joint Distraction Treatment. Orthopaedic Proceedings.

[101] Martin-Alarcon, L., Govedarica, A., Ewoldt, R.H., Bryant, S.L., Jay, G.D., Schmidt, T.A., & Trifkovic, M. (2023). Scale-Dependent Rheology of Synovial Fluid Lubricating Macromolecules. Small, e2306207.

[102] Hsiao, S., Chou, P.H., Hsu, H., & Lue, Y. (2014). Changes of Muscle Mechanics Associated With Anterior Cruciate Ligament Deficiency and Reconstruction. Journal of Strength and Conditioning Research, 28, 390–400.

[103] Bakker, R., Tomescu, S.S., Brenneman, E.C., Hangalur, G., Laing, A.C., & Chandrashekar, N. (2016). Effect of sagittal plane mechanics on ACL strain during jump landing. Journal of Orthopaedic Research, 34.

[104] Zavras, D., Race, A., & Amis, A.A. (2005). The effect of femoral attachment location on anterior cruciate ligament reconstruction: graft tension patterns and restoration of normal anterior–posterior laxity patterns. Knee Surgery, Sports Traumatology, Arthroscopy, 13, 92-100.

[105] Englander, Z.A., Lau, B.C., Wittstein, J.R., Goode, A.P., & DeFrate, L.E. (2021). Patellar Tendon Orientation and Strain Are Predictors of ACL Strain In Vivo During a Single-Leg Jump. Orthopaedic Journal of Sports Medicine, 9.

[106] Xie, F., Yang, L., Guo, L., Wang, Z., & Dai, G. (2009). A novel method for calculating the in situ forces of cruciate ligaments. *Journal of Biomechanical Engineering, 131*(12), 121007. https://doi.org/10.1115/1.3148463

[107] Harbottle, D., Chen, Q., Moorthy, K.B., Wang, L., Xu, S., Liu, Q., Sjøblom, J., & Xu, Z. (2014). Problematic stabilizing films in petroleum emulsions: shear rheological response of viscoelastic asphaltene films and the effect on drop coalescence. Langmuir : the ACS journal of surfaces and colloids, 30 23, 6730-8.

[108] Esfahani, A.M., Rosenbohm, J., Safa, B.T., Lavrik, N.V., Minnick, G., Zhou, Q., Kong, F., Jin, X., Kim, E., Liu, Y., Lu, Y.F., Lim, J.Y., Wahl, J.K., Dao, M., Huang, C., & Yang, R. (2021). Characterization of the strain-rate–dependent mechanical response of single cell–cell junctions. Proceedings of the National Academy of Sciences, 118.

[109] Lynch, T.B., Chahla, J., & Nuelle, C.W. (2021). Anatomy and Biomechanics of the Posterior Cruciate Ligament. The Journal of Knee Surgery, 34, 499 - 508.

[110] LaPrade, C.M., Civitarese, D.M., Rasmussen, M.T., & LaPrade, R.F. (2015). Emerging Updates on the Posterior Cruciate Ligament. The American Journal of Sports Medicine, 43, 3077 - 3092.

[111] Johnson, P., Mitchell, S.M., & Görtz, S. (2018). Graft Considerations in Posterior Cruciate Ligament Reconstruction. Current Reviews in Musculoskeletal Medicine, 11, 521-527.

[112] Schafer, K.A., Tucker, S.M., Griffith, T.B., Sheikh, S., Wickiewicz, T.L., Nawabi, D.H., Imhauser, C.W., & Pearle, A.D. (2016). Distribution of Force in the Medial Collateral Ligament Complex During Simulated Clinical Tests of Knee Stability. The American Journal of Sports Medicine, 44, 1203 - 1208.

[113] Quapp, K. M., & Weiss, J. A. (1998). Material characterization of human medial collateral ligament. *Journal of Biomechanical Engineering, 120*(6), 757–763. https://doi.org/10.1115/1.2834756

[114] Provenzano, P.P., Lakes, R.S., Keenan, T., & Vanderby, R. (2001). Nonlinear

Ligament Viscoelasticity. Annals of Biomedical Engineering, 29, 908-914.

[115] Vena, P., Gastaldi, D., & Contro, R. (2006). A constituent-based model for the nonlinear viscoelastic behavior of ligaments. Journal of biomechanical engineering, 128 3, 449-57.

[116] Zhao, S., Zhang, C., & Zhang, C. (2013). Reconstruction of lateral knee joint stability following resection of proximal fibula tumors. Experimental and Therapeutic Medicine, 7, 405 - 410.

[117] Shahane, S.A., Ibbotson, C., Strachan, R.K., & Bickerstaff, D.R. (1999). The popliteofibular ligament. An anatomical study of the posterolateral corner of the knee. The Journal of bone and joint surgery. British volume, 81 4, 636-42.

[118] Buyukdogan, K., Isik, S., Ayik, G., Tokgözoğlu, M., & Ayvaz, M. (2020). Lateral Collateral Ligament and Biceps Femoris Tendon Fixation with a Suture Anchor to the Tibial Metaphysis after Proximal Fibula En Bloc Resections Preserve Lateral Knee Stability. The Journal of Knee Surgery, 36, 878 - 885.

[119] Chahla, J., S)migielski, R., LaPrade, R.F., & Fulkerson, J.P. (2019). An Updated Overview of the Anatomy and Function of the Proximal Medial Patellar Restraints (Medial Patellofemoral Ligament and the Medial Quadriceps Tendon Femoral Ligament). Sports Medicine and Arthroscopy Review, 27, 136 - 142.

[120] Rong, G., & Wang, Y.C. (1987). The role of cruciate ligaments in maintaining knee joint stability. Clinical orthopaedics and related research, 215, 65-71.

[121] Hansen, P., Bojsen-Moller, J., Aagaard, P., Kjaer, M., & Magnusson, S. P. (2006). Mechanical properties of the human patellar tendon, in vivo. Clinical biomechanics (Bristol, Avon), 21(1), 54–58. https://doi.org/10.1016/j.clinbiomech.2005.07.008

[122] Hashemi, J., Chandrashekar, N., & Slauterbeck, J. (2005). The mechanical properties of the human patellar tendon are correlated to its mass density and are independent of sex. Clinical biomechanics (Bristol, Avon), 20(6), 645–652. https://doi.org/10.1016/j.clinbiomech.2005.02.008

[123] Breda, S. J., van der Vlist, A., de Vos, R. J., Krestin, G. P., & Oei, E. H. G. (2020). The association between patellar tendon stiffness measured with shear-wave elastography and patellar tendinopathy-a case-control study. European radiology, 30(11), 5942–5951. https://doi.org/10.1007/s00330-020-06952-0

[124] Reeves, N. D., Maganaris, C. N., & Narici, M. V. (2003). Effect of strength training on human patella tendon mechanical properties of older individuals. The Journal of physiology, 548(Pt 3), 971–981. https://doi.org/10.1113/jphysiol.2002.035576

[125] LaPrade, R. F., Engebretsen, A. H., Ly, T. V., Johansen, S., Wentorf, F. A., & Engebretsen, L. (2007). The anatomy of the medial part of the knee. The Journal of bone and joint surgery. American volume, 89(9), 2000–2010.

[126] Marcacci, M., Molgora, A.P., Zaffagnini, S., Vascellari, A., Iacono, F., & Presti, M.L. (2003). Anatomic double-bundle anterior cruciate ligament reconstruction with hamstrings. Arthroscopy : the journal of arthroscopic & related surgery : official publication of the Arthroscopy Association of North America and the International Arthroscopy Association, 19 5, 540-6 .

[127] Takeda, S., Tajima, G., Fujino, K., Yan, J., Kamei, Y., Maruyama, M., Kikuchi, S., & Doita, M. (2015). Morphology of the femoral insertion of the lateral collateral ligament and popliteus tendon. Knee Surgery, Sports Traumatology, Arthroscopy, 23, 3049-3054.

[128] Greiner, P., Magnussen, R.A., Lustig, S., Demey, G., Neyret, P., & Servien, E. (2011). Computed tomography evaluation of the femoral and tibial attachments of the posterior cruciate ligament in vitro. Knee Surgery, Sports Traumatology, Arthroscopy, 19, 1876-1883.

[129] Yan, J., Takeda, S., Fujino, K., Tajima, G., & Hitomi, J. (2012). Anatomical Reconsideration of the Lateral Collateral Ligament in the Human Knee: Anatomical Observation and Literature Review. Surgical Science, 03, 484-488.

[130] Balemane, S., Shetty, N., Ramu, A., & Rahman, A. (2022). MRI and functional

assessment of triportal technique in arthroscopic anatomical single-bundle anterior cruciate ligament reconstruction. Journal of Orthopaedics and Spine, 10, 56 - 62.

[131] Spence, K.T., & Forro, S.D. (2018). Anatomy, Bony Pelvis and Lower Limb, Nerves.

[132] Kaplan, P.A., Walker, C.W., Kilcoyne, R.F., Brown, D.E., Tušek, D., & Dussault, R.G. (1992). Occult fracture patterns of the knee associated with anterior cruciate ligament tears: assessment with MR imaging. Radiology, 183 3, 835-8.

[133] Franciozi, C.E., Mameri, E.S., Gracitelli, G.C., Schumacher, F.C., Credidio, M.V., Canuto, S.M., & Kubota, M.S. (2023). Tibial-Sling Triangular Medial Collateral Ligament Reconstruction With Posterior Oblique Ligament Limb. Video Journal of Sports Medicine, 3.

[134] Wang, Y., Yu, Z., Li, J., & Li, Q. (2023). [Diagnosis and treatment progress in the femoral insertion injury of medial collateral ligament of knee]. Zhongguo xiu fu chong jian wai ke za zhi = Zhongguo xiufu chongjian waike zazhi = Chinese journal of reparative and reconstructive surgery, 37 2, 215-220.

[135] Johansen, S. (2006). RUPTURES OF THE LCL AND POSTEROLATERAL CORNER (PLC).

[136] Latiff, S., & Olateju, O.I. (2023). Morphometry of the patellar tendon using a simple tracing method: a gold standard for anterior cruciate ligament reconstruction. Anatomy & Cell Biology, 56, 191 - 199.

[137] Kotiuk, V.V., Kostrub, O.O., Blonskyi, R., Podik, V.A., Smirnov, D., & Haiko, O. (2022). THE STRESS IN THE ACL, ACL GRAFT, AND OTHER JOINT ELEMENTS WHILE WEIGHT-BEARING IN FULL EXTENSION DEPENDING ON THE POSTERIOR TIBIAL SLOPE. Georgian medical news, 331, 54-60.

[138] Hammarstedt, J.E., Guth, J.J., Schimoler, P.J., Kharlamov, A., Miller, M.C., Akhavan, S., & Demeo, P.J. (2021). Biomechanical analysis of ideal knee flexion angle for ACL graft tensioning utilizing multiple femoral and tibial tunnel locations.

Orthopaedic Journal of Sports Medicine, 9.

[139] Nedopil, A.J., Howell, S.M., & Hull, M.L. (2022). Measurement of Tibial Orientation Helps Select the Optimal Insert Thickness to Personalize PCL Tension in a Medial Ball-in-Socket TKA. Journal of Personalized Medicine, 12.

[140] Kuriyama, S., Ishikawa, M., Furu, M., Ito, H., & Matsuda, S. (2014). Malrotated tibial component increases medial collateral ligament tension in total knee arthroplasty. Journal of Orthopaedic Research, 32.

[141] Sekiguchi, K., Nakamura, S., Kuriyama, S., Nishitani, K., Ito, H., Tanaka, Y., Watanabe, M., & Matsuda, S. (2019). Effect of tibial component alignment on knee kinematics and ligament tension in medial unicompartmental knee arthroplasty. Bone & Joint Research, 8, 126 - 135.

[142] Powers, C.M., Chen, Y.J., Farrokhi, S. and Lee, T.Q., 2006. Role of peripatellar retinaculum in transmission of forces within the extensor mechanism. Journal of Bone and Joint Surgery, 88(9), pp.2042-2048.

[143] Sharma, P. and Maffulli, N., 2005. Tendon injury and tendinopathy: Healing and repair. Journal of Bone and Joint Surgery, 87(1), pp.187-202.

[144] Herzog, W. and Read, L.J., 1993. Lines of action and moment arms of the major force-carrying structures crossing the human knee joint. Journal of Anatomy, 182(2), pp.213-230.

[145] Slane, L.C., Bogaerts, S., Thelen, D.G., & Scheys, L. (2017). Nonuniform Deformation of the Patellar Tendon During Passive Knee Flexion. Journal of applied biomechanics, 34 1, 14-22.

[146] Christen, B., Heesterbeek, P. V., Wymenga, A., & Wehrli, U. (2007). Posterior cruciate ligament balancing in total knee replacement: The quantitative relationship between tightness of the flexion gap and tibial translation. *Journal of Bone and Joint Surgery. British Volume, 89*(8), 1046–1050. https://doi.org/10.1302/0301-620X.89B8.18976

[147] Gustke, K.A. (2012). Use of smart trials for soft-tissue balancing in total knee replacement surgery. The Journal of bone and joint surgery. British volume, 94 11 Suppl A, 147-50.

[148] Gollehon, D.L., Torzilli, P.A., & Warren, R.F. (1987). The role of the posterolateral and cruciate ligaments in the stability of the human knee. A biomechanical study. The Journal of bone and joint surgery. American volume, 69 2, 233-42.

[149] Pasque, C.B., Noyes, F.R., Mj, G., Levy, M.S., & Grood, E.S. (2003). The role of the popliteofibular ligament and the tendon of popliteus in providing stability in the human knee. The Journal of bone and joint surgery. British volume, 85 2, 292-8.

[150] Huang, D., Chen, L., Yu, Z., Chen, Q., Lai, J., Li, H., & Liu, G. (2021). Effect of suspension training on neuromuscular function, postural control, and knee kinematics in anterior cruciate ligament reconstruction patients. World Journal of Clinical Cases, 9, 2247 - 2258.

[151] Marcaccio, S.E., Morrissey, P.J., Testa, E.J., & Fadale, P.D. (2023). Role of Quadriceps Tendon Autograft in Primary and Revision Anterior Cruciate Ligament Reconstruction. Jbjs Reviews, 11.

[152] Yasuda, K., Tsujino, J., Tanabe, Y., & Kaneda, K. (1997). Effects of Initial Graft Tension on Clinical Outcome After Anterior Cruciate Ligament Reconstruction. The American Journal of Sports Medicine, 25, 106 - 99.

[153] Brady, M.F., Bradley, M.P., Fleming, B.C., Fadale, P.D., Hulstyn, M.J., & Banerjee, R. (2007). Effects of Initial Graft Tension on the Tibiofemoral Compressive Forces and Joint Position after Anterior Cruciate Ligament Reconstruction. The American Journal of Sports Medicine, 35, 395 - 403.

[154] Cuomo, P., Reddi Boddu Siva Rama, K., Bull, A.M., & Amis, A.A. (2007). The Effects of Different Tensioning Strategies on Knee Laxity and Graft Tension after Double-Bundle Anterior Cruciate Ligament Reconstruction. The American Journal

of Sports Medicine, 35, 2083 - 2090.

[155] Malinowski, K., Sibilska, A., Góralczyk, A., LaPrade, R.F., & Hermanowicz, K. (2019). Superficial Medial Collateral Ligament Reattachment During High Tibial Osteotomy: Regulate Tension, Preserve Stability! Arthroscopy Techniques, 8, e1339 - e1343.

[156] Stephen, J.M., Kaider, D., Lumpaopong, P., Deehan, D.J., & Amis, A.A. (2014). The Effect of Femoral Tunnel Position and Graft Tension on Patellar Contact Mechanics and Kinematics After Medial Patellofemoral Ligament Reconstruction. The American Journal of Sports Medicine, 42, 364 - 372.

[157] Harris, M. D., Cyr, A. J., Ali, A. A., Fitzpatrick, C. K., Rullkoetter, P. J., & Shelburne, K. B. (2016). A combined experimental and computational approach to subject-specific assessment of knee joint laxity. *Journal of Biomechanical Engineering, 138*(8), 081004. https://doi.org/10.1115/1.4033570

[158] Navacchia, A., Myers, C. A., Rullkoetter, P. J., & Shelburne, K. B. (2016). Prediction of in vivo knee joint contact forces using a combined experimental and computational approach. *Journal of Biomechanical Engineering, 138*(3), 031002. https://doi.org/10.1115/1.4032379

[159] Sherman, T. I. (2024). Editorial commentary: Cadaveric biomechanical orthopaedic research is essential and requires quality and validity metrics. *Arthroscopy: The Journal of Arthroscopic & Related Surgery, 40*(8), 2273–2275. https://doi.org/10.1016/j.arthro.2024.02.014

[160] Wascher, D.C., Markolf, K.L., Shapiro, M.S., & Finerman, G.A. (1993). Direct in vitro measurement of forces in the cruciate ligaments. Part I: The effect of multiplane loading in the intact knee. The Journal of bone and joint surgery. American volume, 75 3, 377-86.

[161] Hohmann, E., Waldron, S., Imhoff, A. B., & Tetsworth, K. (2024). The ethics, applications, and contributions of cadaver testing in injury prevention research. *Traffic Injury Prevention.* Advance online publication.

https://doi.org/10.1080/15389588.2024.2376937

[162] Hinterwimmer, S., Baumgart, R., & Plitz, W. (2002). Tension changes in the collateral ligaments of a cruciate ligament-deficient knee joint: an experimental biomechanical study. Archives of orthopaedic and trauma surgery, 122(8), 454–458.

[163] Maletsky, L.P., Shalhoub, S., Fitzwater, F., Eboch, W.M., Dickinson, M., Akhbari, B., & Louie, E. (2015). In Vitro Experimental Testing of the Human Knee: A Concise Review. The Journal of Knee Surgery, 29, 138 - 148.

[164] Prusa, G., Bauer, L., Santos, I., Thorwächter, C., Woiczinski, M., & Kistler, M. (2023). Strain evaluation of axially loaded collateral ligaments: a comparison of digital image correlation and strain gauges. BioMedical Engineering OnLine, 22.

[165] Fox, R. J., Harner, C. D., Sakane, M., Carlin, G. J., & Woo, S. L. (1998). Determination of the in situ forces in the human posterior cruciate ligament using robotic technology. A cadaveric study. The American journal of sports medicine, 26(3), 395–401. https://doi.org/10.1177/03635465980260030901

[166] Sakane, M., Fox, R. J., Woo, S. L., Livesay, G. A., Li, G., & Fu, F. H. (1997). In situ forces in the anterior cruciate ligament and its bundles in response to anterior tibial loads. Journal of orthopaedic research : official publication of the Orthopaedic Research Society, 15(2), 285–293.

[167] Wadugodapitiya, S.I., Sakamoto, M., Tanaka, M., Sakagami, Y., Morise, Y., & Kobayashi, K. (2022). Assessment of knee collateral ligament stiffness by strain ultrasound elastography. Bio-Medical Materials and Engineering, 33, 337 - 349.

[168] Nashed, M., Nassef, M.A., & Louka, A.L. (2017). Role of MRI Assessment of the Patellar Instability. The Egyptian Journal of Hospital Medicine, 69, 1655-1660.

[169] Phatak, N.S., Sun, Q., Kim, S., Parker, D.L., Kent Sanders, R., Veress, A.I., Ellis, B.J., & Weiss, J.A. (2007). Noninvasive Determination of Ligament Strain with Deformable Image Registration. Annals of Biomedical Engineering, 35, 1175-1187.

[170] Csapo, R., Heinrich, D., Vigotsky, A.D., Marx, C., Sinha, S., & Fink, C. (2021). Developing a Technique for the Imaging-Based Measurement of ACL Elongation: A Proof of Principle. Diagnostics, 11.

[171] Moatshe, G., Chahla, J., LaPrade, R.F., & Engebretsen, L. (2017). Diagnosis and treatment of multiligament knee injury: state of the art. Journal of ISAKOS, 2, 152 - 161.

[172] Bae, T.S., & Cho, B.C. (2020). Biomechanical Effect of Tunnel Positions and Pre-tension Forces on Implanted Graft Stress and Strain During Outside-in ACL Reconstruction Surgery: A Simulation Study. International Journal of Precision Engineering and Manufacturing, 21, 519-524.

[173] Khmyzov, S., Yakushkin, E., Karpinsky, M., & Yaresko, O. (2022). Mathematical modeling of the stress-strain state of the knee joint model with aplasia of the cruciate ligaments and after restoration of the ligamentous apparatus. Paediatric Surgery. Ukraine.

[174] Khot, S., Guttal, R., & Babannavar, O. P. (2021). Biomechanics of human knee joint under dynamic conditions. Journal of Mines, Metals and Fuels, 123-128.

[175] Beidokhti, H.N., Janssen, D., Groes, S.V., Boogaard, T.V., & Verdonschot, N. (2016). Subject-specific knee ligaments modeling approaches in finite element analysis: 1D and 3D.

[176] Heegaard, Jean et al. “The biomechanics of the human patella during passive knee flexion.” Journal of biomechanics 28 11 (1995): 1265-79.

[177] Beynnon, B. D. et al. “A sagittal plane model of the knee and cruciate ligaments with application of a sensitivity analysis.” Journal of biomechanical engineering 118 2 (1996): 227-39 .

[178] Wan, Chao-Jie et al. “The effect of the variation in ACL constitutive model on joint kinematics and biomechanics under different loads: a finite element study.” Journal of biomechanical engineering 135 4 (2013): 041002 .

[179] Erdemir, Ahmet Gürkan. "Open Knee: Open Source Modeling and Simulation in Knee Biomechanics." The Journal of Knee Surgery 29 (2015): 107 - 116

[180] Song, Y., Debski, R. E., Musahl, V., Thomas, M., & Woo, S. L. (2004). A three-dimensional finite element model of the human anterior cruciate ligament: a computational analysis with experimental validation. Journal of biomechanics, 37(3), 383–390. https://doi.org/10.1016/s0021-9290(03)00261-6 the study successfully validated the FEM using experimental data, the lack of a comprehensive sensitivity analysis on more complex loading scenarios limits the understanding of the model's robustness across different physiological conditions.

[181] Peña, E., Calvo, B., Martínez, M. A., & Doblaré, M. (2006). A three-dimensional finite element analysis of the combined behavior of ligaments and menisci in the healthy human knee joint. Journal of biomechanics, 39(9), 1686–1701. https://doi.org/10.1016/j.jbiomech.2005.04.030

[182] Frigo, C.A., & Donno, L. (2021). The Effects of External Loads and Muscle Forces on the Knee Joint Ligaments during Walking: A Musculoskeletal Model Study. Applied Sciences.

[183] Zeng, W., Hume, D.R., Lu, Y., Fitzpatrick, C.K., Babcock, C.D., Myers, C.A., Rullkoetter, P.J., & Shelburne, K.B. (2023). Modeling of active skeletal muscles: a 3D continuum approach incorporating multiple muscle interactions. Frontiers in Bioengineering and Biotechnology, 11.

[184] Chen, H., Liu, L., & Zhang, Y. (2023). Finite element analysis of the knee joint stress after partial meniscectomy for meniscus horizontal cleavage tears. BMC Musculoskeletal Disorders, 24.

[185] Uhlrich, S.D., Jackson, R.W., Seth, A., Kolesar, J.A., & Delp, S.L. (2022). Muscle coordination retraining inspired by musculoskeletal simulations reduces knee contact force. Scientific Reports, 12.

[186] Frigo, C.A., & Donno, L. (2021). The Effects of External Loads and Muscle Forces on the Knee Joint Ligaments during Walking: A Musculoskeletal Model

Study. Applied Sciences.

[187] Adachi, T., Kato, Y., Kiyotomo, D., Kawamukai, K., & Machida, Y. (2021). Accuracy Verification of 4dCT Analysis of Knee Joint Movements: A Pilot Study Using a Knee Joint Model and Motion-capture System.

[188] Sandberg, O.H., Kärrholm, J., Olivecrona, H., Röhrl, S.M., Sköldenberg, O., & Brodén, C. (2023). Computed tomography-based radiostereometric analysis in orthopedic research: practical guidelines. Acta Orthopaedica, 94, 373 - 378.

[189] Torkzad, M.R., Påhlman, L., & Glimelius, B. (2010). Magnetic resonance imaging (MRI) in rectal cancer: a comprehensive review. Insights into Imaging, 1, 245 - 267.

[190] Petralia, G., Padhani, A.R., Pricolo, P., Zugni, F., Martinetti, M., Summers, P.E., Grazioli, L., Colagrande, S., Giovagnoni, A., & Bellomi, M. (2018). Whole-body magnetic resonance imaging (WB-MRI) in oncology: recommendations and key uses. La radiologia medica, 124, 218-233.

[191] Nardini, F., Belvedere, C., Sancisi, N., Conconi, M., Leardini, A., Durante, S., & Parenti-Castelli, V. (2020). An Anatomical-Based Subject-Specific Model of In-Vivo Knee Joint 3D Kinematics From Medical Imaging. Applied Sciences.

[192] Fernández-González, P., Koutsou, A., Cuesta-Gómez, A., Carratalá-Tejada, M., Miangolarra-Page, J.C., & Rueda, F.M. (2020). Reliability of Kinovea® Software and Agreement with a Three-Dimensional Motion System for Gait Analysis in Healthy Subjects. Sensors (Basel, Switzerland), 20.

[193] Pfister, A., West, A.M., Bronner, S., & Noah, J.A. (2014). Comparative abilities of Microsoft Kinect and Vicon 3D motion capture for gait analysis. Journal of Medical Engineering & Technology, 38, 274 - 280.

[194] Sabuncu, S., & Yildirim, A. (2021). Gas-stabilizing nanoparticles for ultrasound imaging and therapy of cancer. Nano Convergence, 8.

[195] Qiu, Y., Guan, Y., & Liu, S. (2023). The analysis of infrared high-speed motion

capture system on motion aesthetics of aerobics athletes under biomechanics analysis. PLOS ONE, 18.

[196] Reiser, M., Refior, H.J., Stäbler, A., & Heuck, A. (1994). [MRI in orthopedics: diagnosis of joint disorders]. Der Orthopade, 23 5, 342-8.

[197] Maravi, P., MaraviD, S., Uikey, S., & Kaushal, L. (2015). Role of MRI in Orthopedics.

[198] Hong, A., Liu, J.N., Gowd, A.K., Dhawan, A., & Amin, N.H. (2019). Reliability and Accuracy of MRI in Orthopedics: A Survey of Its Use and Perceived Limitations. Clinical Medicine Insights. Arthritis and Musculoskeletal Disorders, 12.

[199] Leshno, M., Amir, H., & Leshno, D. (2000). [Cost-effectiveness of imaging procedures in knee injuries]. Harefuah, 138 2, 110-7, 174.

[200] Liang, X., Chen, L., Nguyen, D., Zhou, Z., Gu, X., Yang, M., Wang, J., & Jiang, S.B. (2018). Generating synthesized computed tomography (CT) from cone-beam computed tomography (CBCT) using CycleGAN for adaptive radiation therapy. Physics in Medicine & Biology, 64.

[201] Kim, H.W., Park, B.R., & Hong, T.H. (2022). Application of Computed Tomography in the Identification of Hollow Viscus Injuries in Blunt Trauma Patients. Journal of Acute Care Surgery.

[202] Downie, K., McIntire, A., Tobias, J., Krishnaswami, S., & Jafri, M. (2023). Application of a Thoracic CT Decision Rule in the Evaluation of Injured Children: A Quality Improvement Initiative. Journal of Trauma Nursing, 30, 48 - 54.

[203] Kwong, Y., Mel, A. O., Wheeler, G., & Troupis, J. M. (2015). Four-dimensional computed tomography (4DCT): A review of the current status and applications. *Journal of Medical Imaging and Radiation Oncology, 59*(5), 545–554. https://doi.org/10.1111/1754-9485.12326

[204] Morishige, Y., Harato, K., Oki, S., Kaneda, K., Niki, Y., Nakamura, M., & Nagura, T. (2022). Four-dimensional computed tomographic analysis of screw

home movement in patients with anterior cruciate ligament deficient knee — a 3D-3D registration technique. Skeletal Radiology, 51, 1679 - 1685.

[205] Yamashita, J., Hashikawa, K., Kakei, Y., Sekitani, T., & Akashi, M. (2023). Four-Dimensional Computed Tomographic Image Evaluation of the Change of Condylar Movement With and Without Implant-Supported Removable Prostheses in the Fibular Mandible: A Pilot Case Series Report. Cureus, 15.

[206] Carr, R., Maclean, S.B., Slavotinek, J.P., & Bain, G.I. (2018). Four-Dimensional Computed Tomography Scanning for Dynamic Wrist Disorders: Prospective Analysis and Recommendations for Clinical Utility. Journal of Wrist Surgery, 08, 161 - 167.

[207] Trentadue, T.P., Lopez, C., Breighner, R.E., Fautsch, K.J., Leng, S., Holmes III, D.R., Moran, S.L., Thoreson, A.R., Kakar, S., & Zhao, K.D. (2021). Evaluation of Scapholunate Injury and Repair with Dynamic (4d) CT: A Preliminary Report of Two Cases. Journal of Wrist Surgery, 12, 248 - 260.

[208] Adachi, T., Kato, Y., Kiyotomo, D., Kawamukai, K., Takazawa, S., Suzuki, T., & Machida, Y. (2023). Accuracy Verification of Four-Dimensional CT Analysis of Knee Joint Movements: A Pilot Study Using a Knee Joint Model and Motion-Capture System. Cureus, 15.

[209] Song, Y.D., Nakamura, S., Kuriyama, S., Nishitani, K., Ito, H., Morita, Y., Yamawaki, Y., & Matsuda, S. (2021). Biomechanical Comparison of Kinematic and Mechanical Knee Alignment Techniques in a Computer Simulation Medial Pivot Total Knee Arthroplasty Model. The Journal of Knee Surgery.

[210] Bates, N.A., Schilaty, N.D., Nagelli, C.V., Krych, A.J., & Hewett, T.E. (2019). Multiplanar Loading of the Knee and Its Influence on Anterior Cruciate Ligament and Medial Collateral Ligament Strain During Simulated Landings and Noncontact Tears. The American Journal of Sports Medicine, 47, 1844 - 1853.

[211] Uhlrich, S.D., Jackson, R.W., Seth, A., Kolesar, J.A., & Delp, S.L. (2022). Muscle coordination retraining inspired by musculoskeletal simulations reduces

knee contact force. Scientific Reports, 12.

[212] Kang, K., Koh, Y., Son, J., Kwon, O., Lee, J., & Kwon, S.K. (2018). A computational simulation study to determine the biomechanical influence of posterior condylar offset and tibial slope in cruciate retaining total knee arthroplasty. Bone & Joint Research, 7, 69 - 78.

[213] Beynnon, B.D., Yu, J., Huston, D.R., Fleming, B.C., Johnson, R., Haugh, L., & Pope, M.H. (1996). A sagittal plane model of the knee and cruciate ligaments with application of a sensitivity analysis. Journal of biomechanical engineering, 118 2, 227-39.

[214] Andreassen, T.E., Laz, P.J., Erdemir, A.G., Besier, T.F., Halloran, J.P., Imhauser, C.W., Chokhandre, S.K., Schwartz, A., Abdollahi Nohouji, N., Rooks, N.B., Schneider, M.T., Elmasry, S.S., Zaylor, W., Hume, D.R., & Shelburne, K.B. (2023). Deciphering the "Art" in Modeling and Simulation of the Knee Joint: Assessing Model Calibration Workflows and Outcomes. Journal of biomechanical engineering, 1-35.

[215] Burgio, V., Casari, S., Milizia, M., Sanna, F., Spezia, G., Civera, M., Rodriguez Reinoso, M., Bertuglia, A., & Surace, C. (2023). Mechanical properties of animal ligaments: a review and comparative study for the identification of the most suitable human ligament surrogates. Biomechanics and Modeling in Mechanobiology, 22, 1645 - 1683.

[216] Wilke, J., Debelle, H., Tenberg, S., Dilley, A., & Maganaris, C.N. (2020). Ankle Motion Is Associated With Soft Tissue Displacement in the Dorsal Thigh: An in vivo Investigation Suggesting Myofascial Force Transmission Across the Knee Joint. Frontiers in Physiology, 11.

[217] Ding, K., Yang, W., Wang, H., Zhan, S., Hu, P., Bai, J., Ren, C., Zhang, Q., Zhu, Y., & Chen, W. (2021). Finite element analysis of biomechanical effects of residual varus/valgus malunion after femoral fracture on knee joint. International Orthopaedics, 45, 1827 - 1835.

[218] Chokhandre, S.K., Schwartz, A., Klonowski, E., Landis, B., & Erdemir, A.G. (2022). Open Knee(s): A Free and Open Source Library of Specimen-Specific Models and Related Digital Assets for Finite Element Analysis of the Knee Joint. Annals of Biomedical Engineering, 51, 10 - 23.

[219] Brock, K. K., Hollister, S. J., Dawson, L. A., & Balter, J. M. (2002). Technical note: Creating a four-dimensional model of the liver using finite element analysis. Medical Physics, 29(7), 1403–1405. https://pubmed.ncbi.nlm.nih.gov/12148719/

[220] Werner, R., Ehrhardt, J., Schmidt, R., Säring, D., & Handels, H. (2009). Patient-specific finite element modelling of respiratory lung motion using 4D CT image data. Medical Physics, 36(5), 1500–1511. https://pubmed.ncbi.nlm.nih.gov/19544766/

[221] Wong, M. T. (2022). Four-dimensional computed tomography: Musculoskeletal applications. Quantitative Imaging in Medicine and Surgery, 12(8), 4497–4510. https://pmc.ncbi.nlm.nih.gov/articles/PMC9200445/

[222] Adachi, T., Kato, Y., Kiyotomo, D., Kawamukai, K., & Machida, Y. (2021). Accuracy Verification of 4dCT Analysis of Knee Joint Movements: A Pilot Study Using a Knee Joint Model and Motion-capture System.

[223] Adachi, T., Kato, Y., Kiyotomo, D., Kawamukai, K., Takazawa, S., Suzuki, T., & Machida, Y. (2023). Accuracy Verification of Four-Dimensional CT Analysis of Knee Joint Movements: A Pilot Study Using a Knee Joint Model and Motion-Capture System. Cureus, 15.

[224] Kang, K., Kim, S., Son, J., Lee, Y.H., Kim, S., & Chun, H. (2017). Probabilistic evaluation of the material properties of the in vivo subject-specific articular surface using a computational model. Journal of biomedical materials research. Part B, Applied biomaterials, 105 6, 1390-1400.

[225] Watanabe, K., Mutsuzaki, H., Fukaya, T., Aoyama, T., Nakajima, S., Sekine, N., & Mori, K. (2020). Development of a Knee Joint CT-FEM Model in Load

Response of the Stance Phase During Walking Using Muscle Exertion, Motion Analysis, and Ground Reaction Force Data. Medicina, 56.

[226] Indelli, P.F., Giuntoli, M., Zepeda, K., Ghirardelli, S., Valtanen, R.S., & Iannotti, F. (2023). Native knee kinematics is not reproduced after sensor guided cruciates substituting total knee arthroplasty. Journal of Experimental Orthopaedics, 10.

[227] Wang, J., Qi, Y., Bao, H., Xu, Y., Wei, B., Wang, Y., Ma, B., Zhou, H., & Lv, F. (2021). The effects of different repair methods for a posterior root tear of the lateral meniscus on the biomechanics of the knee: a finite element analysis. Journal of Orthopaedic Surgery and Research, 16.

[228] Hu, J., Chen, Z., Xin, H., Zhang, Q., & Jin, Z. (2018). Musculoskeletal multibody dynamics simulation of the contact mechanics and kinematics of a natural knee joint during a walking cycle. Proceedings of the Institution of Mechanical Engineers, Part H: Journal of Engineering in Medicine, 232, 508 - 519.

[229] Dussan-Delvasto, L., Gantiva-Díaz, M., & De La Portilla, C.C. (2021). 3D model of the knee joint as a tool for the study of surgeries and injuries such as ACL reconstruction. 2021 IEEE 2nd International Congress of Biomedical Engineering and Bioengineering (CI-IB&BI), 1-4.

[230] Müller, J.H., Razu, S.S., Erdemir, A.G., & Guess, T.M. (2020). Prediction of patellofemoral joint kinematics and contact through co-simulation of rigid body dynamics and nonlinear finite element analysis. Computer Methods in Biomechanics and Biomedical Engineering, 23, 718 - 733.

[231] Kiapour, A., Quatman, C., Wordeman, S., Goel, V., & Hewett, T. (2014). Finite Element Model of the Knee for Investigation of Injury Mechanisms: Development and Validation. Journal of Biomechanical Engineering, 136(1), 011002. https://doi.org/10.1115/1.4025692

[232] Dastgerdi, A. K., Esrafilian, A., Carty, C. P., Nasseri, A., Yahyaiee Bavil, A., Barzan, M., Korhonen, R. K., Astori, I., Hall, W., & Saxby, D. J. (2023). Validation and evaluation of subject-specific finite element models of the pediatric knee.

Scientific Reports, 13, 18328. https://doi.org/10.1038/s41598-023-45408-5.

[233] Abidin, N.A.Z., Abdul Kadir, M.R., & Ramlee, M.H. (2019). Three Dimensional Finite Element Modelling and Analysis of Human Knee Joint-Model Verification. Journal of Physics: Conference Series, 1372, 012068. https://doi.org/10.1088/1742-6596/1372/1/012068A

[234] Silva, M. P. T., & Ambrósio, J. A. C. (2002). Kinematic data consistency in the inverse dynamic analysis of biomechanical systems. Multibody System Dynamics, 8(3), 219-239. https://doi.org/10.1023/A:1015551309497

[235] Challis, J. H. (1991). Estimating individual muscle forces in human movement (Doctoral thesis, Loughborough University of Technology).

[236] Grood, E. S., & Hefzy, M. S. (1982). An analytical technique for modeling knee joint stiffness—Part I: Ligamentous forces. Journal of Biomechanical Engineering, 104(4), 330-337. https://doi.org/10.1115/1.3138367

[237] Madeti, B. K., Chalamalasetti, S. R., & Bollapragada, S. K. S. (2015). Biomechanics of knee joint—A review. Frontiers of Mechanical Engineering, 10(2), 176-186. https://doi.org/10.1007/s11465-014-0306-x

[238] Komistek, R. D., Kane, T. R., Mahfouz, M., Ochoa, J. A., & Dennis, D. A. (2005). Knee mechanics: A review of past and present techniques to determine in vivo loads. Journal of Biomechanics, 38(2), 215-228. https://doi.org/10.1016/j.jbiomech.2004.02.041

[239] Küpper, J. C., Loitz-Ramage, B., Corr, D. T., Hart, D. A., & Ronsky, J. L. (2007). Measuring knee joint laxity: A review of applicable models and the need for new approaches to minimize variability. Clinical Biomechanics, 22(1), 1-13. https://doi.org/10.1016/j.clinbiomech.2006.08.003

[240] Hefzy, M. S., & Grood, E. S. (1988). Review of knee models. Applied Mechanics Reviews, 41(1), 1-13. https://doi.org/10.1115/1.3151876

[241] Attard, A., & Riches, Philip, degree supervisor.; Department of Biomedical Engineering. (2020). 4D CT based analysis of knee kinematics. https://doi.org/10.48730/enq9-5s03

[242] Yan, M., Liang, T., Zhao, H., Bi, Y., Wang, T., Yu, T., & Zhang, Y. (2024). Model Properties and Clinical Application in the Finite Element Analysis of Knee Joint: A Review. Orthopaedic surgery, 16(2), 289–302. https://doi.org/10.1111/os.13980

[243] Asadirad, R., & Riches, Philip E., degree supervisor.; Kahani, Danial, degree supervisor.; Department of Biomedical Engineering. (2025). Variability in semi-automatic segmentation from CT images : implications for knee joint modelling. https://doi.org/10.48730/5m2a-bt32

[244] Innocenti, B., Pianigiani, S., Ramundo, G., & Thienpont, E. (2016). Biomechanical Effects of Different Varus and Valgus Alignments in Medial Unicompartmental Knee Arthroplasty. The Journal of arthroplasty, 31(12), 2685–2691. https://doi.org/10.1016/j.arth.2016.07.006

[245] Kang, K. T., Son, J., Suh, D. S., Kwon, S. K., Kwon, O. R., & Koh, Y. G. (2018). Patient-specific medial unicompartmental knee arthroplasty has a greater protective effect on articular cartilage in the lateral compartment: A Finite Element Analysis. Bone & joint research, 7(1), 20–27.

[246] Yurova, A.S., Salamatova, V., Lychagin, A.V., & Vassilevski, Y.V. (2021). Automatic detection of attachment sites for knee ligaments and tendons on CT images. International Journal of Computer Assisted Radiology and Surgery, 17, 393-402.

[247] Kang, KT., Kim, SH., Son, J. et al. In vivo evaluation of the subject-specific finite element model for knee joint cartilage contact area. Int. J. Precis. Eng. Manuf. 16, 1171–1177 (2015). https://doi.org/10.1007/s12541-015-0151-9

[248] Hafis, M.B., Farahana, R., Ridzuan, M.J., & Adlina, M.N. (2013). Optimal Coefficient of Friction on Artificial Knee Joint Contact Surfaces. Advanced Materials Research, 716, 565 - 568.

[249] Mow, V. C., & Huiskes, R. (Eds.). (2005). Basic Orthopaedic Biomechanics & Mechano-biology (3rd ed.). Philadelphia, PA: Lippincott Williams & Wilkins.

[250] Lee, D.W., Banquy, X., & Israelachvili, J.N. (2013). Stick-slip friction and wear of articular joints. Proceedings of the National Academy of Sciences, 110, E567 - E574.

[251] Ihnatouski, M., Pauk, J., Karev, D., & Karev, B. (2020). AFM-Based Method for Measurement of Normal and Osteoarthritic Human Articular Cartilage Surface Roughness. Materials, 13.

[252] Hefzy, M. S., and Grood, E. S. (January 1, 1988). "Review of Knee Models." ASME. Appl. Mech. Rev. January 1988; 41(1): 1–13. https://doi.org/10.1115/1.3151876

[253] An, K. N., Kwak, B. M., Chao, E. Y., and Morrey, B. F. (November 1, 1984). "Determination of Muscle and Joint Forces: A New Technique to Solve the Indeterminate Problem." ASME. J Biomech Eng. November 1984; 106(4): 364–367. https://doi.org/10.1115/1.3138507

[254] Mizuno, K., Andrish, J. T., van den Bogert, A. J., & McLean, S. G. (2009). Gender dimorphic ACL strain in response to combined dynamic 3D knee joint loading: implications for ACL injury risk. https://doi.org/10.1016/J.KNEE.2009.04.008</div>

[255] Weinhandl, J. T., Hoch, M. C., Bawab, S. Y., & Ringleb, S. I. (2016). Comparison of ACL strain estimated via a data-driven model with in vitro measurements. Computer Methods in Biomechanics and Biomedical Engineering, 19(14), 1550–1556. https://doi.org/10.1080/10255842.2016.1170120

[256] Sakane, M., Fox, R. J., Woo, S. L., Livesay, G. A., Li, G., & Fu, F. H. (1997). In situ forces in the anterior cruciate ligament and its bundles in response to anterior tibial loads. Journal of orthopaedic research : official publication of the Orthopaedic Research Society, 15(2), 285–293. https://doi.org/10.1002/jor.1100150219

[257] Ma, C. B., Papageogiou, C. D., Debski, R. E., & Woo, S. L.-Y. (2000). Interaction between the ACL graft and MCL in a combined ACL+MCL knee injury using a goat model. Acta Orthopaedica, 71(4), 387–393. https://doi.org/10.1080/000164700317393394

[258] Bell, K. M., Rahnemai-Azar, A. A., Irarrazaval, S., Guenther, D., Fu, F. H., Musahl, V., & Debski, R. E. (2018). In situ force in the anterior cruciate ligament, the lateral collateral ligament, and the anterolateral capsule complex during a simulated pivot shift test. Journal of orthopaedic research : official publication of the Orthopaedic Research Society, 36(3), 847–853. https://doi.org/10.1002/jor.23676)

[259] Heegaard, J., Leyvraz, P. F., Curnier, A., Rakotomanana, L., & Huiskes, R. (1995). The biomechanics of the human patella during passive knee flexion. Journal of biomechanics, 28(11), 1265–1279. https://doi.org/10.1016/0021-9290(95)00059-q)

[260] Lee SJ, Aadalen KJ, Malaviya P, et al. Tibiofemoral Contact Mechanics after Serial Medial Meniscectomies in the Human Cadaveric Knee. The American Journal of Sports Medicine. 2006;34(8):1334-1344. doi:10.1177/0363546506286786

[261] Dong, Y., Hu, G., Dong, Y., Hu, Y., & Xu, Q. (2013). The effect of meniscal tears and resultant partial meniscectomies on the knee contact stresses: a finite element analysis. Computer Methods in Biomechanics and Biomedical Engineering, 17(13), 1452–1463. https://doi.org/10.1080/10255842.2012.753063

[262] Amadi, H.O., Gupte, C.M., Lie, D.T.T. et al. A biomechanical study of the meniscofemoral ligaments and their contribution to contact pressure reduction in the knee. Knee Surg Sports Traumatol Arthr 16, 1004–1008 (2008). https://doi.org/10.1007/s00167-008-0592-0

[263] Poh, S. Y., Yew, K. S., Wong, P. L., Koh, S. B., Chia, S. L., Fook-Chong, S., & Howe, T. S. (2012). Role of the anterior intermeniscal ligament in tibiofemoral

contact mechanics during axial joint loading. The Knee, 19(2), 135–139. https://doi.org/10.1016/j.knee.2010.12.008

[264] Sritharan, P., Schache, A.G., Culvenor, A.G., Perraton, L.G., Bryant, A.L., & Crossley, K.M. (2020). Between-Limb Differences in Patellofemoral Joint Forces During Running at 12 to 24 Months After Unilateral Anterior Cruciate Ligament Reconstruction. The American Journal of Sports Medicine, 48, 1711 - 1719.

[265] Buzzatti, L., Keelson, B., Apperloo, J., Scheerlinck, T., Baeyens, J. P., Van Gompel, G., Vandemeulebroucke, J., de Maeseneer, M., de Mey, J., Buls, N., & Cattrysse, E. (2019). Four-dimensional CT as a valid approach to detect and quantify kinematic changes after selective ankle ligament sectioning. Scientific reports, 9(1), 1291. https://doi.org/10.1038/s41598-018-38101-5

Appendix A

Units: meter	Frame 2			Frame 6					j=1			j=2			j=3		
Node set	X	Y	Z	X	Y	Z	Euclidean distance	Frame No.	$DX_{j=1}$	$DY_{j=1}$	$DZ_{j=1}$	$DX_{j=2}$	$DY_{j=2}$	$DZ_{j=2}$	$DX_{j=3}$	$DY_{j=3}$	$DZ_{j=3}$
P1A	-0.0989	-0.0716	0.35312	-0.0928	-0.0682	0.36198	0.011318523	F06	-0.09276	-0.068206	0.36198	-0.13876	-0.072998	0.36461	-0.11503	-0.061191	0.3352
P1B	-0.1428	-0.0724	0.35354	-0.1388	-0.073	0.36461	0.011811563	F02	-0.098924	-0.071614	0.35312	-0.14283	-0.072363	0.35354	-0.12048	-0.055221	0.32685
P1C	-0.1205	-0.0552	0.32685	-0.115	-0.0612	0.3352	0.011621786	d'/m	0.006164	0.003408	0.00886	0.00407	-0.000635	0.01107	0.00545	-0.00597	0.00835
P2A	-0.0988	-0.0715	0.34593	-0.0944	-0.0712	0.35745	0.012307007	F06	-0.094425	-0.071175	0.35745	-0.13806	-0.073619	0.36435	-0.11178	-0.064989	0.33784
P2B	-0.142	-0.0733	0.35395	-0.1381	-0.0736	0.36435	0.011121674	F02	-0.0987524	-0.0715281	0.3459343	-0.141984	-0.0732647	0.3539496	-0.115223	-0.058869	0.3282385
P2C	-0.1152	-0.0589	0.32824	-0.1118	-0.065	0.33784	0.011895125	d'/m	0.0043274	0.0003531	0.0115157	0.003924	-0.0003543	0.0104004	0.0034425	-0.00612	0.0096015
P3A	-0.1105	-0.0586	0.35235	-0.1075	-0.0574	0.36167	0.009879108	F06	-0.10752	-0.057364	0.36167	-0.13852	-0.063766	0.35075	-0.12403	-0.062606	0.33671
P3B	-0.1431	-0.0603	0.34274	-0.1385	-0.0638	0.35075	0.009835687	F02	-0.1105356	-0.0586109	0.3523454	-0.143063	-0.0603188	0.3427364	-0.128095	-0.057132	0.3281134
P3C	-0.1281	-0.0571	0.32811	-0.124	-0.0626	0.33671	0.010972294	d'/m	0.0030156	0.0012469	0.0093246	0.0045431	-0.0034472	0.0080136	0.0040651	-0.005474	0.0085966
P4A	-0.1046	-0.08	0.35484	-0.101	-0.0783	0.37004	0.015724786	F06	-0.10096	-0.078256	0.37004	-0.13726	-0.073866	0.36258	-0.11799	-0.06585	0.33701
P4B	-0.1414	-0.0729	0.35157	-0.1373	-0.0739	0.36258	0.011793537	F02	-0.10459	-0.080003	0.35484	-0.14138	-0.072921	0.35157	-0.12211	-0.060863	0.32763
P4C	-0.1221	-0.0609	0.32763	-0.118	-0.0659	0.33701	0.011394252	d'/m	0.00363	0.001747	0.0152	0.00412	-0.000945	0.01101	0.00412	-0.004987	0.00938

Node set	X	Y	Z	X	Y	Z	Euclidean distance		$DX_{j=1}$	$DY_{j=1}$	$DZ_{j=1}$	$DX_{j=2}$	$DY_{j=2}$	$DZ_{j=2}$	$DX_{j=3}$	$DY_{j=3}$	$DZ_{j=3}$
F1A	-0.1075	-0.0123	0.39431	-0.1047	-0.0072	0.39476	0.005858604	F06	-0.073867	-0.0079354	0.38285	-0.1506	-0.0042661	0.38128	-0.1047	-0.007187	0.39476
F1B	-0.1518	-0.0084	0.37996	-0.1506	-0.0043	0.38128	0.004463015	F02	-0.077821	-0.013863	0.38336	-0.15176	-0.0083686	0.37996	-0.10752	-0.012302	0.39431
F1C	-0.0778	-0.0139	0.38336	-0.0739	-0.0079	0.38285	0.007143575	d'/m	0.003954	0.0059276	-0.00051	0.00116	0.0041025	0.00132	0.00282	0.0051155	0.00045
F2A	-0.1148	-0.0449	0.42077	-0.1115	-0.0391	0.42228	0.006862668	F06	-0.069048	-0.021869	0.37544	-0.14847	-0.038084	0.38401	-0.11148	-0.039093	0.42228
F2B	-0.1505	-0.0437	0.38206	-0.1485	-0.0381	0.38401	0.00624496	F02	-0.071781	-0.02898	0.37457	-0.15046	-0.043673	0.38206	-0.11483	-0.044889	0.42077
F2C	-0.0718	-0.029	0.37457	-0.0691	-0.0219	0.37544	0.007667627	d'/m	0.002733	0.007111	0.00087	0.00199	0.005589	0.00195	0.00335	0.005796	0.00151
F3A	-0.1366	-0.0082	0.39692	-0.1333	-0.0034	0.39675	0.005929442	F06	-0.070139	-0.0043061	0.3726	-0.14795	0.0033241	0.37031	-0.13327	-0.003357	0.39675
F3B	-0.1502	-0.002	0.36892	-0.148	0.00332	0.37031	0.005920491	F02	-0.073	-0.00964	0.37207	-0.15023	-0.00196	0.36892	-0.13663	-0.00824	0.39692
F3C	-0.073	-0.0096	0.37207	-0.0701	-0.0043	0.3726	0.006075912	d'/m	0.002861	0.0053339	0.00053	0.00228	0.0052841	0.00139	0.00336	0.0048826	-0.00017
F4A	-0.1061	-0.0095	0.373	-0.1053	-0.0054	0.37405	0.004318876	F06	-0.096501	-0.0091322	0.41265	-0.14212	-0.0030816	0.38667	-0.10526	-0.005398	0.37405
F4B	-0.144	-0.0072	0.38448	-0.1421	-0.0031	0.38667	0.005052965	F02	-0.0979	-0.0141	0.41051	-0.14402	-0.00722	0.38448	-0.10606	-0.00951	0.373
F4C	-0.0979	-0.0141	0.41051	-0.0965	-0.0091	0.41265	0.005587114	d'/m	0.001399	0.0049678	0.00214	0.0019	0.0041384	0.00219	0.0008	0.0041122	0.00105

Appendix A 1. The displacements of selected nodes applied in Ansys as remote displacement on the femur and patella along the X, Y, and Z axes between two frames (02 and 06). Units in metres (m); 0.001 m = 1 mm.

Units: meter	Frame 6			Frame 10			
Node set	X	Y	Z	X	Y	Z	Euclidean distance
P1A	-0.0928	-0.0682	0.36198	-0.0865	-0.0686	0.38109	0.020120981
P1B	-0.1388	-0.073	0.36461	-0.1299	-0.0745	0.38458	0.021893575
P1C	-0.115	-0.0612	0.3352	-0.1084	-0.0697	0.35325	0.021001979
P2A	-0.0944	-0.0712	0.35745	-0.0871	-0.0701	0.37602	0.020006496
P2B	-0.1381	-0.0736	0.36435	-0.1316	-0.0731	0.38508	0.021707195
P2C	-0.1118	-0.065	0.33784	-0.1071	-0.0723	0.3551	0.019329516
P3A	-0.1075	-0.0574	0.36167	-0.0984	-0.0607	0.37982	0.020610182
P3B	-0.1385	-0.0638	0.35075	-0.1311	-0.0695	0.36906	0.020568287
P3C	-0.124	-0.0626	0.33671	-0.119	-0.0715	0.35645	0.022219607
P4A	-0.101	-0.0783	0.37004	-0.1	-0.0765	0.39443	0.024475725
P4B	-0.1373	-0.0739	0.36258	-0.13	-0.0745	0.38378	0.022434936
P4C	-0.118	-0.0659	0.33701	-0.1127	-0.0733	0.3556	0.020725354

Frame No.	$DX_{j=1}$	$DY_{j=1}$	$DZ_{j=1}$	$DX_{j=2}$	$DY_{j=2}$	$DZ_{j=2}$	$DX_{j=3}$	$DY_{j=3}$	$DZ_{j=3}$
F10	-0.0865	-0.0686	0.38109	-0.1299	-0.0745	0.38458	-0.1084	-0.0697	0.35325
F06	-0.0928	-0.0682	0.36198	-0.1388	-0.073	0.36461	-0.115	-0.0612	0.3352
d'/m	0.00629	-0.0004	0.01911	0.00885	-0.0015	0.01997	0.00661	-0.0085	0.01805
F10	-0.0871	-0.0701	0.37602	-0.1316	-0.0731	0.38508	-0.1071	-0.0723	0.3551
F06	-0.0944	-0.0712	0.35745	-0.1381	-0.0736	0.36435	-0.1118	-0.065	0.33784
d'/m	0.00736	0.0011	0.01857	0.00642	0.0005	0.02073	0.00471	-0.0073	0.01726
F10	-0.0984	-0.0607	0.37982	-0.1311	-0.0695	0.36906	-0.119	-0.0715	0.35645
F06	-0.1075	-0.0574	0.36167	-0.1385	-0.0638	0.35075	-0.124	-0.0626	0.33671
d'/m	0.00917	-0.0034	0.01815	0.00741	-0.0057	0.01831	0.00501	-0.0089	0.01974
F10	-0.1	-0.0765	0.39443	-0.13	-0.0745	0.38378	-0.1127	-0.0733	0.3556
F06	-0.101	-0.0783	0.37004	-0.1373	-0.0739	0.36258	-0.118	-0.0659	0.33701
d'/m	0.00099	0.00179	0.02439	0.00731	-0.0007	0.0212	0.00531	-0.0075	0.01859

Node set	X	Y	Z	X	Y	Z	Euclidean distance
F1A	-0.1047	-0.0072	0.39476	-0.1003	-0.0058	0.3967	0.005001197
F1B	-0.1506	-0.0043	0.38128	-0.1452	-0.0023	0.38278	0.005978945
F1C	-0.0739	-0.0079	0.38285	-0.07	-0.006	0.38279	0.004318986
F2A	-0.1115	-0.0391	0.42228	-0.1104	-0.039	0.42186	0.001187773
F2B	-0.1485	-0.0381	0.38401	-0.1444	-0.0364	0.38495	0.004532615
F2C	-0.0691	-0.0219	0.37544	-0.0652	-0.0174	0.37773	0.006315604
F3A	-0.1333	-0.0034	0.39675	-0.1318	-0.0018	0.39466	0.002983562
F3B	-0.148	0.00332	0.37031	-0.141	0.00681	0.37256	0.008112824
F3C	-0.0701	-0.0043	0.3726	-0.0659	-0.0047	0.37325	0.004283448
F4A	-0.1053	-0.0054	0.37405	-0.1019	-0.0042	0.37543	0.003797647
F4B	-0.1421	-0.0031	0.38667	-0.1379	-0.0026	0.39099	0.006045709
F4C	-0.0965	-0.0091	0.41265	-0.0934	-0.0077	0.41013	0.004249601

	$DX_{j=1}$	$DY_{j=1}$	$DZ_{j=1}$	$DX_{j=2}$	$DY_{j=2}$	$DZ_{j=2}$	$DX_{j=3}$	$DY_{j=3}$	$DZ_{j=3}$
F10	-0.07	-0.006	0.38279	-0.1452	-0.0023	0.38278	-0.1003	-0.0058	0.3967
F06	-0.0739	-0.0079	0.38285	-0.1506	-0.0043	0.38128	-0.1047	-0.0072	0.39476
d'/m	0.00387	0.00191	-6.00E-05	0.00544	0.00198	0.0015	0.00439	0.00141	0.00194
F10	-0.0652	-0.0174	0.37773	-0.1444	-0.0364	0.38495	-0.1104	-0.039	0.42186
F06	-0.069	-0.0219	0.37544	-0.1485	-0.0381	0.38401	-0.1115	-0.0391	0.42228
d'/m	0.00387	0.00443	0.00229	0.00411	0.00166	0.00094	0.00111	4.80E-05	-0.0004
F10	-0.0659	-0.0047	0.37325	-0.141	0.00681	0.37256	-0.1318	-0.0018	0.39466
F06	-0.0701	-0.0043	0.3726	-0.148	0.00332	0.37031	-0.1333	-0.0034	0.39675
d'/m	0.00422	-0.0004	0.00065	0.00697	0.00349	0.00225	0.00149	0.00152	-0.0021
F10	-0.0934	-0.0077	0.41013	-0.1379	-0.0026	0.39099	-0.1019	-0.0042	0.37543
F06	-0.0965	-0.0091	0.41265	-0.1421	-0.0031	0.38667	-0.1053	-0.0054	0.37405
d'/m	0.00313	0.00139	-0.00252	0.0042	0.0005	0.00432	0.00334	0.00117	0.00138

Appendix A 2. The displacements of selected nodes applied in Ansys as remote displacement on the femur and patella along the X, Y, and Z axes between two frames (Frame 06 and 10). Units in metres (m); 0.001 m = 1 mm.

Units: meter	Frame 10			Frame 14			
Node set	X	Y	Z	X	Y	Z	Euclidean distance
P1A	-0.0865	-0.0686	0.38109	-0.0816	-0.068	0.39517	0.014910753
P1B	-0.1299	-0.0745	0.38458	-0.1244	-0.0729	0.40156	0.01792185
P1C	-0.1084	-0.0697	0.35325	-0.1041	-0.075	0.3708	0.018849615
P2A	-0.0871	-0.0701	0.37602	-0.0817	-0.0682	0.39371	0.018585156
P2B	-0.1316	-0.0731	0.38508	-0.1271	-0.0707	0.40286	0.018506629
P2C	-0.1071	-0.0723	0.3551	-0.1031	-0.0765	0.37258	0.01839329
P3A	-0.0984	-0.0607	0.37982	-0.0923	-0.0606	0.39527	0.016584223
P3B	-0.1311	-0.0695	0.36906	-0.1257	-0.0708	0.38635	0.018154512
P3C	-0.119	-0.0715	0.35645	-0.1139	-0.0746	0.3744	0.018913175
P4A	-0.1	-0.0765	0.39443	-0.0946	-0.0732	0.41063	0.017376059
P4B	-0.13	-0.0745	0.38378	-0.1251	-0.0723	0.40251	0.019464659
P4C	-0.1127	-0.0733	0.3556	-0.1087	-0.0769	0.37347	0.018652848

Frame No.	$DX_{j=1}$	$DY_{j=1}$	$DZ_{j=1}$	$DX_{j=2}$	$DY_{j=2}$	$DZ_{j=2}$	$DX_{j=3}$	$DY_{j=3}$	$DZ_{j=3}$
F14	-0.0816	-0.068	0.39517	-0.1244	-0.0729	0.40156	-0.1041	-0.075	0.3708
F10	-0.0865	-0.0686	0.38109	-0.1299	-0.0745	0.38458	-0.1084	-0.0697	0.35325
d'/m	0.00487	0.00061	0.01408	0.00551	0.00159	0.01698	0.00429	-0.0054	0.01755
F14	-0.0817	-0.0682	0.39371	-0.1271	-0.0707	0.40286	-0.1031	-0.0765	0.37258
F10	-0.0871	-0.0701	0.37602	-0.1316	-0.0731	0.38508	-0.1071	-0.0723	0.3551
d'/m	0.00537	0.00192	0.01769	0.00455	0.00238	0.01778	0.00394	-0.0042	0.01748
F14	-0.0923	-0.0606	0.39527	-0.1257	-0.0708	0.38635	-0.1139	-0.0746	0.3744
F10	-0.0984	-0.0607	0.37982	-0.1311	-0.0695	0.36906	-0.119	-0.0715	0.35645
d'/m	0.00603	9.60E-05	0.01545	0.00539	-0.0013	0.01729	0.00509	-0.0031	0.01795
F14	-0.0946	-0.0732	0.41063	-0.1251	-0.0723	0.40251	-0.1087	-0.0769	0.37347
F10	-0.1	-0.0765	0.39443	-0.13	-0.0745	0.38378	-0.1127	-0.0733	0.3556
d'/m	0.00538	0.00325	0.0162	0.00481	0.00222	0.01873	0.00394	-0.0036	0.01787

Node set	X	Y	Z	X	Y	Z	Euclidean distance
F1A	-0.1003	-0.0058	0.3967	-0.0951	-0.0089	0.39854	0.006340607
F1B	-0.1452	-0.0023	0.38278	-0.1417	-0.0051	0.38179	0.004596021
F1C	-0.07	-0.006	0.38279	-0.0675	-0.0097	0.38691	0.006030725
F2A	-0.1104	-0.039	0.42186	-0.1063	-0.0428	0.42056	0.005740662
F2B	-0.1444	-0.0364	0.38495	-0.1393	-0.0408	0.38594	0.006788547
F2C	-0.0652	-0.0174	0.37773	-0.0602	-0.0183	0.38005	0.005579249
F3A	-0.1318	-0.0018	0.39466	-0.1277	-0.0044	0.39378	0.004928059
F3B	-0.141	0.00681	0.37256	-0.1365	0.00351	0.37312	0.005602276
F3C	-0.0659	-0.0047	0.37325	-0.0611	-0.0078	0.37493	0.005981925
F4A	-0.1019	-0.0042	0.37543	-0.0969	-0.0076	0.377	0.006195758
F4B	-0.1379	-0.0026	0.39099	-0.1367	-0.0061	0.38882	0.004345778
F4C	-0.0934	-0.0077	0.41013	-0.0904	-0.0101	0.41232	0.004414907

	$DX_{j=1}$	$DY_{j=1}$	$DZ_{j=1}$	$DX_{j=2}$	$DY_{j=2}$	$DZ_{j=2}$	$DX_{j=3}$	$DY_{j=3}$	$DZ_{j=3}$
F14	-0.0675	-0.0097	0.38691	-0.1417	-0.0051	0.38179	-0.0951	-0.0089	0.39854
F10	-0.07	-0.006	0.38279	-0.1452	-0.0023	0.38278	-0.1003	-0.0058	0.3967
d'/m	0.00248	-0.0036	0.00412	0.00351	-0.0028	-0.001	0.00518	-0.0032	0.00184
F14	-0.0602	-0.0183	0.38005	-0.1393	-0.0408	0.38594	-0.1063	-0.0428	0.42056
F10	-0.0652	-0.0174	0.37773	-0.1444	-0.0364	0.38495	-0.1104	-0.039	0.42186
d'/m	0.00501	-0.0008	0.00232	0.00511	-0.0044	0.00099	0.0041	-0.0038	-0.0013
F14	-0.0611	-0.0078	0.37493	-0.1365	0.00351	0.37312	-0.1277	-0.0044	0.39378
F10	-0.0659	-0.0047	0.37325	-0.141	0.00681	0.37256	-0.1318	-0.0018	0.39466
d'/m	0.00486	-0.0031	0.00168	0.00449	-0.0033	0.00056	0.0041	-0.0026	-0.0009
F14	-0.0904	-0.0101	0.41232	-0.1367	-0.0061	0.38882	-0.0969	-0.0076	0.377
F10	-0.0934	-0.0077	0.41013	-0.1379	-0.0026	0.39099	-0.1019	-0.0042	0.37543
d'/m	0.00299	-0.0024	0.00219	0.00121	-0.0036	-0.0022	0.00498	-0.0033	0.00157

Appendix A 3. The displacements of selected nodes applied in Ansys as remote displacement on the femur and patella along the X, Y, and Z axes between two frames (Frame 10 and 14). Units in metres (m); 0.001 m = 1 mm.

Units: meter	Frame 14			Frame 18														
Node set	X	Y	Z	X	Y	Z	Euclidean distance	Frame No.	$DX_{j=1}$	$DY_{j=1}$	$DZ_{j=1}$	$DX_{j=2}$	$DY_{j=2}$	$DZ_{j=2}$	$DX_{j=3}$	$DY_{j=3}$	$DZ_{j=3}$
P1A	-0.0816	-0.068	0.39517	-0.0828	-0.0711	0.4053	0.010680614	F18	-0.0828	-0.0711	0.4053	-0.1251	-0.0763	0.41158	-0.10592	-0.0796	0.38215
P1B	-0.1244	-0.0729	0.40156	-0.1251	-0.0763	0.41158	0.010593698	F14	-0.0816	-0.068	0.39517	-0.1244	-0.0729	0.40156	-0.10413	-0.075	0.3708
P1C	-0.1041	-0.075	0.3708	-0.1059	-0.0796	0.38215	0.012379461	d'/m	-0.0012	-0.0032	0.01013	-0.0007	-0.0034	0.01002	-0.00179	-0.0046	0.01135
P2A	-0.0817	-0.0682	0.39371	-0.0831	-0.0706	0.40438	0.011036994	F18	-0.0831	-0.0706	0.40438	-0.1292	-0.073	0.41267	-0.1032	-0.0808	0.38388
P2B	-0.1271	-0.0707	0.40286	-0.1292	-0.073	0.41267	0.010271022	F14	-0.0817	-0.0682	0.39371	-0.1271	-0.0707	0.40286	-0.10313	-0.0765	0.37258
P2C	-0.1031	-0.0765	0.37258	-0.1032	-0.0808	0.38388	0.012087852	d'/m	-0.0014	-0.0025	0.01067	-0.0021	-0.0022	0.00981	-7.00E-05	-0.0043	0.0113
P3A	-0.0923	-0.0606	0.39527	-0.093	-0.0643	0.40465	0.010090513	F18	-0.093	-0.0643	0.40465	-0.1265	-0.0756	0.39847	-0.11752	-0.0803	0.38943
P3B	-0.1257	-0.0708	0.38635	-0.1265	-0.0756	0.39847	0.013069869	F14	-0.0923	-0.0606	0.39527	-0.1257	-0.0708	0.38635	-0.11393	-0.0746	0.3744
P3C	-0.1139	-0.0746	0.3744	-0.1175	-0.0803	0.38943	0.016474706	d'/m	-0.0007	-0.0037	0.00938	-0.0008	-0.0048	0.01212	-0.00359	-0.0057	0.01503
P4A	-0.0946	-0.0732	0.41063	-0.0964	-0.0755	0.42149	0.011245354	F18	-0.0964	-0.0755	0.42149	-0.1246	-0.0768	0.41042	-0.10993	-0.0821	0.38531
P4B	-0.1251	-0.0723	0.40251	-0.1246	-0.0768	0.41042	0.009125548	F14	-0.0946	-0.0732	0.41063	-0.1251	-0.0723	0.40251	-0.10874	-0.0769	0.37347
P4C	-0.1087	-0.0769	0.37347	-0.1099	-0.0821	0.38531	0.012977418	d'/m	-0.0018	-0.0023	0.01086	0.0005	-0.0045	0.00791	-0.00119	-0.0052	0.01184

Node set	X	Y	Z	X	Y	Z	Euclidean distance		$DX_{j=1}$	$DY_{j=1}$	$DZ_{j=1}$	$DX_{j=2}$	$DY_{j=2}$	$DZ_{j=2}$	$DX_{j=3}$	$DY_{j=3}$	$DZ_{j=3}$
F1A	-0.0951	-0.0089	0.39854	-0.0957	-0.0153	0.39814	0.006438038	F18	-0.066	-0.0146	0.3884	-0.1421	-0.0131	0.38299	-0.095698	-0.0153	0.39814
F1B	-0.1417	-0.0051	0.38179	-0.1421	-0.0131	0.38299	0.008121415	F14	-0.0675	-0.0097	0.38691	-0.1417	-0.0051	0.38179	-0.095134	-0.0089	0.39854
F1C	-0.0675	-0.0097	0.38691	-0.066	-0.0146	0.3884	0.005392685	d'/m	0.00155	-0.0049	0.00149	-0.0004	-0.008	0.0012	-0.000564	-0.0064	-0.0004
F2A	-0.1063	-0.0428	0.42056	-0.1075	-0.0491	0.42265	0.006724775	F18	-0.0596	-0.0246	0.38291	-0.1387	-0.047	0.38867	-0.10746	-0.0491	0.42265
F2B	-0.1393	-0.0408	0.38594	-0.1387	-0.047	0.38867	0.006787425	F14	-0.0602	-0.0183	0.38005	-0.1393	-0.0408	0.38594	-0.10627	-0.0428	0.42056
F2C	-0.0602	-0.0183	0.38005	-0.0596	-0.0246	0.38291	0.006928466	d'/m	0.00056	-0.0063	0.00286	0.00057	-0.0062	0.00273	-0.00119	-0.0063	0.00209
F3A	-0.1277	-0.0044	0.39378	-0.1297	-0.0115	0.39468	0.007368401	F18	-0.0601	-0.0147	0.37692	-0.1355	-0.0042	0.37637	-0.12965	-0.0115	0.39468
F3B	-0.1365	0.00351	0.37312	-0.1355	-0.0042	0.37637	0.008426156	F14	-0.0611	-0.0078	0.37493	-0.1365	0.00351	0.37312	-0.12768	-0.0044	0.39378
F3C	-0.0611	-0.0078	0.37493	-0.0601	-0.0147	0.37692	0.0073063	d'/m	0.00099	-0.007	0.00199	0.00095	-0.0077	0.00325	-0.00197	-0.007	0.0009
F4A	-0.0969	-0.0076	0.377	-0.0957	-0.0143	0.3793	0.0072193	F18	-0.0897	-0.0155	0.41412	-0.135	-0.0128	0.39159	-0.095686	-0.0143	0.3793
F4B	-0.1367	-0.0061	0.38882	-0.135	-0.0128	0.39159	0.007377466	F14	-0.0904	-0.0101	0.41232	-0.1367	-0.0061	0.38882	-0.096937	-0.0076	0.377
F4C	-0.0904	-0.0101	0.41232	-0.0897	-0.0155	0.41412	0.005665961	d'/m	0.00067	-0.0053	0.0018	0.00168	-0.0066	0.00277	0.001251	-0.0067	0.0023

Appendix A 4. The displacements of selected nodes applied in Ansys as remote displacement on the femur and patella along the X, Y, and Z axes between two frames (Frame 14 and 18). Units in metres (m); 0.001 m = 1 mm.

Appendix B

Q_i / Units: mm	X (ML)	Y (AP)	Z (SI)
Patella-SUP	-121.03	-63.949	371.13
Patella-MED	-100.57	-75.306	356.93
Patella-LAT	-147.58	-61.001	353.56
(Frame 02)			
Patella-SUP	-117	-60.507	381.53
Patella-MED	-93.315	-71.788	366.98
Patella-LAT	-143.2	-62.13	360.6
(Frame 06)			
Patella-SUP	-110.66	-56.217	397.12
Patella-MED	-87.946	-73.465	387.61
Patella-LAT	-135.9	-64.871	376.36
(Frame 10)			
Patella-SUP	-107.56	-52.276	410.99
Patella-MED	-83.265	-70.282	405.72
Patella-LAT	-130.58	-64.83	393.04
(Frame 14)			
Patella-SUP	-106.94	-55.151	419.27
Patella-MED	-82.832	-72.977	412.41
Patella-LAT	-131.39	-67.987	403.47
(Frame 18)			

Appendix B 1. The Initial coordinate information of selected Nodes which used for patella matching error verification from frame 02 to 18 For example, (Units: mm)

d_i

Units: meter / Frame No.	Node Set P1			Node Set P2			Node Set P3			Node Set P4		
	dx	dy	dz	dx	dy	dz	dx	dy	dz	dx	dy	dz
Frame 02	0.00547	0.00484	0.00871	0.002844	0.004557	0.00938	0.002807	0.004044	0.009578	0.002024	0.004617	0.010263
	0.00624	0.00362	0.01006	0.004008	0.002469	0.012603	0.003993	0.002229	0.012682	0.003484	0.00254	0.014053
	0.00485	-0.00093	0.00865	0.00318	-0.00113	0.007908	0.003205	-0.00122	0.008097	0.002903	-0.00091	0.008017
Frame 06	0.007213	0.003651	0.017255	0.006453	0.007121	0.015597	0.007666	-0.00174	0.018039	0.003304	0.005491	0.017698
	0.007593	0.000949	0.020028	0.006764	0.004026	0.018629	0.006689	-0.00525	0.019143	0.003857	0.000412	0.022591
	0.00725	-0.00297	0.017711	0.005831	-0.00143	0.017072	0.006941	-0.00403	0.019017	0.004494	-0.00138	0.016684
Frame 10	0.005626	0.004027	0.013151	0.003903	0.006131	0.013552	0.006279	0.002695	0.01503	0.006224	0.004019	0.013925
	0.005396	0.002106	0.015958	0.004682	0.004734	0.018038	0.005907	0.001073	0.017066	0.005285	0.001739	0.015849
	0.004949	-0.00043	0.015784	0.004296	-0.00025	0.015721	0.005714	-0.00016	0.016869	0.004834	0.000699	0.016904
Frame 14	-0.0012	-0.00273	0.009501	-0.00233	-0.00127	0.008761	0.000416	-0.00073	0.009275	-0.00227	-0.00275	0.008887
	-0.00101	-0.00269	0.010199	-0.00183	-0.00133	0.011208	-0.00028	-0.00207	0.010519	-0.00145	-0.00229	0.010915
	-0.00114	-0.00378	0.010174	-0.00148	-0.00323	0.009023	-0.00102	-0.00331	0.012682	-0.00114	-0.00462	0.008806

Appendix B 2. The Ansys output results of the displacements (dX, dY, dZ) of the comparison nodes after moving the patella using each driving node set (P1 to P4) for each frame pair, d_i; Units in metres (m); 0.001 m = 1 mm

$$Q'_{i+n} = Q_i + d_i$$

Units: meter / Frame No.	Medial–lateral (ML-X)	Anterior–posterior (AP-Y)	Superior–inferior (SI-Z)	Medial–lateral (ML-X)	Anterior–posterior (AP-Y)	Superior–inferior (SI-Z)	Medial–lateral (ML-X)	Anterior–posterior (AP-Y)	Superior–inferior (SI-Z)	Medial–lateral (ML-X)	Anterior–posterior (AP-Y)	Superior–inferior (SI-Z)
Frame 02	-0.11556	-0.059109	0.37984	-0.118186	-0.059392	0.3805098	-0.118223	-0.059905	0.3807078	-0.119006	-0.059333	0.381393
	-0.09433	-0.071686	0.36699	-0.096563	-0.072837	0.369533	-0.096577	-0.073077	0.369612	-0.097086	-0.072766	0.370983
	-0.14273	-0.061927	0.36221	-0.1444	-0.062133	0.3614679	-0.144375	-0.062225	0.3616573	-0.144677	-0.061911	0.3615766
Frame 06	-0.109787	-0.056856	0.398785	-0.110547	-0.053386	0.397127	-0.109335	-0.062244	0.399569	-0.113697	-0.055016	0.399228
	-0.085722	-0.070839	0.387008	-0.086552	-0.067762	0.385609	-0.086626	-0.07704	0.386123	-0.089458	-0.071376	0.389571
	-0.13595	-0.065099	0.378311	-0.137369	-0.063565	0.377672	-0.136259	-0.066164	0.379617	-0.138706	-0.063514	0.377284
Frame 10	-0.105034	-0.05219	0.410271	-0.106757	-0.050086	0.410672	-0.104381	-0.053522	0.41215	-0.104437	-0.052198	0.411045
	-0.082551	-0.071359	0.403568	-0.083264	-0.068731	0.405648	-0.082039	-0.072392	0.404676	-0.082661	-0.071726	0.403459
	-0.130951	-0.065301	0.392144	-0.131604	-0.065124	0.392081	-0.130186	-0.065033	0.393229	-0.131066	-0.064172	0.393264
Frame 14	-0.108758	-0.05501	0.4204912	-0.109886	-0.053547	0.4197505	-0.107144	-0.053006	0.4202646	-0.109826	-0.05503	0.419877
	-0.084274	-0.072977	0.415919	-0.08509	-0.071613	0.416928	-0.083545	-0.072356	0.416239	-0.084715	-0.072569	0.416635
	-0.131717	-0.068611	0.403214	-0.132056	-0.068062	0.4020626	-0.131596	-0.068136	0.405722	-0.131717	-0.069455	0.4018455

Appendix B 3. Calculates the new coordinates, Q'_{i+n} of the comparison nodes in frame i+n by adding the ANSYS^{TM} displacements to their initial coordinates in frame. Units in metres (m); 0.001 m = 1 mm

$$Q_{difference} = \|Q'_{i+n} - Q_{i+n}\|_2$$

Units: meter / Frame No.	Node Set P1			Node Set P2			Node Set P3			Node Set P4		
	Medial–lateral (ML-X)	Anterior–posterior (AP-Y)	Superior–inferior (SI-Z)	Medial–lateral (ML-X)	Anterior–posterior (AP-Y)	Superior–inferior (SI-Z)	Medial–lateral (ML-X)	Anterior–posterior (AP-Y)	Superior–inferior (SI-Z)	Medial–lateral (ML-X)	Anterior–posterior (AP-Y)	Superior–inferior (SI-Z)
F02'/F06	-0.00144	-0.001398	0.00169	0.001186	-0.001115	0.00102	0.001223	-0.000602	0.000822	0.002006	-0.001174	0.000137
	0.001015	-0.000102	-0.00001	0.003248	0.001049	-0.002553	0.003262	0.001289	-0.002632	0.003771	0.000978	-0.004003
	-0.00047	-0.000203	-0.00161	0.0012	0.000003	-0.000868	0.001175	0.000095	-0.001057	0.001477	-0.000219	-0.000977
F06'/F10	-0.000873	0.000639	-0.001665	0.00076	-0.00347	0.001658	-0.001213	0.008858	-0.002442	0.004362	-0.007229	0.000341
	-0.002224	-0.002626	0.000602	-0.001395	-0.005703	0.002001	-0.00132	0.003575	0.001487	0.001512	-0.002089	-0.001961
	0.00005	0.000228	-0.001951	0.001469	-0.001307	-0.001312	0.000359	0.001293	-0.003257	0.002806	-0.001357	-0.000924
F10'/F14	-0.002526	-0.000086	0.000719	0.001723	-0.002104	-0.000401	-0.002376	0.003436	-0.001478	0.000055	-0.001324	0.001105
	-0.000715	0.001077	0.002152	-0.000001	-0.001551	0.000072	-0.001226	0.00211	0.001044	-0.000604	0.001444	0.002261
	0.000371	0.000471	0.000896	0.001024	0.000294	0.000959	-0.000394	0.000203	-0.000189	0.000486	-0.000658	-0.000224
F14'/F18	0.001818	-0.000141	-0.001221	0.001129	-0.001463	0.000741	-0.002742	-0.000541	-0.000514	0.002683	0.002024	0.000388
	0.001442	0	-0.003509	0.002258	-0.001364	-0.004518	0.000713	-0.000621	-0.003829	0.001883	-0.000408	-0.004225
	0.000327	0.000624	0.000256	0.000666	0.000075	0.001407	0.000205	0.000149	-0.002252	0.000327	0.001468	0.001624

Appendix B 4. Calculated the differences (errors), $Q_{difference}$ between the predicted coordinates and the actual coordinates in the target frame. Units in metres (m); 0.001 m = 1 mm.

Difference
Units: meter

Landmark	Node No. F02	F06	p1-f1 X	Y	Z	p1-f2 X	Y	Z	p1-f3 X	Y	Z	p1-f4 X	Y	Z
Tibia-ANT	79985	85988	0.0008	0.00411	0.00392	0.00139	0.00519	0.00508	0.00288	0.0042	0.00387	0.00019	0.00415	0.00462
Tibia-LAT	69160	87189	0.00035	0.0025	0.00209	0.00064	0.00374	0.00303	0.00183	0.00338	0.0017	-0.0007	0.00232	0.00234
Tibia-MED	74149	79597	0.00063	0.00435	0.00065	0.00102	0.00546	0.00204	0.00226	0.00426	0.00101	-0.0004	0.00323	0.0013

Landmark	F02	F06	p2-f1 X	Y	Z	p2-f2 X	Y	Z	p2-f3 X	Y	Z	p2-f4 X	Y	Z
Tibia-ANT	79985	85988	0.00066	0.00266	0.00401	0.00164	-0.0081	0.00471	0.00329	-0.0092	0.00338	0.00061	-0.0092	0.00418
Tibia-LAT	69160	87189	0.00025	0.00155	0.00233	0.00242	-0.0025	0.0066	0.00372	-0.0032	0.00506	0.00118	-0.0042	0.00575
Tibia-MED	74149	79597	0.00051	0.00322	0.00084	0.00233	-0.0026	0.00624	0.00373	-0.0038	0.00513	0.0011	-0.0048	0.00547

Landmark	F02	F06	p3-f1 X	Y	Z	p3-f2 X	Y	Z	p3-f3 X	Y	Z	p3-f4 X	Y	Z
Tibia-ANT	79985	85988	-0.0086	0.00213	0.00469	0.00109	0.00392	0.00539	0.00289	0.00278	0.00399	0.00061	-0.0092	0.00418
Tibia-LAT	69160	87189	-0.006	-0.0039	0.0045	0.00045	0.0034	0.00363	0.00189	0.00247	0.00197	0.00118	-0.0043	0.00576
Tibia-MED	74149	79597	-0.0068	0.00067	-0.0015	0.00077	0.00454	0.00245	0.00232	0.00334	0.00129	0.0011	-0.0048	0.00549

Landmark	F02	F06	p4-f1 X	Y	Z	p4-f2 X	Y	Z	p4-f3 X	Y	Z	p4-f4 X	Y	Z
Tibia-ANT	79985	85988	0.00051	0.00226	0.0038	0.0011	0.00396	0.00538	0.00325	0.00268	0.00379	0.00013	0.00283	0.00481
Tibia-LAT	69160	87189	6.4E-05	0.00081	0.00201	0.00045	0.00341	0.00362	0.00218	0.00182	0.00159	-0.0007	0.00155	0.0027
Tibia-MED	74149	79597	0.00032	0.00248	0.00053	0.00077	0.00457	0.00243	0.00268	0.00335	0.00113	-0.0004	0.00237	0.00163

Appendix B 5. Manual calculated the tibia displacements difference alone X, Y and Z directions between Frame 02 to 06. Units in metres (m); 0.001 m = 1 mm.

Difference Units: meter	Node No.		p1-f1			p1-f2			p1-f3			p1-f4		
Landmark	F06	F10	X	Y	Z	X	Y	Z	X	Y	Z	X	Y	Z
Tibia-ANT	85988	78061	0.00019	0.00667	-0.001477	0.00177	0.00826	-0.000479	-0.0085	0.0079	-0.0041	-0.0071	0.00583	-0.001285
Tibia-LAT	87189	83627	0.00389	0.00695	8.74E-05	0.00479	0.00956	0.0005809	0.00915	-0.0046	-0.0029	-0.0014	0.00501	0.001703
Tibia-MED	79597	83298	0.00154	0.00883	-0.001175	0.00263	0.01096	0.000322	0.00789	0.01445	-0.0038	-0.0043	0.00834	-0.002278

			p2-f1			p2-f2			p2-f3			p2-f4		
Landmark	F06	F10	X	Y	Z	X	Y	Z	X	Y	Z	X	Y	Z
Tibia-ANT	85988	78061	0.001	0.00776	-0.002214	0.00198	0.01019	-0.00104	0.00842	0.00861	-0.0045	-0.0026	0.0088	-0.002977
Tibia-LAT	87189	83627	0.00419	0.00571	-0.000983	0.00489	0.01035	-3.86E-05	0.01017	0.00183	-0.0043	0.00241	0.00148	-0.000353
Tibia-MED	79597	83298	0.00194	0.00756	-0.001759	0.00277	0.01224	-0.00024	0.0089	0.01323	-0.0032	0.00012	0.01285	-0.003784

			p3-f1			p3-f2			p3-f3			p3-f4		
Landmark	F06	F10	X	Y	Z	X	Y	Z	X	Y	Z	X	Y	Z
Tibia-ANT	85988	78061	0.00456	0.00866	-0.002597	0.00289	0.00686	-0.000452	0.00068	0.00314	-0.0022	-0.0023	0.00522	-0.002557
Tibia-LAT	87189	83627	0.00858	-0.0059	-0.000587	0.00564	0.00568	0.0004553	0.00423	0.00815	-0.0008	0.00274	-0.0019	7.01E-05
Tibia-MED	79597	83298	0.00714	0.01568	-0.002969	0.00376	0.01089	0.000457	0.00176	0.0062	-0.0016	0.0006	0.01152	-0.003287

			p4-f1			p4-f2			p4-f3			p4-f4		
Landmark	F06	F10	X	Y	Z	X	Y	Z	X	Y	Z	X	Y	Z
Tibia-ANT	85988	78061	0.00031	0.00532	-0.001643	0.00215	0.00824	-0.000639	0.00175	0.00476	-0.0025	/	/	/
Tibia-LAT	87189	83627	0.00362	0.00437	-0.000343	0.00529	0.00867	0.0005137	0.00488	0.00755	-0.0014	/	/	/
Tibia-MED	79597	83298	0.0013	0.0054	-0.001208	0.00316	0.01141	6.84E-05	0.00257	0.00669	-0.0017	/	/	/

Appendix B 6. Manual calculated the tibia displacements difference alone X, Y and Z directions between Frame 06 to 10.

Difference Units: meter	Node No.		p1-f1			p1-f2			p1-f3			p1-f4		
Landmark	F10	F14	X	Y	Z	X	Y	Z	X	Y	Z	X	Y	Z
Tibia-ANT	78061	94540	0.00748	0.00293	-0.004	0.00688	0.00534	-0.00429	0.006	0.00303	-0.0043	0.01111	0.00289	-0.004815
Tibia-LAT	83627	73964	0.00487	-0.0007	-7.65E-04	0.00535	-0.0003	0.0004434	0.00442	-0.001	-5E-05	0.00746	-0.0013	-0.002266
Tibia-MED	83298	93223	0.00683	0.00452	-0.0023	0.00708	0.0091	-0.003953	0.00611	0.00579	-0.0036	0.00976	0.00539	-0.002709

			p2-f1			p2-f2			p2-f3			p2-f4		
Landmark	F10	F14	X	Y	Z	X	Y	Z	X	Y	Z	X	Y	Z
Tibia-ANT	78061	94540	0.0073	0.00223	-0.00353	0.00686	0.00489	-0.003896	0.00581	0.00242	-0.0038	0.01082	0.00229	-0.004379
Tibia-LAT	83627	73964	0.00475	-0.0012	-0.00032	0.00544	-0.0006	9.02E-04	0.00429	-0.0014	0.00043	0.00731	-0.0017	-0.001786
Tibia-MED	83298	93223	0.00669	0.00393	-0.0019	0.00715	0.00901	-0.003729	0.00596	0.00532	-0.0032	0.00957	0.00505	-0.002433

			p3-f1			p3-f2			p3-f3			p3-f4		
Landmark	F10	F14	X	Y	Z	X	Y	Z	X	Y	Z	X	Y	Z
Tibia-ANT	78061	94540	0.00782	0.00252	-0.00377	0.0069	0.00473	-0.003942	0.00632	0.00264	-0.0041	0.01129	0.00241	-0.00452
Tibia-LAT	83627	73964	0.00526	-0.0012	-0.00045	0.00542	-0.0007	0.0007854	0.00483	-0.0016	0.00025	0.00767	-0.0018	-0.001939
Tibia-MED	83298	93223	0.00722	0.00452	-0.00222	0.00715	0.00878	-0.003722	0.00652	0.006	-0.0036	0.00997	0.00522	-0.002527

			p4-f1			p4-f2			p4-f3			p4-f4		
Landmark	F10	F14	X	Y	Z	X	Y	Z	X	Y	Z	X	Y	Z
Tibia-ANT	78061	94540	0.00725	0.0029	-0.004	0.00682	0.00552	-0.004365	0.00576	0.0109	-0.0042	0.01077	0.00299	-0.004842
Tibia-LAT	83627	73964	0.00461	-0.0006	-0.00084	0.00529	-9E-05	0.0003774	0.00414	-0.0008	-9E-05	0.00716	-0.0011	-0.002287
Tibia-MED	83298	93223	0.00657	0.00413	-0.00217	0.00702	0.00919	-4.00E-03	0.00584	0.00559	-0.0034	0.00944	0.0053	-0.002708

Appendix B 7. Manual calculated the tibia displacements difference alone X, Y and Z directions between Frame 10 to 14. Units in metres (m); 0.001 m = 1 mm.

Difference Units: meter	Node No.		p1-f1			p1-f2			p1-f3			p1-f4		
Landmark	F14	F18	X	Y	Z	X	Y	Z	X	Y	Z	X	Y	Z
Tibia-ANT	94540	71692	0.00453	0.00394	0.0006	0.00262	0.004633	0.00148	0.00225	0.00366	0.00133	0.00295	0.00365	0.001541
Tibia-LAT	73964	91312	0.00409	-0.0005	-1.13E-05	0.00219	8.96E-05	0.00092	0.00214	-0.0007	0.00094	0.0025	-0.0013	0.001211
Tibia-MED	93223	76097	0.0053	0.00552	-0.00432	0.00339	0.004897	-0.0026	0.00324	0.00416	-0.0032	0.00371	0.00384	-6.45E-05

			p2-f1			p2-f2			p2-f3			p2-f4		
Landmark	F14	F18	X	Y	Z	X	Y	Z	X	Y	Z	X	Y	Z
Tibia-ANT	94540	71692	0.0043	0.00322	0.00115	0.00249	0.004286	0.00185	0.00207	0.0033	0.00181	0.00262	0.00334	0.001965
Tibia-LAT	73964	91312	0.00383	-0.0012	0.000474	0.00214	-1.82E-05	0.00122	0.00195	-0.0009	0.00129	0.00231	-0.0013	0.00157
Tibia-MED	93223	76097	0.00505	0.00478	-0.00373	0.00331	0.004663	-0.0024	0.00306	0.00383	-0.0027	0.00348	0.00362	-0.002246

			p3-f1			p3-f2			p3-f3			p3-f4		
Landmark	F14	F18	X	Y	Z	X	Y	Z	X	Y	Z	X	Y	Z
Tibia-ANT	94540	71692	0.0043	0.00209	0.002593	0.002	0.002836	0.00359	0.00186	0.00183	0.00329	0.00266	0.00204	0.003546
Tibia-LAT	73964	91312	0.00428	-0.0013	0.001697	0.00195	-0.000299	0.00249	0.00221	-0.0013	0.00252	0.00263	-0.0018	0.002941
Tibia-MED	93223	76097	0.00537	0.00451	-0.00318	0.00304	0.003773	-0.0012	0.00319	0.00316	-0.0021	0.00372	0.00304	-0.001321

			p4-f1			p4-f2			p4-f3			p4-f4		
Landmark	F14	F18	X	Y	Z	X	Y	Z	X	Y	Z	X	Y	Z
Tibia-ANT	94540	71692	0.00453	0.00397	0.000649	0.00259	0.004539	0.00158	0.00223	0.00363	0.00137	0.00303	0.00361	0.001596
Tibia-LAT	73964	91312	0.00413	-0.0004	2.58E-05	0.00218	5.77E-05	0.001	0.00215	-0.0006	0.00092	0.00259	-0.0013	0.001268
Tibia-MED	93223	76097	0.00532	0.00563	-0.00435	0.00337	0.004832	-0.0026	0.00325	0.00419	-0.0032	0.00379	0.00387	-0.002496

Appendix B 8. **Manual calculated the tibia displacements difference alone X, Y and Z directions between Frame** 14 **to** 18**.** Units in **metres (m)**; 0.001 m = 1 mm.

Appendix C

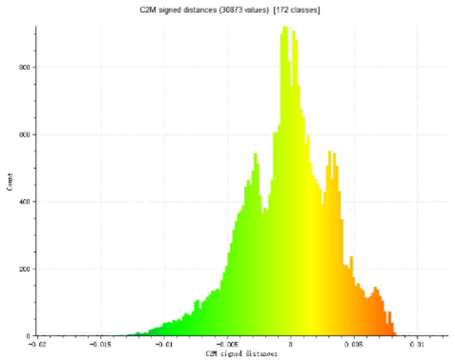

P1-f1

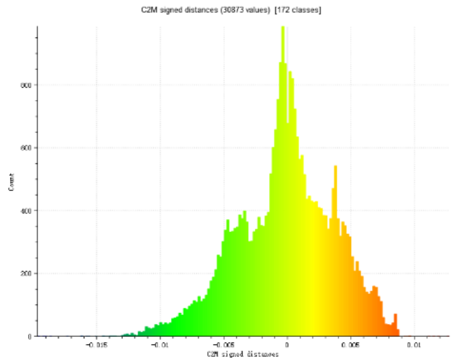

P1-f2

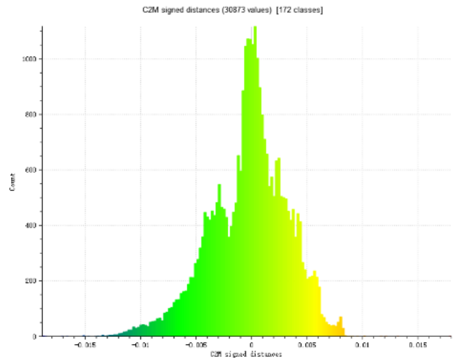

P1-f3

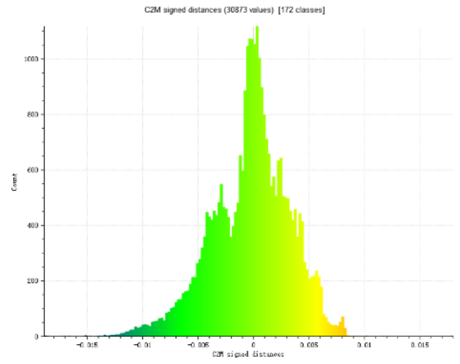

P1-f4

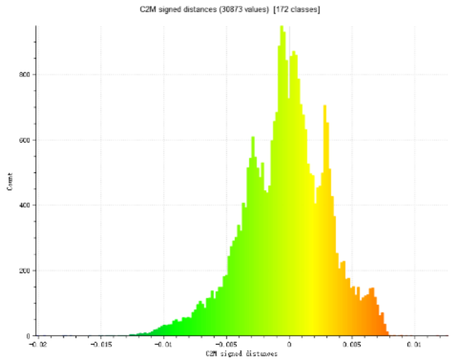

P2-f1

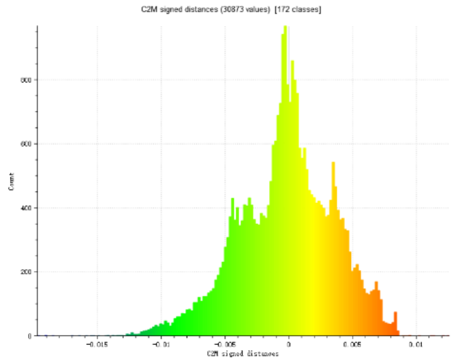

P2-f2

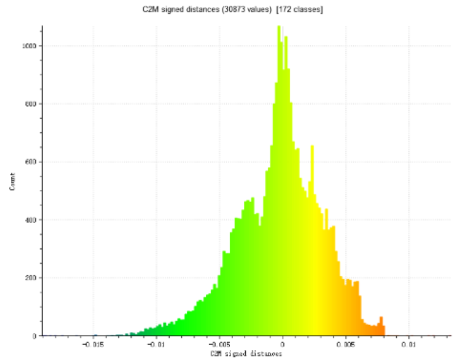

P2-f3

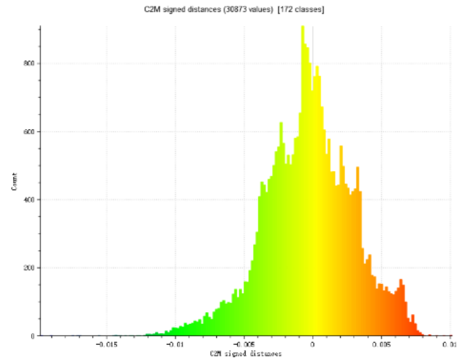

P2-f4

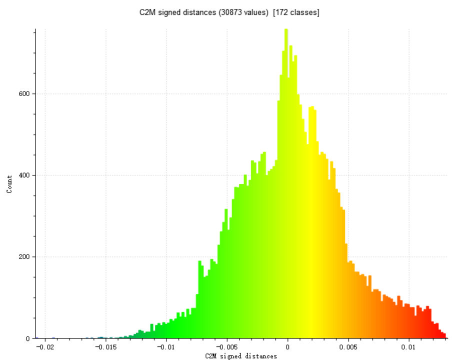

P3-f1

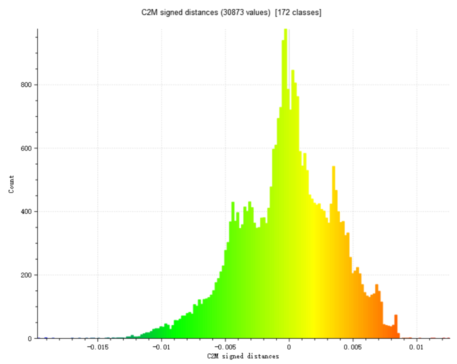

P3-f2

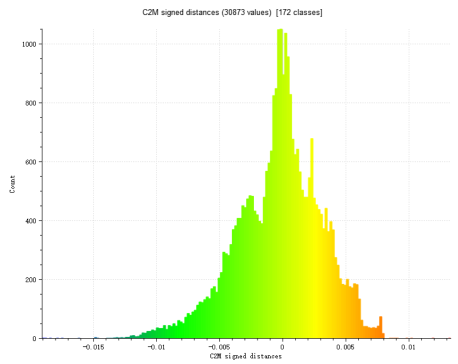

P3-f3

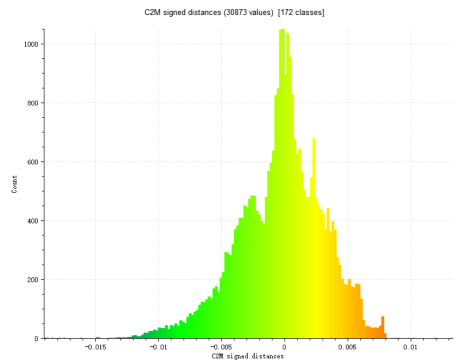

P3-f4

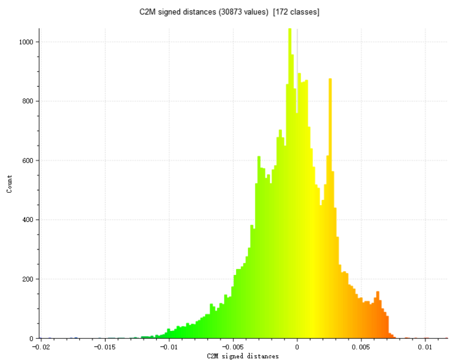

P4-f1

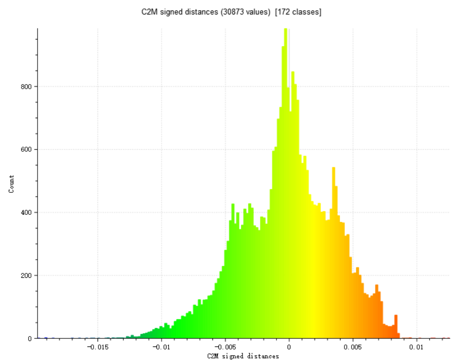

P4-f2

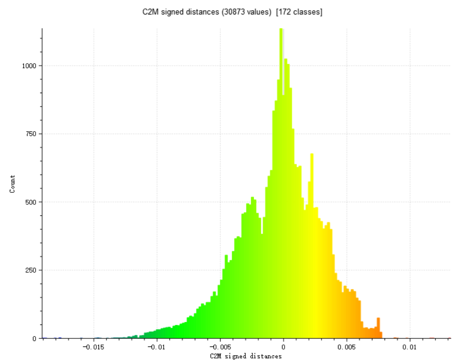

P4-f3

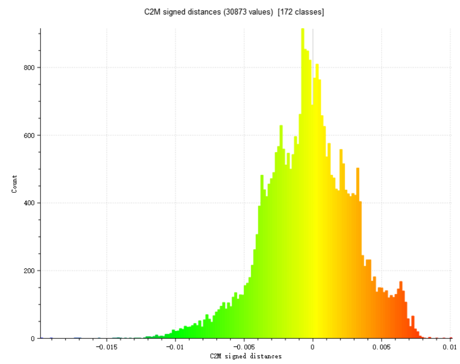

P4-f4

Appendix C 1. Between frame 02 - 06, the component tibia displacement Cloud-compare results. Units in metres (m); 0.001 m = 1 mm.

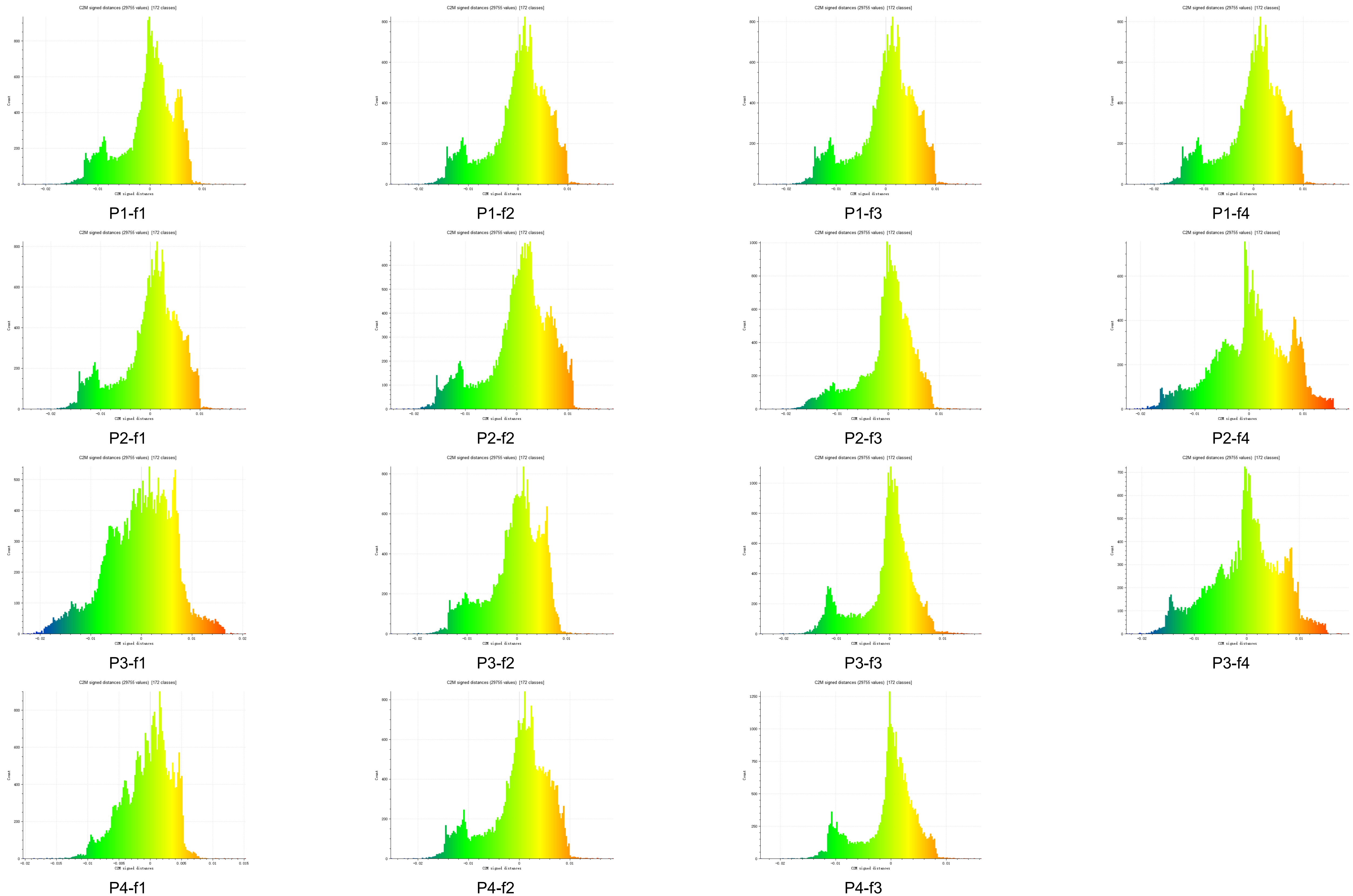

Appendix C 2. Between frame 06 - 10, the component tibia displacement Cloud-compare results. Units in metres (m); 0.001 m = 1 mm.

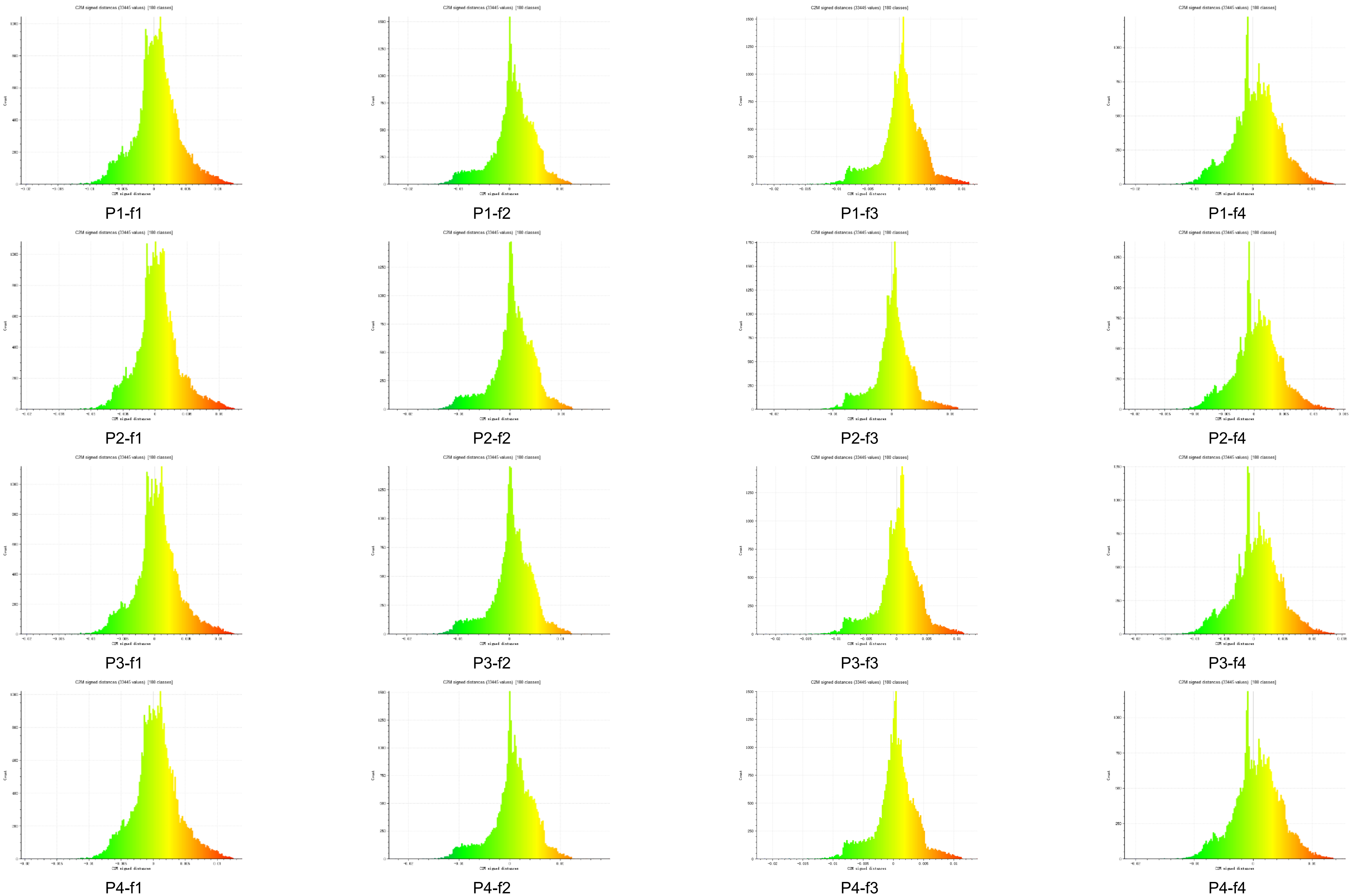

Appendix C 3. Between frame 10 - 14, the component tibia displacement Cloud-compare results. Units in metres (m); 0.001 m = 1 mm.

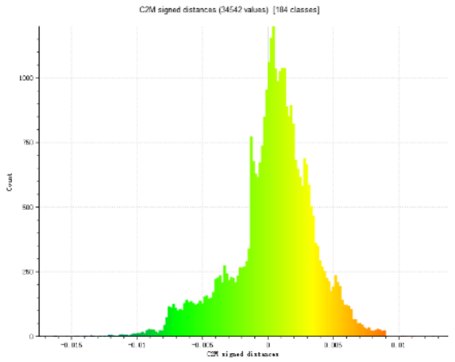

p-f1

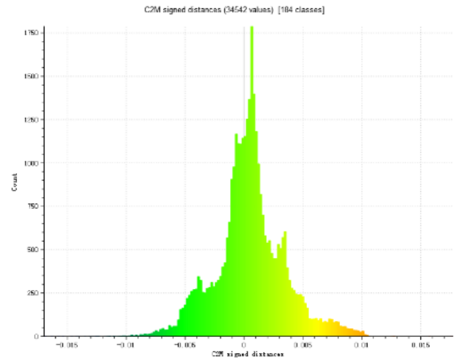

P1-f2

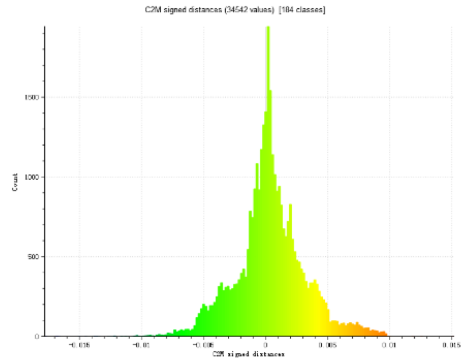

P1-f3

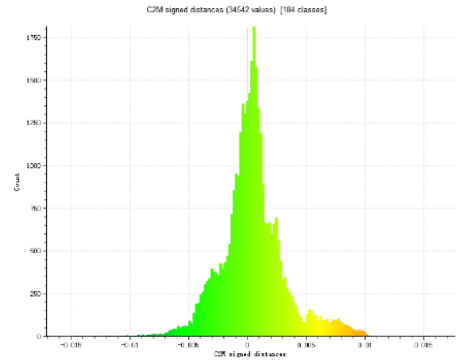

P1-f4

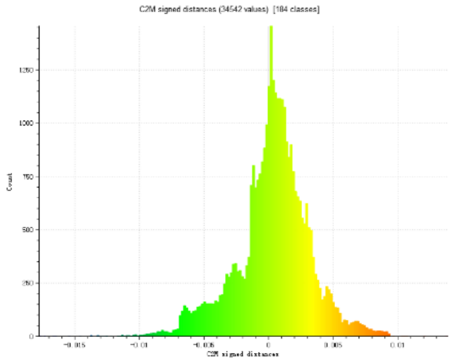

P2-f1

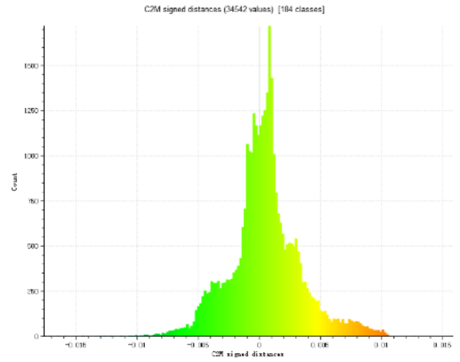

P2-f2

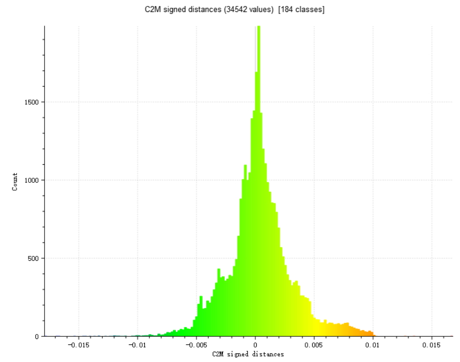

P2-f3

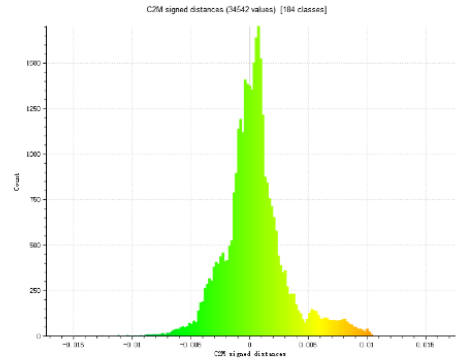

P2-f4

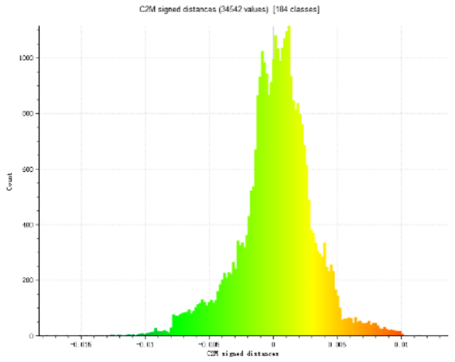

P3-f1

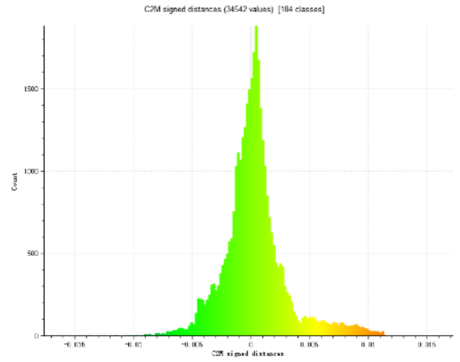

P3-f2

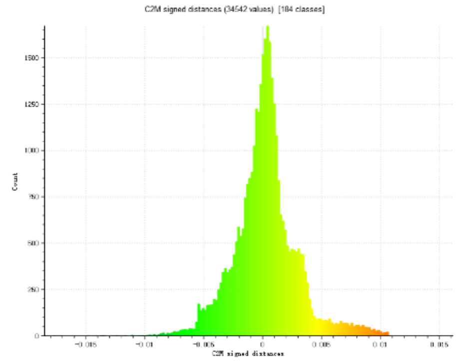

P3-f3

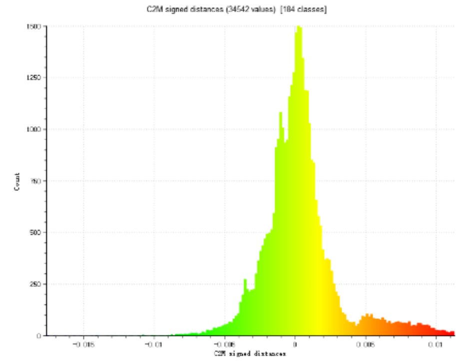

P3-f4

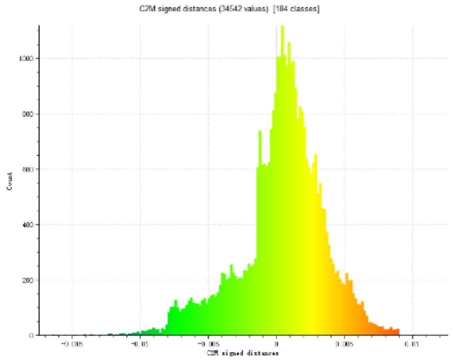

P4-f1

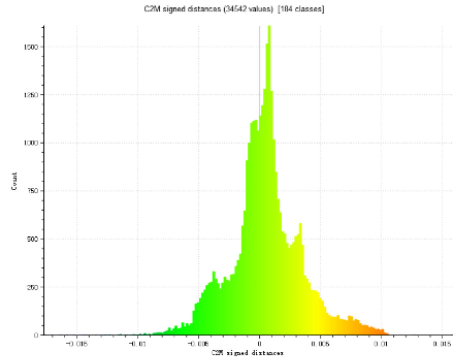

P4-f2

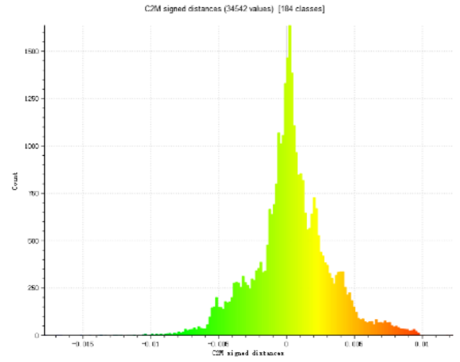

P4-f3

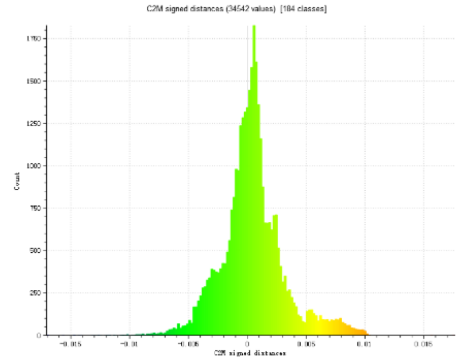

P4-f4

Appendix C 4. Between frame 14 - 18, the component tibia displacement Cloud-compare results. Units in metres (m); 0.001 m = 1 mm.